From thermodynamics to thermometry with single-atom devices

Mark Thomas Mitchison

September 2016

Department of Physics

Imperial College London

Supervised by Dieter Jaksch and Martin B. Plenio

Submitted in part fulfilment of the requirements for the degree of Doctor of Philosophy in Physics of Imperial College London

This thesis presents theoretical research on microscopic measuring devices and thermal machines constructed from single trapped atoms. We study several variants on this theme, with a particular emphasis on their application to ultracold atom physics.

The first part of the thesis is about quantum refrigerators powered by thermal absorption rather than by external work. We propose and detail how such a machine may be practically constructed with a trapped atom placed inside an optical cavity, and employed to cool the atom close to absolute zero temperature using only collimated sunlight as an energy source. We then show that quantum absorption refrigerators in the strong-coupling regime exhibit coherent oscillations, thus enabling one to outperform a typical classical refrigerator by reaching lower temperatures than the steady state in a finite time using quantum coherence.

The second part of the thesis studies the use of impurity atoms as probes of ultracold atomic gases. We discuss two different thermometry methods using impurities which are sensitive to temperature differences on the order of nanokelvin or less. We characterise the precision of the proposed thermometers by explicit calculations in the context of both weakly and strongly interacting atomic Bose gases. Finally, we study impurities immersed in a cold atomic Fermi gas realising a superfluid. We show that the impurities' energy dissipation rate probes the spectrum of density fluctuations in the gas, providing nondestructive access to various properties of the superfluid order parameter along the crossover from a Bardeen-Cooper-Schrieffer (BCS) state to a Bose-Einstein condensate (BEC).

Declaration

I wrote this thesis myself in order to present the products of my doctoral research for examination. The results of others are appropriately cited wherever I have used them. Nevertheless, the context of this thesis is a research field of vast scope, so I am unable to provide an exhaustive list of references to related work. The limited bibliography provided herein reflects partly my specific interests and tastes but mostly my limited knowledge of the literature. I plead forgiveness for any omissions.

In what follows, I avoid the first person singular voice wherever possible, in keeping with academic writing conventions. My use of plural first person pronouns such as "we", "our" and "ours" is usually intended to include either my colleagues and supervisors who helped me to complete this work, or you who are humouring me by reading it. However, in case of doubt, any ostensibly plural first person pronoun may be understood as referring only to *me*, the author, who bears sole responsibility for the shortcomings of this thesis.

— Mark T. Mitchison

The copyright of this thesis rests with the author and is made available under a Creative Commons Attribution Non-Commercial No Derivatives licence. Researchers are free to copy, distribute or transmit the thesis on the condition that they attribute it, that they do not use it for commercial purposes and that they do not alter, transform or build upon it. For any reuse or redistribution, researchers must make clear to others the licence terms of this work.

Acknowledgements

I have been very lucky to have access to not just one, but two outstanding scientists to guide me along the course of my doctoral training. I thank my supervisors Dieter Jaksch and Martin Plenio for their advice, their encouragement, and their physical insight. However, I am most grateful for the complete intellectual liberty and freedom of movement that I have enjoyed over the last few years.

A number of people in their research groups in Oxford and Ulm also deserve my thanks. Juan Jose Mendoza-Arenas was my office mate in Oxford and co-author of my first two papers, and gave me some much-needed help at the beginning of my doctoral studies. During the later part of my PhD, I benefited immensely from collaborating with Tomi Johnson, who was a bountiful source of project ideas and papers, plus general encouragement and pastoral guidance during our meetings in the Clarendon canteen. No graduate of the Jaksch group in recent times could conscionably avoid acknowledging the assistance of Stephen Clark, the erstwhile mainstay of the group's research activities, and the person from whom I learned most of what I know about simulating open quantum systems (often by stealing ideas from his code!). I am grateful to Sarah al-Assam for constant help with her impressive TNT library. I also thank my co-authors Martin Bruderer, Vince Choo, Francesco Cosco, Pierre-Louis Giscard and Dominik Hangleiter: it was an education and a pleasure to work with them all.

A good half of this thesis owes its very existence to a stroke of pure serendipity: a chance meeting with Mischa Woods in the office of Javier Prior, which initiated our collaboration with Marcus Huber. It is a pleasure to thank all three of them for their contributions, and for their friendship. I especially want to thank Javi and Marcus for several generous invitations to visit them in various locations across Europe. These visits were the highlights of my PhD. Through them I met new colleagues in Nicolas Brunner, Pauli Erker, Javier Molina and Ralph Silva, whose collaboration I thankfully acknowledge.

I am grateful to the directors of Imperial College's Centre for Doctoral Training in Controlled Quantum Dynamics — Myungshik Kim, Terry Rudolph, and the late, great Danny Segal — for awarding me my PhD funding and especially for their continued care for student wellbeing. I also thank Miranda Smith for her kindness and her indispensible administrative support from beginning to end. Most importantly, I want to thank my fellow members of CQD Cohort 3 for their camaraderie through the trials, tribulations and triumphs of PhD research. Special mention goes to André Ranchin and Mihai Vidrighin, and the heady mix of palinka, ping pong, kayaking and quantum foundations that we shared during our time living together in Oxford.

Numerous people outside of my working life also deserve acknowledgement. I thank my London friends — especially my housemates Adam, Robbie and Phill — for both distracting me and permitting me space to work, as needed. The love and support of my ultimate study buddy Angelika helped to maintain my sanity while writing this document. My uncle Graeme, whose talk of quantum computation influenced me as a teenage technophile, is partially responsible for the direction I eventually chose. My beloved sister and especially my wonderful and wise parents have ceaselessly given me help, guidance and love, which shaped me profoundly and for which I will be eternally and ineffably grateful. Finally, I dedicate this thesis to my esteemed grandfather Denny, whose best efforts to turn me into a biologist, as he dandled me on his knee while explaining the difference between tRNA and mRNA, apparently did not quite have the desired effect.

"Not only those humble exercises of ours but physics as a whole was marginal, by its nature, by vocation, insofar as it set itself the task of regulating the universe of appearances, whereas the truth, the reality, the intimate essence of things and man exist elsewhere, hidden behind a veil . . . "

— Primo Levi, from *The Periodic Table* (1975)

Contents

Publication list **10**

Author contributions **11**

Introduction and overview **13**

Chapter 1. Open quantum systems theory **17**
1.1 The Lindblad equation . . . 17
1.2 Derivation of the master equation . . . 19
1.3 Energy transport in open quantum networks . . . 24
1.3.1 Tight-binding transport model . . . 25
1.3.2 Spectral density . . . 28
1.3.3 Nonlocal master equation . . . 30
1.3.4 Local master equation . . . 33
1.3.5 Wide-band approximation . . . 34
1.4 Concluding remarks . . . 37

I Quantum absorption refrigerators **41**

Chapter 2. Realising a quantum absorption refrigerator with an atom-cavity system **47**
2.1 Three-body quantum absorption refrigerator . . . 48
2.1.1 Description of the model . . . 48
2.1.2 Virtual qubits and virtual temperatures . . . 49
2.1.3 Figures of merit . . . 51
2.2 Single-cavity refrigerator . . . 52
2.2.1 Description of the model . . . 53
2.2.2 Master equation . . . 55
2.2.3 Line broadening and other constraints . . . 56
2.3 Crossed-cavity absorption refrigerator . . . 58
2.3.1 Description of the model . . . 58
2.3.2 Master equation . . . 60
2.3.3 Phonon dynamics . . . 62
2.3.4 Collective coupling enhancement in many-ion systems . . . 64
2.4 Conclusion . . . 65

Chapter 3. Coherence-assisted single-shot cooling with quantum absorption refrigerators **69**
3.1 General scenario . . . 70
3.2 Thermalisation model . . . 71
3.2.1 Strong-coupling limit . . . 73
3.2.2 Weak-coupling limit . . . 74
3.3 Short-time dynamics of the refrigerator . . . 76
3.4 Effect of initial coherence . . . 77
3.5 Stochastic absorption refrigerator . . . 78
3.6 Comparison with steady-state cooling . . . 79
3.7 Conclusion . . . 81

II Impurity probes in ultracold atomic gases **83**

Chapter 4. Thermometry of cold Bose gases using atomic impurity qubits **87**
4.1 Thermometry by equilibration . . . 88
4.1.1 Description of the system . . . 88
4.1.2 Gaussian approximation for the impurity wave functions . . . 90
4.1.3 Impurity dynamics . . . 92
4.1.4 Thermometry protocols . . . 94
4.1.5 Parallel measurements with multiple impurity probes . . . 97
4.2 Thermometry from work fluctuations . . . 99
4.2.1 Tasaki-Crooks theorem . . . 100
4.2.2 Qubit interferometry . . . 101
4.2.3 Application to the Bose-Hubbard model . . . 103
4.2.4 Tensor-network calculation of the characteristic function . . . 104
4.2.5 Performance of the thermometry protocol . . . 107
4.3 Conclusion . . . 108

Chapter 5. Probing the dynamic structure factor of a neutral Fermi superfluid with impurities **109**
5.1 Theoretical model . . . 110
5.1.1 Fermi superfluid . . . 110
5.1.2 Impurity probe . . . 113
5.1.3 Master equation . . . 115
5.1.4 Form factor in the harmonic approximation . . . 116
5.2 Properties of the spectral function . . . 117
5.2.1 Long-wavelength regime . . . 118
5.2.2 Vicinity of the pair gap . . . 119
5.2.3 Beliaev and Landau damping . . . 120
5.3 Numerical results . . . 121
5.3.1 Measuring the pair gap . . . 121
5.3.2 Separation of discrete and continuous spectra . . . 122
5.4 Conclusion . . . 123

Conclusion and outlook **127**

Bibliography **131**

Appendices

Appendix A. Phase sensitivity analysis for quantum single-shot cooling **153**

Appendix B. Stochastic absorption refrigerator model **157**

Appendix C. Dynamic structure factor in BCS theory **161**
C.1 Static BCS framework 161
C.2 Derivation of the susceptibility 162
C.3 Dynamic structure factor 165

Appendix D. Impurities in a neutral Fermi superfluid **169**
D.1 Single impurity 169
D.2 Multiple impurities 172

Publication list

This thesis is based primarily on the following publications:

[1] *Realising a quantum absorption refrigerator with an atom-cavity system*, M. T. Mitchison, M. Huber, J. Prior, M. P. Woods and M. B. Plenio, Quant. Sci. Tech. **1** 015001 (2016),

[2] *Coherence-assisted single-shot cooling by quantum absorption refrigerators*, M. T. Mitchison, M. P. Woods, J. Prior and M. Huber, New J. Phys. **17** 115013 (2015),

[3] *Nondestructive selective probing of phononic excitations in a cold Bose gas using impurities*, D. Hangleiter, M. T. Mitchison, T. H. Johnson, M. Bruderer, M. B. Plenio and D. Jaksch, Phys. Rev. A **91** 013611 (2015),

[4] *Thermometry of ultracold atoms via nonequilibrium work distributions*, T. H. Johnson, F. Cosco, M. T. Mitchison, D. Jaksch and S. R. Clark, Phys. Rev. A **93** 053619 (2016),

[5] *Probing the dynamic structure factor of a neutral Fermi superfluid along the BCS-BEC crossover using atomic impurity qubits*, M. T. Mitchison, T. H. Johnson and D. Jaksch, Phys. Rev. A **94** 063618 (2016).

The following publications were produced during the doctoral training, but are not covered in great detail in this thesis:

[6] *Transport enhancement from incoherent coupling between one-dimensional quantum conductors*, J. J. Mendoza-Arenas, M. T. Mitchison, S. R. Clark, J. Prior, D. Jaksch and M. B. Plenio, New J. Phys. **16** 053016 (2014),

[7] *An explicit bound for dynamical localisation in an interacting many-body system*, P.-L. Giscard, Z. Choo, M. T. Mitchison, J. J. Mendoza-Arenas and D. Jaksch, arXiv:1402.1421 [quant-ph] (2014).

[8] *Autonomous quantum clocks: does thermodynamics limit our ability to measure time?*, P. Erker, M. T. Mitchison, R. Silva, M. P. Woods, N. Brunner and M. Huber, arXiv:1609.06704 [quant-ph] (2016).

Author contributions

My contributions to the work presented in each chapter of this thesis can be distinguished as follows.

Chapter 1 mainly summarises introductory material in a manner suitable for use later in the thesis. Section 1.3.5 contains some original research of mine under the direction of Martin Plenio, although closely related ideas may be found scattered throughout the literature in one form or another.

Chapter 2 reproduces work published in Ref. [1]. I conceived of the project, performed the calculations and wrote the paper. The other authors of Ref. [1] helped to interpret the results and gave comments on the text.

Chapter 3 reproduces work published in Ref. [2]. I performed the calculations and wrote the majority of the paper. The other authors of Ref. [2] conceived of the project, helped to interpret the results and gave comments on the text. Marcus Huber also wrote some sections of the Introduction and Conclusion, which I have either adapted or removed.

Chapter 4 is based on work published in Refs. [3, 4], which I have adapted to focus on my personal contributions. My principal input to Ref. [3] was to derive the master equation, including the generalisation to multiple impurities, and to write some parts of the paper. The calculation of the tunnelling energy (Fig. 4.2) and the numerical precision analysis (Fig. 4.3 & Table 4.1) were originally performed by Dominik Hangleiter; I have redone these calculations here following methods of my own devising. All calculations presented in Section 4.1 represent my own work. My main contribution to Ref. [4] was to develop the tensor-network algorithm described in Section 4.2.4 with the assistance of Sarah al-Assam, who wrote the core Tensor Network Theory (TNT) library [9] functions on which the algorithm is based; I also wrote some parts of the paper. Figs. 4.8(c,d) are reproduced with permission from Tomi Johnson, who generated them using my data plotted in Figs. 4.8(a,b).

Chapter 5 reproduces work published in Ref. [5]. I conceived of the project, performed the calculations and wrote the paper. The other authors of Ref. [5] helped to interpret the results and gave comments on the text.

Introduction and overview

The quest to transubstantiate matter has enthralled humankind since long before the dawn of science. This goal has itself transmuted throughout the ages according to the needs and abilities of its aspirants. Just as the taming of fire empowered ancient peoples to turn rocks into iron, so the atomic theory of the elements enabled the lucrative science of chemistry to supersede the naive practice of alchemy. In the modern era, physicists are on the cusp of achieving what the alchemists could only dream of: forcing one substance to take on the properties of another. More precisely, the level of control now available over quantum systems across a multitude of platforms, which range from dilute atomic gases to superconducting circuits, enables a physical system with the desired characteristics to be tailor-made by engineering the interactions between its microscopic constituents. This ability promises to open a new chapter in the history of science, since it would facilitate the simulation [10–12] of quantum many-body systems important for chemistry [13,14] and condensed-matter physics [15–23], or indeed full-fledged quantum computation [24, 25].

Such feats of control require experimenters to maximise their information about the system wherever possible. In particular, one generally wishes to minimise initial uncertainty by reliably preparing the system in a low-entropy state. The simplest states to generate are often those in thermal equilibrium, in which case reducing the entropy corresponds to *cooling* the system. Furthermore, if the experiment is to have a useful outcome, the final state of the system must be interrogated by *measuring* some observable accurately and precisely. Effective procedures for both cooling and measurement are therefore important for the development of quantum simulation technology. This is especially true in the context of ultracold atomic gases, since the most interesting quantum states emerge typically at temperatures on the nanokelvin scale, and may exhibit strong or very short-ranged interatomic correlations that confound conventional measurement techniques based on light scattering.

The primary purpose of this thesis is to propose and theoretically investigate new ways to cool and measure quantum systems, with special emphasis on methods involving the manipulation of single trapped atoms. A recurring theme of this work is that the nonequilibrium quantum dynamics of a microscopic system, such as a single atom, may allow one to surpass the performance of standard techniques involving macroscopic cooling or measuring devices. Of course, both cooling and measurement demand the presence of at least one

macroscopic body that is sufficiently complex to induce an irreversible evolution. However, we are mainly interested in situations where one part of the apparatus exhibits manifestly quantum-mechanical behaviour, while the remainder acts merely as a heat reservoir or a classical measuring device. Such scenarios are ideally suited to treatment using the theory of open quantum systems [26–31], which is employed extensively throughout this work.

Let us now briefly outline the structure of the thesis. We begin in Chapter 1 by introducing the necessary concepts and techniques from open quantum systems theory which underlie most of our studies. The remainder of the thesis is split into two nearly independent parts, reflecting the manner in which the research reported herein was conducted. An introduction to the topic in question, together with detailed references to the relevant literature, can be found at the beginning of each of these parts. However, for the sake of motivation we provide here an overview of their contents, as follows.

Part I, comprising Chapters 2 and 3, studies the cooling of microscopic systems by quantum absorption refrigerators (QARs). These are machines powered by the flow of heat from a hot reservoir to a colder one, which can cool without needing an external agent to perform work on the system. This absence of work input lends a certain theoretical elegance to QARs, especially because one may entirely avoid the controversial question of how to define work for quantum systems [32–37]. QARs are also practically appealing, due to their potential for saving energy by harvesting ubiquitous sources of heat or thermal radiation. These properties have recently made QARs the subject of intense scrutiny [38–50] within the broader context of research into thermal machines, such as heat engines, operating at the quantum scale. Historically, this field originated in quantum optics with Scovil and Shulz-DuBois' seminal idea to consider the three-level maser as a heat engine [51], but has since blossomed into a multi-disciplinary program spanning a range of physical architectures, including mesoscopic thermoelectric devices [52, 53], trapped ions [54–56], and photosynthetic reaction centres [57–59].

In this thesis, we are concerned specifically with the application of QARs to the preparation of low-temperature quantum systems such as ultracold atoms. In Chapter 2, which is based on Ref. [1], we provide the first explicit design for a QAR that is able to cool down the motion of a trapped atom using thermal radiation as an energy source. The system comprises an atom or ion confined inside one or two optical cavities, which could be realised in state-of-the-art experiments on cavity quantum electrodynamics [60–66]. We find that, using realistic experimental parameters, sunlight suffices to cool the motion of a trapped ion almost to absolute zero temperature. The success of our scheme relies on the enormous difference between vibrational and optical frequencies, in a similar manner to recent proposals for optomechanical refrigerators [49] and heat engines [67, 68]; however, we also find that this separation of frequency scales necessitates a laser or similar reference system to stabilise the refrigerator. Beyond its practical applications, our work also reveals connections between apparently new concepts from quantum thermodynamics and

decades-old methods for cooling atoms.

In Chapter 3, which is based on Ref. [2], we ask whether quantum coherent effects can improve the operation of QARs. Considering a minimal QAR model consisting of three qubits, we answer this question in the affirmative. Specifically, we find that coherent temperature oscillations enable fast cooling of a target qubit, even reaching lower temperatures than the steady state in a finite time. This counterintuitive effect constitutes one of the first examples where quantum coherence provides a speed-up for thermal machines. Another study [69] published concurrently with Ref. [2] found quantum coherent enhancements for heat engines, while previous research had already shown that coherence could be used to extract work from a single thermal reservoir [70]. Our own work complements and extends these findings by considering the transient dynamics of thermal machines, demonstrating that their short-time evolution can exhibit useful, nonclassical behaviour that may be obscured when considering only their operation in the steady state.

In Part II, which includes Chapters 4 and 5, we change our focus to measuring properties of cold atomic gases using a single impurity atom of a different species as a probe. Such a probe has several advantages, since a trapped impurity is a highly tunable and easily characterised system, which may be localised to submicron length scales, and which minimally perturbs its host gas. These attractive features, in combination with the intrinsic interest of quantum impurity problems, have motivated a substantial body of theoretical work [71–94] and a number of experiments [95–111] studying impurities immersed in ultracold gases.

We focus on simple models involving a trapped, neutral impurity with two relevant states forming a qubit, which is embedded in an ultracold atomic gas. The impurity couples to the gas via collisions with its constituent atoms. It is convenient to model the impurity as an open quantum system, with the gas playing the role of a macroscopic reservoir. By studying the ensuing incoherent dynamics of the qubit, it is possible to extract information on its ultracold gas environment. We are especially interested in situations where such an impurity probe can overcome challenges faced by existing experimental techniques.

For example, the thermometry of ultracold gases is difficult, particularly in strongly interacting systems. In Chapter 4, we examine two different ways to measure the temperature of ultracold Bose gases using impurity atoms, which were proposed in Refs. [3, 4]. The first thermometry technique involves monitoring the energy of an impurity confined by a double-well potential as it equilibrates with the gas. The second method proceeds by using an impurity qubit to extract the probability distributions of work performed in two Hamiltonian quenches [112–114]; these work distributions are related to the temperature by the Tasaki-Crooks theorem [115, 116]. We verify by explicit calculation that, within their respective domains of applicability, both of our proposed thermometry protocols can accurately and precisely measure temperatures in the nanokelvin regime, which may be difficult to access via conventional methods. Interestingly, we find that the second ther-

mometry method is effective even for strongly interacting systems, thus offering a solution to the outstanding problem of generic low-temperature thermometry in highly correlated atomic gases. These results add to a growing theoretical literature on thermometry using quantum probes [71, 72, 117–120], while the first experiments using impurities to infer the temperature of a cold Bose gas have recently been performed [102].

In Chapter 5, we propose an impurity-based probe of the spectrum of density fluctuations in a superfluid of cold fermionic atoms. Density fluctuations in fermionic superfluids are of significant interest [121–126] because they yield information on the crossover from a Bardeen-Cooper-Schrieffer state to a Bose-Einstein condensate [127–129], which is relevant for understanding strongly correlated fermion systems in condensed-matter [130] and high-energy [131] physics. We show that measuring the impurity's energy dissipation rate gives access to several interesting properties of the superfluid, including the excitation gap for creating quasiparticle pairs and the damping of collective oscillations of the fermion condensate. Our work puts forward a novel, nondestructive method for probing the density excitation spectrum of cold atomic gases, which would complement ongoing efforts to measure density fluctuations in Fermi superfluids using Bragg spectroscopy [132–137].

Before we plunge into these investigations, note some conventions used throughout our work. A boldface symbol $\mathbf{k}$ denotes a three-dimensional vector with magnitude k, unless stated otherwise. The Euler constant is denoted by e and the imaginary unit is denoted by i, e.g. $1 + \mathrm{e}^{\mathrm{i}\pi} = 0$. The notations $[\bullet, \bullet]$ and $\{\bullet, \bullet\}$ mean the commutator and the anticommutator, respectively. We work in units where the reduced Planck constant $\hbar = 1$ and the Boltzmann constant $k_B = 1$.

Chapter 1

Open quantum systems theory

In this thesis, we adopt an open-systems approach to physics. Here, the system under study is conceptually divided into two parts: a small subsystem of interest, called the *open system*, and a wider environment representing the remaining degrees of freedom. Virtually any physical problem may be treated within this framework, since we usually want to predict the observable behaviour of only a small part of the universe, this being especially true in atomic physics. The theory of open quantum systems is concerned with predicting the dynamics of the open system, including the most important effects arising due to its unavoidable interaction with the environment. In this preliminary chapter we introduce the basic elements of open-systems theory used throughout this thesis.

Formally, the state of an open quantum system lives in one part of a bipartite Hilbert space $\mathbb{H} = \mathbb{H}_A \otimes \mathbb{H}_B$, where $\mathbb{H}_A$ and $\mathbb{H}_B$ pertain to the open system and environment, respectively. We use the terms "environment", "reservoir" and "bath" interchangeably. The central quantity of interest is the reduced density matrix of the open system $\rho_A(t) = \mathrm{Tr}_B[\rho(t)]$, where $\rho(t)$ is the global state on $\mathbb{H}$ at time t and Tr_B is the trace over $\mathbb{H}_B$. Assuming that the open system together with its environment are isolated from external influences, the exact solution for $\rho_A(t)$ given some initial condition $\rho(0)$ is

$$\rho_A(t) = \mathrm{Tr}_B \left[\mathrm{e}^{-\mathrm{i}Ht} \rho(0) \mathrm{e}^{\mathrm{i}Ht} \right], \tag{1.1}$$

where H is the global Hamiltonian on $\mathbb{H}$. In certain special instances, it may be possible to solve Eq. (1.1) by brute-force methods such as tensor-network algorithms, as appropriate for one-dimensional geometries (such an example is discussed in Chapter 4). However, in the vast majority of cases a direct attack on Eq. (1.1) is doomed to fail, therefore some approximation scheme is needed.

1.1 The Lindblad equation

One of the most common methods for modelling open systems, used frequently throughout this thesis, is the master equation. This is an equation of motion for ρ_A, which approximately accounts for the effect of environmental fluctuations on the open system. In order

for the resulting evolution to be physically meaningful, we demand that it be completely positive and trace-preserving (CPTP). In the simplest case, the dynamics is also Markovian, meaning that the time derivative of ρ_A at time t depends only on $\rho_A(t)$. The most general Markovian master equation generating a linear, CPTP evolution is the Lindblad equation [138, 139]

$$\frac{\mathrm{d}\rho_A}{\mathrm{d}t} = \mathrm{i}[\rho_A, H_S] + \sum_m \gamma_m \left(L_m \rho_A L_m^\dagger - \frac{1}{2} \left\{ L_m^\dagger L_m, \rho_A \right\} \right). \tag{1.2}$$

Here, H_S is a Hamiltonian describing coherent processes, while the Lindblad operators L_m describe incoherent "jumps" occurring at a rate γ_m.

The Lindblad equation may either be postulated on phenomenological grounds, or derived from first principles. In the latter case, the derivation requires the assumption of at least two well-separated dynamical time scales, one fast and one slow. A typical scenario involves a small open system embedded in a many-body environment, which together form an isolated system that evolves unitarily. The open system evolves over a characteristic time τ_A due to its coupling with the bath. Meanwhile, the environment variables relax to equilibrium over a correlation time τ_B. A Markovian master equation can be derived under the condition $\tau_B \ll \tau_A$, meaning that the reservoir is approximately memoryless over the time scales relevant for the open system evolution. Note that, in order for τ_A to be slow, the open system must be coupled *weakly* to its environment, which justifies an additional technical, yet essential, assumption that any initial correlations between the system and the environment can be ignored.

As an example of the above, consider a trapped impurity atom exchanging energy with a cold gas of a different atomic species, as in Part II of this thesis. In this case, τ_A represents the time scale of energy dissipation from the impurity due to its coupling with the gas. Importantly, the impurity atom interacts with *local* degrees of freedom of its environment, e.g. the density of the gas in the impurity's immediate surroundings. If the density of the gas is locally perturbed, it typically returns to equilibrium over a correlation time $\tau_B \sim \ell/c$, where ℓ is the length scale of the perturbation and c is the characteristic velocity of elementary excitations in the gas, e.g. the speed of sound. In the present example, ℓ represents the length scale of the impurity confinement, and thus the Markovian regime of $\tau_B \ll \tau_A$ can be achieved by reducing the effective size of the impurity (so long as the impurity-gas coupling is weak). It is here apparent that Markovianity is related to the small size of the open system in comparison to its environment. A similar principle underpins the effectiveness of the Markov approximation in describing small quantum conductors coupled to macroscopic metal leads, dipole emitters interacting with the electromagnetic radiation field, and many other examples.

Alternatively, the reservoir itself could be subject to external influences, so that the global evolution is not unitary. Scenarios of this type are modelled in Chapter 2. In such

cases, the correlation time τ_B is the inverse of a characteristic rate of energy dissipation from the environment due to its coupling with the outside world. The Markov regime of $\tau_B \ll \tau_A$ is then obtained when the external damping of the reservoir dominates over its weak interaction with the open system.

1.2 Derivation of the master equation

The derivation of the Lindblad equation is textbook material, and variations on the standard theme may be found in, for example, Refs. [26–29], and many other books. Unfortunately, none of these references provide a sufficiently general treatment to satisfy the needs of this thesis. We therefore provide our own derivation of the master equation in this section. This also serves as a starting point for our discussion of open quantum networks in Section 1.3.

We begin with the equation of motion for the global density operator, written generally as

$$\frac{\mathrm{d}\rho}{\mathrm{d}t} = \mathcal{L}\rho. \tag{1.3}$$

The Liouvillian $\mathcal{L}$ is a superoperator, i.e. a linear map taking one operator on $\mathbb{H}$, such as a density matrix, to another operator on $\mathbb{H}$. The Liouvillian is assumed to generate a CPTP evolution. We decompose the Liouvillian as $\mathcal{L} = \mathcal{L}_0 + \mathcal{L}_1 + \mathcal{H}_{AB}$, where $\mathcal{L}_0 = \mathcal{H}_A + \mathcal{L}_B$. Here, and throughout this thesis, a calligraphic $\mathcal{H}$ denotes the superoperator of commutation with the corresponding Hamiltonian, e.g.

$$\mathcal{H}_A\rho = \mathrm{i}[\rho, H_A], \tag{1.4}$$

where H_A describes the largest coherent contribution to the autonomous dynamics of the open system, and acts only on $\mathbb{H}_A$. The Liouvillian $\mathcal{L}_B$ contains all coherent and incoherent contributions acting only on the environment Hilbert space $\mathbb{H}_B$. In the case where the evolution of the reservoir is fully coherent and described by a Hamiltonian H_B, we have $\mathcal{L}_B = \mathcal{H}_B$, i.e.

$$\mathcal{L}_B\rho = \mathrm{i}[\rho, H_B]. \tag{1.5}$$

The term $\mathcal{L}_1$ describes all other coherent or incoherent processes acting only on $\mathbb{H}_A$. Finally, $\mathcal{H}_{AB}$ describes the coupling between system and environment according to the interaction Hamiltonian H_{AB}.

The master equation is derived by treating the terms $\mathcal{L}_1 + \mathcal{H}_{AB}$ as a small perturbation with respect to $\mathcal{L}_0$. We move to an interaction picture defined by [140]

$$\tilde{\rho}(t) = \mathrm{e}^{-\mathcal{L}_0 t}\rho(t). \tag{1.6}$$

In this picture, the evolution equation reads as

$$\frac{\mathrm{d}\tilde{\rho}}{\mathrm{d}t} = \mathcal{L}_1(t)\tilde{\rho}(t) + \mathcal{H}_{AB}(t)\tilde{\rho}(t), \tag{1.7}$$

where $\mathcal{H}_{AB}(t) = \mathrm{e}^{-\mathcal{L}_0 t}\mathcal{H}_{AB}\mathrm{e}^{\mathcal{L}_0 t}$, and similarly for $\mathcal{L}_1(t)$. It is important to note that the action of superoperators such as $\mathcal{L}_0$ is not associative: rather, they are defined to operate on everything appearing to their right.

We now introduce a projector onto the relevant degrees of freedom:

$$\mathcal{P}\rho(t) = \mathrm{Tr}_B[\rho(t)] \otimes \rho_B, \tag{1.8}$$

where ρ_B is some reference state of the environment. One easily checks that $\mathcal{P}^2 = \mathcal{P}$, as required for a projection. The orthogonal complement of $\mathcal{P}$ is denoted by $\mathcal{Q} = 1 - \mathcal{P}$. We assume that the initial quantum state factorises as $\rho(0) = \rho_A(0) \otimes \rho_B$, so that $\mathcal{Q}\rho(0) = 0$, which is justified by the weak-coupling assumption. We consider only reference states which are stationary with respect to $\mathcal{L}_B$, i.e. $\mathcal{L}_B\rho_B = 0$. In the case where the evolution of the environment is purely Hamiltonian, $\mathcal{L}_B = \mathcal{H}_B$, this condition implies that the state ρ_B is diagonal in the energy eigenbasis of H_B, for example a thermal equilibrium state. On the other hand, if the environment undergoes dissipative dynamics then ρ_B is the asymptotic steady state. Finally, we assume that $\mathrm{Tr}_B[\rho_B H_{AB}] = 0$, which can always be satisfied by a suitable redefinition of H_A and H_{AB}. The foregoing assumptions can be formally summarised as

$$[\mathcal{L}_0, \mathcal{P}] = 0, \tag{1.9}$$

$$[\mathcal{L}_1(t), \mathcal{P}] = 0, \tag{1.10}$$

$$\mathcal{P}\mathcal{H}_{AB}(t)\mathcal{P} = 0. \tag{1.11}$$

Inserting the identity operator $1 = \mathcal{P} + \mathcal{Q}$ onto both sides of the evolution equation (1.7), we obtain

$$\frac{\mathrm{d}\mathcal{P}\tilde{\rho}}{\mathrm{d}t} = \mathcal{L}_1(t)\mathcal{P}\tilde{\rho}(t) + \mathcal{P}\mathcal{H}_{AB}(t)\mathcal{Q}\tilde{\rho}(t), \tag{1.12}$$

$$\frac{\mathrm{d}\mathcal{Q}\tilde{\rho}}{\mathrm{d}t} = \mathcal{L}_1(t)\mathcal{Q}\tilde{\rho}(t) + \mathcal{Q}\mathcal{H}_{AB}(t)\mathcal{Q}\tilde{\rho}(t) + \mathcal{Q}\mathcal{H}_{AB}(t)\mathcal{P}\tilde{\rho}(t). \tag{1.13}$$

The solution of Eq. (1.13) is

$$\mathcal{Q}\tilde{\rho}(t) = \mathcal{K}(t,0)\mathcal{Q}\rho(0) + \int_0^t \mathrm{d}t'\, \mathcal{K}(t,t')\mathcal{Q}\mathcal{H}_{AB}(t')\mathcal{P}\tilde{\rho}(t'), \tag{1.14}$$

with the propagator given by

$$\mathcal{K}(t,t') = \mathsf{T}\exp\left\{\int_{t'}^{t} \mathrm{d}s\,[\mathcal{L}_1(s) + \mathcal{Q}\mathcal{H}_{AB}(s)]\right\}, \tag{1.15}$$

where T denotes the usual time ordering. The first term on the right-hand side (RHS) of Eq. (1.14) vanishes since $\mathcal{Q}\rho(0) = 0$. Plugging the remainder of this solution back into Eq. (1.12), we obtain

$$\frac{\mathrm{d}\mathcal{P}\tilde{\rho}}{\mathrm{d}t} = \mathcal{L}_1(t)\mathcal{P}\tilde{\rho}(t) + \int_0^t \mathrm{d}t'\,\mathcal{P}\mathcal{H}_{AB}(t)\mathcal{K}(t,t')\mathcal{H}_{AB}(t')\mathcal{P}\tilde{\rho}(t'), \tag{1.16}$$

where we have used Eq. (1.11). This equation gives the exact formal solution for the time evolution of the open-system density operator. To make progress, we expand the exact propagator $\mathcal{K}(t,t')$ to lowest (zeroth) order in $\mathcal{L}_1$ and $\mathcal{H}_{AB}$, which leads to

$$\frac{\mathrm{d}\mathcal{P}\tilde{\rho}}{\mathrm{d}t} = \mathcal{L}_1(t)\mathcal{P}\tilde{\rho}(t) + \int_0^t \mathrm{d}t'\,\mathcal{P}\mathcal{H}_{AB}(t)\mathcal{H}_{AB}(t')\mathcal{P}\tilde{\rho}(t'). \tag{1.17}$$

Eq. (1.17) is the Nakajima-Zwanzig (NZ) equation. The NZ equation describes the evolution of the open system in terms of a convolution over its past history encoded in $\tilde{\rho}(t')$, making it difficult to solve. This feature can be removed self-consistently by noting that the time derivative of $\mathcal{P}\tilde{\rho}$ is at least first order in small quantities. We can therefore expand the density operator as $\mathcal{P}\tilde{\rho}(t') = \mathcal{P}\tilde{\rho}(t) + (t'-t)\mathrm{d}\mathcal{P}\tilde{\rho}/\mathrm{d}t + \ldots$. Assuming that the rest of the integrand in Eq. (1.17) decays sufficiently quickly, we can therefore write, at the same order of perturbation theory,

$$\frac{\mathrm{d}\mathcal{P}\tilde{\rho}}{\mathrm{d}t} = \mathcal{L}_1(t)\mathcal{P}\tilde{\rho}(t) + \int_0^t \mathrm{d}s\,\mathcal{P}\mathcal{H}_{AB}(t)\mathcal{H}_{AB}(t-s)\mathcal{P}\tilde{\rho}(t), \tag{1.18}$$

where we changed variables to $s = t - t'$. Eq. (1.18) is known as the time-convolutionless (TCL) master equation. It is also possible to obtain Eq. (1.18) from Eq. (1.17) using a more formal perturbative argument (see Ref. [26], for example).

The TCL equation can be put into a more transparent form by expanding the interaction Hamiltonian into tensor products of operators

$$H_{AB} = \sum_m A_m \otimes B_m, \tag{1.19}$$

where A_m (B_m) acts on $\mathbb{H}_A$ ($\mathbb{H}_B$) only. Substituting this expression into Eq. (1.18),

expanding the commutators and then tracing over the environment, we find

$$\begin{aligned}&\mathrm{Tr}_B \int_0^t \mathrm{d}s\, \mathcal{P}\mathcal{H}_{AB}(t)\mathcal{H}_{AB}(t-s)\mathcal{P}\tilde{\rho}(t)\\&= \sum_{m,n}\int_0^t \mathrm{d}s\, \tilde{\Gamma}_{mn}(s)\left[\tilde{A}_m(t-s)\tilde{\rho}_A(t)\tilde{A}_n(t) - \tilde{A}_n^\dagger(t)\tilde{\rho}_A(t)\tilde{A}_m(t-s)\right] + \text{h.c.},\end{aligned} \tag{1.20}$$

where $\tilde{\rho}_A(t) = \mathrm{e}^{\mathrm{i}H_A t}\rho_A(t)\mathrm{e}^{-\mathrm{i}H_A t}$, $\tilde{A}_m(t) = \mathrm{e}^{\mathrm{i}H_A t}A_m\mathrm{e}^{-\mathrm{i}H_A t}$, and we introduced a matrix of reservoir correlation functions

$$\tilde{\Gamma}_{mn}(s) = \mathrm{Tr}_B\left[\tilde{B}_n^\dagger(s)\tilde{B}_m(0)\rho_B\right], \tag{1.21}$$

with $\tilde{B}_n(s) = \mathrm{e}^{\mathcal{L}_B^\dagger s}B_n$, where $\mathcal{L}_B^\dagger$ is the adjoint Liouvillian defined by $\mathrm{Tr}_B[\mathcal{L}_B(P)Q] = \mathrm{Tr}_B[P\mathcal{L}_B^\dagger(Q)]$ for arbitrary operators P and Q acting on $\mathbb{H}_B$.

The master equation description rests on the assumption that the correlation functions (1.21) decay rapidly to zero over some time scale τ_B. Clearly, this can happen only if the environment is very large or subject to some external dissipation. In many cases of physical interest, τ_B is far smaller than any other time scale relevant for the open system's dynamics. In this case, we can make the Markov approximation by taking the upper s-integration limit to infinity in Eq. (1.20). Tracing back through the derivation, this corresponds to extending the time convolution in Eq. (1.16) over the entire past history of the system, thus removing any memory of the initial time $t = 0$. This approximation is often lumped together with the weak-coupling assumption and referred to as the Born-Markov approximation.

In order to write the Born-Markov master equation in a convenient form, we expand the interaction-picture system operators into eigenoperators of the Hamiltonian as

$$\tilde{A}_m(t) = \sum_\nu \mathrm{e}^{-\mathrm{i}\nu t}A_m(\nu), \tag{1.22}$$

where the summation runs over all values of the Bohr frequencies ν of H_A, i.e. the differences between energy eigenvalues. Explicitly, the eigenoperators have the form

$$A_m(\nu) = \sum_{\Omega'-\Omega=\nu} \langle\Omega|A_m|\Omega'\rangle\, |\Omega\rangle\langle\Omega'|, \tag{1.23}$$

where $|\Omega\rangle$ is an eigenstate of H_A with energy Ω, and the sum runs over all values of Ω and Ω' such that $\Omega' - \Omega = \nu$. Plugging this expansion into Eq. (1.20) and making the Markov approximation yields the Redfield dissipator

$$\sum_{m,n}\sum_{\nu,\nu'}\Gamma_{mn}(\nu)\mathrm{e}^{\mathrm{i}(\nu'-\nu)t}\left[A_m(\nu)\tilde{\rho}_A(t)A_n^\dagger(\nu') - A_n^\dagger(\nu')A_m(\nu)\tilde{\rho}_A(t)\right] + \text{h.c.} \tag{1.24}$$

Here we defined the spectral correlation matrix

$$\begin{aligned}\Gamma_{mn}(\nu) &= \int_0^\infty \mathrm{d}t\, \mathrm{e}^{\mathrm{i}\nu t}\tilde{\Gamma}_{mn}(t) \\ &= \pi\mathcal{I}_{mn}(\nu) + \mathrm{i}\mathsf{P}\int_{-\infty}^{\infty}\mathrm{d}\omega\, \frac{\mathcal{I}_{mn}(\omega)}{\nu-\omega},\end{aligned} \tag{1.25}$$

where P denotes the principal value and we introduced the *spectral function* $\mathcal{I}_{mn}(\nu)$ associated with each reservoir correlation function $\tilde{\Gamma}_{mn}(t)$, the two being related by the Fourier transform

$$\tilde{\Gamma}_{mn}(t) = \int_{-\infty}^{\infty}\mathrm{d}\nu\, \mathrm{e}^{-\mathrm{i}\nu t}\mathcal{I}_{mn}(\nu). \tag{1.26}$$

The spectral correlation matrix can be further decomposed into two real contributions

$$\gamma_{mn}(\nu) = \Gamma_{mn}(\nu) + \Gamma^*_{nm}(\nu), \tag{1.27}$$

$$S_{mn}(\nu) = \frac{1}{2\mathrm{i}}\left(\Gamma_{mn}(\nu) - \Gamma^*_{nm}(\nu)\right), \tag{1.28}$$

corresponding to dissipation rates and energy shifts, respectively.

The final assumption needed to obtain a Lindblad equation is the rotating-wave approximation (RWA). Here, we assume that the typical differences between the Bohr frequencies of the open system are much larger than the dissipation rates. More precisely, the RWA requires that $\max\{|\Gamma_{mn}(\nu)|\} \ll \min\{|\nu-\nu'|\}$. If this condition is satisfied, we can neglect the fast-oscillating terms with $\nu \neq \nu'$. This approximation is a kind of coarse-graining in time, in which we effectively average the time evolution over periods much longer than the open-system relaxation time τ_A, where τ_A is given by the inverse of a typical value of $\gamma_{mn}(\nu)$ or $S_{mn}(\nu)$.

After making the RWA, we transform back to the Schrödinger picture, thus arriving at the Lindblad equation

$$\frac{\mathrm{d}\rho_A}{\mathrm{d}t} = \mathrm{i}[\rho_A, H_A + H_{LS}] + \mathcal{L}_1\rho_A + \mathcal{L}_D\rho_A, \tag{1.29}$$

where we defined the Lamb-shift Hamiltonian

$$H_{LS} = \sum_{m,n}\sum_{\nu} S_{mn}(\nu)A^\dagger_n(\nu)A_m(\nu), \tag{1.30}$$

and the dissipator

$$\mathcal{L}_D\rho_A = \sum_{m,n}\sum_{\nu}\gamma_{mn}(\nu)\left(A_m(\nu)\rho_A A^\dagger_n(\nu) - \frac{1}{2}\{A^\dagger_n(\nu)A_m(\nu), \rho_A\}\right). \tag{1.31}$$

The dissipator can be placed in the standard Lindblad form (1.2) by diagonalising the ma-

trix $\gamma_{mn}(\nu)$, such that $\gamma_{mn}(\nu) = \sum_\mu U_{m\mu}(\nu)\gamma_\mu(\nu)U^*_{n\mu}(\nu)$, where $U_{m\mu}(\nu)$ are the elements of a unitary matrix, and $\gamma_\mu(\nu)$ are the eigenvalues of the matrix $\gamma_{mn}(\nu)$. Defining the new Lindblad operators $L_\mu(\nu) = \sum_m U_{m\mu}(\nu)A_m(\nu)$, the dissipator takes the diagonal form

$$\mathcal{L}_D = \sum_{\mu,\nu} \gamma_\mu(\nu)\mathcal{D}[L_\mu(\nu)], \tag{1.32}$$

where here, and throughout this thesis, we use the shorthand notation

$$\mathcal{D}[L]\rho = L\rho L^\dagger - \frac{1}{2}\left\{L^\dagger L, \rho\right\}. \tag{1.33}$$

An important property of the master equation is that it decouples the evolution of the populations and the coherences in the eigenbasis of H_A, so long as H_A has a nondegenerate spectrum [26]. This has important consequences for the nature of the steady-state solution ρ_∞ satisfying $\mathcal{L}\rho_\infty = 0$, assuming such a steady state exists. If it does exist, ρ_∞ must be purely population, since the evolution is trace-preserving. In other words, all coherences in the energy eigenbasis must be damped and eventually die away. If, in addition, the reservoir reference state is thermal, $\rho_B = \mathrm{e}^{-\beta H_B}/\mathcal{Z}_B$, where $\beta = 1/T$ is the temperature and $\mathcal{Z}_B = \mathrm{Tr}\left[\mathrm{e}^{-\beta H_B}\right]$ is the partition function, then the rates satisfy the detailed balance condition $\gamma_{mn}(\nu) = \mathrm{e}^{\beta\nu}\gamma_{nm}(-\nu)$, which implies that the steady state of the master equation is a thermal equilibrium state, $\rho_\infty = \mathrm{e}^{-\beta H_A}/\mathcal{Z}_A$ [26].

1.3 Energy transport in open quantum networks

We now apply the abstract formalism developed in the foregoing sections to an example. We focus on a peculiarly interesting class of open quantum systems: those comprising a network of interacting components or modules. In particular, we are interested in studying the flow of excitations through such a network induced by its coupling to multiple baths at different temperatures or chemical potentials. This scenario is directly relevant for the studies presented in Part I of this thesis, as well as for another publication which we do not include here [6]. We also introduce the spectral density, a function which quantifies the frequency spectrum of the noise induced by the environment, and we discuss its role in determining the character of the dissipative evolution of the open system.

The problem of excitation transport in quantum networks has seen an explosion of interest over the last decade, with theoretical studies based on master equations taking a prominent role. Much of the work in this direction has been fuelled by the development of tensor network techniques for studying nonequilibrium systems in one dimension [141–143]. Experimental inspiration has been drawn from a broad range of scenarios, including exciton transfer in biological [144–146] and artificial [6,147] polymers, mesoscopic electronic devices [148–150], trapped-ion crystals [151], and ultracold atoms in optical lattices [21,23,152,153].

Moreover, quite fundamental topics such as the emergence of Fourier's heat diffusion law from quantum dynamics [154, 155], and nonequilibrium quantum integrable systems [156–162] have been studied within the master equation framework.

Perhaps surprisingly, in light of these advances, there remains no clear consensus on how to correctly model nonequilibrium quantum networks using master equations. Indeed, this question has itself been the subject of several recent, partially contradictory studies [163–167]. In fact, the problem of how to use master equations to describe modular quantum systems has a relatively long pedigree, dating back at least to the 1970s [168]. In the following, we discuss different approaches to this problem in the context of a concrete microscopic model. We certainly do not claim to resolve any of the issues arising in this setting. Instead, we merely aim to shed some meagre light on a rather subtle problem, while introducing several key concepts of general relevance for this thesis along the way.

1.3.1 Tight-binding transport model

Let us now specify a concrete microscopic model. The open system under consideration is a one-dimensional (1D) quantum wire sandwiched between two macroscopic conducting leads. Electrons flow through the wire, driven by a difference in chemical potential or temperature between the leads. Studying this scenario elucidates how the transport properties of mesoscopic conductors depend on the microscopic physics. A similar theory was used in Ref. [6], building on previous work [149, 150, 169], in order to model the transport properties of bulk materials consisting of arrays of weakly coupled 1D chains, including conjugated polymer arrays [147, 170], Bechgaard and Fabre salts [171–173] and spin-chain systems [174–176].

We adopt a highly idealised yet tractable description of the system. Specifically, the quantum wire is modelled as a tight-binding lattice of noninteracting, spin-polarised fermions with a single relevant band of states. The macroscopic metal leads are also modelled by 1D fermionic tight-binding lattices. Thus, the entire system forms an infinite 1D fermionic chain. A distinguished number N of sites in the centre of the chain forms the open system, while the remaining M sites to the left and M sites to the right correspond to the reservoirs, which may be at different temperatures or chemical potentials. The scenario is depicted schematically in Fig. 1.1.

The Hamiltonian of the system can be written as $H = H_L + H_{LC} + H_C + H_{CR} + H_R$, where H_C denotes the Hamiltonian of the central N sites

$$H_C = \epsilon \sum_{j=1}^{N} c_j^\dagger c_j - J \sum_{j=1}^{N-1} \left(c_j^\dagger c_{j+1} + c_{j+1}^\dagger c_j \right). \tag{1.34}$$

Here, ϵ is the on-site binding energy and $J > 0$ is the hopping amplitude. The $c_j^\dagger$ are ladder operators which create a fermion on site j, satisfying $\{c_j, c_{j'}^\dagger\} = \delta_{jj'}$ and $\{c_j, c_{j'}\} = 0$. We

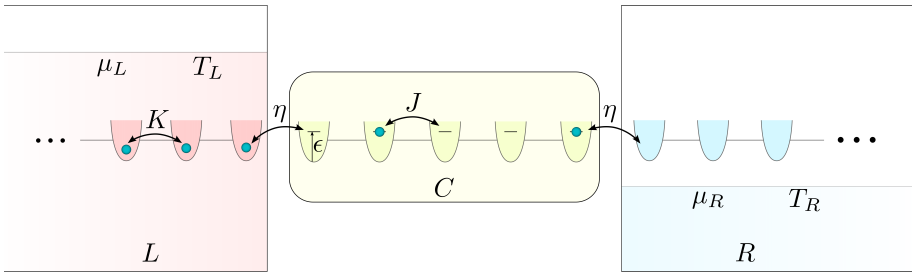


Figure 1.1. Schematic of the tight-binding transport model. Green spheres represent fermions hopping between sites of a 1D lattice. The central N sites of the system form the open system C. A particle current is driven through the open system by its contact with the left (L) and right (R) reservoirs at different temperatures $T_{L/R}$ and chemical potentials $\mu_{L/R}$.

diagonalise H_C by introducing the operators [177]

$$\tilde{c}_n = \sqrt{\frac{2}{N+1}} \sum_{j=1}^{N} \sin\left(\frac{\pi j n}{N+1}\right) c_j, \tag{1.35}$$

whose mode functions are the discrete analogue of standing waves, and in terms of which H_C becomes

$$H_C = \sum_{n=1}^{N} E_n \tilde{c}_n^\dagger \tilde{c}_n, \tag{1.36}$$

with the single-particle dispersion

$$E_n = \epsilon - 2J \cos\left(\frac{\pi n}{N+1}\right). \tag{1.37}$$

This is the typical sinusoidal dispersion relation of a noninteracting lattice model, with bandwidth $4J$.

The left and right reservoir Hamiltonians are given by

$$H_L = -K \sum_{j=1}^{M-1} \left(d_{L,j}^\dagger d_{L,j+1} + d_{L,j+1}^\dagger d_{L,j} \right), \tag{1.38}$$

$$H_R = -K \sum_{j=1}^{M-1} \left(d_{R,j}^\dagger d_{R,j+1} + d_{R,j+1}^\dagger d_{R,j} \right), \tag{1.39}$$

where $d_{L/R,j}^\dagger$ creates a fermion on site j of the left (L) or right (R) reservoir, and $K > 0$ is the hopping amplitude, assumed to be the same for both reservoirs. The coupling between

the open system and the environment is described by

$$H_{LC} = -\eta \left(c_1^\dagger d_{L,M} + d_{L,M}^\dagger c_1 \right), \tag{1.40}$$

$$H_{CR} = -\eta \left(d_{R,1}^\dagger c_N + c_N^\dagger d_{R,1} \right), \tag{1.41}$$

corresponding to hopping of fermions onto and off the chain at each end, with hopping amplitude η.

In order to enforce a finite average number of fermions in the two reservoirs, we work in the grand canonical ensemble. Let μ_L and β_L (μ_R and β_R) be the chemical potential and inverse temperature of the left (right) reservoir, respectively. We denote the number operator for each reservoir by

$$N_\alpha = \sum_{k=1}^{M} d_{\alpha,j}^\dagger d_{\alpha,j}, \tag{1.42}$$

for $\alpha = L, R$. The grand-canonical equilibrium state is thus

$$\rho_B = \frac{1}{\mathcal{Z}_L \mathcal{Z}_R} \mathrm{e}^{-\beta_L (H_L - \mu_L N_L)} \otimes \mathrm{e}^{-\beta_R (H_R - \mu_R N_R)}, \tag{1.43}$$

with $\mathcal{Z}_{L/R}$ the corresponding grand-canonical partition functions.

The reservoir Hamiltonians H_L and H_R can be diagonalised by the unitary transformation

$$d_{L/R,j} = \sqrt{\frac{2}{M+1}} \sum_{k=1}^{M} \sin(q_k j) \tilde{d}_{L/R,k}, \tag{1.44}$$

where $q_k = \pi k/(M+1)$ denotes the discrete (dimensionless) wave number. Under this transformation, the reservoir Hamiltonians become

$$H_\alpha = \sum_{k=1}^{M} \omega_k \tilde{d}_{\alpha,k}^\dagger \tilde{d}_{\alpha,k}, \tag{1.45}$$

$$\tag{1.46}$$

for $\alpha = L, R$, where we introduced the dispersion relation

$$\omega_k = -2K \cos(q_k). \tag{1.47}$$

In the new basis, the interaction Hamiltonians read as

$$H_{LC} = \sum_{k=1}^{M} \lambda_k' \left(c_1^\dagger \tilde{d}_{L,k} + \tilde{d}_{L,k}^\dagger c_1 \right), \tag{1.48}$$

$$H_{CR} = \sum_{k=1}^{M} \lambda_k \left(\tilde{d}_{R,k}^\dagger c_N + c_N^\dagger \tilde{d}_{R,k} \right), \tag{1.49}$$

where we defined the coupling constants $\lambda'_k = (-1)^k \lambda_k$, with

$$\lambda_k = \eta \sqrt{\frac{2}{M+1}} \sin(q_k). \tag{1.50}$$

1.3.2 Spectral density

The scenario described above is a special case of an important and ubiquitous class of open-systems models, in which each reservoir Hamiltonian (1.45) is quadratic in creation and annihilation operators, while the corresponding interaction Hamiltonian (1.48) or (1.49) is linear in these operators. In such cases, the influence of the environment on the open system is characterised by the *spectral density*

$$\mathcal{J}(\nu) = \sum_{k=1}^{M} |\lambda_k|^2 \delta(\nu - \omega_k). \tag{1.51}$$

Note that, since the couplings to both reservoirs differ only by a phase, i.e. $|\lambda_k| = |\lambda'_k|$, the spectral density is the same for both environments.

The spectral density determines the reservoir spectral functions (1.21), up to additional factors depending on chemical potential, temperature, or possibly other thermodynamic potentials describing the state of the reservoir. For concreteness, let us focus specifically on the right lead. Its interaction with the open system is given by Eq. (1.49), which takes the general form[1] (1.19) with $A_1 = c_N$, $A_2 = c_N^\dagger$, $B_1 = \sum_k \lambda_k \tilde{d}_{R,k}$ and $B_2 = B_1^\dagger$. The reservoir spectral functions are thus found to be

$$\begin{aligned} \mathcal{I}_{11}(\nu) &= \mathcal{J}(\nu)[1 - f(\nu)], \\ \mathcal{I}_{22}(\nu) &= \mathcal{J}(\nu) f(\nu), \end{aligned} \tag{1.52}$$

where $f(\nu) = (\mathrm{e}^{\beta(\nu-\mu)} + 1)^{-1}$ is the Fermi-Dirac distribution of fermions in the right lead, and in this subsection we set $\beta_R = \beta$ and $\mu_R = \mu$ for brevity. Eq. (1.52) determines the reservoir correlation functions $\tilde{\Gamma}_{mn}(t)$ via Eq. (1.26). The spectral density must therefore be a smooth function of frequency in order to obtain irreversible dynamics, otherwise $\tilde{\Gamma}_{mn}(t)$ would oscillate periodically rather than decay in time. Furthermore, basic Fourier arguments imply that $\mathcal{J}(\nu)$ must vary slowly over a broad range of frequencies. This latter condition ensures that the decay time scale of $\tilde{\Gamma}_{mn}(t)$ is small and thus that the Markov

[1] Actually, the operators in Eq. (1.49) are composed by the antisymmetric wedge product, as appropriate for anticommuting fermion operators. Although from a mathematical viewpoint this is drastically different from the symmetric tensor product appearing in Eq. (1.19), the end result for the master equation turns out to be the same, in the sense that all other equations from Section 1.2 carry over unchanged. The physical explanation for this is that the master equation contains no information about correlations between open system and environment, and thus the antisymmetry under exchange of their respective excitations is irrelevant. A rigorous justification of these claims using the Jordan-Wigner transformation can be found in Ref. [29].

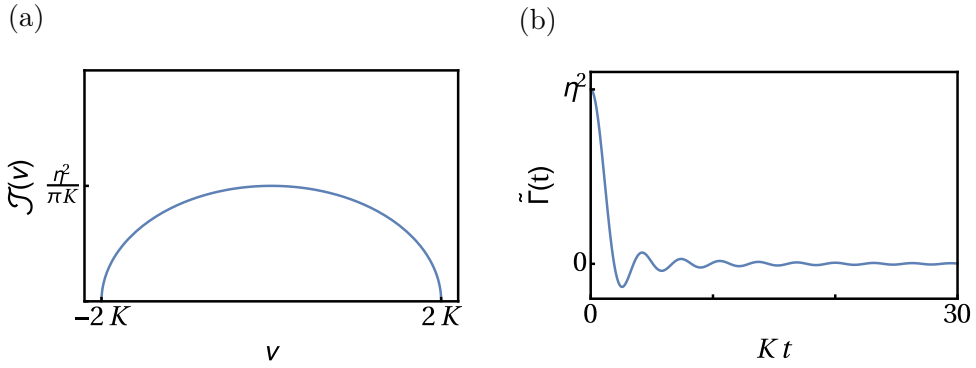


Figure 1.2. Spectral properties of the tight-binding environment model quantified by (a) the spectral density $\mathcal{J}(\nu)$ and (b) the reservoir correlation function $\tilde{\Gamma}(t)$, here shown in the strong-bias limit $|\mu| > 2K$ at zero temperature [Eq. (1.54)].

approximation is valid.

Clearly, Eq. (1.51) cannot represent a smooth function of frequency for any finite M. A smooth spectral density is obtained only in the thermodynamic limit $M \to \infty$, where the separation between consecutive wave numbers $\Delta q = q_{k+1} - q_k = \pi/(M+1)$ tends to zero. Thus, as $M \to \infty$, the summation over q_k can be approximated by an integral over the continuous variable q taking values in the Brillouin zone $q \in [0, \pi]$. Explicitly, using Eqs. (1.47) and (1.50), we find

$$\begin{aligned}\mathcal{J}(\nu) &= \frac{2\eta^2}{\pi} \sum_{k=1}^{M} \Delta q \sin^2(q_k) \delta(\nu + 2K\cos(q_k)) \\ &\to \frac{2\eta^2}{\pi} \int_0^{\pi} \mathrm{d}q \ \sin^2(q) \delta(\nu + 2K\cos(q)) \\ &= \frac{\eta^2}{\pi K} \sqrt{1 - \frac{\nu^2}{4K^2}},\end{aligned} \tag{1.53}$$

for $-2K < \nu < 2K$, while $\mathcal{J}(\nu) = 0$ otherwise. Eq. (1.53) describes a semi-ellipse, whose major axis is the bandwidth $4K$, and whose semi-minor axis is the rescaled coupling strength $\eta^2/\pi K$. This result is attributed to Newns [178], who derived Eq. (1.53) in the course of a study of impurities on a metal surface. The spectral density is plotted in Fig. 1.2(a).

The reservoir bandwidth $4K$ sets the characteristic scale of variation of $\mathcal{J}(\nu)$, and thus determines the decay time τ_B of the correlation functions $\tilde{\Gamma}_{mn}(t)$. To see this, consider the simplest case of zero temperature, where $f(\nu) = \Theta(\mu - \nu)$, with $\Theta(z)$ the Heaviside step function. Then, if $|\mu| > 2K$, either all states in the right lead are occupied, or all of them

are empty. Hence, one of $\tilde{\Gamma}_{11}(t)$ or $\tilde{\Gamma}_{22}(t)$ vanishes, while the other takes the form

$$\begin{aligned}\tilde{\Gamma}(t) &= \int_{-2K}^{2K} \mathrm{d}\nu \, \mathrm{e}^{\mathrm{i}\nu t} \mathcal{J}(\nu) \\ &= \frac{\eta^2 J_1(2Kt)}{Kt},\end{aligned} \tag{1.54}$$

where $J_1(z)$ denotes a Bessel function[2]. We plot $\tilde{\Gamma}(t)$ in Fig. 1.2(b) showing that it vanishes over times much longer than $\tau_B \sim K^{-1}$, which sets the coarse-grained time scale of the Markov approximation. This is rather intuitive, since K governs the rate at which a particle or a hole injected into the reservoir propagates far enough away from the open system that the process can be considered irreversible. We refer to K^{-1} as the vacuum correlation time, since it applies at zero temperature. At finite temperature T, for frequencies within a band of approximate width T centred on μ, the spectral functions (1.52) vary over a scale determined by both T and K. Hence, the nonzero temperature introduces a new time scale $\beta = 1/T$, the thermal correlation time, which governs the decay time of thermal contributions to the reservoir correlation functions.

We now give an explicit relation between the spectral density and the dissipative evolution of the central chain, by deriving a master equation following the steps in Section 1.2. In the notation of that section, the reservoir Hamiltonian is given by $H_B = H_L + H_R$, while the interaction is given by $H_{AB} = H_{LC} + H_{CR}$. However, we still have some freedom in choosing the open-system Hamiltonian H_A. We consider two possible choices in the following.

1.3.3 Nonlocal master equation

The blindingly obvious choice is to set $H_A = H_C$, in which case $\mathcal{L}_1 = 0$. The resulting master equation describes the injection and absorption of fermions by the external leads in terms of transitions between the energy eigenstates of H_C. Specifically, the evolution of the reduced density operator $\rho_C(t)$ describing the central N sites of the chain is given by

$$\frac{\mathrm{d}\rho_C}{\mathrm{d}t} = \mathrm{i}[\rho_C, H_C + \delta H_C] + \sum_{\alpha=L,R} \sum_{n=1}^{N} \gamma_\alpha^-(E_n) \mathcal{D}[\tilde{c}_n]\rho_C + \sum_{\alpha=L,R} \sum_{n=1}^{N} \gamma_\alpha^+(E_n) \mathcal{D}[\tilde{c}_n^\dagger]\rho_C, \tag{1.55}$$

where the Lamb-shift Hamiltonian is

$$\delta H_C = \sum_{n=1}^{N} \delta E_n \tilde{c}_n^\dagger \tilde{c}_n. \tag{1.56}$$

[2]The profusion of J's here is unfortunate, yet difficult to avoid without violating convention. We offer a similar excuse for the notation in Chapter 4.

The energy shifts δE_n and incoherent rates $\gamma^{\pm}_{L/R}(E_n)$ are defined in terms of the spectral density. The shift in energy of the n^{th} eigenstate of the chain is given by

$$\delta E_n = \sum_{\alpha=L,R} \mathsf{P} \int_{-2K}^{2K} \mathrm{d}\nu \, \frac{\mathcal{J}(\nu)}{E_n - \nu}, \tag{1.57}$$

while the rates describing the incoherent loss $(-)$ and gain $(+)$ of fermions by the chain are given by

$$\gamma^{-}_{\alpha}(E_n) = 2\pi \mathcal{J}(E_n)[1 - f_\alpha(E_n)], \tag{1.58}$$

$$\gamma^{+}_{\alpha}(E_n) = 2\pi \mathcal{J}(E_n) f_\alpha(E_n), \tag{1.59}$$

where, for $\alpha = L, R$,

$$f_\alpha(\nu) = \left(\mathrm{e}^{\beta_\alpha(\nu-\mu_\alpha)} + 1\right)^{-1}. \tag{1.60}$$

Eq. (1.58) reflects the Pauli exclusion principle, which suppresses the donation of a fermionic excitation from the chain to the reservoirs if all states with the same energy are already occupied. On the other hand, (1.59) states the obvious fact that the chain cannot absorb a fermion at energy E_n unless some state of that energy in the reservoir is occupied.

Notice that the Lindblad operators entering Eq. (1.55), which are given explicitly by Eq. (1.35), are *nonlocal*, in the sense that they affect every site of the chain simultaneously. This may appear odd, given that physically each bath couples only to a single site of the chain. The origin of this feature is the rotating-wave approximation, which averages the evolution over times much longer than a typical value of $|E_n - E_m|^{-1}$. In fact, this time scale is on the same order as the duration needed for an excitation to cross from one side of the chain to the other. This explains why Eq. (1.55) describes the effect of local bath coupling as a global transformation of the chain, on the coarse-grained time scale of the RWA.

In order to show this explicitly, we consider the limit of $N \gg 1$, and introduce the lattice constant a such that the physical length of the chain is $L = aN$. The dispersion relation of the chain can be written as $E_n = E(p_n) = \epsilon - 2J\cos(ap_n)$, where $p_n = \pi n/L$ denotes the wave number. The group velocity describing the propagation of excitations is then $v = \partial E(p)/\partial p \to 2Ja^2 p \sim Ja/N$ as $p \to 0$. Thus, the time taken for an excitation to propagate the length of the chain is at most $L/v \sim N^2/J$. Meanwhile, the RWA averages over times longer than $|E_n - E_m|^{-1}$, and it is easy to show that indeed $\max\{|E_n - E_m|^{-1}\} \sim N^2/J$.

The advantage of the nonlocal master equation is that it correctly describes the relaxation to thermal equilibrium when the temperatures and chemical potentials of the two baths are the same, i.e. $\beta_{L/R} = \beta$ and $\mu_{L/R} = \mu$. This is because, as discussed at the end of Section 1.2, this master equation leads to a steady-state that is diagonal in the energy

eigenbasis of H_C. Furthermore, the incoherent rates satisfy the detailed balance condition $\gamma_\alpha^-(\nu) = \mathrm{e}^{\beta_\alpha(\nu-\mu_\alpha)}\gamma_\alpha^+(\nu)$. This ensures that the steady-state solution of the master equation is the correct equilibrium state

$$\rho_{\mathrm{eq}} = \frac{1}{\mathcal{Z}_C}\mathrm{e}^{-\beta(H_C-\mu N_C)}, \tag{1.61}$$

where $N_C = \sum_j c_j^\dagger c_j$ is the number operator for the chain. This may be proven using the easily verified results $[H_C, \delta H_C] = 0$ and $\rho_{\mathrm{eq}}\tilde{c}_n = \mathrm{e}^{\beta(E_n-\mu)}\tilde{c}_n\rho_{\mathrm{eq}}$. It is then straightforward to show by direct substitution of Eq. (1.61) into Eq. (1.55) that $\mathcal{L}\rho_{\mathrm{eq}} = 0$.

On the other hand, one may be interested in the case where a temperature or chemical potential imbalance exists between the reservoirs. In this scenario, one expects the stationary state ρ_∞ to support a nonzero energy or particle current through the chain. For example, the particle current through the chain is represented by the operator

$$I_j = \mathrm{i}J\left(c_{j+1}^\dagger c_j - c_j^\dagger c_{j+1}\right). \tag{1.62}$$

The current operator is thus defined so that the discrete continuity equation representing conservation of the local particle density $n_j = c_j^\dagger c_j$ is satisfied as an operator identity,

$$\frac{\mathrm{d}n_j}{\mathrm{d}t} + I_j - I_{j-1} = 0, \tag{1.63}$$

where the time derivative is evaluated using the Heisenberg equation of motion generated by H_C [179]. Hence one should find that $\mathrm{Tr}[\rho_\infty I_j] \neq 0$ whenever $\mu_L \neq \mu_R$ or $\beta_L \neq \beta_R$.[3]

In fact, as discovered by the authors of Ref. [163], the nonlocal master equation (1.55) erroneously predicts that $\mathrm{Tr}[\rho_\infty I_j] = 0$ identically in all cases. This is because the steady state is guaranteed to be diagonal in the basis of energy eigenvectors $|\Omega\rangle$ of H_C. However, it is straightforward to demonstrate that

$$\langle\Omega|I_j|\Omega\rangle = 0, \tag{1.64}$$

and therefore that any statistical mixture of energy eigenstates also yields a null expectation value for the current. Indeed, one finds using the transformation (1.35) that all diagonal elements of the current operator (1.62) vanish in the energy eigenbasis of H_C. It is also clear that the property (1.64) is satisfied by any other reasonable definition of a current operator, since the stationary energy eigenstates of any particle-conserving 1D system with open boundary conditions obviously do not support a current.

[3] Excluding the singular parameter regime where opposed temperature and chemical potential gradients lead to a cancellation of the current.

1.3.4 Local master equation

An alternative approach to deriving a master equation, following Ref. [163] (see also Ref. [164]), is to assume that the sites of the network are coupled together only weakly. That is, we assume that $J \ll \epsilon$, and write the central system Hamiltonian as $H_C = H_\epsilon + H_J$, with $H_\epsilon = \epsilon N_C$ and

$$H_J = -J \sum_{j=1}^{N-1} \left(c_j^\dagger c_{j+1} + c_{j+1}^\dagger c_j \right). \tag{1.65}$$

Then we treat $H_A = H_\epsilon$ as the dominant contribution to the open-system autonomous dynamics, while the inter-site coupling is treated as a perturbation by setting

$$\mathcal{L}_1 \rho = \mathrm{i}[\rho, H_J]. \tag{1.66}$$

In this case, the dissipation is described in terms of the local injection and absorption of fermions at the boundary sites of the chain. Explicitly, the master equation reads as

$$\frac{\mathrm{d}\rho_C}{\mathrm{d}t} = \mathrm{i}[\rho_C, H_C + \delta H_C] + \gamma \left((1 - f_L)\mathcal{D}[c_1] + f_L \mathcal{D}[c_1^\dagger] + (1 - f_R)\mathcal{D}[c_N] + f_R \mathcal{D}[c_N^\dagger] \right) \rho_C, \tag{1.67}$$

where $\gamma = 2\pi \mathcal{J}(\epsilon)$, and $f_{L/R} = f_{L/R}(\epsilon)$, and the Lamb-shift contribution affects only the first and last site of the chain,

$$\delta H_C = \delta\epsilon \left(c_1^\dagger c_1 + c_N^\dagger c_N \right), \tag{1.68}$$

with

$$\delta\epsilon = \mathsf{P} \int_{-2K}^{2K} \mathrm{d}\nu \, \frac{\mathcal{J}(\nu)}{\epsilon - \nu}. \tag{1.69}$$

It is customary to neglect the Lamb-shift term, which is assumed to be small.

The local master equation approach turns out to be the most useful for studying steady-state energy transport, since the nonequilibrium steady state ρ_∞ can support a current, i.e. $\mathrm{Tr}[\rho_\infty I_j] \neq 0$. The exact solution for the stationary state of (1.67) is calculated in Ref. [156]. One finds that the system is a ballistic conductor, meaning that the current is independent of the length of the chain in the limit of $N \to \infty$, keeping the temperatures and chemical potentials of the leads fixed. This prediction is in agreement with linear-response theory [180], but holds for arbitrary large differences of temperature or chemical potential. The local master equation (1.67) has been extended to diverse scenarios including intra-chain density-density interactions [143, 149, 157, 161], local dephasing processes [150, 181], disordered on-site energies [182], and generalisations to multiple chains coupled together coherently [183] or incoherently [6].

An apparent drawback of the local master equation approach is that, when the reser-

voirs are at the same temperature and chemical potential, the stationary state is

$$\rho_{\rm loc} = \frac{{\rm e}^{-\beta(\epsilon-\mu)N_C}}{{\rm Tr}\left[{\rm e}^{-\beta(\epsilon-\mu)N_C}\right]}, \tag{1.70}$$

which differs from the correct thermal equilibrium state (1.61), in general. Eq. (1.70) describes a product state with vanishing correlations between the sites of the chain. This feature could be expected from the derivation of Eq. (1.67), which treats the intersite coupling J as a perturbative parameter. The stationarity of $\rho_{\rm loc}$ can be proved easily along the same lines as in Section 1.3.3, using the properties $\gamma_\alpha^+ = {\rm e}^{\beta\mu}\gamma_\alpha^-$, $c_j\rho_{\rm loc} = {\rm e}^{\beta\mu}\rho_{\rm loc}c_j$, and $[H_C, N_C] = 0$.

1.3.5 Wide-band approximation

It is rather interesting to note that the local master equation (1.67) can be derived under a different set of assumptions that we call the wide-band approximation (WBA). This derivation gives better insight into the character and validity of the local Lindblad formulation of the problem. Let us return to the general expression for the Redfield dissipator (1.24) with $H_A = H_C$, reproduced here for convenience as

$$\sum_{m,n}\sum_{\nu,\nu'}\Gamma_{mn}(\nu){\rm e}^{{\rm i}(\nu'-\nu)t}\left[A_m(\nu)\tilde{\rho}_A(t)A_n^\dagger(\nu') - A_n^\dagger(\nu')A_m(\nu)\tilde{\rho}_A(t)\right] + {\rm h.c.}. \tag{1.71}$$

Here ν represents a Bohr frequency of the full interacting Hamiltonian of the central system H_C. In Section 1.2, the Redfield dissipator was massaged into Lindblad form via the RWA, which in practice means crossing off terms with $\nu \neq \nu'$. Instead we take a different route and make the wide-band assumption

$$\Gamma_{mn}(\nu) \approx \Gamma_{mn}(\nu') = \bar{\Gamma}_{mn}, \tag{1.72}$$

i.e. the spectral correlation matrix is approximately independent of frequency. More precisely, the validity of the WBA rests on the condition

$$\left|\frac{{\rm d}\Gamma_{mn}(\nu)}{{\rm d}\nu}\right| \ll \left|\frac{\Gamma_{mn}(\nu)}{\delta\nu}\right|, \tag{1.73}$$

where $\delta\nu$ corresponds to a typical difference between the Bohr frequencies ν. This assumption means that the variation of the spectral correlation matrix over a typical Bohr frequency ν is negligible in comparison to the mean value of $\Gamma_{mn}(\nu) \approx \bar{\Gamma}_{mn}$.

Within the WBA the summations over ν, ν' in Eq. (1.71) are trivially completed with

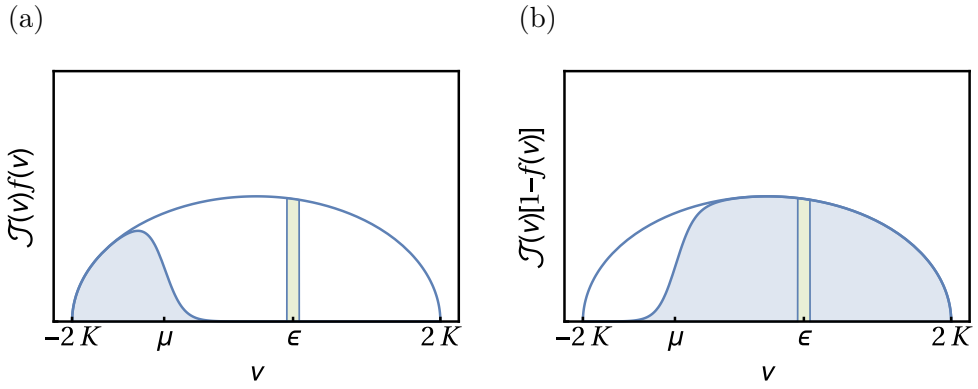


Figure 1.3. Spectral functions at low temperature $T \ll |\mu|$. The semi-ellipse shows the spectral density $\mathcal{J}(\nu)$, with the blue shaded region representing the contribution from (a) occupied states $\mathcal{J}(\nu)f(\nu)$ or from (b) unoccupied states $\mathcal{J}(\nu)[1-f(\nu)]$. The WBA is valid when the height of the blue shaded region varies slowly across the frequency range relevant for the open system, shown as a green band of width $4J$ centred on $\nu = \epsilon$.

the aid of Eq. (1.22). Transforming back to the Schrödinger picture, we find

$$\frac{\mathrm{d}\rho_A}{\mathrm{d}t} = \mathrm{i}[\rho, H_A + H_{LS}] + \sum_{m,n} \gamma_{mn} \left(A_m \rho_A A_n^\dagger - \frac{1}{2}\{A_n^\dagger A_m, \rho_A\} \right), \tag{1.74}$$

where

$$H_{LS} = \sum_{m,n} S_{mn} A_n^\dagger A_m, \tag{1.75}$$

and we defined the energy shifts and incoherent rates

$$\gamma_{mn} = \bar{\Gamma}_{mn} + \bar{\Gamma}_{nm}^*, \tag{1.76}$$

$$S_{mn} = \frac{1}{2\mathrm{i}} \left(\bar{\Gamma}_{mn} - \bar{\Gamma}_{nm}^* \right). \tag{1.77}$$

Eq. (1.74) can be put into Lindblad form by diagonalising the matrix of rates γ_{mn}. Note that the RWA was not necessary to obtain a Lindblad equation in this case.

In the specific scenario of a quantum network where each site couples locally to an independent bath, one generally finds that $\bar{\Gamma}_{mn} \propto \delta_{mn}$ and therefore no diagonalisation is necessary. As a result, the Lindblad operators A_m are simply the operators appearing in the decomposition of the interaction Hamiltonian (1.19). Thus, a local interaction between the open system and the reservoirs automatically leads to a local Lindblad equation in the context of the WBA. Essentially the same idea was introduced in Ref. [184] in the different context of dissipation from a coupled atom-cavity system.

Now let us examine the validity of this approach in the context of our tight-binding transport model, with $H_A = H_C$ the Hamiltonian of the central chain. The wide-band assumption (1.73) can only be satisfied if the spectral function $\mathcal{I}(\nu)$, and therefore also

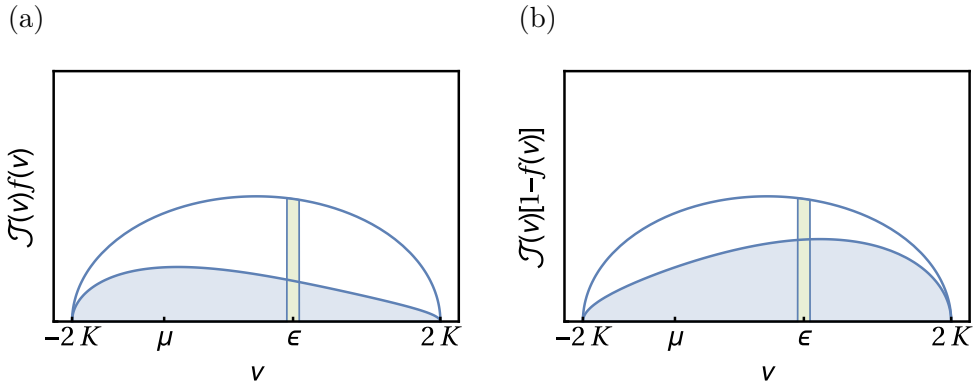


Figure 1.4. Contributions to the spectral correlation matrix at high temperature $T \gtrsim |\mu|$, as in Fig. 1.3. Here the temperature must satisfy $T \gg 2J$ in order for the WBA to be valid.

both the spectral density $\mathcal{J}(\nu)$ and the distribution functions $f_{L/R}(\nu)$, are approximately constant over the entire spectrum of H_C, $\epsilon - 2J < \nu < \epsilon + 2J$, in which case we may as well set $\nu = \epsilon$.

Referring to Eq. (1.53), the approximation $\mathcal{J}(\nu) \approx \mathcal{J}(\epsilon)$ is valid if $K \gg J$, i.e. the environment bandwidth must be very large in comparison to the open-system bandwidth. This is the well-known wide-band limit which is frequently invoked in quantum transport studies (see, for example, Ref. [185]). Note that this does not imply any condition on the relative magnitudes of J and ϵ. In fact, ϵ may even be comparable to K, so long as K remains sufficiently large for the Markov approximation to hold. Validity of the Markov approximation requires that $K \gg \gamma$, a condition which is consistent with, yet distinct from, the wide-band assumption.

The Fermi-Dirac functions $f_{L/R}(\nu)$ can be treated as constant in two different scenarios. At low temperatures such that $T \ll |\mu|$, the distribution functions $f_{L/R}(E_n)$ only differ significantly from their zero-temperature values in a thin frequency band of width T near $\nu = \mu$ (see Fig. 1.3). Thus, if the Fermi energy μ lies far outside the relevant frequency range $[\epsilon - 2J, \epsilon + 2J]$, we can treat $f_{L/R}(\nu)$ as a constant equal to its value at zero temperature. In particular, we obtain Eq. (1.67) with $f_{L/R} = 0, 1$. The distribution functions can also be treated as approximately constant if the temperature is very large, so that $T \gg 2J$ (see Fig. 1.4). In this case, we again obtain Eq. (1.67), but where now $f_{L/R}$ may take any value.

Importantly, when the reservoirs are at equilibrium with each other so that $\mu_{L/R} = \mu$, $T_{L/R} = T$ and $f_{L/R} = f$, the steady state solution (1.70) is actually equivalent to the correct equilibrium state (1.61), assuming the WBA is valid. In the low-temperature regime of strong bias, Eq. (1.70) describes a state where all sites of the chain are occupied ($f = 1$) or empty ($f = 0$), which is precisely the form of the true equilibrium state when $|\mu| \gg T$ and $|\mu \pm T| \gg 2J$, as necessary for the validity of the WBA at low temperatures.

On the other hand, in the high-temperature regime the WBA requires that $\beta J \to 0$, so that H_J can be neglected in the exponent of Eq. (1.61), leading directly to Eq. (1.70).

In summary, the local master equation (1.67) can be justified without resorting to any assumptions on the smallness of the inter-site coupling J with respect to the on-site energies ϵ or to the incoherent rates γ. Instead, we have shown within the framework of the WBA that the relevant comparison is between J and the bandwidth of the environment, which in the present model is set by $T_{L/R}$, $\mu_{L/R}$ and K. As a result, the local approach is shown to be valid only in two temperature regimes. Either the temperature is so low that the problem is effectively at zero temperature, or the temperature is much larger than any other energy scale of the open system, and thus effectively infinite. This may explain the apparent inconsistency of the local Lindblad model with thermodynamic considerations, such as the vanishing of the heat current [143] or apparent violations of the second law [165] when the reservoir temperatures differ.

1.4 Concluding remarks

To conclude this chapter, let us summarise the main results and their relevance for the remainder of this thesis. In Section 1.2 we gave a derivation of the master equation that is sufficiently general to cover the scenarios studied in this document. Furthermore, we showed that a certain arbitrariness exists in the derivation of the master equation. We illustrated this point using the specific example of charge transport through a quantum wire driven out of equilibrium by a chemical potential or temperature gradient. In particular, different master equations — with either local or global Lindblad operators — qualitatively disagree in their predictions for local observables such as currents.

In the following two chapters comprising Part I of this thesis, we will study similar nonequilibrium energy transport problems using master equations. In these examples, our choice of master equation will be largely driven by practical considerations. The system studied in Chapter 2 is not amenable to a global Lindblad description, simply because the open system's Hamiltonian is too complex to diagonalise. However, in Chapter 3 we study a simpler system in which both the local and global dissipation models may be used in their corresponding domains of validity. On the other hand, in Part II we consider only localised open systems interacting with a single bath and thus no ambiguity arises when deriving the master equation.

We have also introduced the spectral density function $\mathcal{J}(\nu)$, which is important for describing open quantum systems linearly coupled to a quadratic thermal environment. We shall find similarly defined spectral density functions to play an essential role in the majority of subsequent chapters, although an explicit form for $\mathcal{J}(\nu)$ may not be needed in all cases. However, in Chapter 5 we will discuss a problem in which a spectral density cannot be defined in general, because the system-environment interaction is not linear. In

that case, we need to use the more general spectral function $\mathcal{I}(\nu)$.

Part I

Quantum absorption refrigerators

The development of classical thermodynamics in the 19th century underpinned the Industrial Revolution, and the enormous economic growth and social developments that ensued. Now, in the 21st century, another great technological revolution beckons, enabled by our control of quantum systems. In order to understand and optimise the energy demands of burgeoning quantum technologies, we require a theory that unifies two pillars of physics: quantum mechanics and thermodynamics. The first part of this thesis details our original contribution to this new field of quantum thermodynamics.

Most interesting physical processes take place within a thermal environment. Exchanging energy with the thermal background naturally drives systems towards equilibrium, and this flow of energy can be used to power other processes. For example, a heat engine performs work by capturing some of the heat passing from a hot body into its environment. More generally, any system out of thermal equilibrium is a resource which can facilitate an otherwise difficult task. Thermodynamics provides a framework to quantify such resources. In the case of a macroscopic heat engine, the maximum amount of work that can be extracted is limited by the second law of thermodynamics, which states that the total entropy must be nondecreasing. This leads in particular to Carnot's famous universal bound on efficiency [186].

Quantum thermodynamics is about the value of quantum resources, such as finite-dimensional Hilbert spaces or highly entangled states, in the context of a ubiquitous thermal environment. One approach to quantum thermodynamics uses the powerful formalism of resource theories originating from the study of entanglement [187], which systematically quantify the value of certain quantum states under a restricted set of transformations. For example, thermodynamics can be formulated as a resource theory of nonequilibrium states under energy-conserving unitary transformations [188]. The second law of thermodynamics can be understood as a statement about the interconvertibility of different nonequilibrium resources, e.g. high-temperature thermal energy or work. In particular, one resource state can be transformed into another only if the total free energy decreases, which implies the Carnot bound for macroscopic heat engines. Applying the resource-theoretic framework to state transformations on microscopic systems reveals an entire family of constraints including and extending the second law [33, 188, 189], which restrict the efficiency and work that can be extracted from small heat engines [190]. However, the situation in quantum thermodynamics is richer still, due to the variety of available resources besides work, such as entanglement [191, 192] and coherence [193–196].

Resource theories reveal general kinematical constraints on thermodynamic transformations which are independent of the implementation. However, such theoretical insights can only be put to practical use by a physical device. Thus it is also important to explicitly study the dynamics of quantum thermal machines. These are nonequilibrium open quantum systems in contact with one or more thermal environments [197, 198], which harness energy currents to perform a variety of different tasks. Realisations of quantum thermal

machines have been proposed in diverse contexts, such as cavity optomechanics [49, 67], cold atoms [199] and ions [54–56], mesoscopic conductors [52, 53, 200–202] and even biological systems [57–59], with applications including work extraction [203], entanglement generation [204], time keeping [8] and cooling [38, 39, 205, 206], to cite but a few examples from a vast literature.

In the following, we focus specifically on quantum absorption refrigerators (QARs), which are cooling machines powered by heat rather than work. Although such devices have existed since the invention of thermodynamics, they have attracted renewed interest from quantum physicists [116] for at least two reasons. QARs are attractive to the theorist because they dispense of the need for externally supplied work, whose precise definition in a quantum setting is debatable [32–37]. Perhaps more importantly, QARs potentially offer tremendous practical reductions in energy expenditure. This is because quantum systems are typically manipulated and cooled using coherent fields, which consume a macroscopic quantity of power merely in order to influence microscopic degrees of freedom. Conversely, an absorption chiller may be powered by ubiquitous sources of thermal energy, such as excess heat generated by another process, or indeed sunlight. In principle, absorption refrigerators can therefore function at no additional energy cost beyond that required to build the device in the first place.

In the recent theoretical literature, a number of QAR models have been proposed and studied [38–46]. In some cases, these models exhibit new, occasionally controversial, behaviours that are absent from their classical counterparts. For example, quantum correlations have variously been argued to improve cooling [207], or to play no operational role [208], depending on the model considered. Performance advantages due to nonequilibrium [45, 47] or spatially correlated [46] states of the heat reservoirs have been discussed. Moreover, a handful of concrete experimental proposals for QARs have been put forward [48–50], which would constitute proofs of principle if built. However, a practical use for QARs in quantum technology is still lacking.

This thesis addresses this deficiency by studying how QARs might be used to prepare cold quantum systems for subsequent quantum science and technology applications. For example, cooling of atomic motion is an essential precursor to a broad range of experiments with trapped atoms and ions. Chapter 2 reports our work published in Ref. [1], where we propose and study a QAR comprising a trapped atom or ion placed inside an optical cavity. We predict that it is possible with state-of-the-art technology to cool a trapped ion almost to its motional ground state using a thermal light source such as sunlight. We nonetheless find that a laser or similar reference system is necessary to stabilise the cavity frequencies. This work connects the theoretical literature on quantum thermal machines to practical sideband cooling techniques well known in quantum optics. Our proposal also represents perhaps the first example of a QAR which could reach cold enough temperatures to be useful for quantum technologies.

In Chapter 3 we shift focus onto the transient dynamics of QARs, rather than their steady-state properties. This chapter is based on our publication [2]. We consider in particular a simplified QAR model comprising three qubits. Cooling of qubits to low entropy states is desirable for various quantum information processing tasks which require approximately pure states as input [24]. Interestingly, we find that coherence in the machine drives oscillations in the temperature of the target qubit, allowing one to transiently achieve lower temperatures than the steady state with appropriate timing. This work reveals a new role for quantum coherence in improving the performance of thermal machines.

Chapter 2

Realising a quantum absorption refrigerator with an atom-cavity system

In this chapter, we describe the basic theory of the quantum absorption refrigerator, and introduce an experimental design in the context of cavity quantum electrodynamics (QED). This reproduces work published in Ref. [1].

Cooling of atomic motion is an essential precursor to a broad range of experiments with trapped atoms and ions. The development of laser cooling techniques represents a major achievement of late 20^{th} century physics, having enabled spectacular advances in our ability to study and manipulate quantum systems in the laboratory. Quantum absorption refrigerators (QARs) offer an interesting alternative, since they cool in principle using only a source of heat, without the need for work supplied by an external field such as a laser. However, the application of such devices to practical tasks in quantum technology, such as the refrigeration of trapped atoms, has barely been studied thus far.

In order to fill this gap, we introduce and study a novel design for a QAR in a cavity optomechanical set-up using trapped atoms [60–63] or ions [64–66]. We identify the necessary ingredients for the construction of such a machine, which include high-finesse optical cavities whose line width is smaller than the oscillation frequency of the trapped atom, although neither strong coupling nor high cooperativity are needed. Assuming that the necessary conditions are met, we show that driving the cavity with incoherent thermal light leads to significant cooling of the atomic motion. In particular, we predict that sunlight may be used to cool a trapped ion down to its motional ground state with high fidelity. Interestingly, we find that a laser is indispensable even in this context, however its role in our set-up is not to perform work, but rather to provide a stable frequency reference. Furthermore, the refrigeration cycle in our scheme can be easily understood by direct analogy with laser sideband cooling. This establishes a direct connection between the abstract theory of QARs and practical cooling techniques that are well known in atomic physics.

Trapped-ion systems have already proved to be a successful experimental testing ground for quantum thermodynamics, with the recent proposal and subsequent realisation of a heat engine using a single ion as the working medium [54–56]. However, it is not yet

clear how useful work could be extracted from such a device. In contrast, we focus on cooling, a task that has a clear practical application in quantum state preparation. We also note that several practical laser cooling schemes for trapped atoms using optical cavities already exist [209–212]. Our proposal differs from all of these, primarily because the energy for cooling is provided by a thermal source such as sunlight. Finally, we mention a closely related recent article [49], describing a QAR comprising a nanomechanical oscillator interacting with a pair of optical resonators. Our scheme works by a similar mechanism, but relies on a different interaction Hamiltonian, and is capable of achieving temperatures lower by many orders of magnitude, even with much less intense thermal light input. We aim to elucidate the connections between schemes such as that of Ref. [49], conventional sideband cooling, and other QAR models discussed in the recent theoretical literature.

2.1 Three-body quantum absorption refrigerator

We begin by introducing some fundamental concepts which form the basis for our work in Part I of this thesis. In particular, we provide a concise, general exposition of the abstract model of the three-body QAR, which was introduced in Refs. [38, 39]. We also take this opportunity to explain the useful concepts of virtual qubits and virtual temperatures, and to justify the figures of merit used to characterise refrigerator performance in subsequent sections.

2.1.1 Description of the model

The three-body quantum absorption refrigerator comprises three subsystems with Hamiltonian

$$H = \sum_{j=A,B,C} H_j, \tag{2.1}$$

where the operators H_j act nontrivially on subsystem j only. Subsystem A is the body to be cooled. We assume that it has an equally spaced energy spectrum with level splitting E_A, i.e.

$$H_A = E_A \sum_{n=0}^{D-1} n \left|n\right\rangle\!\left\langle n\right|, \tag{2.2}$$

where D is the local Hilbert space dimension (possibly infinite). This general form may describe a qubit, a spin or a harmonic oscillator. We also assume that H_B and H_C each possess at least one pair of eigenstates differing in energy by E_j, such that

$$E_A + E_B = E_C. \tag{2.3}$$

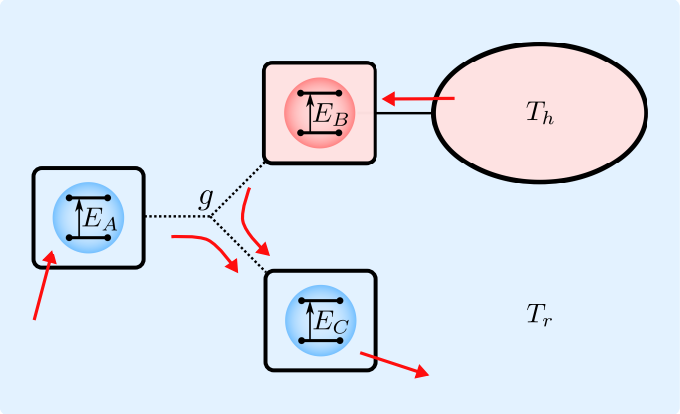


Figure 2.1. Illustration of a quantum absorption refrigerator comprising three mutually interacting subsystems, each possessing a transition of energy E_j, such that $E_A + E_B = E_C$. Subsystem B couples to a heat reservoir at temperature T_h while the others interact with the environment at room temperature T_r. Red arrows show the direction of steady-state heat flow through the machine.

The form of H_B and H_C is otherwise arbitrary. The subsystems are coupled together by a three-body interaction

$$V = g\left(L_A L_B L_C^\dagger + L_A^\dagger L_B^\dagger L_C\right), \tag{2.4}$$

where g is the interaction energy and L_j is a lowering operator connecting pairs of Hamiltonian eigenstates separated by an energy E_j, i.e.

$$[H, L_j] = -E_j L_j, \tag{2.5}$$

while $L_j^\dagger$ is the corresponding raising operator. The condition (2.3) ensures that $[H, V] = 0$, so that the interaction (2.4) enacts resonant transitions between degenerate energy eigenstates of H.

Cooling is achieved by coupling subsystem B to a hot thermal bath at temperature $T_h > T_r$, while subsystems A and C remain coupled to the environment at temperature T_r. Energy exchange between the subsystems then allows heat to naturally flow from the hot reservoir to the colder environment. However, due to the specific form of the interaction (2.4), subsystem C can only absorb a quantum of energy from the hot body B by simultaneously absorbing energy from A, thus leading to the cooling of A. The heat flow through the refrigerator is illustrated in Fig. 2.1.

2.1.2 Virtual qubits and virtual temperatures

The concepts of virtual qubits and virtual temperatures provide a convenient and intuitive way to analyse autonomous thermal machines [203], i.e. those which operate without external control or timing. A virtual qubit is a pair of states in the composite Hilbert space

of subsystems B and C which directly couples to the target subsystem A. By choosing the parameters of the system appropriately, the virtual qubit can be placed at an effective virtual temperature which may be lower than T_r. The operation of the refrigerator can then be understood as a simple thermalisation process between A and the virtual qubit.

To make this notion explicit, we observe that the interaction Hamiltonian (2.4) can be written as

$$V = g\left(L_A L_v^\dagger + L_A^\dagger L_v\right), \tag{2.6}$$

where $L_v = L_B^\dagger L_C$. Eqs. (2.3) and (2.5) together imply that

$$[H, L_v] = -E_A L_v. \tag{2.7}$$

This means that L_v is a lowering operator connecting pairs of states differing by an energy E_A in the composite Hilbert space of B and C. Each of these pairs of states is called a virtual qubit. The interaction (2.6) then describes resonant energy exchange between the virtual qubits and A.

When each subsystem is at thermal equilibrium with its respective bath, the populations of the virtual qubit states are thermally distributed at a virtual temperature

$$T_v = \frac{E_A}{E_C/T_r - E_B/T_h}. \tag{2.8}$$

That is to say, each pair of virtual qubit states is populated in the ratio e^{-E_A/T_v}. As long as the parameters of the refrigerator are chosen so that $T_v < T_r$, subsystem A will be pushed towards a lower temperature as it equilibrates with the virtual qubits under the interaction (2.6). This effect is counteracted by the thermalising influence of the reservoir interacting with A, thus establishing a heat current flowing from the environment surrounding A into the refrigerator. See Ref. [203] for a more complete discussion of virtual qubits and temperatures.

To conclude this subsection, we briefly mention that if the assumption that $T_h > T_r$ is relaxed, one can arrange for T_v to take any value by adjusting the bath temperatures and energy splittings. If $T_v > T_r$, then the steady-state temperature of A is increased and the system operates as a heat pump. On the other hand, if $T_v < 0$ the machine tries to induce population inversion in the state of A, which can be thought of as the quantum analogue of a classical heat engine lifting a weight [203]. In the following, we restrict our attention to the absorption chiller mode, where $T_h \gg T_r$. However, our results could be applied equally well to the construction and study of autonomous quantum heat pumps and engines.

2.1.3 Figures of merit

In order to analyse the performance of a refrigerator, one must choose figures of merit. The appropriate figure of merit depends on the problem at hand, as we now explain.

Coefficient of performance and cooling power

From one viewpoint, the refrigerator can be seen as a device which extracts heat from the environment surrounding subsystem A. Thus, the refrigerator performance is characterised by the stationary heat currents flowing to and from the reservoirs. The cooling power $\dot{Q}_A$ gives the heat current into the refrigerator from the environment of A, while $\dot{Q}_B$ gives the input power corresponding to the heat current flowing in from the hot reservoir. Therefore, the relevant figure of merit is the coefficient of performance $\epsilon = \dot{Q}_A/\dot{Q}_B$.

Note that this point of view makes sense only if the reservoirs connected to subsystems A and C are considered as separate entities. If subsystems A and C are in fact connected to the same environment, the net effect of the machine is simply to dump $\dot{Q}_B$ energy per unit time from the hot reservoir into this environment.

Assuming that the reservoirs connected to A and C are independent, we can estimate the coefficient of performance using the equations of motion for the mean local energies of subsystems A and B,

$$\frac{\mathrm{d}\langle H_j\rangle}{\mathrm{d}t} = \dot{Q}_j + \mathrm{i}gE_j\left\langle L_A L_B L_C^\dagger - L_A^\dagger L_B^\dagger L_C\right\rangle \tag{2.9}$$

for $j = A, B$, where the second term on the RHS follows from the Heisenberg equation generated by the interaction Hamiltonian (2.4). The specific form of the energy current $\dot{Q}_j$ depends on the dissipation model considered. In the case where the interaction of the refrigerator qubits with the thermal baths is described by a Hamiltonian interaction H_{int}, the current reads as $\dot{Q}_j = \mathrm{i}\langle[H_{\mathrm{int}}, H_j]\rangle$. In the stationary state, the derivatives of the mean energies vanish, leading to the following simple expression for the coefficient of performance

$$\epsilon = \frac{E_A}{E_B}. \tag{2.10}$$

We see that the coefficient of performance grows without limit as E_A is increased while holding E_B fixed (assuming that Eq. (2.3) is always satisfied). It is important to note that our approximate analysis ignores the contribution of the interaction energy to the heat currents, and is therefore only strictly correct in the weak-coupling limit of vanishingly small g [208].

Achievable temperature and cooling time

In the above scenario, one uses a microscopic machine to cool a *macroscopic* body, namely the reservoir connected to A. Perhaps a more appropriate application of a quantum refrigerator is to cool a *microscopic* system, namely subsystem A itself. From this viewpoint, the most important figure of merit is the achievable temperature (or more generally, the achievable energy and entropy) of subsystem A.

The achievable steady-state temperature can be estimated from the virtual temperature given by Eq. (2.8). This takes its minimal value when the temperature of the hot bath is large, from which we find

$$\lim_{T_h \to \infty} T_v = \frac{E_A}{E_C} T_r = \frac{\epsilon}{1+\epsilon} T_r, \tag{2.11}$$

where we have used Eqs. (2.3) and (2.10) to rewrite the virtual temperature in terms of the coefficient of performance ϵ. We find that the virtual temperature is minimised when ϵ is small. This illustrates that the standard thermodynamic measures of steady-state refrigerator performance are essentially irrelevant when the task at hand is to cool a quantum system having a finite energy.

Since the refrigerator is out of equilibrium, the thermodynamic temperature of A may not be strictly defined. For our purposes, it is sufficient to adopt the mean energy $\langle H_A \rangle$ as a figure of merit, rather than the temperature. This also provides an adequate measure of entropy, since the von Neumann entropy of a state with mean energy $\langle H_A \rangle$ is upper-bounded by that of a Gibbs state having the same mean energy. If the cooling is subject to time constraints, the cooling time (e.g. the time taken for $\langle H_A \rangle$ to reach its lowest value) is also a measure of performance. However, the cooling time is not a universal figure of merit since it may depend on the initial conditions.

In this thesis, we adopt the present framework: the objective is to cool subsystem A, rather than its environment. This viewpoint is particularly appropriate for quantum technology applications. Here, the motivation for cooling a quantum system is typically to maximise the efficiency of subsequent control operations by reducing uncertainty over the initial conditions, i.e. by minimising the entropy of the quantum system. We therefore neglect traditional efficiency measures such as the coefficient of performance ϵ, choosing rather to focus on the mean energy of the subsystems constituting the refrigerator, in particular that of the target body A.

2.2 Single-cavity refrigerator

In this section, we introduce an idealised model of a quantum absorption refrigerator comprising a trapped atom inside a single optical cavity. In order to simplify the analysis, several details are disregarded in this section. Nevertheless, this simplified model is sufficient to illustrate the physical principles involved. The present toy model also has the

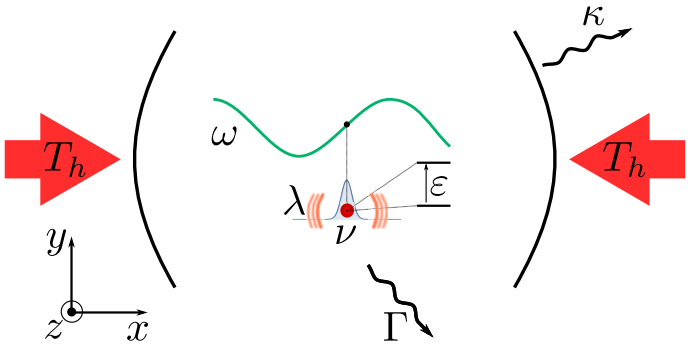


Figure 2.2. Schematic of the single cavity set-up. The trap potential minimum coincides with an electric-field node of a cavity mode with frequency $\omega = \varepsilon - \nu$. Dissipation leads to line widths Γ and κ for the electronic transition and the cavity mode, respectively, while λ is the intrinsic heating rate of the atomic motion in the trap.

advantage of making the connection with laser sideband cooling obvious, while demonstrating some of the practical limitations which arise in the cavity QED setting.

2.2.1 Description of the model

We consider a single atom or ion of mass M confined in the x direction by a harmonic potential with oscillation frequency $\nu/2\pi$. The atom is assumed to possess a pair of relevant internal electronic states $|\downarrow\rangle$ and $|\uparrow\rangle$ separated by an energy ε. The trap is placed inside an optical cavity whose axis is aligned in the x direction. The minimum of the harmonic potential is placed at a node of the electric field of a cavity mode with frequency $\omega/2\pi$ chosen such that $\omega = \varepsilon - \nu$. We assume that $\omega \sim \varepsilon$ and $\varepsilon, \omega \gg \nu$, as appropriate for typical optical and vibrational frequencies. The geometry of the problem is depicted schematically in Fig. 2.2.

The free Hamiltonian of the system is

$$H_1 = \nu a^\dagger a + \omega b^\dagger b + \varepsilon \sigma^+ \sigma^-, \tag{2.12}$$

where the bosonic ladder operators $a^\dagger$ and $b^\dagger$ respectively create motional quanta (phonons) and light quanta (photons), while $\sigma^- = |\downarrow\rangle\langle\uparrow| = (\sigma^+)^\dagger$ is the atomic lowering operator. We have assumed that all other electronic states and vibrational or cavity modes are off-resonant and can be neglected.

The interaction between the atom and the cavity field in the dipole approximation reads as [213, 214]

$$V_1 = g \sin\left[\eta\left(a + a^\dagger\right)\right]\left(b + b^\dagger\right)\left(\sigma^- + \sigma^+\right), \tag{2.13}$$

where g is the cavity coupling constant and the Lamb-Dicke parameter is defined as $\eta = \omega/\sqrt{2Mc_0^2\nu}$, with c_0 the speed of light in vacuum. The form of the interaction (2.13)

reflects the symmetry of the problem when the harmonic potential minimum coincides exactly with an electric field node. The electric field operator then changes sign under a parity transformation of the atomic centre-of-mass coordinate. This gives rise to a selection rule allowing only transitions between motional states of opposite parity. Since the vibrational energy eigenstates have definite parity, the absorption or emission of a photon must therefore be accompanied by a change in the number of phonons.

We now show that the system realises a QAR and estimate its virtual temperature. We work in the limit $\eta \ll 1$, which requires that the cavity mode wavelength is much larger than the characteristic length scale of atomic motion. We can therefore invoke the Lamb-Dicke approximation (LDA) and expand Eq. (2.13) to first order in η. We also make the RWA by discarding counter-rotating terms at optical frequency, leading to

$$V_1 \approx g\eta \left(a + a^\dagger\right) \left(b\sigma^+ + b^\dagger\sigma^-\right). \tag{2.14}$$

Assuming that terms counter-rotating at frequency $\pm 2\nu$ can also be neglected, we finally obtain

$$V_1 \approx g\eta \left(ab\sigma^+ + a^\dagger b^\dagger\sigma^-\right). \tag{2.15}$$

We therefore find under these assumptions that the system exhibits a three-body interaction of the type (2.4). Note that the approximation leading to Eq. (2.15) is valid only when $g\eta \ll 2\nu$. Eq. (2.15) also assumes that the line widths of relevant transitions are much smaller than the trap frequency ν, as discussed in detail in Section 2.2.3.

The heat reservoir is provided by coupling thermal light at a high temperature T_h into the cavity resonator. Assuming that the thermal light source is well collimated, the electronic transition couples only to the ambient radiation field at room temperature $T_r \ll T_h$, which leads to spontaneous emission. Meanwhile, the motion of the atom undergoes intrinsic heating, for example due to fluctuations of the trap potential.

The virtual qubit states in the machine are the pairs $\{|n_b, \downarrow\rangle, |n_b - 1, \uparrow\rangle\}$, where $|n_b\rangle$ denotes a Fock state with n_b quanta in the cavity mode. The virtual temperature of the refrigerator is therefore

$$T_v = \frac{\nu}{\varepsilon/T_r - \omega/T_h}. \tag{2.16}$$

Since $T_h \gg T_r$ and $\nu \ll \varepsilon$, we find that

$$\frac{T_v}{T_r} \approx \frac{\nu}{\varepsilon}. \tag{2.17}$$

The ratio of frequencies is typically $\nu/\varepsilon \sim 10^{-8}$ or less, implying that very low virtual temperatures are achievable.

The refrigerator operation can be understood by a straightforward analogy with laser sideband cooling. The optical cavity behaves as a filter which singles out frequencies

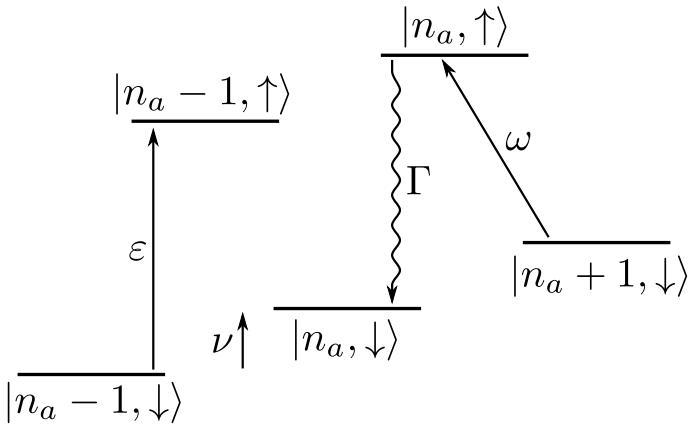


Figure 2.3. Level scheme showing the manifold of electronic and vibrational states for the single-cavity configuration. Thermal cavity photons resonant with the red sideband transition are absorbed, then the electronic state is reset by spontaneous emission, driving the system down the ladder of vibrational states.

close to the red sideband $\omega_{\text{red}} = \varepsilon - \nu$. Pumping the cavity with thermal light increases the number of photons with the correct frequency to drive the red sideband transition. Spontaneous emission then resets the electronic state, completing the cooling cycle (see Fig. 2.3). So long as the blue sideband frequency $\omega_{\text{blue}} = \varepsilon + \nu$ is far off-resonant, the absorption of thermal cavity photons drives the motion towards its ground state.

2.2.2 Master equation

In order to study the dynamics of the model, we employ a quantum master equation for the density operator ρ of the form

$$\frac{\mathrm{d}\rho}{\mathrm{d}t} = \mathrm{i}[\rho, H_1 + V_1] + \sum_{j=a,b,\sigma} \mathcal{L}_j \rho. \tag{2.18}$$

The superoperators $\mathcal{L}_j$ are dissipative contributions due to the coupling of each subsystem to its respective reservoir. The term $\mathcal{L}_a$ describes motional heating, $\mathcal{L}_b$ corresponds to the thermal pumping of the cavity, while $\mathcal{L}_\sigma$ relates to spontaneous emission.

The motional heating is described by

$$\mathcal{L}_a = \lambda(1 + \bar{n}_a^{-1})\mathcal{D}[a] + \lambda\mathcal{D}[a^\dagger], \tag{2.19}$$

where $\bar{n}_a = (\mathrm{e}^{\nu/T_r} - 1)^{-1}$ is the equilibrium phonon number at room temperature. Since in a typical trap $\bar{n}_a$ is very large, the dissipator (2.19) describes approximately linear growth of the phonon number at a constant heating rate λ. Pumping of the cavity with thermal light is described by

$$\mathcal{L}_b = 2\kappa(1 + \bar{n}_b)\mathcal{D}[b] + 2\kappa\bar{n}_b\mathcal{D}[b^\dagger], \tag{2.20}$$

where κ is the cavity line width and $\bar{n}_b = (\mathrm{e}^{\omega/T_h} - 1)^{-1}$ is the equilibrium photon number at temperature T_h. For simplicity, we have assumed here that the thermal driving is applied to both sides of the cavity. Spontaneous emission is described by the Liouvillian

$$\mathcal{L}_\sigma = \Gamma \int_{-1}^{1} \mathrm{d}u \; \Pi(u) \mathcal{D}[\mathrm{e}^{\mathrm{i}\eta u(a+a^\dagger)}\sigma^-], \tag{2.21}$$

where $\Pi(u)$ is the angular distribution of emitted photons as a function of $u = \cos\theta$, with θ the angle subtended from the x axis by the photon wave vector. Note that we have neglected the absorption term proportional to $\bar{n}_\sigma = (\mathrm{e}^{\varepsilon/T_r} - 1)^{-1}$, which is an excellent approximation under typical experimental conditions.

2.2.3 Line broadening and other constraints

Unfortunately, the single-cavity refrigerator suffers from several severe practical limitations. The most important of these is due to line broadening. The picture illustrated in Fig. 2.3, described by the Hamiltonian (2.15), is valid when the sideband transitions are "sharp", in the sense of having a well-defined frequency. However, thermal dissipation implies some unavoidable energy uncertainty due to the finite lifetime of the states involved. Significant cooling is only possible in the sideband-resolved regime, where the frequency uncertainty of the relevant transitions is much less than ν. Otherwise, line broadening brings the blue sideband transition partially onto resonance, leading to heating rather than cooling. In particular, this means that we must have $\lambda, \kappa, \Gamma < \nu$ for effective refrigeration.

In order to illustrate the effect of line broadening, we compute the steady-state phonon occupation $n_a(\infty) = \mathrm{Tr}[a^\dagger a \rho_\infty]$, where ρ_∞ is the stationary quantum state satisfying $\mathrm{d}\rho_\infty/\mathrm{d}t = \mathcal{L}\rho_\infty = 0$, with $\mathcal{L}$ given by the RHS of Eq. (2.18). The problem is simplified by taking the interaction Hamiltonian (2.14) under the LDA and RWA, and making the approximation $\bar{n}_a^{-1} \approx 0$, leaving just five free parameters governing the phonon population dynamics: λ, η, κ, $\bar{n}_b$ and Γ. We compute the stationary state by representing $\mathcal{L}$ as a matrix and solving the eigenvalue equation $\mathcal{L}\rho_\infty = 0$. The integral in Eq. (2.21) is numerically approximated by a trapezoidal rule. We take $\Pi(u) = 3(1 + u^2)/8$, as appropriate for a point dipole aligned perpendicularly to the cavity axis. Sampling a grid of 100 evenly spaced points in the interval $u \in [-1, 1]$ is sufficient to obtain convergence. The resulting Liouvillian matrix has low sparsity and is therefore challenging to diagonalise, which limits the achievable Hilbert space dimension considerably. We use 21 phonon states and 4 cavity photon states in total. This is insufficient for a quantitatively accurate calculation, since we obtain occupation numbers that are appreciable in comparison to the dimension of truncated phonon Hilbert space. Nevertheless, the results serve as a useful basis to discuss qualitative trends.

The calculated dependence of $n_a(\infty)$ on the dissipation rates κ and Γ is plotted for some

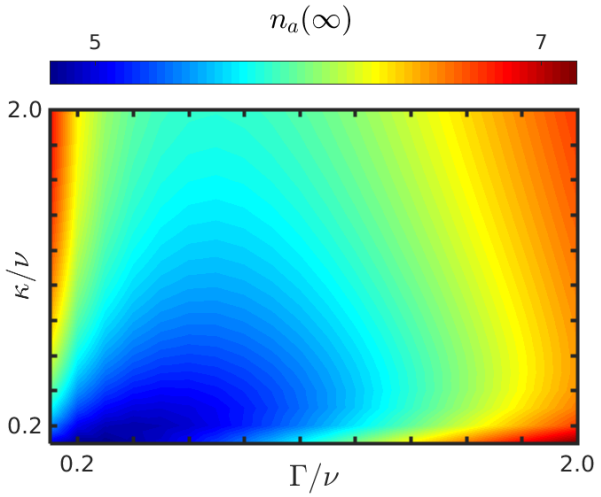


Figure 2.4. Qualitative dependence of the steady-state phonon occupation $n_a(\infty)$ on the spontaneous emission rate Γ and the cavity decay constant κ, with $\eta = 0.05$, $g = \nu$, $\bar{n}_b = 10^{-3}$ and $\lambda = 0$.

example parameters in Fig. 2.4. We see that the optimum operating regime is $\kappa, \Gamma \ll \nu$, as expected. The performance deteriorates rapidly as Γ or κ is increased above the trap frequency ν. Increasing the spontaneous emission rate has a particularly adverse effect, because the recoil momentum of emitted photons leads to further motional heating (see Eq. (2.21)). This is highly problematic, because the spontaneous emission rate in atomic two-level systems is fixed by Nature and may be on the order of tens or hundreds of megaherz, much larger than a typical vibrational frequency.

The deleterious effect of line broadening is worsened when the trap potential minimum is not placed exactly on the electric-field node of the cavity. Outside of the sideband-resolved regime, we have found that the system is remarkably sensitive to small misalignments of the trapping potential: displacements of a few nanometres away from the cavity field node lead to an almost complete disappearance of the cooling effect. This can be understood as follows. Away from the node, cavity photons may be emitted and absorbed without affecting the vibrational state of the atom. Photon absorption in particular depletes the cavity field and reduces the effective temperature of the hot reservoir. Although these transitions, which occur at the so-called carrier frequency ε, are off-resonant in principle, they become important when levels are broadened.

Finally, in order to enforce the resonance condition $\omega = \varepsilon - \nu$, it is necessary to stabilise the length of the cavity to prevent frequency drift. This may be achieved, for example, by continuously driving the cavity with a laser field and using the Pound-Drever-Hall technique [215]. Importantly, this stabilisation can be performed using other polarisation modes or different cavity harmonics from those directly relevant for the refrigerator's operation. Of course, this use of an external laser field means that the machine is not truly autonomous.

However, the laser does not supply any work used directly for cooling. Rather, its role is to provide a stable frequency reference.

2.3 Crossed-cavity absorption refrigerator

In this section we describe a detailed model of a quantum absorption refrigerator comprising a trapped atom within a pair of perpendicular optical cavities. The purpose of the additional cavity is to ameliorate the adverse effects of spontaneous emission. We predict that such a machine powered by sunlight can cool a trapped ion to near its motional ground state, and explicitly delineate the parameter regime in which this is possible.

2.3.1 Description of the model

As in Section 2.2.1, we consider a harmonically trapped atom or ion of mass M, possessing a pair of electronic states $|\downarrow\rangle$ and $|\uparrow\rangle$ separated by energy ε. In this section we explicitly model the atomic motion in both the x and y directions, although it will shortly be shown that the y coordinate decouples from the dynamics for our chosen configuration. For simplicity of presentation, we make the inessential assumption of equal oscillation frequencies in both the x and y directions, given by $\nu/2\pi$.

The atom is placed inside a pair of optical cavities b and c, with axes aligned in the x and y direction, respectively. These cavities have relevant modes at frequencies $\omega_b/2\pi$ and $\omega_c/2\pi$. The minimum of the trap potential is placed a distance d_b from a node of the electric field in cavity b, and a distance d_c from an antinode of cavity c. The geometry of the problem is indicated in Fig. 2.5.

The free Hamiltonian of the system is

$$H_2 = \nu a_x^\dagger a_x + \nu a_y^\dagger a_y + \omega_b b^\dagger b + \omega_c c^\dagger c + \varepsilon \sigma^+ \sigma^-, \tag{2.22}$$

where $a_x^\dagger$ (a_y) creates motional excitations in the x direction (y direction), $b^\dagger$ ($c^\dagger$) creates photons in the cavity parallel to the x axis (y axis), and $\sigma^- = |\downarrow\rangle\langle\uparrow| = (\sigma^+)^\dagger$. The light-matter interaction Hamiltonian reads as

$$\begin{aligned} V_2 = {} & g_b \sin\left[\delta_b + \eta_b\left(a_x + a_x^\dagger\right)\right]\left(b + b^\dagger\right)\left(\sigma^- + \sigma^+\right) \\ & + g_c \cos\left[\delta_c + \eta_c\left(a_y + a_y^\dagger\right)\right]\left(c + c^\dagger\right)\left(\sigma^- + \sigma^+\right), \end{aligned} \tag{2.23}$$

where g_j is the coupling constant, $\eta_j = \omega_j/\sqrt{2Mc_0^2\nu}$ is the Lamb-Dicke parameter, and $\delta_j = d_j\omega_j/c_0$ is the dimensionless misalignment for cavity $j = b, c$. As before, all other cavity and vibrational modes and electronic states are assumed be far off-resonant.

Assuming that $\eta_j, \delta_j \ll 1$, we expand Eq. (2.23) to first order in small quantities and

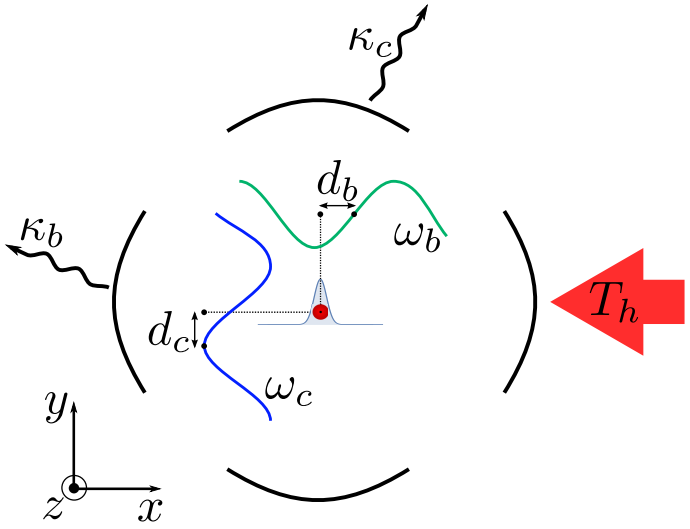


Figure 2.5. Schematic of the crossed-cavity set-up. An atom is trapped close to an electric-field node of cavity mode b and an antinode of cavity mode c. Pumping mode b with thermal light results in cooling of the atomic motion. A similar configuration was studied in Ref. [216], in the context of dissipative entanglement generation.

make the RWA, which yields

$$V_2 \approx \tilde{g}_b \eta_b \left(a_x + a_x^\dagger\right)\left(b\sigma^+ + b^\dagger\sigma^-\right) + \tilde{g}_c\left(c\sigma^+ + c^\dagger\sigma^-\right) + h_b\left(b\sigma^+ + b^\dagger\sigma^-\right), \tag{2.24}$$

where $\tilde{g}_{b,c} = g_{b,c}\cos\delta_{b,c}$ and $h_b = g_b \sin\delta_b$. We see that, to lowest order, the excitation of phonons in the y direction is suppressed close to the antinode of cavity c. The motion in the y direction is therefore neglected from here on. In order to simplify the notation we also set $a_x = a$ and $\eta_b = \eta$.

We demand that the cavities be tuned to two-photon resonance with the red sideband, $\omega_c - \omega_b = \nu$, yet detuned from the carrier by an amount $\Delta = \omega_c - \varepsilon$, where $\varepsilon \gg |\Delta| \gg g_{b,c}$. Direct excitation of the internal state of the atom, and the associated spontaneous emission, is thus strongly suppressed. However, due to the resonance condition $\omega_c = \omega_b + \nu$, the cavities can coherently exchange photons, assisted by the creation or destruction of phonons. In the following subsection, we show that this process is described by an effective interaction

$$V_{\text{eff}} = k\left(abc^\dagger + a^\dagger b^\dagger c\right), \tag{2.25}$$

where $k = \tilde{g}_b\tilde{g}_c\eta/\Delta$. This obviously corresponds to the general form (2.4).

The refrigerator is powered by pumping cavity mode b with hot thermal light at temperature T_h, while cavity mode c couples to the radiation field at room temperature T_r. The virtual qubit states for this system are the pairs $\{|n_b, n_c\rangle, |n_b - 1, n_c + 1\rangle\}$. The virtual

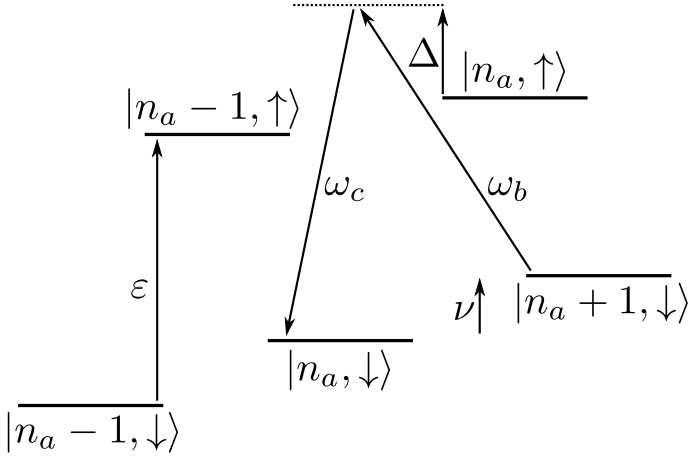


Figure 2.6. Level scheme for the crossed-cavity configuration showing the direct analogy with Raman sideband cooling. Cooling on the red sideband occurs via a two-photon transition in which photons are exchanged between the two cavities. Spontaneous emission from the excited electronic state is suppressed by the detuning Δ.

temperature is given by

$$T_v = \frac{\nu}{\omega_c/T_r - \omega_b/T_h} \approx \frac{\nu}{\omega_c} T_r, \tag{2.26}$$

since $T_h \gg T_r$ and $\omega_c \gg \nu$, and we see again that very low virtual temperatures can be obtained.

The operation of the refrigerator can be understood by analogy with Raman laser sideband cooling (see Fig. 2.6). Addressing the red sideband with a two-photon transition avoids populating the fast-decaying excited electronic state. The line width of the transition is therefore determined by the cavity decay rates, which in principle may be made much smaller than the spontaneous emission rate. This makes achieving the sideband-resolved regime a feasible prospect in this system.

The cavity lengths must be actively stabilised in order to avoid frequency drift away from the resonance condition $\omega_c - \omega_b = \nu$. As described in Section 2.2.3, this stabilisation can be performed noninvasively using a laser. This makes the double-cavity refrigerator not truly autonomous. However, we emphasise again that the role of the laser is to provide a frequency reference, rather than to directly perform work used for cooling.

2.3.2 Master equation

The density operator of the full system, including the electronic degrees of freedom, satisfies the master equation

$$\frac{\mathrm{d}\rho}{\mathrm{d}t} = \mathrm{i}[\rho, H_2 + V_2] + \sum_{j=a,b,c,\sigma} \mathcal{L}_j \rho, \tag{2.27}$$

where $\mathcal{L}_a$ and $\mathcal{L}_\sigma$ are respectively defined by Eqs. (2.19) and (2.21). The coupling of cavity b to the external electromagnetic field is described by

$$\mathcal{L}_b = \kappa_b \left(2 + \bar{n}_b\right) \mathcal{D}[b] + \kappa_b \bar{n}_b \mathcal{D}[b^\dagger], \tag{2.28}$$

where κ_b is the cavity line width and $\bar{n}_b = \left(\mathrm{e}^{\omega_b/T_h} - 1\right)^{-1}$ is the equilibrium photon number at temperature T_h. Eq. (2.28) represents thermal driving applied to only one side of cavity b, while the other side couples to the vacuum (which approximates the electric field at room temperature). Cavity c couples to the environment via the Liouvillian

$$\mathcal{L}_c = 2\kappa_c \mathcal{D}[c], \tag{2.29}$$

where κ_c is the corresponding line width, and we have neglected the absorption term proportional to $\bar{n}_c = (\mathrm{e}^{\omega_c/T_r} - 1)^{-1}$.

We note that direct excitation of the electronic degrees of freedom is suppressed by the large detuning $|\Delta| \gg \tilde{g}_{b,c}, h_b$. Furthermore, Γ will typically be the largest dissipative frequency scale in the system, so that correlations between the electronic degrees of freedom and the rest of the system decay rapidly on the time scales relevant for the dynamics of the atomic motion. These assumptions enable us to simplify the model by adiabatically eliminating the excited electronic state within a Born-Markov approximation.

Specifically, we use the techniques detailed in Chapter 1 to derive a master equation for the reduced density matrix $\rho_{abc}(t) = \mathrm{Tr}_\sigma[\rho(t)]$ projected onto the electronic ground state manifold, where Tr_σ denotes the trace over the electronic degrees of freedom. In the notation of Chapter 1, we have $\mathcal{P}\rho = \rho_{abc} \otimes \langle\downarrow|\rho|\downarrow\rangle$, $H_B = \varepsilon\sigma^+\sigma^-$, $\mathcal{L}_B = \mathcal{H}_B + \mathcal{L}_\sigma$, $H_A = H_2 - H_B$, $\mathcal{L}_1 = \mathcal{L}_a + \mathcal{L}_b + \mathcal{L}_c$, and $H_{AB} = V_2$, with the latter taken in the LDA and given by Eq. (2.24). We also neglect the atom's recoil momentum associated with spontaneous emission of photons, a step which is justified by the following perturbative argument. We observe from Eq. (2.21) that $\mathcal{L}_\sigma = \Gamma\mathcal{D}[\sigma^-] + O(\eta^2\Gamma)$, assuming that the spontaneous emission is isotropic, i.e. $\Pi(u) = \Pi(-u)$. Taking just the zeroth-order term in η is justified if $\eta^2\Gamma$ is on the same order or smaller than the energy scales entering the interaction Hamiltonian H_{AB}. In this case, a careful analysis [1] shows that terms of order $\eta^2\Gamma$ are comparable in magnitude to the higher-order contributions from H_{AB} which are also neglected.

The resulting master equation is

$$\frac{\mathrm{d}\rho_{abc}}{\mathrm{d}t} = \mathrm{i}[\rho_{abc}, H_{abc} + \delta H_{abc} + V_{\mathrm{eff}}] + \mathcal{L}_{\mathrm{se}}\rho_{abc} + \sum_{j=a,b,c} \mathcal{L}_j \rho_{abc}, \tag{2.30}$$

where, in the limit $|\Delta| \gg \Gamma, \nu$, we find

$$H_{abc} = \nu a^\dagger a + \omega_b b^\dagger b + \omega_c c^\dagger c, \tag{2.31}$$

$$\delta H_{abc} = \frac{2\tilde{g}_b^2\eta^2}{\Delta} a^\dagger a b^\dagger b + \frac{\tilde{g}_b^2\eta^2 + h_b^2}{\Delta} b^\dagger b + \frac{\tilde{g}_c^2}{\Delta} c^\dagger c, \tag{2.32}$$

$$\mathcal{L}_{\rm se} = \frac{\Gamma\sqrt{\tilde{g}_b^2\eta^2 + \tilde{g}_c^2}}{\Delta^2}\mathcal{D}[\tilde{g}_b\eta ab + \tilde{g}_c c] + \frac{\tilde{g}_b^2\eta^2\Gamma}{\Delta^2}\mathcal{D}[a^\dagger b] + \frac{h_b^2\Gamma}{\Delta^2}\mathcal{D}[b], \tag{2.33}$$

while $V_{\rm eff}$ is given by Eq. (2.25). The generator $\mathcal{L}_{\rm se}$ describes additional dissipative processes due to spontaneous emission from the excited state, which are suppressed by a factor of order Γ/Δ relative to the coherent contributions δH_{abc} and $V_{\rm eff}$.

We now summarise the approximations underlying Eq. (2.30). The assumption of negligible population of the excited electronic state is valid so long as the detuning is sufficiently large, i.e.

$$\tilde{g}_b\eta, h_b, \tilde{g}_c \ll |\Delta|. \tag{2.34}$$

We have also neglected the motional recoil due to spontaneous emission. This is justified when the spontaneous emission is isotropic and the system is deep in the Lamb-Dicke regime, so that

$$\eta^2\Gamma \lesssim \tilde{g}_b\eta, h_b, \tilde{g}_c. \tag{2.35}$$

The Born-Markov assumption requires the memory time of the electronic degrees of freedom to be much shorter than the characteristic time scales of the effective evolution, which implies that

$$k, \kappa_b, \kappa_c, \delta E \ll \Gamma, \tag{2.36}$$

where δE represents any energy shift appearing in δH_{abc}. Finally, in order to put the master equation (2.30) into Lindblad form, we must perform a rotating-wave approximation, valid when

$$k, \kappa_b, \kappa_c, \delta E \ll \nu, \tag{2.37}$$

which corresponds to the definition of the sideband-resolved regime for this system.

2.3.3 Phonon dynamics

In this subsection, we characterise the performance of the refrigerator in terms of the steady-state phonon occupation $n_a(\infty)$, focusing specifically on cooling using sunlight as an energy source. We take representative parameters pertaining to $^{171}\mathrm{Yb}^+$ (listed in Table 2.1). This species is a good choice due to its large mass and correspondingly small photon recoil, in addition to the existence of a closed dipole-allowed cooling transition. However, one could equally well consider other species of ion or neutral atom.

From here on we set $g_{b,c} = g$, $\kappa_{b,c} = \kappa$, and $d_{b,c} = d$ for simplicity. We compute

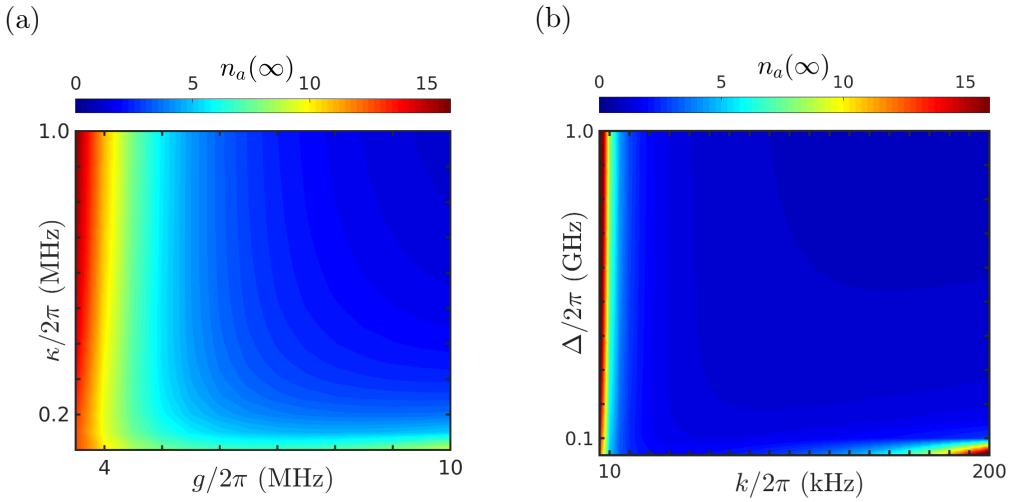


Figure 2.7. Steady-state phonon occupation of the crossed-cavity absorption refrigerator driven by sunlight. Parameters are given in Table 2.1, with (a) fixed $\Delta/2\pi = 100$ MHz and variable g and κ, and (b) fixed $\kappa/2\pi = 0.5$ MHz and variable k and Δ.

$n_a(\infty) = \mathrm{Tr}[a^\dagger a \rho_\infty]$ by solving $\mathrm{d}\rho_\infty/\mathrm{d}t = \mathcal{L}\rho_\infty = 0$, with $\mathcal{L}$ defined by the RHS of Eq. (2.30). We use a truncated Hilbert space with 71 phonon states and 4 states per cavity mode. Such a small Hilbert space dimension for the cavity modes is justified since the mean number of cavity photons in the steady state is $n_b(\infty) \approx 10^{-3}$ and $n_c(\infty) < 10^{-4}$ in cavities b and c, respectively, for all parameters considered. We have checked that decreasing the Hilbert space dimension leads to negligible changes in the results.

Our predictions for $n_a(\infty)$ are shown in Fig. 2.7. We observe that sunlight at $T_h = 5800$ K is sufficient to drive the phonon almost to its ground state, so long as the effective coupling constant k is sufficiently large. In Fig. 2.7(a) we show that, in the regime of effective cooling, the steady-state phonon occupation is reduced by increasing κ for fixed g. Nevertheless, κ must remain smaller than ν for the system to remain in the sideband-resolved regime (Eq. (2.37)), which represents a key factor limiting the achievable steady-state phonon occupation. In Fig. 2.7(b) we demonstrate that increasing Δ for fixed k can improve performance by suppressing incoherent effects associated with spontaneous emission.

In the limit of $|\Delta| \gg \Gamma$ and $k \ll \kappa$, we can give a rough analytical estimate of the relaxation time. In this regime, we can derive an effective evolution equation for the

T_h	T_r	$\nu/2\pi$	η	$\varepsilon/2\pi$	$\Gamma/2\pi$	λ	d
5800 K	300 K	5 MHz	0.041	810 THz	20 MHz	10 quanta/s	10 nm

Table 2.1. Table of parameters used in numerical calculations.

motional degrees of freedom by tracing over the cavity modes. In particular, we project the cavity modes onto the thermal states ρ_b and ρ_c which are the fixed points of their respective local dissipators, i.e. they satisfy $\mathcal{L}_b\rho_b = 0$ and $\mathcal{L}_c\rho_c = 0$. We then derive a master equation for the motional mode described by the reduced density operator $\rho_a = \mathrm{Tr}_{bc}[\rho_{abc}]$. In the notation of Chapter 1, we have $\mathcal{P}\rho_{abc} = \rho_a \otimes \rho_b \otimes \rho_c$, $H_A = \nu a^\dagger a$, $H_B = H_{abc} - H_A$, $\mathcal{L}_B = \mathcal{H}_B + \mathcal{L}_b + \mathcal{L}_c$, $\mathcal{L}_1 = \mathcal{L}_a$, and $H_{AB} = V_{\text{eff}}$. The energy shifts represented by δH_{abc} lead to higher-order corrections and are neglected. The resulting equation of motion can be solved to give the phonon population as a function of time

$$n_a(t) = n_\infty + \mathrm{e}^{-\gamma t}\left(n_0 - n_\infty\right), \tag{2.38}$$

where $n_\infty = \lambda/\gamma$ is the steady-state phonon number, $n_0 = n_a(0)$ is the initial population, and the relaxation rate is $\gamma = k^2\bar{n}_b/\kappa$.

2.3.4 Collective coupling enhancement in many-ion systems

Now we generalise to the scenario where multiple atoms are trapped inside the cavities. We focus in particular on ion-trap systems, where the Coulomb interaction couples the motion of the different ions. The normal vibrational modes of the system are thus small collective oscillations about the mechanical equilibrium. We shall see that if N ions of the same species are placed inside the crossed-cavity refrigerator, an N-fold enhancement of the coupling between photons and phonons can be obtained.

The free Hamiltonian of the system is

$$H_2 = \nu a^\dagger a + \omega_b b^\dagger b + \omega_c c^\dagger c + \sum_{j=1}^{N} \varepsilon_j \sigma_j^+ \sigma_j^-. \tag{2.39}$$

Here, $a^\dagger$ creates a phonon of a normal mode with frequency $\nu/2\pi$, σ_j^- is the atomic lowering operator for atom j and we have allowed for variations of the electronic transition frequencies ε_j, due to inhomogeneous magnetic fields, for example. All other modes and electronic states are assumed to be off-resonant. The interaction Hamiltonian in the LDA and RWA reads as

$$\begin{aligned} V_2 = \sum_{j=1}^{N} \Big\{ & \tilde{g}_b(\mathbf{r}_j)\eta_j \left(a + a^\dagger\right)\left(b\sigma_j^+ + b^\dagger\sigma_j^-\right) \\ & + \tilde{g}_c(\mathbf{r}_j)\left(c\sigma_j^+ + c^\dagger\sigma_j^-\right) + h_b(\mathbf{r}_j)\left(b\sigma_j^+ + b^\dagger\sigma_j^-\right)\Big\}, \end{aligned} \tag{2.40}$$

where $\tilde{g}_{b,c}(\mathbf{r}_j) = g_{b,c}(\mathbf{r}_j)\cos\delta_{b,c}(\mathbf{r}_j)$, $h_b(\mathbf{r}_j) = g_b(\mathbf{r}_j)\sin\delta_b(\mathbf{r}_j)$, with $g_{b,c}(\mathbf{r}_j)$ the cavity coupling constants for the ion with equilibrium position $\mathbf{r}_j$, while η_j are the Lamb-Dicke parameters and $\delta_{b,c}(\mathbf{r}_j) = d_{b,c}(\mathbf{r}_j)\omega_{b,c}/c_0$ are the dimensionless misalignments, where $d_b(\mathbf{r}_j)$

($d_c(\mathbf{r}_j)$) is the distance in the x direction (y direction) between $\mathbf{r}_j$ and the field node of cavity b (antinode of cavity c).

We assume again that the cavities are detuned from the electronic transition frequencies, $\omega_c = \varepsilon_j + \Delta_j = \omega_b + \nu$, with $\varepsilon_j \gg |\Delta_j| \gg g_{b,c}(\mathbf{r}_j)$. After adiabatically eliminating the electronic excited states according to the same procedure as in Section 2.3.2, we find an effective interaction of the form

$$V_{\text{eff}} = k_{\text{coll}} \left(abc^\dagger + a^\dagger b^\dagger c \right). \tag{2.41}$$

In the limit $|\Delta_j| \gg \Gamma$, the collective coupling constant is found to be

$$k_{\text{coll}} = \sum_{j=1}^{N} \frac{\tilde{g}_b(\mathbf{r}_j)\tilde{g}_c(\mathbf{r}_j)\eta_j}{\Delta_j}. \tag{2.42}$$

We also find independent, additive contributions from each ion in the form of Eqs. (2.32) and (2.33).

The effective collective coupling k_{coll} can be either enhanced or suppressed compared to the single-particle case, depending on the symmetry of the normal mode in question. For example, let us take $N = 2$ and assume that $\tilde{g}_{b,c}(\mathbf{r}_1) = \tilde{g}_{b,c}(\mathbf{r}_2) = \tilde{g}_{b,c}$ and $\Delta_1 = \Delta_2 = \Delta$. For the stretch mode, with $\eta_1 = -\eta_2$, we find that $k_{\text{coll}} = 0$. On the other hand, for the centre-of-mass mode, with $\eta_1 = \eta_2 = \eta$, we find a two-fold enhancement of the coupling, i.e. $k_{\text{coll}} = 2k$, where $k = \tilde{g}_b\tilde{g}_c\eta/\Delta$ is the single-ion effective coupling. In general, the centre-of-mass oscillations experience enhanced collective coupling, since for this vibrational mode $\eta_j = \eta$ is constant.

Note that the rate of heating may also increase with the number of ions. For example, the heating rate for the centre-of-mass mode increases proportionally to N, assuming spatially correlated trap potential fluctuations [217]. However, according to the estimate given by Eq. (2.38), the steady-state phonon occupation and relaxation time scale as k_{coll}^{-2}. We therefore expect an N-fold enhancement of the refrigerator's performance when cooling the centre-of-mass mode of N ions.

2.4 Conclusion

To summarise, we have analysed the possibility of creating a QAR in the setting of cavity QED. In particular, we have shown that it is possible to construct a refrigerator which cools the motion of a trapped atom using sunlight. This would constitute perhaps the first example of a quantum absorption chiller which can achieve technologically useful temperatures.

In principle, such a refrigerator powered by sunlight costs nothing to operate in daylight hours (under clement weather conditions). This is clearly an improvement on power-hungry

and thermodynamically inefficient cooling lasers. In practice however, we find that the technical difficulty of stabilising the cavity frequencies makes the use of a laser, or similar frequency reference system, unavoidable with present technology.

Commercially available laser systems enjoy stability, reliability and flexibility, spanning a range of optical and ultra-violet frequencies. These properties are unmatched by optical cavities currently available in cavity QED experiments. Therefore, absorption chillers of the kind we envisage are unlikely to supersede laser-driven cooling schemes in the near future. Nevertheless, our results demonstrate that if the intrinsic stability of optical resonators can be improved, QARs could in principle play a useful role in quantum state preparation.

A more immediately relevant feature of our proposal is that it offers a versatile experimental platform to study the physics of QARs. One advantage of our scheme is that the frequencies of — and the couplings between — different degrees of freedom are tunable by means of external control fields, or by modifying the cavity lengths mechanically. We have also shown that the coupling can be enhanced N-fold when N ions of the same species are incorporated inside the refrigerator. Note that experiments investigating collective cavity coupling enhancement in trapped-ion systems have already achieved $N \sim 500$ [218, 219]. In addition, detailed control over the coupling between each ion and a cavity has recently been demonstrated for $N = 5$ [220], which is already sufficient to obtain significant enhancement.

Another attractive feature of the cavity QED setting is the wide variety of measurements that are available. For example, a different species of ion placed inside the trap could be used to make nondemolition measurements of steady-state properties, such as the phonon number [151]. One could also continuously and nondestructively monitor the state of the cavity fields using appropriately placed photodetectors. This would yield direct information on the rate of energy dissipation into the environment, as well as opening up a new potential arena for exploring quantum thermodynamics with measurement feedback [221,222]. Nonthermal or non-Markovian reservoirs could be engineered by modifying the spectrum or statistics of the radiation incident on the cavity [223], or by tickling the ion-trap electrodes with suitably filtered electrical noise [224]. We also note that analogous set-ups using different kinds of quantum emitters such as superconducting qubits, quantum dots or diamond color centers may be envisaged.

On a conceptual level, our study provides a number of further insights. We found a simple and intuitive interpretation of quantum absorption refrigerators in terms of sideband transitions. The present context of atomic cooling makes the connection between these two concepts manifest, however this link is in fact completely general. Any three-body absorption refrigerator can be understood in terms of a red sideband transition, which is excited by the absorption of quanta from a thermally populated auxiliary system, itself connected to a hot reservoir. The role of the second, colder reservoir is to then quickly reset the state of the refrigerator by a transition at the carrier frequency (that is, at frequency

ε), leaving the target system with one less quantum of energy. Thus, sideband transitions provide an alternative framework for understanding QARs which is complementary to the standard picture in terms of virtual qubits and temperatures.

We also found that, just as in laser sideband cooling, the existence of blue sideband transitions limits the thermal dissipation rates and the three-body interaction strength to be less than the frequency of the target subsystem, i.e. one must be in the sideband-resolved regime. This constraint is rather general, because blue sideband transitions (or more generally, off-resonant transitions) exist for any absorption refrigerator governed by an interaction Hamiltonian composed of a single product of Hermitian operators (rather than a sum of such products). We thus expect a similar sideband-resolved condition to generically constrain the achievable power and other relevant thermodynamic quantities describing these machines.

As we have shown, an absorption refrigerator transferring energy from motional degrees of freedom to optical photons can achieve remarkably low temperatures in principle. This results from the huge separation between vibrational and optical frequencies, leading to extremely small virtual temperatures (see Eq. (2.26)). The same principle underlies other recent proposals to build thermal machines using cavity optomechanical systems [49, 67]. However, this separation of frequency scales also implies an instability of the system to relatively small fluctuations or drifts of the optical frequencies. This suggests that a practical operating regime for truly autonomous quantum thermal machines will be such that the natural frequencies of the constituent subsystems are commensurate with each other.

In the present example, the effects of frequency drift can be overcome by weakly driving the cavity with a laser. This indicates that the truly essential resource for cooling in the quantum regime is a stable frequency reference, or equivalently an *accurate clock*. Given such a frequency reference, we have shown that chaotic thermal energy suffices to cool the system almost to its ground state. If one adopts the view that the heat energy driving the absorption refrigerator is a free resource, the performance of the machine is then ultimately limited by the efficiency of the frequency reference or clock. In the next chapter we consider a different example in which accurate timing is a useful resource for cooling by quantum absorption refrigerators. A natural question thus arises regarding the fundamental thermodynamic limitations on clocks, accounting for the energy required to measure the clock [225] and any effect of correlations between the clock and the thermal machine [226–228]. We are currently investigating this intriguing problem by treating the clock itself as an autonomous thermal machine, but our results are presented elsewhere [8].

Chapter 3

Coherence-assisted single-shot cooling with quantum absorption refrigerators

In this chapter, we study the transient dynamics of quantum absorption refrigerators, showing that quantum oscillations can lead to a speed-up in cooling. This reproduces work presented in Ref. [2].

Designing thermal machines that can be enhanced by quantum dynamics is a pivotal challenge in the field of quantum thermodynamics. Previous research into possible quantum advantages for heat engines and refrigerators has focused almost exclusively on their operation in the steady state. However, in many applications one wishes to reach low temperatures as rapidly as possible, in which case understanding the short-time behaviour is essential. In particular, the cooling may be applied only transiently, after which the cold object is extracted for use. As a somewhat frivolous yet illustrative example, consider the problem of refrigerating a beverage on a hot day. Maximum enjoyment is obtained if the beverage can be cooled and then consumed quickly, at a temperature significantly lower than that of the environment. A more serious example could be the initialisation of a register of qubits for quantum information processing, where the aim is to produce states with high purity (low entropy). Fast cooling is advantageous here since it may reduce the overall time taken to complete the quantum information protocol. Both of these situations exemplify what we call *single-shot cooling*: the one-time application of a refrigeration device in order to considerably and rapidly reduce the temperature of the object in question.

In the following, we study single-shot cooling with a three-qubit quantum absorption refrigerator (QAR). By considering variations of the basic processes underlying energy dissipation and transport, we elucidate the role of coherence in the operation of such a device. Furthermore, we demonstrate that dramatic improvements can be obtained in both the cooling time and the achievable temperatures by taking advantage of coherent oscillations that appear in the transient dynamics of the refrigerator. Most importantly, the presence of coherence in the device allows one to reach lower temperatures than the steady state. This use of quantum coherence in order to cool below the steady-state temperature

we refer to as *quantum single-shot cooling*.

3.1 General scenario

We shall primarily be concerned with generic, qualitative features of the transient evolution of QARs. In order to simplify the presentation and our calculations, we focus on the most basic QAR model which conforms to the general framework described in Section 2.1. Specifically, we consider a QAR comprising three qubits described by standard Pauli operators $\sigma_i^{x,y,z}$, with the free Hamiltonian

$$H_0 = \frac{1}{2}\sum_{i=1}^{3} E_i \sigma_i^z. \tag{3.1}$$

Throughout this chapter, we adopt $E_1 = 1$ as our unit of energy, and thus E_1^{-1} as the unit of time. The qubits are coupled together according to the three-body interaction

$$V = g\,|001\rangle\langle 110| + \text{h.c.}, \tag{3.2}$$

where the computational basis states $|0\rangle$, $|1\rangle$ denote the eigenvectors of σ^z. As usual, we demand the resonance condition $E_3 = E_1 + E_2$. The interaction (3.2) then drives resonant transitions within the *transport subspace* spanned by the states $|001\rangle$ and $|110\rangle$.

For clarity, we refer to the qubits indexed by $i = 1, 2, 3$ as the target, the source and the sink, respectively. The target qubit is the system to be cooled. The source qubit is connected to a hot bath at temperature $T_2 = T_h$, while the remaining two qubits are connected to independent reservoirs at the ambient temperature $T_1 = T_3 = T_r$. The pair of states $\{|01\rangle, |10\rangle\}$ of the source and sink qubits comprises the machine's virtual qubit. This is associated with the virtual temperature

$$T_v = \frac{E_1}{\beta_3 E_3 - \beta_2 E_2}, \tag{3.3}$$

where $\beta_i = 1/T_i$ denotes the inverse temperature of the reservoir connected to qubit i.

The general set-up that we have in mind is illustrated in Fig. 3.1(a). We assume that all three qubits are initially in thermal equilibrium with their respective reservoirs. If $\rho_A(t)$ denotes the reduced state of the refrigerator qubits at time t, then the initial state is

$$\rho_A(0) = \bigotimes_{i=1}^{3} \frac{\mathrm{e}^{-\beta_i E_i \sigma_i^z/2}}{\mathrm{Tr}\left[\mathrm{e}^{-\beta_i E_i \sigma_i^z/2}\right]}. \tag{3.4}$$

At $t = 0$ the interaction (3.2) between the qubits is switched on. The aim is then to *prepare* the target qubit in a low-entropy state. (We emphasise that this is quite different

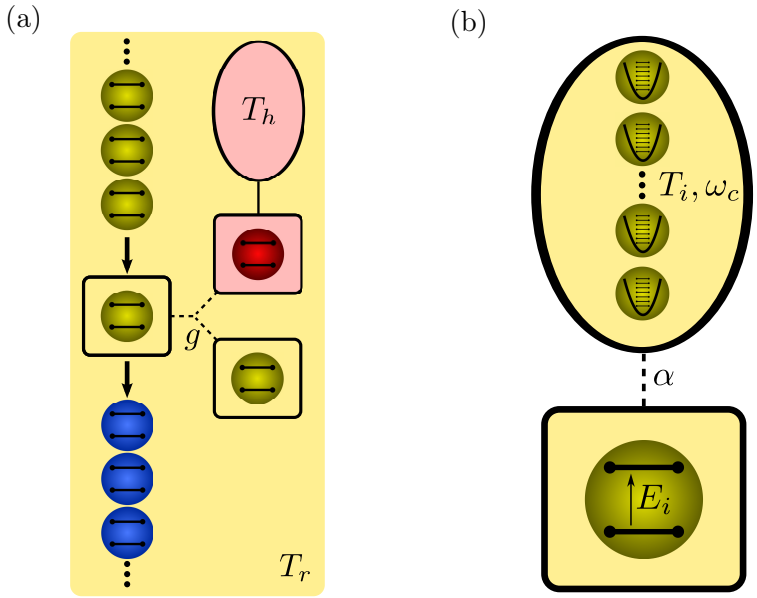


Figure 3.1. Cartoon illustrating our theoretical set-up. (a) A stream of thermal qubits passes sequentially through a quantum absorption refrigerator. Each thermal qubit interacts with the refrigerator for a finite time, and exits the device at a lower temperature. (b) The thermal reservoirs are modelled by infinite collections of harmonic oscillators, characterised by an Ohmic spectral density with bandwidth ω_c and a dimensionless coupling strength α.

from the usual objective considered by previous authors, namely to *maintain* the target qubit at a low temperature.) Once the lowest achievable temperature has been reached at time t_0, our cooling protocol is complete, and the target qubit may be extracted for use, for example, in quantum information processing. Classically, we usually expect that the lowest achievable temperature occurs only as $t \to \infty$. The existence of a finite optimal extraction time t_0 is the essence of the quantum single-shot cooling protocol. If we suppose now that there exists a large supply of qubits thermalised at the ambient temperature T_r, we can perform the same procedure repeatedly to produce a steady stream of low-entropy qubits.

3.2 Thermalisation model

In order to quantitatively analyse the refrigerator, we use a standard model of thermal dissipation whereby each qubit is locally coupled to reservoirs consisting of infinite collections of harmonic oscillators spanning a broad range of frequencies, depicted in Fig. 3.1(b). The reservoirs are described by the Hamiltonian $H_B = \sum_{i=1}^{3} H_{B_i}$, with

$$H_{B_i} = \sum_{\mathbf{k}} \omega_{i,\mathbf{k}} b_{i,\mathbf{k}}^{\dagger} b_{i,\mathbf{k}}, \tag{3.5}$$

where the bosonic mode operators satisfy canonical commutation relations $[b_{i,\mathbf{k}}, b^\dagger_{j,\mathbf{k}'}] = \delta_{ij}\delta_{\mathbf{k}\mathbf{k}'}$ and $[b_{i,\mathbf{k}}, b_{j,\mathbf{k}'}] = 0$. The reservoirs are taken to be in a product of thermal equilibrium states

$$\rho_B = \bigotimes_{i=1}^{3} \frac{\mathrm{e}^{-\beta_i H_{B_i}}}{\mathcal{Z}_i}. \tag{3.6}$$

The qubit-bath interaction is given by

$$H_{AB} = \sum_{i=1}^{3} \sigma_i^x \otimes \sum_{\mathbf{k}} \left(\lambda_{i,\mathbf{k}} b_{i,\mathbf{k}} + \lambda^*_{i,\mathbf{k}} b^\dagger_{i,\mathbf{k}} \right), \tag{3.7}$$

with constants $\lambda_{i,\mathbf{k}}$ that control the strength of the coupling of qubit i to its associated bath. The spectral density of each bath is defined by

$$\mathcal{J}_i(\nu) = \sum_{\mathbf{k}} |\lambda_{i,\mathbf{k}}|^2 \delta(\nu - \omega_{i,\mathbf{k}}). \tag{3.8}$$

We choose identical spectral densities for each bath $\mathcal{J}_i(\nu) = \mathcal{J}(\nu)$ of the form

$$\mathcal{J}(\nu) = \alpha \nu \mathrm{e}^{-\nu/\omega_c}. \tag{3.9}$$

The effect of the baths is therefore characterised by their temperature and two dynamical parameters: a dimensionless coupling strength α and a frequency cut-off ω_c leading to a bath memory time of order ω_c^{-1}. Markovian dynamics is obtained when ω_c is much larger than all other frequency scales and $\alpha \ll 1$, so that the dissipation rates are much smaller than the natural frequencies $\{E_i\}$ of the qubits.

For future reference, we note that Eq. (3.9) is called an Ohmic spectral density because it is proportional to frequency for small values of ν. More generally, spectral densities which vanish like ν^s as $\nu \to 0$ are classified according to the value of the exponent s as Ohmic ($s = 1$), sub-Ohmic ($s < 1$) or super-Ohmic ($s > 1$). For simplicity, we specialise to the Ohmic case in this chapter. Nevertheless, since we work in the Markovian limit, many of our main qualitative conclusions hold also for other spectral densities, such as the super-Ohmic spectral densities found more commonly in quantum optics applications. Some special features of the dynamics under super-Ohmic dissipation are discussed briefly at the end of the chapter.

In deriving the master equation, some care must be taken when treating the effect of the coupling between the qubits on their thermalisation dynamics. We obtain two different master equations depending on the magnitude of g, as described below.

3.2.1 Strong-coupling limit

The first master equation is valid in the strong-coupling limit, where g is so large that the effect of the interaction V on the dissipative dynamics cannot be neglected. In this case, thermal dissipation is described in terms of incoherent transitions between energy eigenstates of the coupled three-qubit Hamiltonian $H_0 + V$. The interaction V splits the degenerate states spanning the transport subspace into two new eigenstates $|\pm\rangle = (|110\rangle \pm |001\rangle)/\sqrt{2}$ with energies $E_3 \pm g$, while all other eigenstates of $H_0 + V$ are identical to those of H_0.

The master equation is derived following the procedure in Chapter 1, with $H_A = H_0 + V$, $\mathcal{L}_1 = 0$, and H_B given by Eq. (3.5). The result is

$$\frac{\mathrm{d}\rho_A}{\mathrm{d}t} = \mathrm{i}[\rho_A, H_0 + V] + \sum_{i=1}^{3} \sum_{\nu} \gamma_i(\nu) \mathcal{D}[A_i(\nu)]\rho_A, \tag{3.10}$$

where the Lindblad operators are

$$\begin{aligned} A_1(E_1) &= |011\rangle\langle 111| + |000\rangle\langle 100|, \\ A_1(E_1 + g) &= \frac{1}{\sqrt{2}}\big(|010\rangle\langle +| - |-\rangle\langle 101|\big), \\ A_1(E_1 - g) &= \frac{1}{\sqrt{2}}\big(|+\rangle\langle 101| + |010\rangle\langle -|\big), \end{aligned} \tag{3.11}$$

$$\begin{aligned} A_2(E_2) &= |101\rangle\langle 111| + |000\rangle\langle 010|, \\ A_2(E_2 + g) &= \frac{1}{\sqrt{2}}\big(|100\rangle\langle +| - |-\rangle\langle 011|\big), \\ A_2(E_2 - g) &= \frac{1}{\sqrt{2}}\big(|+\rangle\langle 011| + |100\rangle\langle -|\big), \end{aligned} \tag{3.12}$$

$$\begin{aligned} A_3(E_3) &= |100\rangle\langle 101| + |010\rangle\langle 011|, \\ A_3(E_3 + g) &= \frac{1}{\sqrt{2}}\big(|000\rangle\langle +| + |-\rangle\langle 111|\big), \\ A_3(E_3 - g) &= \frac{1}{\sqrt{2}}\big(|+\rangle\langle 111| - |000\rangle\langle -|\big), \end{aligned} \tag{3.13}$$

while the dissipation rates are given by $\gamma_i(\nu) = 2\pi\mathcal{I}_i(\nu)$, in terms of the bath spectral functions

$$\mathcal{I}_i(\nu) = \begin{cases} \mathcal{J}(\nu)[1 + n_i(\nu)] & (\nu > 0) \\ \mathcal{J}(|\nu|)n_i(|\nu|) & (\nu < 0), \end{cases} \tag{3.14}$$

where $n_i(\nu) = (\mathrm{e}^{\beta_i \nu} - 1)^{-1}$ is the Bose-Einstein distribution for the bath connected to

qubit i. We have neglected the Lamb-shift renormalisation of the energy levels of $H_0 + V$. This master equation was first derived by Correa et al. [208].

3.2.2 Weak-coupling limit

The second master equation is useful for exploring the weak-coupling limit, when $g \lesssim \gamma_i(\nu)$. In this case, the canonical rotating-wave approximation is unjustified, because counter-rotating terms at frequencies of order g are not negligible on the typical time scale of the incoherent refrigerator evolution. Therefore, a different approximation scheme is needed. The most direct route to obtain an alternate master equation is to set $H_A = H_0$ and $\mathcal{L}_1\rho = \mathrm{i}[V, \rho]$, leading to a description in terms of local thermal dissipators acting independently on each qubit. Explicitly, the weak-coupling master equation takes the form

$$\frac{\mathrm{d}\rho_A}{\mathrm{d}t} = \mathrm{i}[\rho_A, H_0 + V] + \sum_{i=1}^{3} \gamma_i(E_i)\mathcal{D}[\sigma_i^-]\rho_A + \sum_{i=1}^{3} \gamma_i(-E_i)\mathcal{D}[\sigma_i^+]\rho_A, \tag{3.15}$$

where $\sigma_i^{\pm} = (\sigma_i^x \pm \mathrm{i}\sigma_i^y)/2$, the rates $\gamma_i(\nu)$ are defined by Eq. (3.14), and we have again neglected the Lamb-shift terms.

In Ref. [2], in common with much of the literature on open many-body systems, the local Lindblad equation (3.15) was justified by the self-consistent assumption that $g \lesssim \gamma_i(\pm E_i) \ll E_i$. However, it is interesting to note that the local master equation for the three-qubit absorption refrigerator can also be derived in situations when g is not smaller than the incoherent rates, using a hybrid approximation scheme combining the wide-band approximation and the rotating-wave approximation.

In order to do this, we set $H_A = H_0 + V$ and return to Eq. (1.71) for the Redfield dissipator, which in the present case may be written as

$$\sum_{i=1}^{3} \sum_{\nu,\nu'} \Gamma_i(\nu)\mathrm{e}^{\mathrm{i}(\nu'-\nu)t} \left[A_i(\nu)\tilde{\rho}_A(t)A_i^\dagger(\nu') - A_i^\dagger(\nu')A_i(\nu)\tilde{\rho}_A(t)\right] + \mathrm{h.c.}, \tag{3.16}$$

with Lindblad operators $A_i(\nu)$ given by Eqs. (3.11)–(3.13), while the bath correlation functions are found from Eq. (1.25) to be

$$\Gamma_i(\nu) = \pi\mathcal{I}_i(\nu) + \mathrm{i}\mathsf{P}\int_{-\infty}^{\infty} \mathrm{d}\omega\, \frac{\mathcal{I}_i(\omega)}{\nu - \omega}. \tag{3.17}$$

We now assume that $g \ll E_i$, and that the spectral function $\mathcal{I}_i(\nu)$ varies slowly over frequencies of order g. This justifies the *partial* wide-band approximation $\mathcal{I}_i(E_i \pm g) \approx \gamma_i(E_i)$, from which it follows that $\Gamma_i(E_i \pm g) \approx \Gamma_i(E_i)$, and also that $\Gamma_i(-E_i \pm g) \approx \Gamma_i(-E_i)$ by a similar argument. However, we make no assumption about the relative magnitudes of $\Gamma_i(\pm E_i)$. Then, assuming that $|\Gamma_i(E_i)| \ll E_i$, we make a *partial* rotating-

wave approximation by crossing off terms in Eq. (3.16) where $|\nu' - \nu| \sim E_i$ but retaining counter-rotating terms where $|\nu' - \nu| \sim g$. Under these approximations, Eq. (3.16) splits into two separate pieces

$$\sum_{i=1}^{3} \sum_{\nu,\nu'>0} \Gamma_i(E_i) \mathrm{e}^{\mathrm{i}(\nu'-\nu)t} \Big[A_i(\nu) \tilde{\rho}_A(t) A_i^\dagger(\nu') - A_i^\dagger(\nu') A_i(\nu) \tilde{\rho}_A(t) \Big]$$
$$+ \sum_{i=1}^{3} \sum_{\nu,\nu'<0} \Gamma_i(-E_i) \mathrm{e}^{\mathrm{i}(\nu'-\nu)t} \Big[A_i(\nu) \tilde{\rho}_A(t) A_i^\dagger(\nu') - A_i^\dagger(\nu') A_i(\nu) \tilde{\rho}_A(t) \Big] + \text{h.c.}, \tag{3.18}$$

where the first line involves a sum over positive Bohr frequencies $\nu, \nu' = E_i, E_i \pm g$, while the second line includes the corresponding negative frequencies. Finally, we transform back to the Schrödinger picture and make use of the identity

$$\sum_{\nu>0} A_i(\nu) = \sigma_i^-, \tag{3.19}$$

whence the local master equation (3.15) is obtained after absorbing the Lamb-shift terms into H_0.

This alternative derivation is valid so long as $T_i \gg g$ and $g \ll E_i \ll \omega_c$, so that the correlation function (3.17) varies slowly over frequencies of order g, i.e. the condition (1.73) must be satisfied for $\delta\nu \sim g$. More precisely, assuming the imaginary part of Eq. (3.17) to be negligible, we require that

$$\left(\frac{\mathrm{d}\mathcal{I}_i(\nu)}{\mathrm{d}\nu} \right)_{\nu=\pm E_i} \ll \frac{\mathcal{I}_i(\pm E_i)}{g}. \tag{3.20}$$

This expression can be evaluated using the explicit forms for the spectral function (3.14) and the spectral density (3.8). For $\nu = E_i$ we obtain

$$|1 - \beta_i E_i n_i(E_i)| \ll \frac{E_i}{g}, \tag{3.21}$$

where we have used the fact that $E_i \ll \omega_c$. For $\nu = -E_i$ we likewise obtain

$$|1 - \beta_i E_i [1 + n_i(E_i)]| \ll \frac{E_i}{g}. \tag{3.22}$$

The inequalities (3.21) and (3.22) are always satisfied if $E_i \gg g$ and $T_i \gg g$.

The foregoing results give rise to some ambiguity, since the conditions (3.21) and (3.22) are also compatible with the strong-coupling master equation (3.10) if $\gamma_i(E_i) \ll g$. Thus it is not necessarily clear which master equation is the correct one to use. Here we simply sidestep this issue by excluding the ambiguous parameter regime from our calculations. Since the two master equations (3.10) and (3.15) have been shown to predict different

fundamental limits for the efficiency of quantum absorption refrigerators [208], resolving the ambiguity nonetheless remains an interesting open problem.

3.3 Short-time dynamics of the refrigerator

We now present our quantitative results, obtained by numerical solution of the equations of motion. Our first observation is that sufficiently strong coherent coupling between the qubits drives damped Rabi oscillations of the local qubit populations. However, unlike Rabi oscillations due to local driving fields, the three-body interaction (3.2) does not induce any local coherences between the qubit populations. The reduced state of each qubit is diagonal at all times and may therefore be assigned an effective temperature

$$\tilde{T}_i(t) = \frac{-E_i}{2\tanh^{-1}\langle\sigma_i^z(t)\rangle}. \tag{3.23}$$

To illustrate this feature of the short-time dynamics, we plot several examples of the evolution of the target qubit temperature in Fig. 3.2, which demonstrate that the Rabi oscillations allow the target qubit to reach lower temperatures than the steady state. In the strong-coupling regime we find damped temperature oscillations with the approximate period π/g [solid line in Fig. 3.2(a)]. Therefore, the optimal quantum single-shot cooling procedure consists of extracting the target qubit after a time $t_0 \approx \pi/(2g)$. In contrast, when g is much smaller than the relaxation rate, these oscillations are over-damped so that no temperature minimum occurs in a finite time [solid line in Fig. 3.2(b)]. Nevertheless, we have found that quantum single-shot cooling is possible over a very broad range of parameters, so long as the coupling g is significantly larger than the relaxation rate.

The physical origin of the temperature oscillations is the exchange of energy between the refrigerator qubits due to the interaction (3.2). Our second important observation is that this energy transport is driven by coherence in the transport subspace. This can be seen straightforwardly by examining the Heisenberg equations of motion for the local energy expectation values $h_i = E_i\langle\sigma_i^z\rangle/2$. The resulting expression for the target qubit is of the form [cf. Eq. (2.9)]

$$\frac{\mathrm{d}h_1}{\mathrm{d}t} = \dot{Q}_1(t) - 2gE_1\mathrm{Im}\mathcal{C}(t). \tag{3.24}$$

This equation represents an energy balance between the rate of heat absorbed from the bath $\dot{Q}_1(t)$ and the coherent flow of energy into the other qubits, which is proportional to the imaginary part of the coherence in the transport subspace:

$$\mathcal{C}(t) = \mathrm{Tr}\left[\rho_A(t)|010\rangle\langle 101|\right]. \tag{3.25}$$

Eqs. (3.24) & (3.25) give a direct link between the presence of coherence and the flow of energy across the refrigerator. We expect an analogous relationship to hold for any

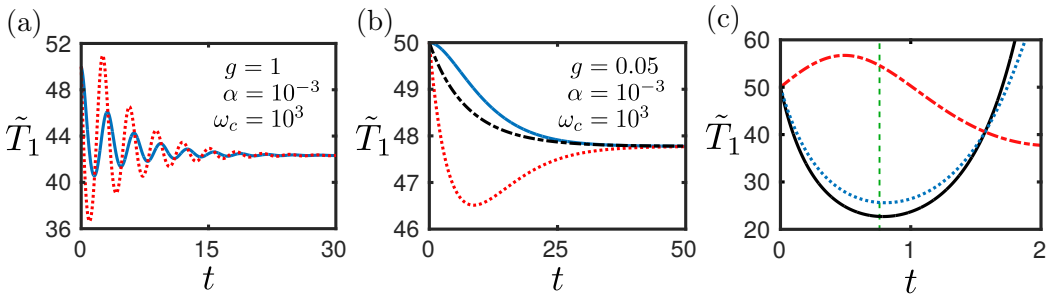


Figure 3.2. Effective temperature dynamics of the target qubit, with $E_1 = 1$, $E_2 = 2$, $T_r = T_1 = T_2 = 50$ and $T_h = T_3 = 100$. (a–b) Blue solid lines indicate the evolution of an initial thermal product state (3.4), red dotted lines depict the evolution with 1% of the maximum coherence added to the initial state. (a) Strong-coupling regime. (b) Weak-coupling regime, plotted with the corresponding stochastic model (black dot-dashed line). (c) Short-time effective temperature dynamics of an ensemble of target qubits, where coherence with some phase noise is added to the initial state. The magnitude of the initial coherence is 5% of the maximum and the phase uncertainties are $\delta\phi = 0$ (black solid line), $\delta\phi = \pi/4$ (blue dotted line) and $\delta\phi = \pi$ (red dot-dashed line). The temperature minimum in the absence of phase noise is shown by the green vertical dashed line. The data shown in (c) are calculated using the strong-coupling master equation with the same parameters as (a).

quantum refrigerator in which energy transport between distinct subsystems occurs via coherent Hamiltonian evolution.

3.4 Effect of initial coherence

To further elucidate the fundamental role of coherence in energy transport, we consider a situation where some coherence in the transport subspace is added to the initial state, without modifying the thermally distributed populations. In order to ensure the positivity of the quantum state, the magnitude of this coherence is upper bounded by $|\mathcal{C}(0)| < \mathcal{C}_{\max}$, where

$$\mathcal{C}_{\max} = \prod_{i=1}^{3} \frac{1}{2} \operatorname{sech}\left(\frac{\beta_i E_i}{2}\right). \tag{3.26}$$

For the examples in Figs. 3.2(a–b) we have also plotted the dynamics with a very small amount of initial coherence $\mathcal{C}(0) = \mathrm{i}\mathcal{C}_{\max}/100$. We find that the amplitude of the temperature oscillations is noticeably enhanced in all three cases. In the weak-coupling example plotted [red dotted line in Fig. 3.2(b)], the initial coherence gives the most dramatic advantage, since now the temperature minimum occurs in finite time. Initial coherence is actually a necessary ingredient for quantum single-shot cooling in this case and thus should be considered as an additional nonclassical resource to the free energy of the hot bath.

Note that, according to Eq. (3.24), the phase of $\mathcal{C}(0)$ determines the direction of the initial flow of energy into the qubit. Therefore, it is even possible, for example, to heat the

qubit by adding initial coherence with the opposite phase, even when the system behaves as a refrigerator in the steady state. Likewise, one can transiently cool even when the steady-state behaviour is that of a heat pump. Similar phase effects have recently been described in Ref. [229], where the authors show that bath fluctuations can revert the detailed balance condition in certain open quantum systems, creating a net flux of energy from the environment into the open system.

Due to the aforementioned sensitivity of the dynamics to the phase of the coherence, it is important to consider the impact of any phase uncertainty resulting from imperfect initial state preparation. Specifically, we suppose that the initial coherence is given by $\mathcal{C}(0) = ir\mathrm{e}^{\mathrm{i}\phi}$, where ϕ is a zero-mean random variable. Assuming that the cooling protocol is performed repeatedly on multiple qubits, the relevant quantity to consider is the temperature of the ensemble of target qubits. For the rest of this section it should be understood that the term temperature refers to the property of the ensemble: we do not consider the temperature fluctuations of individual qubits here.

The introduction of phase noise leads to two effects: an increase of the minimum temperature, and a shift in the time at which this minimum occurs. In Appendix A we provide an approximate analytical quantification of the impact of phase noise, assuming that the phase fluctuations are small and Gaussian. We have also numerically investigated the case of non-Gaussian phase noise, in particular the case where ϕ is uniformly distributed in the range $\phi \in [-\delta\phi/2, +\delta\phi/2]$. Some examples of the resulting temperature dynamics of the target qubit ensemble are plotted in Fig. 3.2(c).

We find that a narrow phase noise distribution leads to a small shift in the minimum temperature [blue dotted line in Fig. 3.2(c)]. The most deleterious impact is obtained when the phase noise distribution is very broad, so that the temperature minimum is shifted to a much later time. Extracting the target qubit at the expected minimum may actually lead to heating of the target qubit [red dot-dashed line in Fig. 3.2(c)]. On the other hand, it may be possible to predict the dynamics of the ensemble temperature in advance, e.g. because the phase noise distribution is known. In this case it is possible to extract the target qubit at the appropriate time to obtain some temperature advantage, unless this time is so late that thermal dissipation damps away the coherent oscillations.

3.5 Stochastic absorption refrigerator

In the previous two sections, we presented strong evidence that coherence is a useful resource that may be harnessed to produce a significant advantage to single-shot cooling. On the other hand, we can show that coherence is not a necessary ingredient for quantum absorption refrigerators operating in the steady state. This is because energy transport can also be described by a stochastic process in which excitations are transferred incoherently between the qubits. Such a classical description is appropriate in the presence of strong

dephasing, which in our case comes directly from the thermal baths (see Ref. [69] for an alternative dephasing model in the context of power refrigerators).

As a concrete example, we derive in Appendix B an effective master equation describing the asymptotic relaxation of the populations in the computational basis, valid when the coupling g is much smaller than the dissipation rates. Our analysis follows Ref. [166], where it was shown that coherent propagation of a quantum particle on a lattice under strong local dephasing can be approximated by a stochastic hopping process. In our case, the dephasing occurs due to the coupling to the thermal baths, which destroys the coherences in the computational basis at a characteristic rate

$$\Gamma = \frac{1}{2}\sum_{i=1}^{3}\left[\gamma_i(E_i) + \gamma_i(-E_i)\right], \tag{3.27}$$

where $\gamma_i(\nu)$ is defined above Eq. (3.14). In the limit where $g \ll \Gamma$, we can derive a closed equation of motion for the populations, describing their dynamics over times coarse-grained on the scale Γ^{-1}. This effective master equation describes transport in terms of a simple rate equation, where population is stochastically transferred between the states $|010\rangle$ and $|101\rangle$ at a rate $2g^2/\Gamma$ [see Eq. (B.15)].

The effective master equation accurately describes the long-time temperature dynamics of the target qubit on its approach to the steady state, as we show by explicit comparison with the weak-coupling master equation in Fig. 3.2(b). We see that there is no difference between the quantum and classical model in terms of the temperatures which can be achieved in the steady state. This result demonstrates that three-qubit refrigerators are capable of cooling even when their dynamics is entirely classical. In the transient regime, on the other hand, the temperature dynamics are qualitatively different in the quantum and classical cases. Classical refrigeration models described by stochastic rate equations generically exhibit pure exponential relaxation, precluding the possibility of single-shot cooling below the steady-state temperature. This lies in stark contrast to the generic behaviour we have found in strongly coupled quantum absorption refrigerators, i.e. temperature oscillations enabling us to rapidly achieve temperatures lower than the steady state.

3.6 Comparison with steady-state cooling

Returning now to the fully quantum case, we would like to compare the performance of quantum single-shot cooling and steady-state refrigeration. Let us define the temperature advantage $\Delta T = T_\infty - \tilde{T}_1(t_0)$ as the difference between the steady-state temperature T_∞ of the target qubit and the quantum single-shot cooling minimum $\tilde{T}_1(t_0)$. This is an important figure of merit quantifying the advantage gained from quantum single-shot

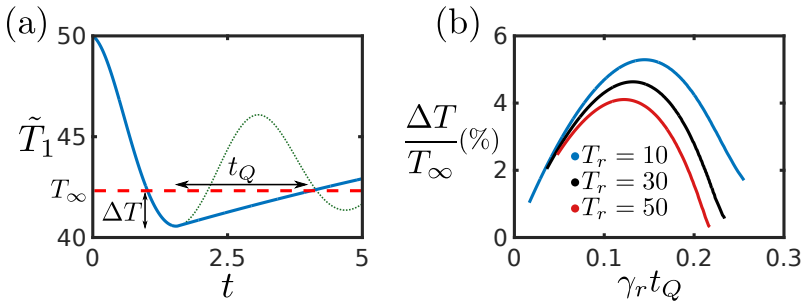


Figure 3.3. (a) Example evolution using the same parameters as Fig. 3.2(a), with (blue solid line) and without (green dotted line) a switch-off of the interaction at time $t_0 = \pi/(2g)$, illustrating the quantum temperature and time advantages ΔT and t_Q, respectively. The steady-state temperature T_∞ is shown by the red dashed line. (b) Trade-off between the fractional temperature advantage and the time advantage (in units of the relaxation time γ_r^{-1}), with the same parameters as (a) apart from the temperatures. Each line shows the results for a fixed room temperature T_r and a range of hot bath temperatures $T_h \in [T_r + 1, T_r + 200]$. The value of t_Q decreases as T_h is increased in each case.

cooling compared to steady-state cooling. Once the target qubit is decoupled from the refrigerator at time t_0, its temperature increases as it equilibrates with the environment. The advantage gained from quantum single-shot cooling lasts only until the temperature of the target qubit grows larger than the steady-state temperature, which occurs at a time t_1. This motivates us to define the quantum advantage time $t_Q = t_1 - t_0$, which is another important quantity characterising the performance of the quantum single-shot refrigerator compared to its steady-state counterpart. See Fig. 3.3(a) for a graphical depiction of these quantities.

For simplicity, in this section we work in the strong-coupling limit, where there always exists some quantum single-shot cooling advantage and the optimal switch-off time is given approximately by $t_0 \approx \pi/(2g)$. In this case, the quantum advantage time t_Q tends to decrease as either of the bath temperatures T_r and T_h is increased. Of course, as the room temperature is varied, the rate of equilibration of the target qubit with its environment changes, which in turn affects the value of t_Q. In order to remove this trivial dependence on T_r, we measure the quantum advantage time in units of the relaxation time γ_r^{-1}, where $\gamma_r = [\gamma_1(E_1) + \gamma_1(-E_1)]/2$ is the arithmetic mean of the thermal gain and decay rates acting on the target qubit in isolation[1].

For a given set of fridge energies $\{E_i, g\}$ and a fixed room temperature T_r, one would like to optimise the temperature of the free energy source T_h to obtain the largest fractional temperature advantage $\Delta T/T_\infty$ and also the longest possible advantage time t_Q. We show in Fig. 3.3(b) that there exists a trade-off between these two quantities, which can-

[1]Mathematically, γ_r is the spectral gap of the Liouvillian $\mathcal{L}_{\text{targ}}$ governing the dynamics of the target qubit after it is decoupled from the refrigerator. That is, γ_r is the real part of the eigenvalue(s) of $\mathcal{L}_{\text{targ}}$ with the largest (negative) real part, which determines the asymptotic decay rate towards equilibrium.

not be simultaneously maximised. This trade-off is reminiscent of the competing goals of efficiency and power when optimising thermal machines that operate in the steady state. Interestingly, there exists a "sweet spot" where the fractional temperature advantage is maximised, while the advantage time remains adequately large. This immediately suggests a favourable operating regime in which the quantum single-shot cooling protocol is preferable to steady-state cooling. However, in a practical setting the optimum refrigerator parameters will of course depend on the specific application in question. Finally, it is worth noting that introducing coherence in the transport subspace into the initial quantum state further enhances the fractional temperature advantage for a given t_Q, thus coherence is also a useful resource in this context.

3.7 Conclusion

In this chapter, we studied the dynamics of three-qubit absorption refrigerators using a standard model of thermal dissipation. In the strong-coupling regime we encountered oscillations in the energy of the target qubit, enabling it to reach effective temperatures below that of the steady state in a finite time. With the right timing, these oscillations can be exploited in a quantum single-shot cooling protocol to yield a constant stream of low-entropy qubits, which could be subsequently used for quantum information processing, for instance. This constitutes another example in which quantum thermal machines may prove useful for quantum state preparation in the context of quantum technology.

Interestingly, we found that the quantum single-shot cooling effect is dramatically enhanced by adding coherence to the initial state. This result provides further evidence that coherence is a useful resource in quantum thermodynamics, which has lately been highlighted by a number of other authors. Indeed, it has been shown that coherence can improve the performance of heat engines driven by external work [69] (this study was published concurrently with the paper [2] on which this chapter is based). In the resource-theoretic formulation of quantum thermodynamics, coherence is a resource [230–232] which is nonincreasing under thermal operations (i.e. energy-conserving unitaries in the presence of a thermal ancilla) [193, 194], and from which work can be extracted [192, 195, 233]. Coherence may also play the role of a catalyst, but only for infinite-dimensional quantum systems [234]. More recently, the energy cost of creating coherence was quantified in Ref. [196], a study which was directly motivated by our findings presented in this chapter.

Experimental implementation of quantum single-shot cooling calls for strong coupling, so that the rate of coherent energy transport exceeds the rate of thermal dissipation. This parameter regime is difficult to achieve in many of the experimental realisations of quantum absorption refrigerators that have been proposed thus far [48–50], including the atom-cavity implementation discussed in Chapter 2. However, a very recent article has proposed that quantum single-shot cooling can be realistically demonstrated using present technology

in a circuit QED platform involving three coupled microwave resonators [235]. In addition, it has been shown that quantum single-shot cooling is possible in the weak-coupling limit [236], or in the complete absence of steady-state cooling [237], providing yet more motivation to experimentally study transient effects in quantum absorption refrigerators.

Precise, accurate timing and the ability to switch the qubit-qubit interaction off and on are essential prerequisites for quantum single-shot cooling, yet we have not accounted for the thermodynamic cost of these operations. There exist several interesting options for future work in this direction. It is possible to envisage a scenario where the switching is performed by another dynamical system: a quantum clock. One may consider coherent clocks undergoing Hamiltonian evolution [227, 228], or dissipative clocks which are driven by thermal noise in a similar manner to the quantum absorption refrigerator [8]. In future work we will study the efficacy and resource cost of quantum single-shot cooling schemes with a quantum clock included explicitly in the theoretical description, as well as possible experimental realisations of such schemes.

An alternative possibility in this regard concerns engineering the system in order to minimise the need for accurate timing. For example, our preliminary calculations using strongly coupled three-qubit absorption refrigerators under super-Ohmic dissipation demonstrate that, for certain parameters, a quantum single-shot cooling advantage exists for almost all times later than some threshold. Such behaviour would greatly reduce the necessary timing accuracy, but more work is needed in order to check whether this rather odd behaviour is physically realisable or merely some artefact of the approximations used to derive the Lindblad equation. Such verification could be performed using advanced tensor network simulations to model the effect of the environment with numerical exactitude [238, 239].

Aside from any practical use, our results help to elucidate the role of quantum effects in thermodynamics. As we show using the stochastic absorption refrigerator, weakly coupled three-qubit fridges operating in the steady state are in some sense equivalent to classical ones, as one can achieve identical steady-state temperatures from a classical stochastic model. On the other hand, the coherent transport of energy inducing oscillations in the population of the target qubits constitutes a unique quantum feature. This suggests that investigating the transient regime of microscopic machines may reveal further advantages from quantum dynamics to take thermal engines and refrigerators beyond the classically possible.

Part II

Impurity probes in ultracold atomic gases

Ultracold atomic gases are clean, isolated systems whose constituents have well-controlled interactions with each other. These features make them promising candidates for a variety of applications, ranging from quantum computation and simulation [15–23] to gravitational sensing [240–242]. However, the potential of cold-atom systems both for fundamental science and for emerging quantum technologies can only be fully unlocked with the ability to measure their properties with accuracy and precision.

In the search to find new and improved methods to probe ultracold gases, nondestructive techniques are particularly interesting because a single realisation of the system can be reused for multiple measurements. One attractive approach in this regard involves monitoring the evolution of an atom of a different species confined within the gas, i.e. an impurity. Theoretical studies indicate that such probes could yield information on diverse features of cold atomic gases, including effective dimensionality [71], temperature [72], Hamiltonian parameters [73] or energy spectra [74], and topological invariants [75], to name just a few examples. In many cases, impurity-based measurements may be more accurate and precise than their conventional counterparts, or enable localised probing of the gas on submicron length scales that are inaccessible using direct optical imaging.

Aside from their metrological applications, impurities immersed in ultracold gases can be used to investigate basic scientific questions bridging quantum optics and many-body physics. Proposals in this direction include the study and simulation of problems such as electron-phonon coupling in condensed-matter [76, 77] and biological [78] systems, superfluid flow around an obstacle [79], the Anderson orthogonality catastrophe [80, 81], non-Markovian dynamics [82–84], Unruh radiation [85], and the Gibbons-Hawking effect [86].

Although the majority of the literature in this area is still theoretical, impressive experimental progress has been made towards the controlled immersion of impurities in cold atomic gases. In the majority of cases the impurity is realised with a neutral atom [95–106], but researchers have also experimented with more exotic charged impurities [107–111]. Indeed, the first impurity-based measurements of the density [108] and the temperature [102] of a Bose-Einstein condensate have already been performed. Nevertheless, plenty of theoretical work remains to be done as experimental capabilities inevitably develop further. This second part of the thesis describes our contribution to this growing body of research.

Chapter 4, which is based on Refs. [3, 4], focuses on measuring the temperature of cold Bose gases using impurities. We describe two proposals designed to overcome challenges that existing thermometry techniques face at the lowest temperatures. In a departure from conventional thermometry methods, we show that tracking the nonequilibrium dynamics of the probe can lead to significant performance improvements in certain regimes, including those involving temperatures on the order of nanokelvin. We illustrate the feasibility of our schemes by explicit calculations for both weakly interacting and strongly interacting Bose systems that can be realised in cold-atom experiments.

In Chapter 5 we consider probing the spectrum of dynamic density fluctuations in an

atomic Fermi gas. The latter forms a superfluid manifesting the crossover from a Bardeen-Cooper-Schrieffer (BCS) condensate of Cooper pairs to a Bose-Einstein condensate (BEC) of diatomic molecules. We show that coupling an impurity to the Fermi gas gives non-destructive access to the superfluid's order parameter and various other properties of its excitation spectrum, which can be inferred by measuring the impurity's rate of vibrational energy loss. Our model may also be of independent interest in the field of open quantum systems, because dissipation occurs by the emission of phonons which, unusually, may themselves be strongly damped.

Chapter 4

Thermometry of cold Bose gases using atomic impurity qubits

In this chapter, we describe two impurity-based methods to measure the temperature of cold atomic Bose gases in different regimes. The work presented here is based on Refs. [3, 4].

Thermometry is one of the basic measurements in the experimental physicist's toolbox. In the context of cold atoms, temperature measurements are important in general for the simulation of condensed-matter systems, and specifically for studying fluctuation effects [243, 244], equilibration [245–247], many-body localisation [248], and various other applications. However, precisely measuring the low temperatures relevant for ultracold gases can be a formidable challenge.

The temperature of a dilute atomic gas is conventionally inferred from time-of-flight imaging [15, 249] or by scattering light from the sample in situ [250, 251], methods which probe the density of atoms in momentum or coordinate space, respectively. Unfortunately, these are destructive measurement techniques, whose precision is significantly reduced at temperatures on the order of nanokelvin or less [252], while spatial resolution is restricted by the fundamental and practical limitations of optical components. Moreover, such techniques are infeasible for the majority of strongly correlated systems, where the Hamiltonian is unsolvable and thus the temperature dependence of accessible observables cannot be calculated and compared to the measurement outcomes.

In this chapter, we describe two different thermometry methods that avoid these shortcomings by using an impurity qubit as a probe. First, we introduce a technique based on observing the equilibration of a qubit dissipatively coupled to cold atomic gas. We study the application of this probe to the thermometry of a weakly confined Bose-Einstein condensate. Second, we consider an entirely different scheme where the qubit's mean energy does not change, but rather its state controls a Hamiltonian quench on the system of interest. Monitoring the decoherence of the qubit reveals the characteristic function of the work performed in the quench [112, 113], which can ultimately be used to infer the temperature [114] via the Tasaki-Crooks theorem [115, 116]. We simulate the application of this method to a one-dimensional lattice gas of cold bosonic atoms. In all cases, we verify that

our thermometry protocols retain accuracy and precision down to the nanokelvin regime.

Our work can be placed in the context of previous literature on measuring the temperature of cold atomic gases using impurities [71, 72]. Since the completion of Refs. [3, 4], thermometry has been experimentally demonstrated using impurities immersed in a cold Bose gas [102], although using somewhat different methods from the ones proposed here. Nevertheless, this experiment clearly demonstrates both the motivation and many of the technical ingredients (see also Refs. [96, 97, 100, 253–255]) required to bring our proposals to fruition.

4.1 Thermometry by equilibration

In this section we consider thermometry of a Bose-Einstein condensate (BEC) using an impurity atom trapped in a double-well potential. The impurity excites and absorbs phononic quasiparticles in the background gas, thus dissipating energy and eventually reaching thermal equilibrium with the BEC. By measuring the mean energy of the probe one thus infers the temperature. We also discuss an alternative method based on observing the nonequilibrium dynamics of the probe, which is appropriate for thermometry under time constraints.

4.1.1 Description of the system

Our thermometer consists of an impurity atom of species A and mass M, immersed in a cold atomic gas of bosonic species B and mass m forming a Bose-Einstein condensate. The impurity is confined by a species-selective, symmetric double-well potential $V_A(\mathbf{r})$, as shown schematically in Fig. 4.1. The potential has minima at positions $+\mathbf{L}/2$ and $-\mathbf{L}/2$. We work in the limit of slow tunnelling, $J \ll \omega_0$, where J is the rate of tunnelling between the potential minima, and ω_0 is the frequency of small harmonic oscillations close to each minimum. This is the case when the potential is deep and the barrier separating the minima is large. Assuming that $T \ll \omega_0$, with T the temperature of the Bose gas, we may restrict our attention to the qubit comprising the lowest two motional energy eigenstates of the impurity. These eigenstates are taken to be the symmetric and antisymmetric superpositions $|1\rangle = (|+\rangle + |-\rangle)/\sqrt{2}$ and $|0\rangle = (|+\rangle - |-\rangle)/\sqrt{2}$, where $|\pm\rangle$ are orthogonal states localised near the potential minima at $\pm\mathbf{L}/2$. The impurity Hamiltonian can thus be written

$$H_A = J\sigma^z. \tag{4.1}$$

The primary advantage of the double-well system is that the qubit energy splitting $2J$ can be comparable to the thermal energy corresponding to nanokelvin. This facilitates thermometry at ultralow temperatures, as we describe in the following.

The interaction between the impurity and the gas is given in the s-wave pseudopotential

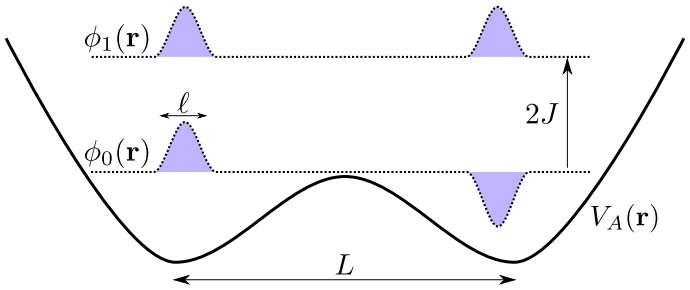


Figure 4.1. Energy level structure of the thermometer. An impurity atom trapped by a double-well potential $V_A(\mathbf{r})$ has a pair of low-lying energy eigenstates $\phi_0(\mathbf{r})$ and $\phi_1(\mathbf{r})$ corresponding to antisymmetric and symmetric superpositions of localised states. These comprise a qubit with energy splitting $2J$.

approximation by

$$H_{AB} = \kappa \sum_{\mu,\nu=\pm} |\mu\rangle\langle\nu| \otimes \int \mathrm{d}^3\mathbf{r}\; \phi_\mu(\mathbf{r})\phi_\nu(\mathbf{r})\varrho(\mathbf{r}), \tag{4.2}$$

where $\kappa = 2\pi\bar{a}/\bar{m}$, with $\bar{a}$ the s-wave scattering length describing A-B collisions and $\bar{m} = mM/(m+M)$ the reduced mass, while $\phi_\pm(\mathbf{r}) = \langle\mathbf{r}|\pm\rangle$ are the coordinate wave functions of the localised impurity states, and $\varrho(\mathbf{r}) = \Psi^\dagger(\mathbf{r})\Psi(\mathbf{r})$ is the local density of the Bose gas, with $\Psi(\mathbf{r})$ the atomic field operator which annihilates a boson at position $\mathbf{r}$.

We suppose that the potential confining the gas varies slowly enough compared to the length scale L of the impurity that the BEC can be approximated as homogeneous. We model the dynamics of the gas using the Bogoliubov theory [256], which is valid well below the BEC transition temperature so that the condensate density is commensurate with the mean atomic density ϱ_0. The elementary excitations of the gas are density waves in the condensate with wave vector $\mathbf{q}$ and frequency $\omega_\mathbf{q}$. These are interpreted in the quantum theory in terms of quasiparticles carrying momentum $\mathbf{q}$ and energy $\omega_\mathbf{q}$, governed by the Hamiltonian

$$H_B = \sum_{\mathbf{q}\neq 0} \omega_\mathbf{q} b_\mathbf{q}^\dagger b_\mathbf{q}, \tag{4.3}$$

which describes an independent collection of quantum harmonic oscillators, with canonical ladder operators $b_\mathbf{q}$ indexed by the quasiparticle momentum. The well-known Bogoliubov quasiparticle dispersion relation is $\omega_\mathbf{q} = \sqrt{\varepsilon_\mathbf{q}(\varepsilon_\mathbf{q} + 2g\varrho_0)}$, where $\varepsilon_\mathbf{q} = q^2/2m$ is the bare kinetic energy and $g = 4\pi a_s/m$ is the coupling constant describing collisions between the bosons, with a_s the corresponding s-wave scattering length. The dispersion relation $\omega_\mathbf{q}$ smoothly interpolates between the sound-like behaviour $\omega_\mathbf{q} \approx cq$ as $\mathbf{q} \to 0$, with $c = \sqrt{g\varrho_0/m}$ the speed of sound, and the free-particle result $\omega_\mathbf{q} \approx \varepsilon_\mathbf{q}$ as $\mathbf{q} \to \infty$. The transition between the sound-like and particle-like regimes occurs around momenta of order ξ^{-1}, where $\xi = (8\pi\varrho_0 a_s)^{-1/2}$ is the healing length. The healing length is the characteristic

length scale of the BEC: it corresponds to the distance over which the density of the gas changes in response to a localised perturbation. The natural energy scale of the gas is $1/(2m\xi^2) = g\varrho_0$.

We assume that the double-well potential minima are sufficiently far apart that the localised impurity wave functions have negligible spatial overlap, i.e. $\phi_+(\mathbf{r})\phi_-(\mathbf{r}) \approx 0$. We can therefore neglect the off-diagonal terms with $\mu \neq \nu$ in Eq. (4.2). The density can be written in the Bogoliubov approximation as

$$\varrho(\mathbf{r}) \approx \varrho_0 + \frac{1}{\sqrt{V}} \sum_{\mathbf{q}\neq 0} \sqrt{M_{\mathbf{q}}} \left(\mathrm{e}^{\mathrm{i}\mathbf{q}\cdot\mathbf{r}} b_{\mathbf{q}} + \mathrm{e}^{-\mathrm{i}\mathbf{q}\cdot\mathbf{r}} b_{\mathbf{q}}^\dagger \right), \tag{4.4}$$

where V is a fictitious quantisation volume and $M_{\mathbf{q}} = \varrho_0 \varepsilon_{\mathbf{q}}/\omega_{\mathbf{q}}$. We thus obtain the interaction Hamiltonian

$$H_{AB} = \sigma^x \otimes \sum_{\mathbf{q}\neq 0} \left(\lambda_{\mathbf{q}} b_{\mathbf{q}} + \lambda_{\mathbf{q}}^* b_{\mathbf{q}}^\dagger \right) + \mathbb{1} \otimes \sum_{\mathbf{q}\neq 0} \left(\lambda'_{\mathbf{q}} b_{\mathbf{q}} + \lambda'^*_{\mathbf{q}} b_{\mathbf{q}}^\dagger \right), \tag{4.5}$$

where we have introduced the coupling constants

$$\lambda_{\mathbf{q}} = \frac{\kappa}{2} \sqrt{\frac{M_{\mathbf{q}}}{V}} \int \mathrm{d}^3\mathbf{r}\, \mathrm{e}^{\mathrm{i}\mathbf{q}\cdot\mathbf{r}} \left(|\phi_+(\mathbf{r})|^2 - |\phi_-(\mathbf{r})|^2 \right), \tag{4.6}$$

$$\lambda'_{\mathbf{q}} = \frac{\kappa}{2} \sqrt{\frac{M_{\mathbf{q}}}{V}} \int \mathrm{d}^3\mathbf{r}\, \mathrm{e}^{\mathrm{i}\mathbf{q}\cdot\mathbf{r}} \left(|\phi_+(\mathbf{r})|^2 + |\phi_-(\mathbf{r})|^2 \right). \tag{4.7}$$

The first term of Eq. (4.5) describes changes of the impurity motional state driven by fluctuations in the density difference between the minima of the double-well potential. The resulting exchange of energy leads to the emission and absorption of phonons in the BEC. The second term of Eq. (4.5) describes a displacement of the phonon modes due to the average impurity density, which has no effect on the impurity dynamics at lowest order. The situation may be compared with atom-photon interactions in quantum electrodynamics, where changes of the atomic internal state are associated with the emission and absorption of electromagnetic quanta. In the present case, the excitations generated in the gas span a range of momenta $\mathbf{q}$ determined by the coupling constants $\lambda_{\mathbf{q}}$ and $\lambda'_{\mathbf{q}}$, which in turn are fixed by the geometry of the impurity system via Eqs. (4.6) and (4.7).

4.1.2 Gaussian approximation for the impurity wave functions

In order to evaluate the coupling constants and the tunnelling energy, we choose a simple, tractable model for the impurity potential and wave functions. Specifically, we consider an optical lattice generated by two pairs of counter-propagating laser beams with wave

vectors $\pm\mathbf{k}$ and $\pm 2\mathbf{k}$ lying parallel to $\mathbf{L}$ [253–255]. This gives rise to the potential [3]

$$V(\mathbf{r}) = V_0 \left[\cos^2(2\mathbf{k}\cdot\mathbf{r}) - 4v\cos^2(\mathbf{k}\cdot\mathbf{r})\right] \exp\left(-\frac{1}{2}\frac{r_\perp^2}{w^2}\right), \tag{4.8}$$

where V_0 is the lattice depth, v is the relative intensity of the two beams, $r_\perp$ is the radial coordinate perpendicular to $\mathbf{k}$, and w is the beam width. The distance between the potential minima $\arccos(v)/k$ and the barrier height $V_0(1-v^2)$ can be varied by tuning the relative intensity of the beams in the range $0 \leq v \leq 1$. The localised impurity states are modelled using the Gaussian ansatz

$$\phi_\pm(\mathbf{r}) = \phi(\mathbf{r} \pm \mathbf{L}/2), \qquad \phi(\mathbf{r}) = (\pi\ell^2)^{-3/2}\, \mathrm{e}^{-r^2/2\ell^2}, \tag{4.9}$$

We must have $L \gg \ell$ in order to be consistent with our assumption that $\phi_+(\mathbf{r})\phi_-(\mathbf{r}) \approx 0$. This condition also ensures that the impurity wave functions are almost orthogonal, since $\langle +|-\rangle = \mathrm{e}^{-L^2/4\ell^2} \approx 0$ in this approximation. Using Eq. (4.9), we find the coupling constants to be given by

$$\lambda_{\mathbf{q}} = -\mathrm{i}\kappa\sqrt{\frac{M_{\mathbf{q}}}{V}} \sin\left(\frac{\mathbf{q}\cdot\mathbf{L}}{2}\right) \mathrm{e}^{-\ell^2 q^2/4}, \tag{4.10}$$

$$\lambda'_{\mathbf{q}} = \kappa\sqrt{\frac{M_{\mathbf{q}}}{V}} \cos\left(\frac{\mathbf{q}\cdot\mathbf{L}}{2}\right) \mathrm{e}^{-\ell^2 q^2/4}. \tag{4.11}$$

We find explicit values for ℓ, L and J variationally within the subspace spanned by the orthonormal states $(\phi_+(\mathbf{r}) \pm \phi_-(\mathbf{r}))/N_\pm$, where the $\phi_\pm(\mathbf{r})$ are given by Eq. (4.9) and $N_\pm = \sqrt{2(1 \pm \mathrm{e}^{-L^2/4\ell^2})}$ are normalisation factors correcting for the finite overlap between $\phi_\pm(\mathbf{r})$. First, we find the values of ℓ and L that minimise the energy expectation value of the antisymmetric ground state. Note that, in general, the value of L thus found does not exactly coincide with the distance between the minima of the double-well potential. Then, $2J$ is estimated as the average difference in energy between the two basis states, using the variationally determined values for ℓ and L. We simplify our calculations by assuming that $\ell \ll L \ll w$, and neglecting terms of order $O(\ell/w)$. This is an excellent approximation for the parameters considered in this work, where ℓ is smaller than one optical wavelength, while L is on the order of several such wavelengths.

As we show in the following subsection, the detector is sensitive to phonon modes whose energy coincides with the tunnelling energy J. Choosing realistic parameters for the impurity potential and the gas [102], we show in Fig. 4.2 that J can be varied over a spectrum of energies ranging from the picokelvin regime up to several tens of nanokelvin by controlling the well separation L and width ℓ of the localised impurity wave functions. As a result, the detector can be made sensitive to the occupation of phonon modes with very small energy, thus facilitating precise thermometry at ultralow temperatures. At the same

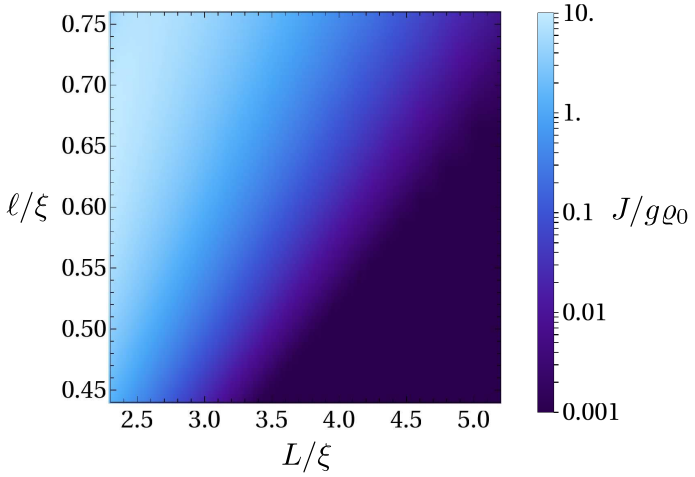


Figure 4.2. Tunnelling energy J as a function of the separation L and width ℓ of impurity states localised in either well, expressed in the natural units of the BEC. We use a ^{133}Cs impurity trapped by the potential (4.8) with $k = 2\pi/(1580\text{ nm})$, $V_0 \in [100E_r, 3000E_r]$ where $E_r = k^2/2M$ is the recoil energy, and $v \in [0, 1]$. For the gas we take $\xi = 870$ nm and $g\varrho_0 = 3.7$ nK, corresponding to a BEC of ^{87}Rb atoms at density $\varrho_0 = 10^{13}$ cm^{-3} [102].

time, the characteristic length scales of the probe can be on the order of the healing length, which itself is typically comparable to an optical wavelength and also to the interatomic separation in the BEC [257]. Thus, the thermometer can in principle probe a very localised region within the gas.

4.1.3 Impurity dynamics

The essential property of the impurity system for thermometry is its equilibration with the thermally occupied phonon modes of the gas. We describe this process by a Lindblad equation within the Born-Markov and rotating-wave approximations, derived straightforwardly from Eqs. (4.3), (4.1) and (4.5), following the procedure in Chapter 1 with $\mathcal{L}_1 = 0$. We take the phonon modes of the BEC reservoir to be initially in thermal equilibrium, i.e. $\rho_B = \mathrm{e}^{-\beta H_B}/\mathcal{Z}$, with $\beta = 1/T$ the inverse temperature to be measured.

The resulting master equation for the impurity density operator is

$$\frac{\mathrm{d}\rho_A}{\mathrm{d}t} = \mathrm{i}[\rho_A, H_A] + \gamma^- \mathcal{D}[\sigma^-]\rho_A + \gamma^+ \mathcal{D}[\sigma^+]\rho_A, \tag{4.12}$$

where

$$\gamma^- = \mathcal{J}(2J)[1 + n(2J)], \tag{4.13}$$

$$\gamma^+ = \mathcal{J}(2J)n(2J), \tag{4.14}$$

with $n(2J) = (\mathrm{e}^{2\beta J} - 1)^{-1}$ the Bose-Einstein distribution and the spectral density defined

as usual by

$$\mathcal{J}(\nu) = \sum_{\mathbf{q}} |\lambda_{\mathbf{q}}|^2 \delta(\nu - \omega_{\mathbf{q}}). \tag{4.15}$$

We are primarily interested in the dynamics of the populations of the impurity energy eigenstates as a function of time. The rates satisfy the detailed balance property $\gamma^-/\gamma^+ = \mathrm{e}^{2\beta J}$, meaning that the impurity populations relax to thermal equilibrium as time passes. In particular, the solution for $\langle\sigma^z(t)\rangle = \mathrm{Tr}[\rho_A(t)\sigma^z]$ with initial condition $\langle\sigma^z(0)\rangle = \langle\sigma^z\rangle_0$ is

$$\langle\sigma^z(t)\rangle = \mathrm{e}^{-\Gamma t}\langle\sigma^z\rangle_0 + \left(1 - \mathrm{e}^{-\Gamma t}\right)\langle\sigma^z\rangle_\infty, \tag{4.16}$$

where $\Gamma = \gamma^+ + \gamma^-$ sets the overall energy dissipation rate and $\langle\sigma^z\rangle_\infty = -\tanh(\beta J)$ is the asymptotic solution corresponding to the thermal equilibrium distribution.

In order to find explicit values for the incoherent rates, we pass to the thermodynamic limit via the standard prescription $(2\pi)^3 \sum_{\mathbf{q}} \to V \int \mathrm{d}^3\mathbf{q}$ and evaluate Eq. (4.15) to obtain

$$\mathcal{J}(\nu) = \frac{\kappa^2 \varrho_0}{8\pi^2 m} \frac{q_\nu^4}{\nu} \left|\frac{\mathrm{d}\omega_{\mathbf{q}}}{\mathrm{d}q}\right|^{-1}_{q=q_\nu} [1 - \mathrm{sinc}(q_\nu L)] \exp\left(-\frac{\ell^2 q_\nu^2}{2}\right), \tag{4.17}$$

where q_ν is the magnitude of a wave vector $\mathbf{q}_\nu$ such that $\omega_{\mathbf{q}_\nu} = \nu$. The soft low-frequency cut-off for $q_\nu L \ll 1$ arises physically because density fluctuations at wavelengths much greater than L are correlated at the two potential minima. High frequencies such that $q_\nu \ell \gg 1$ are exponentially suppressed due to destructive interference between outgoing propagation modes of the gas atoms. Specifically, summing the amplitudes describing scattering of atoms from an extended region of linear dimension ℓ leads to near-complete cancellation for momentum transfer $q \gg \ell$. Note that this last conclusion is strictly true only within the first Born approximation of scattering theory [258], and is a consequence of our perturbative derivation of the master equation.

If the impurity is weakly confined so that $\ell \gg \xi$, then only phonon modes with sound-like dispersion $\omega_{\mathbf{q}} \approx cq$ contribute to the spectral density. In this case, we obtain the simpler expression

$$\mathcal{J}(\nu) = \alpha \omega_\ell^{-2} \nu^3 \left[1 - \mathrm{sinc}\left(\frac{\nu}{\omega_L}\right)\right] \exp\left(-\frac{\nu^2}{2\omega_\ell^2}\right), \tag{4.18}$$

where we defined the dimensionless coupling $\alpha = \kappa^2 \varrho_0/(8\pi^2 m \ell^2 c^3)$ and the frequencies $\omega_L = c/L$ and $\omega_\ell = c/\ell$. At low frequencies we find $\mathcal{J}(\nu) \sim \nu^5$, so that this spectral density is classified as super-Ohmic according to the nomenclature introduced in Chapter 3.

Finally, let us discuss the validity of the approximations underlying the master equation. The Born-Markov approximation is valid so long as $\tau_B, \beta \ll \Gamma^{-1}$, where τ_B is the vacuum correlation time and $\beta = 1/T$ is the thermal correlation time. The vacuum correlation time can be estimated as the inverse of the high-frequency cut-off entering the spectral

density (4.17), and therefore ranges from $\tau_B \approx \ell/c$ for $\ell \gg \xi$, to $\tau_B \approx 2m\ell^2$ for $\ell \ll \xi$. The rotating-wave approximation is valid so long as $2J \gg \Gamma$. We have verified that these inequalities are satisfied in the examples which follow.

4.1.4 Thermometry protocols

We now demonstrate that the impurity qubit may be used to precisely measure the temperature T of the gas in the nanokelvin regime. We describe two different methods in the following.

Equilibrium method

The simplest route to thermometry is also the most familiar one, analogous to the standard procedure for measuring temperatures with a mercury thermometer or similar. Namely, the impurity is allowed to equilibrate completely with the gas, and then the temperature is inferred from the impurity's final energy distribution. According to Eq. (4.16), the asymptotic population of the impurity ground state, for example, is $[1 + \tanh(\beta J)]/2$. Thus a measurement of the final ground state population yields the temperature $T = 1/\beta$ assuming that the tunnelling energy J is known. The latter can be measured via independent experiments, for example by observing the evolution of the impurity density starting from a state localised in either the right or left well [255].

An important question is the attainable measurement precision given finite resources, i.e. how the experimental temperature uncertainty scales with the number of measurements N_{meas}. In order for this method to be precise we must have $2J \sim T$, as used in Ref. [3]. More explicitly, it was shown in Ref. [118] that a qubit with energy splitting $2J$ can reach its optimal thermometry precision when $\beta J \tanh(\beta J) = 1$, corresponding to $\beta J \approx 1.2$. As illustrated in Fig. 4.2, it is possible to achieve $J \sim 1$ nK and therefore precisely probe the nanokelvin regime using this method.

Nonequilibrium method

The equilibrium thermometry method requires waiting for the probe to achieve thermal equilibrium. However, in some cases the available time may be limited by intrinsic motional heating or decoherence of the double-well qubit, or by the finite lifetime of the atomic gas sample. In order to overcome this time constraint, we propose a method of nonequilibrium thermometry whereby the temperature is inferred from the rate of energy dissipation of the probe. In particular, thermometry proceeds by comparison of two dissipation rates Γ and Γ', measured at the unknown temperature T and a known reference temperature[1] T',

[1]The reference temperature T' may be sufficiently large so that, for example, time-of-flight imaging can be reliably used to measure it.

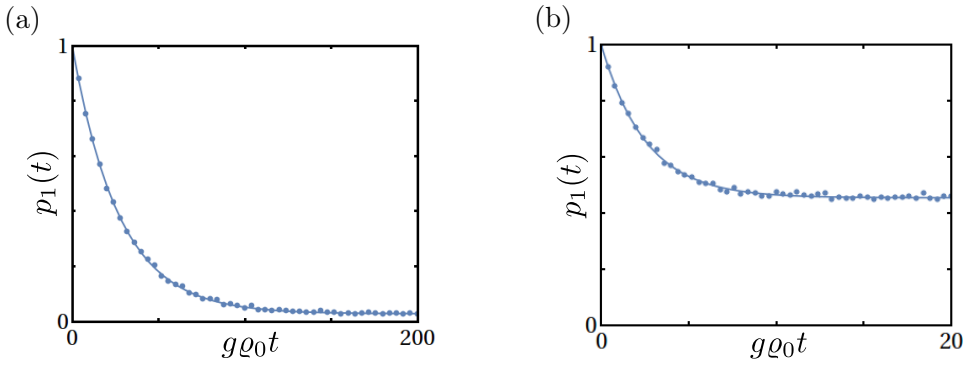


Figure 4.3. Simulated evolution of the impurity excited-state population $p_1(t)$ for the parameters in Table 4.1 at temperatures (a) $T = 0.5g\varrho_0$ and (b) $T' = 10g\varrho_0$. Solid lines show the exact evolution, points show simulated estimators based on $N_{\mathrm{meas}} = 5000$ measurements.

respectively. The ratio of these rates yields T from the relation

$$\frac{\Gamma'}{\Gamma} = \frac{\tanh(\beta J)}{\tanh(\beta' J)}, \tag{4.19}$$

where $\beta' = 1/T'$ and J is again assumed to be known from independent measurements. This method of thermometry by measuring nonequilibrium rates of change differs fundamentally from conventional thermometry based on observing populations in equilibrium. As discussed in Ref. [3], the nonequilibrium technique can be expected to achieve good precision in the range $2J \lesssim T$ and therefore nanokelvin temperatures are also accessible by this method.

Comparison of methods

In order to benchmark our protocols and check their feasibility, we have calculated the evolution of the thermometer using the parameters listed in Table 4.1. This allows us to verify that the assumptions underlying the master equation (4.12) are satisfied self-consistently and to estimate the typical equilibration timescale. We assume that the impurity is initially prepared in its excited motional state in all cases. The results of our calculation are

L	ℓ	J	κ	T	T'	N_{meas}	$(\Delta T/T)_{\mathrm{eq}}$	$(\Delta T/T)_{\mathrm{noneq}}$
3.1ξ	0.60ξ	$0.89g\varrho_0$	$5.4g$	$0.5g\varrho_0$	$10g\varrho_0$	5000	2.6%	12%

Table 4.1. Table of numerical parameters used in the simulations, and the resulting precision for each thermometry method. The impurity parameters L, ℓ and J are obtained using the values given in the caption of Fig. 4.2 with $V_0 = 500E_r$ and $v = 0.6$. The impurity-gas coupling ratio κ/g corresponds to a ^{133}Cs impurity in a BEC of ^{87}Rb [102].

displayed in Fig. 4.3.

We have also simulated the shot noise resulting from a finite number of measurements, which allows us to estimate the precision of each thermometry method. For the equilibrium method, we compute an estimator $\langle\hat{\sigma^z}\rangle_\infty$ for the final population inversion $\langle\sigma^z\rangle_\infty$ in a simulated experiment with N_{meas} measurements. In each simulated measurement, the population of the impurity excited state is drawn randomly from a binomial distribution with success probability $p = (1 + \langle\sigma^z\rangle_\infty)/2$. An estimator for the temperature $\hat{T} = 1/\hat{\beta}$ is then found using $\langle\hat{\sigma^z}\rangle_\infty = -\tanh(\hat{\beta}J)$. Repeating this procedure many times yields a sample of values of $\hat{T}$, whose standard deviation is our estimate of the temperature uncertainty ΔT. For example, using $N_{\text{meas}} = 5000$ we find a fractional uncertainty of $(\Delta T/T)_{\text{eq}} = 2.6\%$ for $T = 0.5 g\varrho_0$, where $g\varrho_0 \sim$ nK in a typical experiment.

For the nonequilibrium method, we consider N_{meas} measurements taken at various times, each one simulated as before by drawing populations randomly from a binomial distribution with $p = (1 + \langle\sigma^z(t)\rangle)/2$. This procedure is performed at both temperatures T and T', leading to estimators $\hat{\Gamma}$ and $\hat{\Gamma}'$ for the dissipation rates by fitting the results Eq. (4.16). An estimator for the temperature $\hat{T}$ is then computed from Eq. (4.19), yielding ΔT as the standard deviation of $\hat{T}$ after many repetitions. Using $N_{\text{meas}} = 5000$ at times $g\varrho_0 t = 1, 2, \ldots, 50$ for the evolutions at temperature T and T', we obtain $(\Delta T/T)_{\text{noneq}} = 12\%$ with the nonequilibrium method.

These results demonstrate that both the equilibrium and nonequilibrium methods are capable of precise thermometry at nanokelvin temperatures. While the equilibrium method is more precise and needs fewer measurements, it requires waiting for equilibration to occur fully. Given typical values of $g\varrho_0 \sim 2\pi \times 100$ Hz, in Fig. 4.3(a) we see an equilibration time on the order of seconds. The equilibrium method is not feasible in situations where this equilibration time is comparable to or longer than the coherence time of the impurity, the lifetime of the gas sample, or the inverse heating rate of the impurity motion due to spontaneous emission or trap potential fluctuations. For example, Ref. [255] reported a double-well qubit having a coherence time on the order of 10 ms. In this case, it would be necessary to speed up equilibration by increasing the impurity-gas coupling, e.g. via a Feshbach resonance [259].

On the other hand, the nonequilibrium method allows for effective thermometry after a much shorter evolution time, but at the cost of many more measurements and potentially reduced precision. An additional advantage of the nonequilibrium method is that it probes regimes of the impurity evolution where both energy eigenstates are appreciably populated. This is in contrast to the equilibrium method, which may involve measuring very small populations and thus may be more susceptible to systematic errors.

4.1.5 Parallel measurements with multiple impurity probes

As we have seen, good measurement precision requires a large number of experimental repetitions. One attractive route to reducing the number of repeated experiments is to simultaneously observe many impurities immersed within a single realisation of the Bose gas. A measurement of $N_{\rm imp}$ impurities provides $N_{\rm imp}$ independent estimates of the eigenstate populations, assuming that the impurities remain uncorrelated with each other despite their mutual interaction with the Bose gas. In the following, we show how to configure the impurities so that this is indeed the case.

To do this, we extend our master equation to describe the dynamical generation of correlations between multiple impurities. In particular, we consider $N_{\rm imp}$ double-well impurity probes interacting with a common BEC reservoir. For simplicity, we assume that all the impurities are identical and aligned parallel to each other, so that the two minima of the potential confining impurity j are located at the positions $\mathbf{x}_j \pm \mathbf{L}/2$. We also assume that the impurities are sufficiently far apart that they do not overlap directly. The only interaction between them is then due to their mutual coupling with the Bose gas.

The autonomous Hamiltonian of the impurities is

$$H_A = \sum_{j=1}^{N_{\rm imp}} J\sigma_j^z, \tag{4.20}$$

where σ_j^z denotes the Pauli operator associated with impurity j. The impurity-gas interaction Hamiltonian is

$$\begin{aligned} H_{AB} &= \kappa \sum_{j=1}^{N_{\rm imp}} \sum_{\mu,\nu=\pm} |\mu_j\rangle\langle\nu_j| \otimes \int \mathrm{d}^3\mathbf{r}\; \phi_\mu(\mathbf{r}-\mathbf{x}_j)\phi_\nu(\mathbf{r}-\mathbf{x}_j)\varrho(\mathbf{r}) \\ &= \sum_{j=1}^{N_{\rm imp}} \left[\sigma_j^x \otimes \sum_{\mathbf{q}} \left(\lambda_{\mathbf{q}} \mathrm{e}^{\mathrm{i}\mathbf{q}\cdot\mathbf{x}_j} b_{\mathbf{q}} + \lambda_{\mathbf{q}}^* \mathrm{e}^{-\mathrm{i}\mathbf{q}\cdot\mathbf{x}_j} b_{\mathbf{q}}^\dagger\right) + \mathbb{1} \otimes \sum_{\mathbf{q}} \left(\lambda'_{\mathbf{q}} \mathrm{e}^{\mathrm{i}\mathbf{q}\cdot\mathbf{x}_j} b_{\mathbf{q}} + \lambda'^*_{\mathbf{q}} \mathrm{e}^{-\mathrm{i}\mathbf{q}\cdot\mathbf{x}_j} b_{\mathbf{q}}^\dagger\right)\right], \end{aligned} \tag{4.21}$$

where $|\pm_j\rangle$ are the states of impurity j localised near the potential minima of its double-well potential, while the coupling constants $\lambda_{\mathbf{q}}$, $\lambda'_{\mathbf{q}}$ are defined by Eq. (4.6) and given explicitly by Eq. (4.10). The second line above follows from the Bogoliubov approximation for the density (4.4) and the assumption that $\phi_+(\mathbf{r})\phi_-(\mathbf{r}) \approx 0$.

The master equation describing the evolution of the impurity density matrix ρ_A is

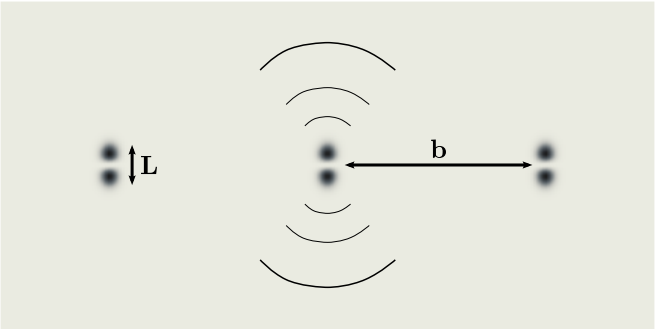


Figure 4.4. Directionality of acoustic dipole radiation emitted by the impurities. Arranging the impurities in a regular array such that the lattice vector **b** is perpendicular to the double-well orientation **L** leads the impurities to decouple completely from one another.

derived under the same assumptions as in Section 4.1.3. The result is

$$\frac{\mathrm{d}\rho_A}{\mathrm{d}t} = \mathrm{i}[\rho_A, H_A] + \mathrm{i}\sum_{j\neq k}\eta_{jk}[\rho_A, \sigma_j^+\sigma_k^-] + \sum_{j,k}\gamma_{jk}^+\left(\sigma_j^+\rho_A\sigma_k^- - \frac{1}{2}\{\sigma_k^-\sigma_j^+, \rho_A\}\right) + \sum_{j,k}\gamma_{jk}^-\left(\sigma_j^-\rho_A\sigma_k^+ - \frac{1}{2}\{\sigma_k^+\sigma_j^-, \rho_A\}\right). \tag{4.22}$$

The parameters appearing above can be expressed in terms of the spectral densities

$$\mathcal{J}_{jk}(\nu) = \sum_{\mathbf{q}}|\lambda_{\mathbf{q}}|^2\cos\left(\mathbf{q}\cdot\mathbf{r}_{jk}\right)\delta(\nu-\omega_{\mathbf{q}}), \tag{4.23}$$

where $\mathbf{r}_{jk} = \mathbf{x}_j - \mathbf{x}_k$ denotes the separation between impurities j and k. Note that Eq. (4.23) reduces to the standard definition (4.15) for $j = k$. Explicitly, the incoherent rates read as

$$\gamma_{jk}^- = 2\pi\mathcal{J}_{jk}[1+n(2J)], \tag{4.24}$$

$$\gamma_{jk}^+ = 2\pi\mathcal{J}_{jk}(2J)n(2J), \tag{4.25}$$

while the coherent interaction strength is

$$\eta_{jk} = \mathsf{P}\int_0^\infty \mathrm{d}\omega\,\frac{2\omega}{4J^2-\omega^2}\mathcal{J}_{jk}(\omega). \tag{4.26}$$

We have neglected the bath-induced renormalisation of the local qubit energies, since these do not affect the population dynamics.

The impurities affect each other in two distinct ways: a direct, coherent interaction mediated by the exchange of phonons [90], and an indirect, incoherent growth of classical correlations due to their mutual interaction with the BEC reservoir. Both of these effects

are strongly dependent on the configuration of the impurities in space. It is possible to completely suppress the generation of correlations between the probes by placing an array of double-well impurities separated by a lattice vector $\mathbf{b}$ such that $\mathbf{b}\cdot\mathbf{L}=0$ and $b \gg L$, as shown in Fig. 4.4. This ultimately stems from the directional dependence of the phonon radiation emanating from each double-well impurity, which is strongest in the direction parallel to $\mathbf{L}$, but vanishes in the far-field limit in directions perpendicular to $\mathbf{L}$. This is entirely analogous to the directionality of the sound emanating from a classical acoustic dipole [260].

Let us now demonstrate the above claims. Evaluating Eq. (4.23) in the thermodynamic limit as usual, we find that it depends on the function

$$\Phi_{jk}(q) = \frac{1}{4\pi}\int_{S^2} \mathrm{d}\Sigma_{\mathbf{q}}\ \sin^2\left(\frac{\mathbf{q}\cdot\mathbf{L}}{2}\right)\cos\left(\mathbf{q}\cdot\mathbf{r}_{jk}\right), \tag{4.27}$$

where $\mathrm{d}\Sigma_{\mathbf{q}}$ denotes the surface element on the unit sphere in $\mathbf{q}$-space. This function encapsulates the dependence of $\mathcal{J}_{jk}(\nu)$ on the impurities' separation $\mathbf{r}_{jk}$. In the far-field limit $r_{jk} \gg L$, we find that

$$\Phi_{jk}(q) \approx \sin^2\left(\frac{q\hat{\mathbf{r}}_{jk}\cdot\mathbf{L}}{2}\right)\mathrm{sinc}(qr_{jk}), \tag{4.28}$$

where $\hat{\mathbf{r}}_{jk}$ is a unit vector parallel to $\mathbf{r}_{jk}$. Eq. (4.28) describes the distribution of phonon radiation from each impurity. In particular, if the impurities are arranged so that $\mathbf{r}_{jk}\cdot\mathbf{L}=0$, as illustrated in Fig. 4.4, the function $\Phi_{jk}(q)$ vanishes for all $j \neq k$. In this case, each impurity evolves independently according to the master equation (4.12).

It is therefore possible using N_{imp} impurities interacting with a single realisation of the BEC to obtain N_{imp} independent measurements of the impurity eigenstate populations. (See Ref. [3] for a detailed description of how the state preparation and readout could be achieved in a realistic optical lattice set-up.) Since $N_{\mathrm{imp}} \sim 100$ is easily achievable, this leads to a drastic reduction in the number of gas samples needed in order to estimate the temperature of the preparation.

4.2 Thermometry from work fluctuations

In Section 4.1.4, we saw that focusing on the nonequilibrium dynamics of a probe can overcome the limitations of conventional thermometry at low temperatures, such as the need to fine-tune the probe's characteristic energy or to wait a prohibitively long time for equilibration. Similar schemes were reported in Refs. [71, 72]. However, these approaches rely on the detailed understanding of the BEC and its excitations afforded by Bogoliubov theory, which is only valid for weakly interacting Bose gases. A general approach for thermometry of strongly correlated systems is still missing.

In this section, we consider an alternative thermometry method based on the nonequilibrium dynamics of a probe qubit, which is applicable in principle to a cold-atom system with an *arbitrary* Hamiltonian. This approach is based on the Tasaki-Crooks relation, which describes the temperature dependence of the fluctuations of work performed on a generic quantum system undergoing a Hamiltonian quench. These work fluctuations can be measured using a probe qubit coupled to the system of interest. Interestingly, there is no need to match the energy splitting of the qubit to the thermal energy. The only requirement is control over the coupling between the system and the two states of the qubit thermometer, which is readily achieved by using an atomic impurity as the probe. The protocol thus realises near-ideal thermometry within its domain of applicability, which corresponds to temperatures commensurate with or lower than the characteristic energy scales of the system. This is precisely the temperature regime of greatest interest for cold-atom physics, and also a challenging one for conventional equilibration thermometry.

4.2.1 Tasaki-Crooks theorem

The Tasaki-Crooks theorem is a property of the distribution of work performed on a system during a Hamiltonian quench, which may be described as follows. Consider a system, such as a cold atomic gas, with the time dependent Hamiltonian

$$H(\lambda_Q(t)) = H_0 + \lambda_Q(t)V, \tag{4.29}$$

where H_0 is the bare Hamiltonian, V is a perturbation, and $\lambda_Q(t)$ is an externally controlled quench parameter for times $t \in [0, \tau]$. We assume that at $t = 0$ the system is in the thermal equilibrium state $\rho_\beta(\lambda_Q(0))$, where $\rho_\beta(\lambda) = \mathrm{e}^{-\beta H(\lambda)}/\mathcal{Z}(\lambda)$, with $\mathcal{Z}(\lambda) = \mathrm{Tr}[\mathrm{e}^{-\beta H(\lambda)}]$ the partition function. The eigenvectors and eigenvalues of the initial Hamiltonian $H(\lambda_Q(0))$ are denoted $|\Omega_n\rangle$ and Ω_n, respectively. After the quench is finished at time $t = \tau$, we have a new Hamiltonian $H(\lambda_Q(\tau))$ with eigenvectors $\left|\bar{\Omega}_n\right\rangle$ and energies $\bar{\Omega}_n$. For our purposes, the work W is defined as the difference between the outcomes of two projective energy measurements performed at times $t = 0$ and $t = \tau$ [32]. The work is therefore a stochastic variable with probability distribution

$$P_Q(W) = \frac{1}{\mathcal{Z}(\lambda_Q(0))} \sum_{m,n} \mathrm{e}^{-\beta\Omega_n} |\left\langle \bar{\Omega}_m \right| U_Q \left| \Omega_n \right\rangle|^2 \delta(\bar{\Omega}_m - \Omega_n - W), \tag{4.30}$$

where $U_Q = \mathsf{T} \exp[-\mathrm{i} \int_0^\tau \mathrm{d}t \; H(\lambda_Q(t))]$ is the unitary evolution operator describing the quench.

Now consider a quench $\lambda_F(t)$, with $\lambda_F(0) = \lambda_i$ and $\lambda_F(\tau) = \lambda_f$, and its time reverse $\lambda_B(t) = \lambda_F(\tau - t)$. The corresponding work distributions are denoted $P_F(W)$ and $P_B(W)$ for the forward (F) and backward (B) quench, respectively. The quotient of these work

distributions is related to the temperature by the Tasaki-Crooks theorem [115, 116]

$$\ln\left[\frac{P_F(W)}{P_B(-W)}\right] = \beta(W - \Delta F), \tag{4.31}$$

where $\Delta F = \ln[\mathcal{Z}(\lambda_i)/\mathcal{Z}(\lambda_f)]$ is the difference in free energy between the thermal states of $H(\lambda_i)$ and $H(\lambda_f)$. Knowledge of both forward and backward work distributions thus gives access to the temperature. The Tasaki-Crooks relation (4.31) holds generically for a Hamiltonian quench in an isolated system: the actual forms of the Hamiltonian and of the quench are entirely arbitrary.

4.2.2 Qubit interferometry

A direct measurement of the work distributions requires many projective energy measurements. While this is possible for small systems such as individual trapped ions [261, 262], it becomes totally infeasible for a many-body system such as a cold atomic gas. Instead, we take a different approach based on coupling an ancillary qubit to the system of interest [112–114].

Consider a probe qubit P with Hamiltonian eigenstates $|0\rangle$ and $|1\rangle$ separated by an energy Δ, and a system of interest S with Hamiltonian H_0. The probe couples to the system via the Hamiltonian

$$H_I(t) = (\eta_0(t)\,|0\rangle\langle 0| + \eta_1(t)\,|1\rangle\langle 1|) \otimes V, \tag{4.32}$$

where V is an arbitrary operator acting on the system of interest. The total Hamiltonian is thus $H(t) = H_0 + \Delta\,|1\rangle\langle 1| + H_I(t)$. At $t = 0$, the couplings are given by $\eta_0(0) = \eta_1(0) = \lambda_Q(0)$ and the system is prepared in the state $\rho(0) = |+\rangle\langle +| \otimes \rho_\beta(\lambda_Q(0))$, where $|+\rangle = (|0\rangle + |1\rangle)/\sqrt{2}$. This can be achieved by, for example, allowing the probe to reach thermal equilibrium with $\beta\Delta \gg 1$ (an easily satisfied condition at low temperature) and subsequently applying a Hadamard rotation to the qubit. The couplings $\eta_{0,1}(t)$ then individually trace out the quench path $\lambda_Q(t)$ but with a delay u, i.e.

$$\begin{aligned}
\eta_0(t) &= \begin{cases} \lambda_Q(t) & (0 \le t \le \tau) \\ \lambda_Q(\tau) & (\tau \le t \le \tau + u), \end{cases} \\
\eta_1(t) &= \begin{cases} \lambda_Q(0) & (0 \le t \le u) \\ \lambda_Q(t-u) & (u \le t \le \tau + u). \end{cases}
\end{aligned} \tag{4.33}$$

The required evolution of the couplings is indicated schematically in Fig. 4.5.

At time $t = \tau + u$, the coherence of the probe qubit density matrix $\rho_P(t) = \mathrm{Tr}_S[\rho(t)]$ is given by [112, 113]

$$\langle 1|\rho_P(t+u)|0\rangle = \frac{1}{2}\mathrm{e}^{-\mathrm{i}\Delta(\tau+u)}\chi_Q(u), \tag{4.34}$$

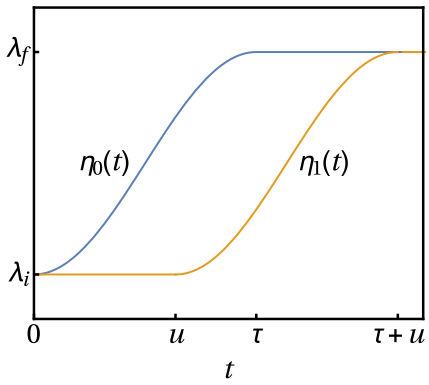


Figure 4.5. Evolution of the couplings (4.33) required for the qubit interferometry protocol. An example for the forward quench is shown.

where we defined

$$\chi_Q(u) = \mathrm{Tr}\left[U_Q \mathrm{e}^{-\mathrm{i}uH(\lambda_Q(0))}\rho_\beta(\lambda_Q(0))U_Q^\dagger \mathrm{e}^{\mathrm{i}uH(\lambda_Q(\tau))}\right]. \tag{4.35}$$

This is none other than the characteristic function of the work distribution, being related to $P_Q(W)$ by Fourier transform

$$P_Q(W) = \mathrm{Re}\left[\frac{1}{\pi}\int_0^\infty \mathrm{d}u\ \mathrm{e}^{-\mathrm{i}uW}\chi_Q(u)\right]. \tag{4.36}$$

Hence, a measurement of the probe coherence (4.34) for many different values of u yields the characteristic function up to a known phase, and thus the work probability distribution after performing the Fourier transform (4.36). Repeating this procedure for both the forward and backward quenches and reconstructing the corresponding work distributions yields the temperature from the Tasaki-Crooks theorem (4.31).

Importantly, the universality of the Tasaki-Crooks theorem means that minimal understanding of the system is needed to implement this protocol. In particular, the system Hamiltonian H_0 may be arbitrarily complex or even unknown. It is in this sense that the protocol realises near-ideal thermometry. One does require the ability to couple each state of the probe to the same operator V, with couplings $\eta_j(t)$ that can be independently varied along the same quench $\lambda_F(t)$ with some delay u, as well as reversed in time to give $\lambda_B(t)$. If these conditions are met, the actual values of V and $\lambda_{F,B}(t)$ are immaterial, in principle.

In practice, any thermometer benefits from optimisation, and this protocol is no exception. In particular, the quench should be chosen so that the fluctuations of the nonequilibrium work are on the order of the temperature or larger. This ensures that the ratio of work distributions on the left-hand side of Eq. (4.31) can be accurately and precisely inferred over a large enough range of values of the work W to extract a good straight-line fit for β. Faced with an unknown system, the experimenter may therefore need to make

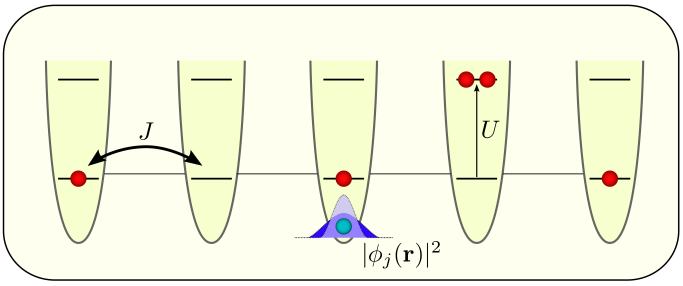


Figure 4.6. Schematic of an optical lattice system realising a Bose-Hubbard model with hopping J and on-site interaction U. An impurity confined to the central lattice site with a state-dependent density $|\phi_j(\mathbf{r})|^2$ probes the temperature.

some adjustments in order to find an appropriate quench. We emphasise that this optimisation can be based purely on observations of the qubit evolution, without resorting to direct measurements on the system of interest. Nevertheless, it is clearly important to use a probe qubit whose interaction with the system is highly controllable and well understood over a range of energies.

In the context of cold atomic gases, a probe qubit comprising an atomic impurity satisfies these requirements well. In the following, as in Section 4.1, we consider density-density coupling, which is appropriate for an impurity interacting with a host gas of a different species. At low temperatures, this interaction is characterised by a small number of parameters, such as s-wave scattering lengths, which may be accurately measured via independent experiments and controlled by means of external fields. Furthermore, the range of interaction energies between the impurity atom and the atomic gas naturally coincides with the characteristic energies of interaction between the gas atoms themselves. It is therefore apparent that the nonequilibrium work fluctuations induced by an atomic impurity are well suited to characterise temperatures that are on the same order or smaller than the natural energy scales of the cold-atom system.

4.2.3 Application to the Bose-Hubbard model

We now consider the application of the thermometry protocol to a paradigmatic cold-atom system: a bosonic gas in a one-dimensional optical lattice of N sites realising the Bose-Hubbard model [263, 264], depicted schematically in Fig. 4.6. The Bose-Hubbard Hamiltonian is

$$H_0 = -J \sum_{m=1}^{N-1} \left(b_m^\dagger b_{m+1} + b_{m+1}^\dagger b_m \right) + \sum_{m=1}^{N} \left(\frac{U}{2} b_m^\dagger b_m^\dagger b_m b_m - \mu b_m^\dagger b_m \right), \tag{4.37}$$

with tunnelling amplitude J, on-site interaction strength U and chemical potential μ. The ladder operators $b_m^\dagger = \int \mathrm{d}^3\mathbf{r}\ w_m(\mathbf{r})\Psi^\dagger(\mathbf{r})$ create an atom localised on site m, with corresponding Wannier function $w_m(\mathbf{r})$.

The probe qubit comprises two spin states of an impurity atom confined to a central lattice site c, coupled to the gas by a contact density-density interaction. Neglecting spin-changing collisions, this takes the form (4.32), with $V = b_c^\dagger b_c$ the local bosonic density on site c and $\eta_j = \kappa_j \int \mathrm{d}^3\mathbf{r}\ |w_c(\mathbf{r})|^2|\phi_j(\mathbf{r})|^2$, where κ_j is the collisional coupling to the background gas and $\phi_j(\mathbf{r})$ is the wave function of the impurity in state $j = 0, 1$. The couplings can be varied using optical or magnetic Feshbach resonances to change $\kappa_{0,1}$ [96, 97]. Alternatively, a state-dependent potential can be used to compress or rarefy the densities $|\phi_{0,1}(\mathbf{r})|^2$ or to shift the mean impurity position with respect to the gas [265].

4.2.4 Tensor-network calculation of the characteristic function

In order to compute the work characteristic function for the Bose-Hubbard model, we have developed a tensor-network algorithm using functions from the open-source TNT library [9]. We proceed by writing the quantum state as a matrix product operator (MPO) [141, 142] and then performing imaginary- and real-time evolution using the time-evolving block decimation (TEBD) algorithm [266, 267]. This allows us to directly and accurately solve Eq. (4.35) in a truncated Hilbert space with a finite number of bosons permitted to occupy each lattice site. In the following, we concisely outline our method; see Ref. [268] for a detailed pedagogical introduction to tensor-network algorithms.

The state of a quantum lattice system with N sites and local Hilbert space dimension d can be represented in MPO form

$$\rho = \sum_{i_1,\ldots,i_N=1}^{d} \sum_{j_1,\ldots,j_N=1}^{d} \mathrm{Tr}\left[A_1^{(i_1 j_1)} \cdots A_M^{(i_N j_N)}\right] |i_1 \cdots i_M\rangle\langle j_1 \cdots j_N| \,. \tag{4.38}$$

Here, the matrix elements of the density operator are given by the trace over a product of matrices $A_l^{(i_l j_l)}$ of maximum dimension $D \times D$, where the bond dimension D quantifies the correlations between lattice sites. The states $\{|i_l\rangle\}$ constitute a complete orthonormal basis for the Hilbert space on lattice site l. The set of matrices $A_l^{(i_l j_l)}$ may also be considered as elements of a single combined tensor A_l of dimension $D \times d \times D \times d$. Together the tensors A_l can represent an arbitrary quantum state, for sufficiently large d and D. In a bosonic system, however, both the physical dimension d and the bond dimension D must be truncated, in general, in order to obtain a tractable numerical representation.

The time-evolution operator over a small time step δt is approximated by a product of two-site gates using a second-order Suzuki-Trotter "staircase" decomposition, see Ref. [269] for details. The tensor network representing the time evolution of the quantum state is depicted schematically in Fig. 4.7(a). The TEBD algorithm proceeds by sweeping across

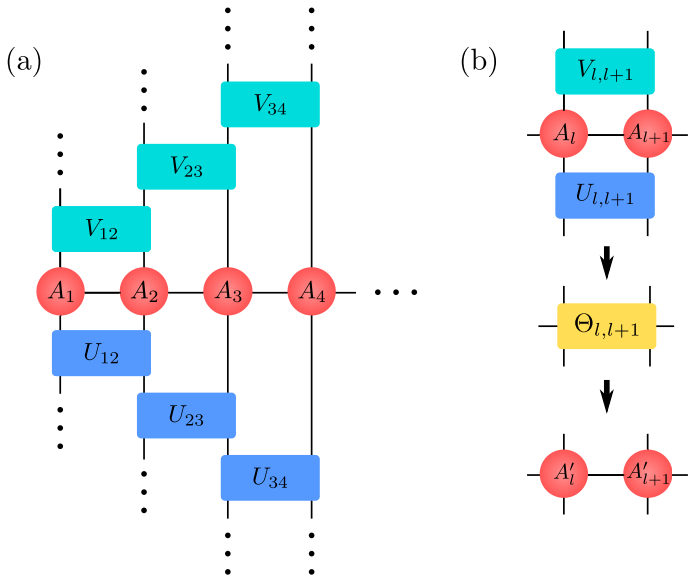


Figure 4.7. (a) Schematic depicting one part of a tensor network representing the time evolution of an MPO (red circles) generated by a product of two-site gates $U_{l,l+1}$ and $V_{l,l+1}$ acting on the MPO from the left and right, respectively. (b) Time evolution proceeds by contraction of nearest-neighbour pairs of MPO tensors $A_l A_{l+1}$ with two-site gates above and below, resulting in a new tensor $\Theta_{l,l+1}$. This tensor is then decomposed into a product of tensors $A'_l A'_{l+1}$ via an SVD. Retaining only the largest D singular values in the SVD maintains an efficient MPO representation at each time step.

this tensor network and applying two-site gates sequentially to pairs of nearest-neighbour tensors $A_l A_{l+1}$ appearing in the MPO representation of the quantum state in Eq. (4.38). The result is a new tensor $\Theta_{l,l+1}$ formed by contracting the A tensors with two-site gates above and below. A singular value decomposition (SVD) is then performed on $\Theta_{l,l+1}$, resulting in a new pair of tensors $A'_l A'_{l+1}$ [Fig. 4.7(b)]. Only the largest D singular values at most are retained after the SVD, so that an efficient MPO representation of the quantum state is maintained at each time step. Repeating this procedure across the entire system over S small time steps δt leads to the desired numerical evolution over a time duration $t = S\delta t$.

In order to find the initial thermal state, we use the identity

$$\rho_\beta(\lambda) = \frac{1}{\mathcal{Z}(\lambda)} \mathrm{e}^{-\beta H_0/2} \hat{\mathbb{1}} \mathrm{e}^{-\beta H_0/2}. \tag{4.39}$$

The right-hand side of this equation can be calculated using the TEBD algorithm as outlined above, after a Wick rotation to imaginary time $t \to -\mathrm{i}\beta/2$ and taking the initial state to be the system-wide identity operator $\mathbb{1}$. The MPO representation of the identity operator is given simply by $A_l^{(i_l j_l)} = \delta_{i_l j_l}$.

The characteristic function (4.35) may then be calculated by performing real-time evo-

lution to find the operator

$$X_Q(u) = U_Q \mathrm{e}^{-\mathrm{i}uH(\lambda_Q(0))} \rho_\beta(\lambda_Q(0)) U_Q^\dagger \mathrm{e}^{\mathrm{i}uH(\lambda_Q(\tau))}, \tag{4.40}$$

such that $\chi_Q(u) = \mathrm{tr}\{X_Q(u)\}$. The unitary $U_Q = \mathsf{T}\exp[-\mathrm{i}\int_0^\tau \mathrm{d}t H(\lambda_Q(t))]$ is performed by discretising the quench path into steps $\lambda_{Qk} = \lambda_Q(k\delta t)$, with $k = 1, \ldots, K$ and $\tau = K\delta t$. Discrete time evolution under the TEBD algorithm reproduces the quench unitary, since

$$U_Q \approx \prod_{k=K}^{1} \mathrm{e}^{-\mathrm{i}\delta t H(\lambda_{Qk})}, \tag{4.41}$$

for sufficiently small δt.

Despite the efficiency of the tensor-network representation, the calculation of $\chi_Q(u)$ using this method is not without challenges. Our implementation of the algorithm suffers from a numerical instability that may lead to a failure of the SVD after a certain number of time steps during the real-time evolution part of the calculation. The instability seems to be associated with a large imbalance in the magnitudes of matrix elements of successive tensors in the network, e.g. the elements of the first tensor could be on the order of 10^{-7} times smaller than those of the second. This disparity appears quite suddenly after a certain evolution time. Unfortunately, we were not able to completely fix this issue nor to identify its fundamental origin.

However, we found that stability can be somewhat improved by dividing each matrix $A_l^{(i_l j_l)}$ by its matrix norm (the square root of the sum of its elements) after each time step. The accumulated product of these norms then multiplies expectation values to give the final result. Nonetheless, the instability limits the number of singular values that can be kept after each SVD. Specifically, we limit the truncation error — as quantified by the sum of all discarded singular values — to a maximum of 10^{-6} per SVD, which in practice corresponds to keeping about $D \approx 50$ singular values in the calculations described in the following section. We also find that fairly fast quenches, i.e. with τ chosen to be small compared to the natural time scales of the system, have favourable numerical properties. This is because the characteristic function $\chi_Q(u)$ decays to zero more rapidly in this case, allowing us to restrict the numerics to relatively short evolution times.

Note that the Hamiltonian (4.37) conserves the total number of atoms $\sum_m b_m^\dagger b_m$, which is fixed in a typical experiment. However, the imaginary-time evolution (4.39) used to obtain the thermal state does not permit us to work within a fixed atom-number sector, since we start from the identity operator on the full Hilbert space. Hence, we must work in the grand canonical ensemble by introducing a chemical potential μ to fix the mean particle number. Nevertheless, it is possible to use the atom-number conservation law to greatly improve the efficiency of the calculation by taking advantage of the block structure of the tensors entering the representation (4.38); see Ref. [268] for details.

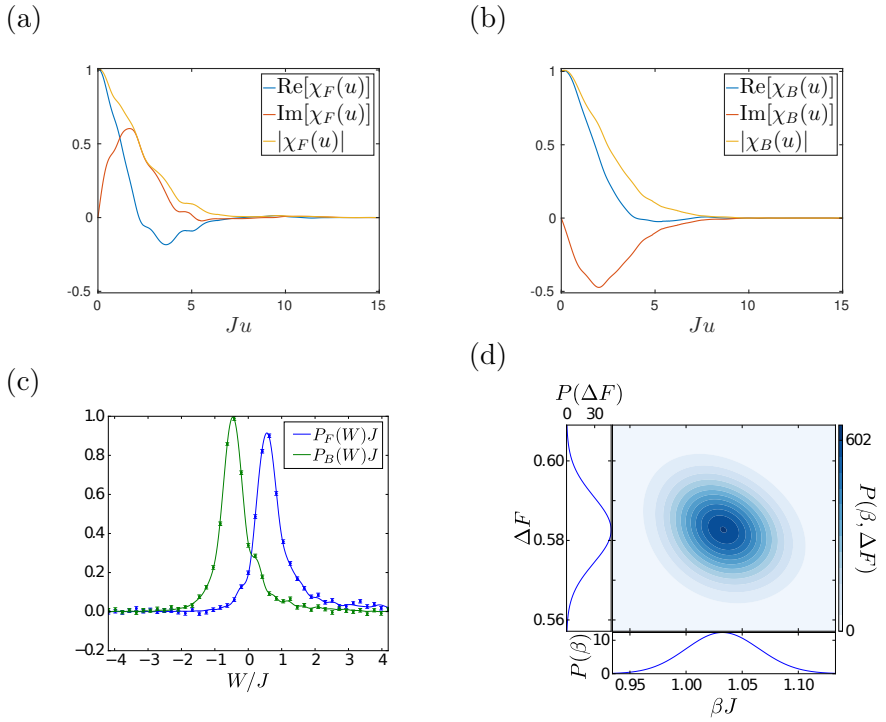


Figure 4.8. (a-b) Work characteristic function calculated from Eq. (4.35) using a modified TEBD algorithm. The simulation parameters are $\beta J = 1$, $N = 11$, $U = 4J$, $\mu = -J$, $J\tau = 0.1$ and $\lambda_F(t) = 2J\sin^2(\pi t/2\tau)$. (c-d) Figures reproduced from Ref. [4], showing (c) the corresponding forward and backward work probability distributions and (d) the estimated probability distributions for the inverse temperature β and free energy difference ΔF, reconstructed from $N_{\text{samp}} = 500$ samples within a time window of width $Ju_{\max} = 15$ with $N_{\text{meas}} = 500$ measurements per sample.

4.2.5 Performance of the thermometry protocol

In order to check the feasibility of our thermometry scheme, we use the tensor-network method to simulate the evolution of the probe density matrix coherence (4.34) for some model parameters, shown in Fig. 4.8(a-b). We focus on the regime of moderately strong interactions, where $U \gtrsim J$, which is poorly understood in comparison to the superfluid ($J \gg U$) or Mott insulator ($U \gg J$) limits. The chemical potential μ is chosen to ensure near-unit filling per site in thermal equilibrium, $\langle b_m^\dagger b_m \rangle \gtrsim 1$. We use a local Hilbert space dimension of $d = 5$, corresponding to a maximum number of bosons per site $\langle b_m^\dagger b_m \rangle_{\max} = 4$.

In an experiment, estimating the temperature using the observed coherence involves two fundamental sources of measurement error. First, only a finite number of discrete samples of $\chi_Q(u)$ can be taken at various times u_j; we assume $u_j = ju_{\max}/N_{\text{samp}}$, for $j = 1, 2, \ldots N_{\text{samp}}$. Upon performing the Fourier transform (4.36), this leads to aliasing due to the finite spacing between samples and spectral leakage due to the finite time window $u_{\max}$. Second, each sample is subject to shot noise due to the finite number

N_{meas} of measurements used to estimate it. In Ref. [4], a toolbox of Bayesian inference techniques was developed which enable the construction of an experimental probability distribution $P(\beta)$ for the inverse temperature, while accounting for these error sources. As shown in Fig. 4.8(d), simulating this procedure using our numerical data indicates that the temperature can be accurately inferred with an error of a few percent. This remains true even when $\beta J \sim 1$, where J may be on the order of nanokelvin.

4.3 Conclusion

In summary, we have considered two different schemes for thermometry using impurities in ultracold gases. We have shown that, in each case, accurate and precise thermometry is possible in the nanokelvin regime. Furthermore, these methods are inherently nondestructive and capable of micron-scale spatial resolution.

In the context of weakly interacting Bose gases, we proposed the use of a double-well qubit to detect the occupation of phonon modes close to the tunnelling energy J. Once the probe reaches equilibrium, the temperature can be read off from the Boltzmann distribution of the impurity energy levels. Alternatively, we showed that the temperature can be extracted by measuring the energy dissipation rate of the probe as it relaxes to equilibrium. This method overcomes the need to wait for a prohibitively long time for equilibration, at the expense of making many more measurements.

For strongly interacting systems, we put forward a different approach based on measuring the fluctuations of the work performed on a system driven out of equilibrium by its coupling to an impurity qubit probe. As a specific example, we studied thermometry of the Bose-Hubbard model, but this technique may be applied in principle to arbitrary cold-atom systems, with minimal knowledge required in advance. This advantage comes at a cost, namely the need for exquisite control over the interaction between the probe qubit and the cold-atom system, as well as a very large number of measurements. Furthermore, it must be possible to perform a quench such that the nonequilibrium work fluctuations are comparable to the thermal energy of the system. We have argued that atomic impurity probes can be expected to satisfy the aforementioned requirements quite generally, and are therefore excellent candidates for generic thermometry of cold atoms at very low temperatures.

Chapter 5

Probing the dynamic structure factor of a neutral Fermi superfluid with impurities

In this chapter, we present a proposal to measure the dynamic structure factor of an atomic Fermi gas with tunable attractive interactions using a trapped impurity atom. This reproduces work published in Ref. [5].

Dilute gases of cold fermionic atoms with tunable interactions offer a unique platform to study the BCS-BEC crossover [127–129]. This fascinating property of Fermi superfluids is broadly relevant for understanding strongly correlated fermion systems, ranging from high-T_c superconductors [130] to quark-gluon plasmas [131]. A key observable for probing the physics of the crossover in ultracold gases is their density fluctuations, which reveal the spatial correlations between atoms [133, 134, 270–274], the spectrum of collective excitations [121–123, 275–277] and the appearance of bound pairs [132, 278]. However, despite the considerable effort recently devoted to characterising the spectrum of density fluctuations across the BCS-BEC crossover (for example, Refs. [124–126] and references therein), a comprehensive picture is still lacking.

Density fluctuations in homogeneous systems are characterised by the *dynamic structure factor* $S(\mathbf{q}, \nu)$, which plays a central role in the linear response theory of many-body systems [279]. In a cold-atom setting, $S(\mathbf{q}, \nu)$ can be measured via Bragg spectroscopy [280–282]. This method suffers from several shortcomings, however, including its destructive nature and the difficulty of performing local measurements [137]. Accessing small wave vectors $\mathbf{q}$ is also challenging, especially in fermionic systems [135], even though much of the interesting collective behaviour occurs in the low-$\mathbf{q}$ regime. As discussed in Chapter 4 in the context of thermometry, impurity-based measurements can avoid such drawbacks. It is therefore worthwhile to consider the use of impurities to probe $S(\mathbf{q}, \nu)$ instead [79].

For this purpose, we study an impurity trapped by an anharmonic potential immersed in a neutral Fermi superfluid, which could be realised in a state-of-the-art cold-atom set-up. This constitutes a novel model of an open quantum system coupled dissipatively to an interacting quantum gas, where the latter supports both bosonic phonons and fermionic

quasiparticle-quasihole pair excitations. By relating the dissipation rate of the impurity's vibrational energy to $S(\mathbf{q}, \nu)$, we show that observing the impurity's evolution allows one to measure the superfluid order parameter and probe the coupling between the bosonic and fermionic excitations. More generally, we put forward a nondestructive method to probe the dynamic structure factor of a degenerate quantum gas, which is valid for arbitrarily strong interactions between the gas atoms, and can access a spectrum of length scales ranging from the typical wavelength of collective modes to much less than the interatomic distance. In addition, the impurity's environment behaves as a highly tunable phononic thermal reservoir whose excitations may themselves be strongly damped, making our model an unusual open quantum system of fundamental interest in its own right.

Previous research on trapped impurity probes in atomic Fermi gases has focused mainly on the noninteracting limit [80,81]. In the context of interacting Fermi superfluids, theorists have investigated the effect on superfluidity of doping by static impurities [283] and the problem of polaron formation by mobile impurities [284–286]. The influence of interactions between the background gas atoms on the dynamics of a trapped impurity has previously only been studied explicitly for Bose-Einstein condensates [83, 84]. Our work therefore extends the theoretical literature on trapped impurity probes to the setting of fermionic superfluids with tunable interactions. Given the recent surge of experimental progress on the immersion of impurities in Fermi gases [103–106], the implementation of our proposal seemingly lies within reach.

5.1 Theoretical model

The system of interest is an impurity atom of species A and mass M, immersed in a cold atomic gas of fermionic species B with mass m and two relevant (hyperfine) spin states. The impurity is confined by a species-selective potential that does not affect the fermions. The trapping potential for the fermions varies slowly on the length scale of the impurity, so that the gas can be well approximated as homogeneous. Our theoretical models for the superfluid and the impurity are described separately in the following subsections.

5.1.1 Fermi superfluid

The characteristic length and energy scales for a homogeneous Fermi gas with mean number density ϱ_0 are fixed by the Fermi wave vector $k_F = (3\pi^2\varrho_0)^{1/3}$ and the Fermi energy $E_F = k_F^2/2m$. At low temperatures, the dominant interaction between the fermions corresponds to collisions between opposite spins in the s-wave channel, described by a scattering length a_s that can be tuned to any value via a Feshbach resonance [259]. The properties of the system vary markedly as a function of the scattering length, ranging from a BCS condensate of Cooper pairs as $1/k_F a_s \to -\infty$, through the strongly interacting unitary gas at $1/k_F a_s = 0$, to a BEC of diatomic molecules as $1/k_F a_s \to +\infty$.

We use the standard BCS mean-field (saddle-point) approximation to describe the superfluid [287–289]. Below the condensation temperature T_c, this theory is accurate in the BCS or BEC limits, and is expected to give a qualitatively correct interpolation across the entire crossover [290]. The salient aspects of the model are summarised below; further details can be found in Appendix C and Refs. [128, 289–292], for example.

The grand-canonical Hamiltonian of the gas is given by

$$H_B = \sum_{s=\uparrow,\downarrow} \int \mathrm{d}^3\mathbf{r}\ \Psi_s^\dagger(\mathbf{r}) \left(-\frac{\nabla^2}{2m} - \mu \right) \Psi_s(\mathbf{r}) + g \int \mathrm{d}^3\mathbf{r}\ \Psi_\uparrow^\dagger(\mathbf{r}) \Psi_\downarrow^\dagger(\mathbf{r}) \Psi_\downarrow(\mathbf{r}) \Psi_\uparrow(\mathbf{r}). \tag{5.1}$$

Here, $\Psi_s^\dagger(\mathbf{r})$ is the atomic field operator which creates a fermion with internal state s at position $\mathbf{r}$, μ is the chemical potential, and g is the coupling constant of a contact pseudopotential describing interatomic collisions. Below T_c, the effective attraction between the fermions leads to the formation of a condensate of Cooper or molecular pairs described by the superfluid order parameter

$$\begin{aligned} \Delta(\mathbf{r}) &= g \langle \Psi_\downarrow(\mathbf{r}) \Psi_\uparrow(\mathbf{r}) \rangle \\ &= \frac{g}{V} \sum_{\mathbf{k},\mathbf{q}} \mathrm{e}^{\mathrm{i}\mathbf{q}\cdot\mathbf{r}} \langle c_{\mathbf{k}+\mathbf{q}/2\downarrow} c_{-\mathbf{k}+\mathbf{q}/2\uparrow} \rangle, \end{aligned} \tag{5.2}$$

where the angle brackets denote a thermal average. On the second line, the field operators have been expanded in terms of plane-wave mode functions

$$\Psi_s(\mathbf{r}) = \frac{1}{\sqrt{V}} \sum_{\mathbf{k}} \mathrm{e}^{\mathrm{i}\mathbf{k}\cdot\mathbf{r}} c_{\mathbf{k}s}, \tag{5.3}$$

where $c_{\mathbf{k}s}^\dagger$ creates an atom with definite momentum $\mathbf{k}$ and internal state s, and V is a fictitious quantisation volume. The translation invariance of the system dictates that $\Delta(\mathbf{r}) = \Delta$ is spatially constant at equilibrium, meaning that condensation occurs into pair states with zero centre-of-mass momentum, i.e. $\mathbf{q} = 0$. We use a gauge in which $\Delta = \Delta^*$.

The gas supports two distinct kinds of elementary excitation above the ground state. The first corresponds to collective oscillations of the superfluid order parameter. This oscillatory motion can be decomposed into normal modes of frequency $\omega_\mathbf{q}$ and wave vector $\mathbf{q}$, which are interpreted in the quantum theory as phonons carrying energy $\omega_\mathbf{q}$ and momentum $\mathbf{q}$. The phonons have bosonic character since they correspond to the collective motion of fermion pairs with centre-of-mass momentum $\mathbf{q} \neq 0$. This kind of excitation has a discrete spectrum, in the sense that each wave vector $\mathbf{q}$ corresponds to a unique frequency $\omega_\mathbf{q}$. In the limit $\mathbf{q} \to 0$, the phonon dispersion relation becomes sound-like, $\omega_\mathbf{q} \to cq$, with c the speed of sound. This manifests the gapless Goldstone mode associated with the U(1) symmetry that is spontaneously broken in the superfluid ground state. Note that a gapless collective mode is a unique feature of the cold-atom system, since in charged

superconductors the Goldstone mode acquires a gap equal to the plasma frequency via the Anderson-Higgs mechanism [293].

Alternatively, if sufficient energy is supplied to the condensate, a bound pair may be broken apart. This creates two fermionic quasiparticles[1] with dispersion relation $E_{\mathbf{k}} = \sqrt{\Delta^2 + \xi_{\mathbf{k}}^2}$, where $\xi_{\mathbf{k}} = \varepsilon_{\mathbf{k}} - \mu$, $\varepsilon_{\mathbf{k}} = k^2/2m$, and μ is the chemical potential. Thus, the minimum energy of such a pair excitation is given by the pair gap $\Theta_0 = \min_{\mathbf{k},\mathbf{k}'}\{E_{\mathbf{k}} + E_{\mathbf{k}'}\}$, i.e.

$$\Theta_0 = \begin{cases} 2|\Delta| & (\mu \geq 0) \\ 2\sqrt{\Delta^2 + \mu^2} & (\mu < 0). \end{cases} \tag{5.4}$$

More generally, the energy of a quasiparticle pair carrying centre-of-mass momentum $\mathbf{q}$ can take any value above the threshold frequency $\Theta_{\mathbf{q}} = \min_{\mathbf{k}}\{E_{\mathbf{k}+\mathbf{q}/2} + E_{\mathbf{k}-\mathbf{q}/2}\}$. Thus, the spectrum of pair excitations at wave vector $\mathbf{q}$ is continuous.

From here on, our analysis is restricted to temperatures well below the pair excitation gap, $T \ll \Theta_0$, so that all quasiparticle modes are unoccupied to an excellent approximation. In this case, the order parameter and chemical potential are determined by the equations of state [290]

$$\frac{m}{4\pi a_s} = \frac{1}{V}\sum_{\mathbf{k}} \left(\frac{1}{2\varepsilon_{\mathbf{k}}} - \frac{1}{2E_{\mathbf{k}}} \right), \tag{5.5}$$

$$\varrho_0 = \frac{1}{V}\sum_{\mathbf{k}} \left(1 - \frac{\xi_{\mathbf{k}}}{E_{\mathbf{k}}} \right), \tag{5.6}$$

which we solve self-consistently to find Δ and μ as a function of $1/k_F a_s$. The speed of sound can be calculated using these equations in conjunction with the thermodynamic relation [294] $mc^2/\varrho_0 = \partial\mu/\partial\varrho_0$, which was shown in Ref. [123] to yield

$$c^2 = \frac{1}{3m^2} \frac{\Delta^2 J_2 J_4}{\Delta^2 J_2^2 + J_\xi^2}, \tag{5.7}$$

where we defined

$$J_2 = \frac{1}{V}\sum_{\mathbf{k}} \frac{1}{E_{\mathbf{k}}^3}, \qquad J_4 = \frac{1}{V}\sum_{\mathbf{k}} \frac{k^2}{E_{\mathbf{k}}^3}, \qquad J_\xi = \frac{1}{V}\sum_{\mathbf{k}} \frac{\xi_{\mathbf{k}}}{E_{\mathbf{k}}^3}. \tag{5.8}$$

The order parameter, chemical potential and sound speed are plotted as a function of $1/k_F a_s$ in Fig. 5.1 for various values in the vicinity of the crossover. In the BCS limit, we have $\Delta \ll E_F$, $\mu \approx E_F$, and $c \approx v_F/\sqrt{3}$, the latter being the well known expression for the Bogoliubov-Anderson sound speed [293], where $v_F = k_F/m$ is the Fermi velocity. On the other hand, in the BEC limit we have $\Delta \gg E_F$, with $c \approx \sqrt{\pi a_s \varrho_0}/m = \sqrt{4\pi a_b \varrho_b}/m_b$ the

[1] We neglect the possibility of creating a lone quasiparticle by injecting or extracting single atoms into or from the condensate.

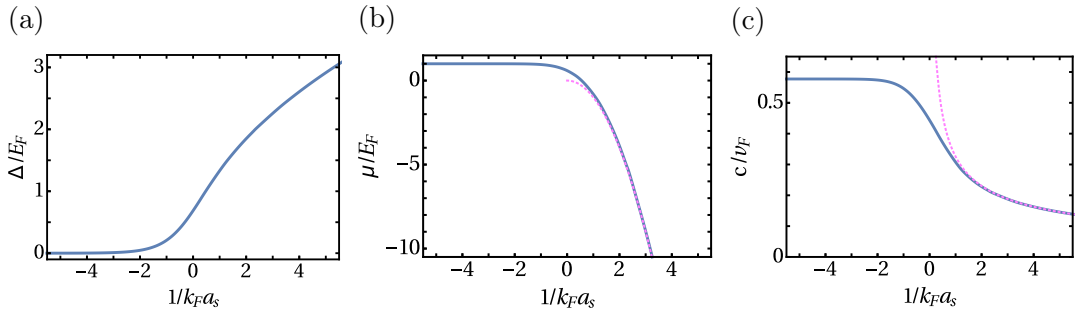


Figure 5.1. Evolution of the (a) order parameter, (b) chemical potential (solid line) and molecular binding energy (dotted line), and (c) speed of sound predicted by BCS theory (solid line) and the limiting case of a molecular BEC (dotted line), as described in the main text.

Bogoliubov sound speed of a BEC of diatomic molecules with mass $m_b = 2m$, density $\varrho_b = \varrho_0/2$ and scattering length $a_b = 2a_s$, while $\mu \approx -1/(2ma_s^2)$ approximates the molecular binding energy.

5.1.2 Impurity probe

We consider an impurity atom confined by a strongly anharmonic potential, so that the lowest two energy levels of its centre-of-mass motion are well separated in energy from the rest. We can thus restrict our attention to the qubit comprising these states, described by the Hamiltonian

$$H_A = \omega_0 \sigma^+ \sigma^-, \tag{5.9}$$

where $\omega_0/2\pi$ is the frequency of small oscillations close to the potential minimum. All other motional and internal states of the impurity are assumed to be far off-resonant or otherwise negligible. The level structure is depicted schematically in Fig. 5.2(a).

We suppose that impurity-gas collisions are elastic and independent of spin. This assumption may hold approximately [101, 103], or as an exact consequence of rotation symmetry if the impurity is spinless and the host gas comprises species with the same total hyperfine spin [104, 105]. The coupling between the impurity and the gas is modelled using an s-wave contact pseudopotential, which in the qubit subspace is formally identical to Eq. (4.2). This can be written in the form

$$H_{AB} = \sum_{m,n=0,1} |m\rangle\langle n| \otimes \frac{1}{V} \sum_{\mathbf{q}\neq 0} \lambda_{\mathbf{q}}^{(mn)} \varrho_{\mathbf{q}}. \tag{5.10}$$

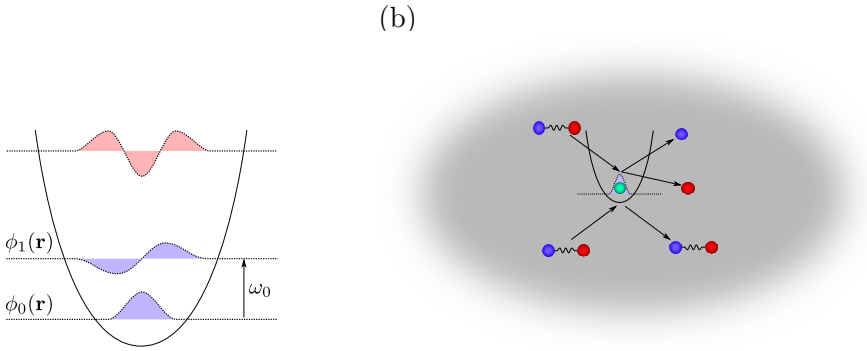


Figure 5.2. (a) Level scheme of an impurity qubit comprising the lowest two energy eigenstates $\phi_0(\mathbf{r})$ and $\phi_1(\mathbf{r})$ of an anharmonic potential, which are well separated in energy from higher excited states. (b) Scattering of fermions by the impurity may either impart momentum to bound pairs in the condensate, or break pairs apart. The former process creates a phonon, the latter creates a pair excitation.

Here, $\varrho_{\mathbf{q}}$ signifies the Fourier transform of the fermion density $\varrho(\mathbf{r}) = \sum_s \Psi_s^\dagger(\mathbf{r})\Psi_s(\mathbf{r})$, i.e.

$$\begin{aligned}\varrho_{\mathbf{q}} &= \int \mathrm{d}^3\mathbf{r}\, \mathrm{e}^{-\mathrm{i}\mathbf{q}\cdot\mathbf{r}}\varrho(\mathbf{r}) \\ &= \sum_{s=\uparrow,\downarrow}\sum_{\mathbf{k}} c^\dagger_{\mathbf{k}-\mathbf{q}/2,s}c_{\mathbf{k}+\mathbf{q}/2,s},\end{aligned} \tag{5.11}$$

while the impurity-gas coupling constants are given by

$$\lambda_{\mathbf{q}}^{(mn)} = \kappa \int \mathrm{d}^3\mathbf{r}\, \mathrm{e}^{\mathrm{i}\mathbf{q}\cdot\mathbf{r}}\phi_m(\mathbf{r})\phi_n(\mathbf{r}), \tag{5.12}$$

where $\phi_n(\mathbf{r}) = \langle \mathbf{r}|n\rangle$, for $n = 0, 1$, are real-valued impurity energy eigenfunctions, and $\kappa = 2\pi\bar{a}/\bar{m}$, with $\bar{a}$ the interspecies s-wave scattering length and $\bar{m} = mM/(m+M)$ the reduced mass.

As discussed in the following subsection and shown explicitly in Appendix D, only the terms in Eq. (5.10) with $m \neq n$ contribute to the impurity's incoherent dynamics. We can thus simplify the interaction Hamiltonian to the form

$$H_{AB} \approx \frac{1}{V}\sum_{\mathbf{q}\neq 0}\left(\lambda_{\mathbf{q}}\sigma^+ \otimes \varrho_{\mathbf{q}} + \lambda^*_{\mathbf{q}}\sigma^- \otimes \varrho^\dagger_{\mathbf{q}}\right), \tag{5.13}$$

where $\lambda_{\mathbf{q}} = \lambda_{\mathbf{q}}^{(10)}$. Note that the operators $\varrho_{\mathbf{q}}$ ($\varrho^\dagger_{\mathbf{q}}$) annihilate (create) excitations of momentum $\mathbf{q}$ in the gas, without changing the number of atoms. This leads to a physical interpretation of Eq. (5.13) in terms of the production and destruction of phonons or quasiparticle pairs by the impurity, over a range of momenta fixed by the coupling constants $\lambda_{\mathbf{q}}$. The relevant scattering processes are illustrated in Fig. 5.2(b).

5.1.3 Master equation

We now show that the impurity dynamics probes the spectrum of density fluctuations in the gas. To that end, we derive a Lindblad equation for the reduced density matrix $\rho_A(t) = \mathrm{Tr}_B[\rho(t)]$ under the Born-Markov and rotating-wave approximations, following the derivation of Chapter 1 with $\mathcal{L}_1 = 0$ and H_A, H_B and H_{AB} given by Eqs. (5.9), (5.1) and (5.10), respectively. We assume that the gas is initially in a thermal state $\rho_B = \mathrm{e}^{-\beta H_B}/\mathcal{Z}_B$ at temperature $T = 1/\beta$, and absorb the environment-induced renormalisation of the impurity vibrational frequency into the definition of H_A. Technical details of the master equation derivation can be found in Appendix D.

The resulting Lindblad equation may be written as

$$\frac{\mathrm{d}\rho_A}{\mathrm{d}t} = \mathrm{i}[\rho_A, H_A] + \gamma^- \mathcal{D}[\sigma^-]\rho_A + \gamma^+ \mathcal{D}[\sigma^+]\rho_A. \tag{5.14}$$

The gain and loss rates are given by $\gamma^{\pm} = 2\pi\mathcal{I}(\mp\omega_0)$, where we have introduced the spectral function of the fermionic environment

$$\mathcal{I}(\nu) = \frac{1}{V}\sum_{\mathbf{q}\neq 0} |\lambda_{\mathbf{q}}|^2 S(\mathbf{q}, \nu). \tag{5.15}$$

This is defined in terms of the dynamic structure factor (DSF)

$$S(\mathbf{q}, \nu) = \frac{1}{2\pi}\int_{-\infty}^{\infty} \mathrm{d}t \int \mathrm{d}^3\mathbf{r}\, \mathrm{e}^{\mathrm{i}(\nu t - \mathbf{q}\cdot\mathbf{r})}\mathcal{C}(\mathbf{r}, t), \tag{5.16}$$

where the autocorrelation function of the density fluctuations is

$$\mathcal{C}(\mathbf{r} - \mathbf{r}', t - t') = \left\langle \delta\varrho(\mathbf{r}, t)\delta\varrho(\mathbf{r}', t')\right\rangle, \tag{5.17}$$

with $\delta\varrho(\mathbf{r}, t) = \varrho(\mathbf{r}, t) - \varrho_0$, while $\varrho(\mathbf{r}, t) = \mathrm{e}^{\mathrm{i}H_B t}\varrho(\mathbf{r})\mathrm{e}^{-\mathrm{i}H_B t}$ denotes the Heisenberg-picture evolution generated by H_B. Eqs. (5.14)–(5.17) establish a direct connection between the incoherent dynamics of the impurity and the density fluctuations of the superfluid. Here we need to use the more general spectral function (5.15) rather than a spectral density, because the temperature dependence of $\mathcal{I}(\nu)$ does not generally factorise, as would be the case for a linear, harmonic environment [cf. Eq. (1.52)]. Note that only the dissipative couplings $\lambda_{\mathbf{q}} = \lambda_{\mathbf{q}}^{(10)}$, corresponding to the simplified Hamiltonian (5.13), enter the master equation through the spectral function (5.15).

The detailed balance condition $S(\mathbf{q}, \nu) = \mathrm{e}^{\beta\nu}S(\mathbf{q}, -\nu)$ implies that $\gamma^- = \mathrm{e}^{\beta\omega_0}\gamma^+$. Therefore, the impurity's energy eigenstate populations relax to equilibrium according to Eq. (4.16), with overall decay rate $\Gamma = \gamma^+ + \gamma^-$ and asymptotic population inversion $\langle\sigma^z\rangle_\infty = -\tanh(\beta\omega_0/2)$. From here on, we focus primarily on the case where $\omega_0 \gg T$, so that the population of the impurity excited state undergoes pure exponential decay

$p_1(t) = \langle 1|\rho_A(t)|1\rangle = \mathrm{e}^{-\Gamma t} p_1(0)$, with $\Gamma = 2\pi\mathcal{I}(\omega_0)$ to a good approximation. Varying the trap frequency from one measurement to the next enables reconstruction of Γ as a function of ω_0 over many experimental runs, from which properties of the DSF can be inferred due to the relation (5.15), as we discuss in detail in subsequent sections.

The measurement signal from each experiment can be increased by simultaneously observing many impurities immersed within a single realisation of the Fermi gas, so long as these impurities remain uncorrelated. In Appendix D, we show how to configure the impurities in space such that their evolution is independent despite their mutual interaction with the gas. In particular, as in Chapter 4, the impurities should be arranged so that their separation vector is orthogonal to the direction of the relevant motional excitations of the impurities. Since the impurities both radiate and absorb density waves anisotropically, they decouple from one another in such an arrangement (see Fig. 4.4).

We conclude this subsection by briefly reviewing the approximations underlying the master equation (5.14). Our basic assumption is that the environment vacuum correlation time τ_B is the shortest time scale of the problem (the thermal correlation time is irrelevant since we assume $\omega_0 \gg T$). We can approximate the vacuum correlation time by $\tau_B \approx \ell/c$, where c is the speed of sound, which estimates the time taken for a spontaneously emitted phonon to irreversibly propagate away from the impurity's domain of influence (see Section 5.2.1). The Born-Markov approximation then requires that $\Gamma \ll c/\ell$, while the rotating-wave approximation is valid when $\Gamma \ll \omega_0$. Both of these inequalities are satisfied in all the examples which follow.

5.1.4 Form factor in the harmonic approximation

Isotropy of the superfluid implies that $S(\mathbf{q}, \nu)$ is independent of the direction of $\mathbf{q}$. Working in the thermodynamic limit via the substitution $(2\pi)^3 \sum_{\mathbf{q}} \to V \int \mathrm{d}^3\mathbf{q}$, we find that Eq. (5.15) is equivalent to

$$\mathcal{I}(\nu) = \kappa^2 \int \frac{\mathrm{d}^3\mathbf{q}}{(2\pi)^3}\, \Phi(q) S(\mathbf{q}, \nu), \tag{5.18}$$

where we defined the dimensionless form factor

$$\Phi(q) = \frac{1}{4\pi\kappa^2} \int_{S^2} \mathrm{d}\Sigma_{\mathbf{q}}\, |\lambda_{\mathbf{q}}|^2, \tag{5.19}$$

with $\mathrm{d}\Sigma_{\mathbf{q}}$ the surface element on the unit sphere in $\mathbf{q}$-space. The form factor encapsulates the effect of the impurity's geometry on its dissipative dynamics.

In order to explicitly evaluate the form factor, we choose a simple approximation for the impurity potential and wave functions enabling us to gain analytical insight into the problem. Specifically, we assume that the impurity potential is isotropic, and use the eigenfunctions of the simple harmonic oscillator, with the excited state correspond-

ing to motion in the z direction (the validity of these approximations is discussed in the following paragraph). Neglecting a normalisation factor, these wave functions are $\phi_n(\mathbf{r}) \propto H_n(z/\ell)\mathrm{e}^{-r^2/2\ell^2}$, where $H_n(z/\ell)$ is the n^{th} Hermite polynomial as a function of the z coordinate expressed in units of the natural oscillator length $\ell = \sqrt{1/M\omega_0}$. The form factor in this approximation is given by

$$\Phi(q) = \frac{1}{6}\ell^2 q^2 \mathrm{e}^{-\ell^2 q^2/2}. \tag{5.20}$$

Let us now discuss the validity of the assumptions leading to Eq. (5.20). The harmonic approximation correctly captures the symmetry of the impurity eigenfunctions for a parity-invariant potential, yet neglects distortions due to the anharmonicity of the potential. Quantitative corrections may therefore be necessary for strongly anharmonic potentials. In addition, the first excited state of an isotropic potential is triply degenerate, apparently conflicting with the two-level approximation for the impurity. However, the additional degenerate sublevels can be consistently neglected, because the rate of environment-induced transitions between the excited sublevels vanishes within the Born-Markov approximation, due to the super-Ohmic nature of the reservoir. This conclusion remains true even at finite temperature, so long as $T \ll \Theta_0$. This point is discussed in more detail in Appendix D. We emphasise that the assumption of isotropic and harmonic eigenfunctions is inessential, and that detailed knowledge of the impurity wave functions is not necessary for the implementation of our proposal.

5.2 Properties of the spectral function

In this section, we discuss the general and qualitative properties of the spectral function. In order to find $\mathcal{I}(\nu)$, we first calculate $S(\mathbf{q},\nu)$ in Appendix C, using a dynamical extension of BCS theory which takes into account variations of the order parameter induced by local density perturbations. Incorporating the dynamics of the order parameter is necessary in order to preserve gauge invariance and to recover the contribution of the collective mode to the DSF [293, 295]. It is easiest to first compute the linear susceptibility $\chi(\mathbf{q},\nu)$, whose imaginary part is related to $S(\mathbf{q},\nu)$ by the fluctuation-dissipation theorem [279, 296]

$$S(\mathbf{q},\nu) = \frac{-1}{\pi(1-\mathrm{e}^{-\beta\nu})}\mathrm{Im}\left[\chi(\mathbf{q},\nu+\mathrm{i}\epsilon)\right], \tag{5.21}$$

where ϵ is a positive infinitesimal. Identical results for the susceptibility can be obtained using various formally different methods, including the collisionless kinetic equation [123] and related operator equations of motion [125, 297], the random-phase approximation [298, 299], and functional integration [126]. Our approach based on the kinetic equation generalises the calculation of Combescot et al. [123] to finite temperature, and may be of independent

interest since we use only elementary methods to obtain $S(\mathbf{q},\nu)$.

5.2.1 Long-wavelength regime

In the limit of very long wavelengths, $\mathbf{q}\to 0$, the collective mode dispersion relation is linear $\omega_{\mathbf{q}} = cq$. In this regime, the DSF takes the universal form

$$S(\mathbf{q},\nu) = \frac{\varrho_0\varepsilon_{\mathbf{q}}}{\omega_{\mathbf{q}}}\left[(1+n_{\mathbf{q}})\delta(\nu-\omega_{\mathbf{q}}) + n_{\mathbf{q}}\delta(\nu+\omega_{\mathbf{q}})\right], \tag{5.22}$$

where $n_{\mathbf{q}} = n(\omega_{\mathbf{q}}) = (\mathrm{e}^{\beta\omega_{\mathbf{q}}}-1)^{-1}$ is the Bose-Einstein distribution. This describes the possibility to absorb or emit a collective mode excitation (phonon) with wave vector $\mathbf{q}$ and frequency $\omega_{\mathbf{q}} = cq$. Eq. (5.22) exhausts the f-sum and compressibility sum rules [279]

$$\int_{-\infty}^{\infty}\mathrm{d}\nu\;\nu S(\mathbf{q},\nu) = \varrho_0\varepsilon_{\mathbf{q}}, \tag{5.23}$$

$$\int_{-\infty}^{\infty}\mathrm{d}\nu\;\lim_{\mathbf{q}\to 0}\frac{S(\mathbf{q},\nu)}{\nu} = \frac{\varrho_0}{2mc^2}, \tag{5.24}$$

which follow from consistency with particle conservation laws and hydrodynamics, respectively. Therefore, if we consider only wave vectors small enough that the above sum rules hold, the collective mode is the only relevant excitation at *any* frequency. In particular, this is expected to be a good approximation for wave vectors $\zeta q \ll 1$, where $\zeta = c/|\Delta|$ is the coherence length [122].

Now, let us consider impurity potentials such that $\ell \gg \zeta$. In this case, the form factor (5.20) samples only wave vectors in the regime where Eq. (5.22) holds. Thus, the spectral function takes the general form

$$\mathcal{I}(\nu) = \begin{cases} \mathcal{J}(\nu)[1+n(\nu)] & (\nu>0) \\ \mathcal{J}(|\nu|)n(|\nu|) & (\nu<0), \end{cases} \tag{5.25}$$

where the spectral density is

$$\mathcal{J}(\nu) = \sum_{\mathbf{q}}|\tilde{\lambda}_{\mathbf{q}}|^2\delta(\nu-\omega_{\mathbf{q}}), \tag{5.26}$$

and we have defined a rescaled coupling $\tilde{\lambda}_{\mathbf{q}} = \lambda_{\mathbf{q}}\sqrt{\varrho_0\varepsilon_{\mathbf{q}}/V\omega_{\mathbf{q}}}$. Note that Eqs. (5.25) and (5.26) take the form of the spectral function and spectral density for a linear, harmonic, bosonic environment [cf. Eqs. (3.14) and (3.8)]. At this level of approximation, the fermionic superfluid thus behaves identically to a bosonic reservoir at low frequencies.

The spectral density can be evaluated explicitly to yield

$$\mathcal{J}(\nu) = \alpha\omega_\ell^{-4}\nu^5\exp\left(-\frac{\nu^2}{2\omega_\ell^2}\right), \tag{5.27}$$

with the dimensionless coupling strength $\alpha = \kappa^2\varrho_0/(24\pi^2 m\ell^2 c^3)$ and the frequency cutoff $\omega_\ell = c/\ell = \tau_B^{-1}$, where τ_B is the environment correlation time discussed in Section 5.1.3. For smaller values of ℓ, the environment correlation time can be expected to differ from ω_ℓ^{-1}. However, decreasing ℓ couples the impurity to even higher frequency modes of the gas. We expect this to result in an even shorter correlation time, and thus we conclude that $\tau_B \lesssim \omega_\ell^{-1}$, in general.

Note that Eq. (5.27) has the same super-Ohmic behaviour $\mathcal{J}(\nu) \sim \nu^5$ in the limit $\nu \to 0$ as the spectral density (4.18) describing an impurity in a BEC. The different prefactors in each case arise from the differing form factors for a single-well or double-well vibrational qubit. We also emphasise that Eq. (5.27) retains the same qualitative frequency dependence across the entire crossover, since altering the interaction strength $1/k_F a_s$ affects only the coupling α and the frequency cut-off ω_ℓ through the changing value of c.

5.2.2 Vicinity of the pair gap

For frequencies in the vicinity of the pairing gap, $\nu \sim \Theta_0$, the qualitative behaviour of the spectral function varies significantly along the crossover. At frequencies below the pairing gap, $\nu < \Theta_0$, the DSF takes the form

$$S(\mathbf{q}, \nu) = M_{\mathbf{q}}\delta(\nu - \omega_{\mathbf{q}}). \tag{5.28}$$

This is similar to Eq. (5.22), but here the spectral weight $M_{\mathbf{q}}$ and the dispersion relation $\omega_{\mathbf{q}}$ are given by complicated expressions which must be computed numerically, in general (see Appendix C). We have also neglected the Bose-Einstein factors describing the distribution of phonons, since by assumption $T \ll \Theta_0$ and thus the modes with frequencies $\omega_{\mathbf{q}} \sim \Theta_0$ are not thermally populated.

From Eq. (5.18), we find the exact, albeit formal, expression

$$\mathcal{I}(\nu) = \kappa^2\Phi(q_\nu)M_{\mathbf{q}_\nu}D_{\mathrm{ph}}(\nu), \tag{5.29}$$

where the wave vector $\mathbf{q}_\nu$ is defined by $\omega_{\mathbf{q}_\nu} = \nu$ and we introduced the phonon density of states

$$D_{\mathrm{ph}}(\nu) = \int \frac{\mathrm{d}^3\mathbf{q}}{(2\pi)^3}\,\delta(\nu - \omega_{\mathbf{q}}). \tag{5.30}$$

The spectral function (5.29) is seen to arise from three factors. The first term $\kappa^2\Phi(q)$ is geometrical in origin, describing how the impurity's density profile affects the transfer of momentum to scattered gas atoms. In order to interpret the weight $M_{\mathbf{q}}$, we insert a complete set of energy eigenstates into Eq. (5.16), resulting in the formal Källén-Lehmann representation

$$S(\mathbf{q}, \nu) = \frac{1}{V}\sum_n \left|\left\langle \Omega_n \middle| \varrho_{\mathbf{q}}^\dagger \middle| \Omega_0 \right\rangle\right|^2 \delta(\nu - \Omega_n), \tag{5.31}$$

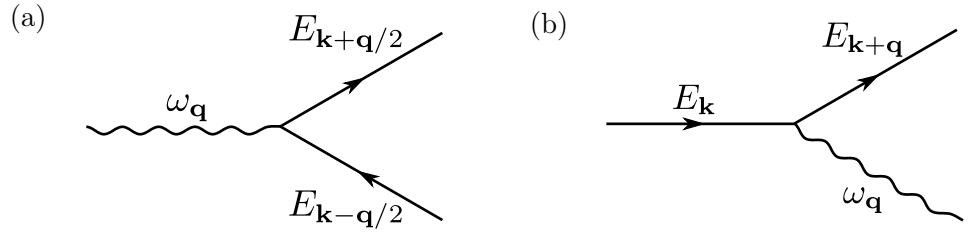


Figure 5.3. Diagrammatic representation of (a) Beliaev and (b) Landau decay due to the coupling between phonons (wiggly lines) and fermionic quasiparticles (straight lines), with time increasing from left to right.

where the sum runs over all eigenstates $|\Omega_n\rangle$ of H_B having energy Ω_n above the ground state $|\Omega_0\rangle$. Comparison of Eqs. (5.28) and (5.31) leads to the heuristic identification $M_{\mathbf{q}} \sim |\langle 1_{\mathbf{q}}| \varrho^\dagger_{\mathbf{q}} |\Omega_0\rangle|^2$, where $|1_{\mathbf{q}}\rangle$ represents an excited state occupied by a single phonon of frequency $\omega_{\mathbf{q}}$. Thus, $M_{\mathbf{q}}$ quantifies the ease with which a collective excitation can be created from the ground state by single-particle scattering processes described by the operator $\varrho^\dagger_{\mathbf{q}}$. The final factor entering Eq. (5.29) gives the density of single-phonon states $D_{\mathrm{ph}}(\nu)$ available to be excited by such a process.

5.2.3 Beliaev and Landau damping

At frequencies above the pairing gap, the DSF cannot be written in a simple form, thus we give here only a qualitative description. For $\nu > \Theta_0$, there is sufficient energy to break apart pairs within the condensate into two fermionic quasiparticles. As a result, $S(\mathbf{q}, \nu)$ gains contributions from a continuum of frequencies at each wave vector, due to two effects. First, direct pair production from the condensate generating excitations carrying total momentum $\mathbf{q}$ is allowed for all frequencies $\nu > \Theta_{\mathbf{q}}$ (recall that $\Theta_{\mathbf{q}}$ is the threshold frequency which lower-bounds the pair continuum). Second, high-frequency phonons with energy $\omega_{\mathbf{q}} > \Theta_{\mathbf{q}}$ can decay into a pair of fermionic quasiparticles, as shown diagrammatically in Fig. 5.3(a). This so-called Beliaev damping leads to a finite lifetime τ_{Bel} for the phonons, and thus the discrete peak of the collective mode (5.28) is broadened into a Lorentzian of width τ^{-1}_{Bel}.

We note in passing that a second decay channel for phonons exists at finite temperature due to the possibility of scattering from thermally excited fermionic quasiparticles, depicted in Fig. 5.3(b). These so-called Landau processes lead to a finite lifetime for even low-frequency phonons with $\omega_{\mathbf{q}} \ll \Theta_0$, and thus the expressions (5.22) and (5.28) are, strictly speaking, broadened into Lorentzian peaks even for $\nu < \Theta_0$. However, Landau damping is irrelevant at the low temperatures of interest in this chapter, $T \ll \Theta_0$, since the population of thermally excited quasiparticle pairs is negligible.

5.3 Numerical results

We now illustrate our results by explicitly calculating the decay rate of the impurity for several examples. We choose parameters taken from the experiments reported in Ref. [103]. The DSF is computed using Eq. (5.21) at $T = 0$, with ϵ finite but chosen small enough to obtain convergence; we have found $\epsilon = 0.01E_F$ to be adequate. The decay rate is then calculated from Eq. (5.18). Note that the impurity confinement length $\ell = 1/\sqrt{M\omega_0}$ entering the form factor (5.19) also varies as function of ω_0 in our calculations.

Our numerical results are summarised in Figs. 5.4 and 5.5, and discussed in detail in the following subsections.

5.3.1 Measuring the pair gap

In the BCS limit, with $1/k_F a_s$ large and negative, there is a sharp peak in the decay rate occuring exactly at $\omega_0 = \Theta_0$. This behaviour extends even to the regime of fairly small, negative $1/k_F a_s$, as shown in Fig. 5.4(a) where we plot an example for $1/k_F a_s = -0.5$. The peak at $\omega_0 = \Theta_0$ is a consequence of the well-known divergence in the density of states in the BCS limit. To see this clearly, in Fig. 5.4(b) we plot the dispersion relation of the collective mode, which reproduces the calculation of Combescot et al. [123]. The plot shows that $\omega_{\mathbf{q}}$ bends to become almost flat as it approaches and then merges with the pair continuum. This indicates that $D_{\rm ph}(\nu) \sim |\mathrm{d}\omega_{\mathbf{q}}/\mathrm{d}q|^{-1}_{\omega_{\mathbf{q}}=\nu}$ increases sharply as $\nu \to \Theta_0$.

On the other hand, at unitarity quite a different behaviour can be observed, as shown in Fig. 5.4(d). Here, the decay rate is a local minimum at $\omega_0 = \Theta_0$. The collective mode dispersion $\omega_{\mathbf{q}}$ remains approximately linear almost all the way into the continuum [123], as plotted in Fig. 5.4(e). This implies that the phonon density of states grows approximately quadratically $D_{\rm ph}(\nu) \sim \nu^2$ as the pair gap is approached. However, the increase of $D_{\rm ph}(\nu)$ is counteracted by the behaviour of $M_{\mathbf{q}}$ shown in Fig. 5.4(f), which decreases as the collective mode merges into the continuum. For higher frequencies $\omega_0 > \Theta_0$, the decay rate increases again sharply due to the contribution of pair excitations, leading to a larger volume of phase space available for scattering.

In summary, in the BCS and unitary regimes the pair gap Θ_0 can be inferred from the extremal values of the decay rate as a function of the impurity trapping frequency. In each case, this extremal behaviour can be understood from the manner in which the discrete spectrum of the collective mode merges with the continuous spectrum of pair excitations. In the BCS regime, the density of phonon states increases sharply at the pair gap, leading to a maximum in the impurity decay rate. Conversely, in the unitary regime the decay rate is minimised at the pair gap due to a decrease in the spectral weight of the collective mode. This property of the unitary gas can be interpreted as a "stiffness" of the ground state against excitation by single-particle scattering processes at frequencies comparable to the pair gap.

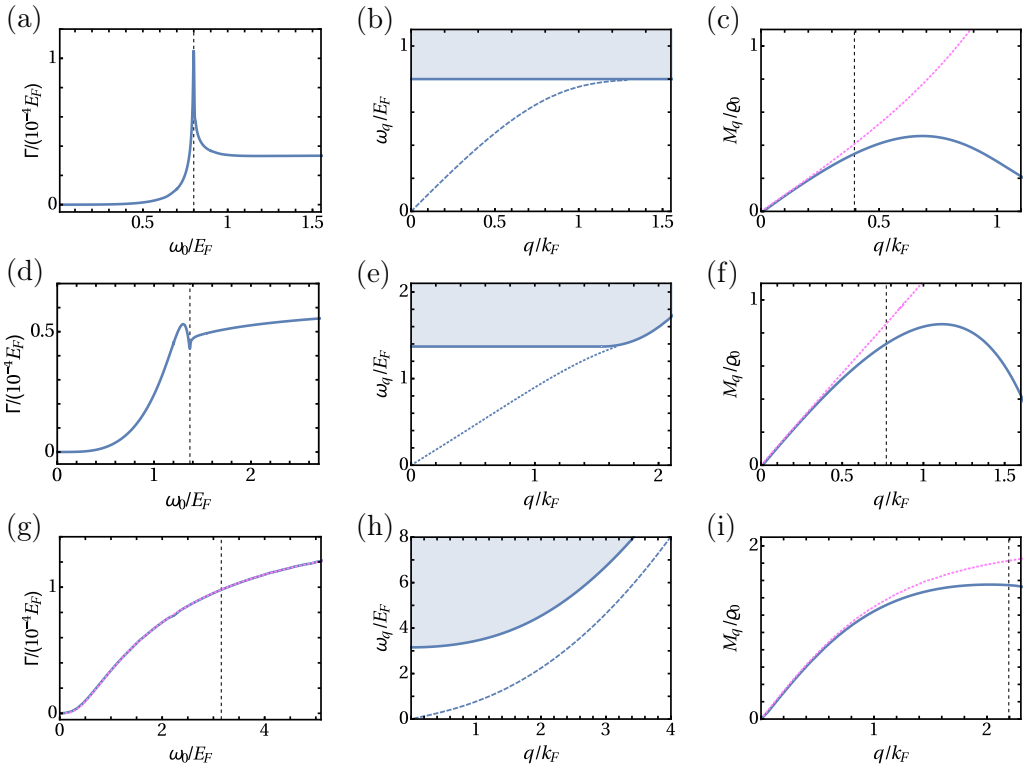


Figure 5.4. Results at $T = 0$ for (a-c) $1/k_F a_s = -0.5$, (d-f) $1/k_F a_s = 0$, and (g-i) $1/k_F a_s = 1.0$. (a,d,g) Impurity decay rate Γ against vibrational frequency ω_0 (solid line), and pair gap Θ_0 (vertical dashed line); (g) the contribution from the discrete pole of the collective mode (i.e. neglecting Beliaev processes) is shown by the pink dotted line. (b,e,h) Dispersion relation of the collective mode $\omega_{\mathbf{q}}$ (dashed line) relative to the threshold frequency $\Theta_{\mathbf{q}}$ (solid line) lower-bounding the pair continuum (shaded region). (c,f,i) Spectral weight $M_{\mathbf{q}}$ of the collective mode (solid line), the long-wavelength approximation $M_{\mathbf{q}} \approx \varrho_0 \varepsilon_{\mathbf{q}}/\omega_{\mathbf{q}}$ (dotted line), and the inverse coherence length ζ^{-1} (vertical dashed line). Parameters are $M/m = 40/6$ and $\kappa = 0.18 E_F/k_F^3$, which describes a ^{40}K impurity in a ^{6}Li gas at density $\varrho_0 = 2.1 \times 10^{12}$ cm^{-3}, corresponding to $E_F \approx 2\pi \times 13$ kHz and $k_F \approx 2\pi/(160\text{ nm})$ [103].

Note that the transition between these two qualitatively different behaviours occurs smoothly as unitarity is approached, as shown in Fig. 5.5(a). As a result, we find an intermediate regime $-0.3 \lesssim 1/k_F a_s \lesssim -0.1$ in which the extremal points of Γ do not coincide with the pair gap. It should be noted that our results are dependent on the BCS model, which is not expected to accurately describe the Fermi gas near unitarity. This regime would therefore be particularly interesting to explore experimentally.

5.3.2 Separation of discrete and continuous spectra

In the BEC regime, the decay rate is instead a monotonically increasing function of frequency, as shown in Fig. 5.4(g) for $1/k_F a_s = 1.0$. In particular, there are no remarkable features at the pair gap $\omega_0 = \Theta_0$. This can be understood from the fact that the collective

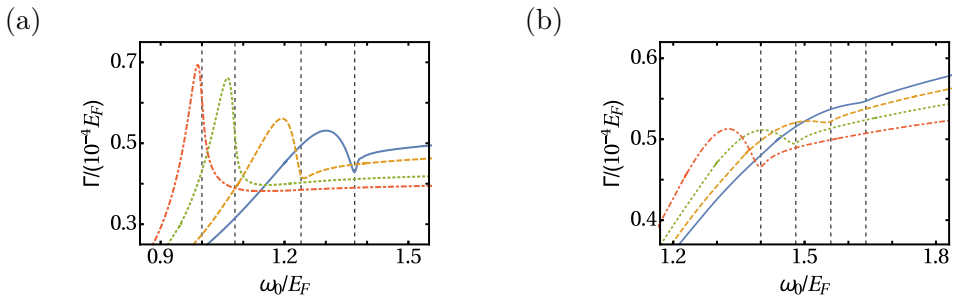


Figure 5.5. (a) Transition between BCS and unitary regimes, showing the decay rate for $1/k_F a_s = -0.31$ (dot-dashed line), -0.24 (dotted line), -0.11 (dashed line), and 0 (solid line). (b) Transition between unitary and BEC regimes, showing the decay rate for $1/k_F a_s = 0.02$ (dot-dashed line), 0.08 (dotted line), 0.14 (dashed line), and 0.20 (solid line). (a,b) The pair gap Θ_0 for each example is shown by the vertical dashed lines. The parameters are the same as in Fig. 5.4.

mode no longer merges with the pair continuum for $1/k_F a_s > 0.16$ [123], as shown in Fig. 5.4(h). Mathematically, this means that the equation $\omega_{\mathbf{q}} = E_{\mathbf{k}+\mathbf{q}/2} + E_{\mathbf{k}-\mathbf{q}/2}$ has no solution. Physically, this describes the impossibility of a phonon decaying into a quasi-particle pair while conserving energy and momentum. As a result, the broadening of the phonon mode due to Beliaev damping is essentially negligible.

In order to illustrate this, we have calculated the impurity decay rate assuming that only a single frequency $\nu = \omega_{\mathbf{q}}$ contributes to $S(\mathbf{q}, \nu)$ for each value of $\mathbf{q}$, i.e. calculating the spectral function using Eqs. (5.28) and (5.29). The result of this approximation is shown by the pink dotted line in Fig. 5.4(g), which coincides almost perfectly with the more accurate calculation taking Beliaev processes into account. Note that this implies that the direct production of pairs from the static condensate is also negligible. The behaviour at $1/k_F a_s = 1.0$ is therefore already in agreement with the standard picture of a Bose-Einstein condensate in which the only significant contribution to the density fluctuations comes from long-lived excitations of the collective mode [279].

We also calculate some examples from the transition regime $0 < 1/k_F a_s \lesssim 0.2$, shown in Fig. 5.5(b). We see that the feature at $\omega_0 = \Theta_0$ vanishes for rather small values of $1/k_F a_s$, as the collective mode separates from the pair continuum. By measuring the frequency dependence of Γ for various values of $1/k_F a_s$, it should thus be possible to pinpoint the separation of discrete and continuous spectra in an experiment.

5.4 Conclusion

We have studied the evolution of a qubit comprising two vibrational energy levels of an anharmonically confined impurity, interacting with a neutral Fermi superfluid. We have related the impurity's spectral function to the dynamic structure factor of the superfluid. Our results indicate that various features of the superfluid's energy spectrum along the

BCS-BEC crossover can be probed using such an impurity. These include the divergence in the density of BCS quasiparticle states, the energy gap for pair excitations in the BCS and unitary regimes, and the separation of discrete and continuous excitation spectra as the BEC limit is approached. At finite temperature, we also expect information on Landau damping to become available. Furthermore, our set-up represents an interesting testing ground for more sophisticated theories of the unitary Fermi gas that go beyond the simple BCS saddle-point approximation used here.

Using experimentally achievable parameters, we predict decay rates on the order of $\Gamma \sim 10^{-4} E_F \sim 10$ Hz, which are measurable within the typical lifetime of a cold atomic gas, and could be further increased at higher superfluid densities. The examples we consider require impurities confined on length scales on the order of $\ell \gtrsim 0.1 k_F^{-1} \sim 10$ nm, which is straightforwardly achievable using a heavy impurity in an optical dipole trap. The initial state of the impurity can be prepared using a moving optical lattice potential, while readout can be achieved by, for example, band mapping combined with time-of-flight imaging [15]. We thus conclude that our proposal represents a feasible alternative to Bragg scattering that is nondestructive and offers nanometre-scale spatial resolution in principle.

For simplicity, we have considered only two energy levels of the impurity. However, it is straightforward to generalise our results to describe transitions between multiple vibrational levels. One interesting possibility to consider in this regard is the sympathetic cooling of harmonically trapped impurities using the Fermi superfluid as a cold reservoir [87–89]. Our results already indicate that the cooling rate could be greatly increased in the BCS regime by tuning the impurity trapping frequency to equal the pair excitation gap and thus take advantage of the divergent density of states.

Beyond the possibility of probing properties of the gas itself, our set-up represents an interesting open quantum system in its own right. An unusual feature of our model is the possibility of exciting both discrete and continuous quasiparticle modes in the reservoir, which moreover are coupled together nontrivially. This leads to distinctive features in the spectral function in the BCS and unitary regimes. In the BCS regime, the peak at frequencies commensurate with the pair gap is reminiscent of resonances appearing in the spectral density of vibronic reservoirs coupled to photosynthetic systems, which are currently the subject of intense research effort in the field of quantum biology [238, 300, 301]. Such peaks are typically associated with non-Markovian effects, although more sophisticated theoretical techniques would be required to explore this possibility in our case. Furthermore, at temperatures comparable to the pair gap we expect qualitatively new features to appear in the spectral function, due either to Landau damping or to the onset of the normal state as the critical condensation temperature is approached. Both of these effects could be explored within the present framework.

In summary, a trapped impurity coupled to a neutral Fermi superfluid may constitute a useful experimental probe of density fluctuations, but also represents a novel platform to

explore the physics of open quantum systems. The problem thus merits further theoretical and experimental study.

Conclusion and outlook

Reliable, efficient cooling methods and accurate, precise measuring devices are essential prerequisites for quantum simulation and other scientific applications of cold-atom systems. Motivated by these needs, we have proposed and studied refrigerators and experimental probes operating at the single-atom level. We focused in particular on what advantages may be gained by harnessing the quantum dynamics of microscopic systems driven out of equilibrium.

In Part I, we studied cooling with quantum absorption refrigerators (QARs). We first proposed a physical realisation of a QAR using an atom-cavity system in Chapter 2. We predicted that such a machine can cool the motion of a trapped atom nearly to absolute zero temperature using sunlight; however, we found that a laser or similar reference was needed to stabilise the frequencies in practice. In Chapter 3, we discovered the existence of coherent oscillations in strongly coupled QARs, which may transiently reach lower temperatures than the steady state. With the right timing, coherence in the machine thus enables one to surpass the performance of a macroscopic cooling device by reaching the coldest possible temperature after a short time.

The findings of Part I indicate that an accurate clock, or equivalently a stable frequency reference, serves as a useful resource in quantum thermodynamics. The major thrust of our immediate further work will therefore be to quantify the thermodynamic resources needed to run such a clock, taking its quantum mechanical nature explicitly into account. Another interesting avenue for future research will be to explore how correlations between small thermal machines and their environment [302] affect their operation. We also recall that, as discussed in Chapter 1, some uncertainty remains over precisely how to model the dynamics of modular open systems such as QARs, even in the strictly Markovian regime. We continue to investigate this subtle problem, since any new insights in this direction would constitute valuable progress for the theory of quantum thermal machines.

In Part II, we proposed methods to probe ultracold atomic gases with trapped impurity atoms. Chapter 4 studied two different ways to measure temperature using impurity qubits. In the first method, thermometry is performed by observing the impurity's equilibration with the background gas. The second technique involves extracting the statistics of work fluctuations via the decoherence of an impurity as it controls a Hamiltonian quench on the cold-atom system of interest. In each case, we described how the nonequilibrium

dynamics of the microscopic probe enabled precise and accurate thermometry in the challenging nanokelvin temperature regime. These claims were supported by an evaluation of each method's performance through explicit calculations for a weakly interacting Bose-Einstein condensate (BEC) and a strongly interacting Bose-Hubbard lattice, respectively. In Chapter 5, we considered using an impurity to probe a neutral Fermi superfluid realising the crossover from a Cooper-pair condensate to a molecular BEC. We found that the impurity's vibrational relaxation dynamics reveals features of the superfluid's density fluctuations encoded in the dynamic structure factor, specifically the pair energy gap and the contact between the collective and individual pair excitation spectra.

A very interesting subject for future work regards the possibility of using impurities to probe instantaneous correlations between atoms in a host gas. In fact, this question formed a major part of our research efforts throughout the doctoral training, but unfortunately led mostly to negative results that have not been detailed here. Probing instantaneous correlations, i.e. a correlation function of two operators evaluated at a single time, turns out to be rather difficult with impurities immersed in weakly confined gases, although this fact is not immediately obvious.

For example, one might expect that impurities would prove ideal for measuring the short-range antibunching correlations between atoms in a BEC (predicted in 1957 [303] but thus far unobserved!) since these appear only over nanometre-scale distances, which are well below the diffraction limit for optical imaging but certainly comparable to the characteristic confinement length of a strongly trapped impurity. However, an impurity confined to smaller length scales couples to phonon modes of the surrounding gas with higher frequencies. These high-frequency modes typically adjust their state to the presence of the impurity faster than the probe can perform its measurement, thus obstructing any attempt to observe instantaneous properties of the gas. This behaviour can already be expected from the findings of Part II, where we showed that the environment correlation time is approximately proportional to the impurity confinement length [see Eqs. (4.18) and (5.27)]. Note that this problem does not appear to arise in lattice systems, probably because of the band gap in their energy spectrum. Indeed, measurements of instantaneous density correlations in atomic lattice gases using impurities seem to be a promising future prospect [304], although time-of-flight imaging of density correlations is already available in this setting [305].

Nevertheless, we remain undeterred from our investigation of impurity-based methods to probe short-range correlations in weakly trapped ultracold gases, particularly because very few alternatives with nanometre spatial resolution are available. One interesting possibility for future work is to consider an impurity probe that is sensitive to the local density of atoms in its vicinity. Such a probe could be realised using laser-induced Raman transitions that couple the continuum of delocalised BEC states to a single localised state carrying a different spin, the latter being trapped by a spin-dependent potential [73]. Such

a probe of the local density (atom number), when monitored *continuously*, is analogous to a photodetector measuring the local light intensity (photon number). In theory, spatial antibunching of the atoms would translate into sub-Poissonian atom-counting statistics in such an experiment, if sufficient temporal resolution could be achieved. However, practical details regarding the feasibility of this proposal remain to be calculated in future work.

In conclusion, both thermodynamics and thermometry (and indeed other kinds of measurements) with single-atom devices can benefit from the unique features of quantum dynamics. In particular, refrigerators and probes whose working substance is a single atom constitute experimentally realisable and highly interesting open quantum systems. Furthermore, such devices could act as useful enabling technologies for quantum science and simulation, with a range of applications that is expected to increase as we progress inexorably down the path towards controlling the properties of matter at the atomic level.

Bibliography

[1] M. T. Mitchison, M. Huber, J. Prior, M. P. Woods, and M. B. Plenio. Realising a quantum absorption refrigerator with an atom-cavity system. *Quant. Sci. Tech.*, 1:015001, 2016.

[2] M. T. Mitchison, M. P. Woods, J. Prior, and M. Huber. Coherence-assisted single-shot cooling by quantum absorption refrigerators. *New J. Phys.*, 17(11):115013, 2015.

[3] D. Hangleiter, M. T. Mitchison, T. H. Johnson, M. Bruderer, M. B. Plenio, and D. Jaksch. Nondestructive selective probing of phononic excitations in a cold Bose gas using impurities. *Phys. Rev. A*, 91:013611, 2015.

[4] T. H. Johnson, F. Cosco, M. T. Mitchison, D. Jaksch, and S. R. Clark. Thermometry of ultracold atoms via nonequilibrium work distributions. *Phys. Rev. A*, 93:053619, 2016.

[5] M. T. Mitchison, T. H. Johnson, and D. Jaksch. Probing the dynamic structure factor of a neutral Fermi superfluid along the BCS-BEC crossover using atomic impurity qubits. *Phys. Rev. A*, 94:063618, 2016.

[6] J. J. Mendoza-Arenas, M. T. Mitchison, S. R. Clark, J. Prior, D. Jaksch, and M. B. Plenio. Transport enhancement from incoherent coupling between one-dimensional quantum conductors. *New J. Phys.*, 16(5):053016, 2014.

[7] P.-L. Giscard, Z. Choo, M. T. Mitchison, J. J. Mendoza-Arenas, and D. Jaksch. An explicit bound for dynamical localisation in an interacting many-body system. *arXiv:1402.1421 [quant-ph]*, 2014.

[8] P. Erker, M. T. Mitchison, R. Silva, M. P. Woods, N. Brunner, and M. Huber. Autonomous clocks: does thermodynamics limit our ability to measure time. arXiv:1609.06704 [quant-ph], 2016.

[9] S. Al-Assam, S. R. Clark, D. Jaksch, and TNT Development Team. TNT Library Alpha Version, http://www.tensornetworktheory.org, 2012.

[10] Richard P Feynman. Simulating physics with computers. *Int. J. Theor. Phys.*, 21(6):467, 1982.

[11] S. Lloyd. Universal quantum simulators. *Science*, 273(5278):1073, 1996.

[12] T. H. Johnson, S. R. Clark, and D. Jaksch. What is a quantum simulator? *Euro. Phys. J. Quant. Tech.*, 1(1):1, 2014.

[13] I. Kassal, J. D. Whitfield, A. Perdomo-Ortiz, M.-H. Yung, and A. Aspuru-Guzik. Simulating chemistry using quantum computers. *Ann. Rev. Phys. Chem.*, 62(1):185–207, 2011. PMID: 21166541.

[14] P. J. J. O'Malley, R. Babbush, I. D. Kivlichan, J. Romero, J. R. McClean, R. Barends, J. Kelly, P. Roushan, A. Tranter, N. Ding, B. Campbell, Y. Chen, Z. Chen, B. Chiaro, A. Dunsworth, A. G. Fowler, E. Jeffrey, E. Lucero, A. Megrant, J. Y. Mutus, M. Neeley, C. Neill, C. Quintana, D. Sank, A. Vainsencher, J. Wenner, T. C. White, P. V. Coveney, P. J. Love, H. Neven, A. Aspuru-Guzik, and J. M. Martinis. Scalable quantum simulation of molecular energies. *Phys. Rev. X*, 6:031007, 2016.

[15] I. Bloch, J. Dalibard, and W. Zwerger. Many-body physics with ultracold gases. *Rev. Mod. Phys.*, 80:885, 2008.

[16] D. Jaksch and P. Zoller. The cold atom Hubbard toolbox. *Ann. Phys.*, 315(1):52, 2005.

[17] M. Lewenstein, A. Sanpera, V. Ahufinger, B. Damski, De A. S., and U. Sen. Ultracold atomic gases in optical lattices: mimicking condensed matter physics and beyond. *Adv. Phys.*, 56(2):243, 2007.

[18] T. Esslinger. Fermi-Hubbard physics with atoms in an optical lattice. *Ann. Rev. Cond. Matt. Phys.*, 1(1):129, 2010.

[19] D. Greif, T. Uehlinger, G. Jotzu, L. Tarruell, and T. Esslinger. Short-range quantum magnetism of ultracold fermions in an optical lattice. *Science*, 340:1307, 2013.

[20] S. Krinner, D. Stadler, D. Husmann, J.-P. Brantut, and T. Esslinger. Observation of quantized conductance in neutral matter. *Nature*, 517(7532):64, 2015.

[21] D. Husmann, S. Uchino, S. Krinner, M. Lebrat, T. Giamarchi, T. Esslinger, and J.-P. Brantut. Connecting strongly correlated superfluids by a quantum point contact. *Science*, 350(6267):1498, 2015.

[22] M. Schreiber, S. S. Hodgman, P. Bordia, H. P. Lüschen, M. H. Fischer, R. Vosk, E. Altman, U. Schneider, and I. Bloch. Observation of many-body localization of interacting fermions in a quasirandom optical lattice. *Science*, 349(6250):842, 2015.

[23] C. Hofrichter, L. Riegger, F. Scazza, M. Höfer, D. R. Fernandes, I. Bloch, and S. Fölling. Direct probing of the Mott crossover in the SU(n) Fermi-Hubbard model. *Phys. Rev. X*, 6:021030, 2016.

[24] M. L. Nielsen and I. L. Chuang. *Quantum Computation and Quantum Information.* Cambridge University Press, Cambridge, 2000.

[25] S. Debnath, N. M. Linke, C. Figgatt, K. A. Landsman, K. Wright, and C. Monroe. Demonstration of a small programmable quantum computer with atomic qubits. *Nature*, 536(7614):63, 2016.

[26] H. P. Breuer and F. Petruccione. *The Theory of Open Quantum Systems.* Oxford University Press, Oxford, 2007.

[27] C. W. Gardiner and P. Zoller. *Quantum Noise*. Springer, Berlin Heidelberg, 3rd edition, 2004.

[28] N. G. Van Kampen. *Stochastic Processes in Physics and Chemistry*. Elsevier, Amsterdam, 3rd edition, 2007.

[29] G. Schaller. *Open Quantum Systems Far from Equilibrium*. Springer, Berlin Heidelberg, 2014.

[30] R. Alicki and K. Lendi. *Quantum Dynamical Semigroups and Applications*. Springer, Berlin Heidelberg, 2007.

[31] U. Weiss. *Quantum Dissipative Systems*. World Scientific, Singapore, 4th edition, 2012.

[32] P. Talkner, E. Lutz, and P. Hänggi. Fluctuation theorems: Work is not an observable. *Phys. Rev. E*, 75:050102, 2007.

[33] M. Horodecki and J. Oppenheim. Fundamental limitations for quantum and nanoscale thermodynamics. *Nat. Comm.*, 4:2059, 2013.

[34] P. Skrzypczyk, A. J. Short, and S. Popescu. Work extraction and thermodynamics for individual quantum systems. *Nat. Comm.*, 5:4185, 2014.

[35] A. E. Allahverdyan. Nonequilibrium quantum fluctuations of work. *Phys. Rev. E*, 90:032137, 2014.

[36] P. Solinas and S. Gasparinetti. Full distribution of work done on a quantum system for arbitrary initial states. *Phys. Rev. E*, 92:042150, 2015.

[37] D. Egloff, O. C. O. Dahlsten, R. Renner, and V. Vedral. A measure of majorization emerging from single-shot statistical mechanics. *New J. Phys.*, 17:073001, 2015.

[38] N. Linden, S. Popescu, and P. Skrzypczyk. How small can thermal machines be? The smallest possible refrigerator. *Phys. Rev. Lett.*, 105:130401, 2010.

[39] A. Levy and R. Kosloff. Quantum absorption refrigerator. *Phys. Rev. Lett.*, 108:070604, 2012.

[40] A. Levy, R. Alicki, and R. Kosloff. Quantum refrigerators and the third law of thermodynamics. *Phys. Rev. E*, 85:061126, 2012.

[41] D. Gelbwaser-Klimovsky and G. Kurizki. Heat-machine control by quantum-state preparation: From quantum engines to refrigerators. *Phys. Rev. E*, 90:022102, 2014.

[42] L. A. Correa. Multistage quantum absorption heat pumps. *Phys. Rev. E*, 89:042128, 2014.

[43] R. Silva, P. Skrzypczyk, and N. Brunner. Small quantum absorption refrigerator with reversed couplings. *Phys. Rev. E*, 92:012136, 2015.

[44] J. Wang, Y. Lai, Z. Ye, J. He, Y. Ma, and Q. Liao. Four-level refrigerator driven by photons. *Phys. Rev. E*, 91:050102, 2015.

[45] B. Leggio, B. Bellomo, and M. Antezza. Quantum thermal machines with single nonequilibrium environments. *Phys. Rev. A*, 91:012117, 2015.

[46] P. Doyeux, B. Leggio, R. Messina, and M. Antezza. Quantum thermal machine acting on a many-body quantum system: Role of correlations in thermodynamic tasks. *Phys. Rev. E*, 93:022134, 2016.

[47] L. A. Correa, J. P. Palao, D. Alonso, and G. Adesso. Quantum-enhanced absorption refrigerators. *Sci. Rep.*, 4:3949, 2014.

[48] Y.-X. Chen and S.-W. Li. Quantum refrigerator driven by current noise. *Europhys. Lett.*, 97(4):40003, 2012.

[49] A. Mari and J. Eisert. Cooling by heating: Very hot thermal light can significantly cool quantum systems. *Phys. Rev. Lett.*, 108:120602, 2012.

[50] D. Venturelli, R. Fazio, and V. Giovannetti. Minimal self-contained quantum refrigeration machine based on four quantum dots. *Phys. Rev. Lett.*, 110:256801, 2013.

[51] H. E. D. Scovil and E. O. Schulz-DuBois. Three-level masers as heat engines. *Phys. Rev. Lett.*, 2:262, 1959.

[52] F. Mazza, R. Bosisio, G. Benenti, V. Giovannetti, R. Fazio, and F. Taddei. Thermoelectric efficiency of three-terminal quantum thermal machines. *New J. Phys.*, 16(8):085001, 2014.

[53] B. Sothmann, R. Sánchez, and A. N. Jordan. Thermoelectric energy harvesting with quantum dots. *Nanotechnology*, 26(3):032001, 2015.

[54] O. Abah, J. Roßnagel, G. Jacob, S. Deffner, F. Schmidt-Kaler, K. Singer, and E. Lutz. Single-ion heat engine at maximum power. *Phys. Rev. Lett.*, 109:203006, 2012.

[55] J. Roßnagel, O. Abah, F. Schmidt-Kaler, K. Singer, and E. Lutz. Nanoscale heat engine beyond the Carnot limit. *Phys. Rev. Lett.*, 112:030602, 2014.

[56] J. Roßnagel, S. T. Dawkins, K. N. Tolazzi, O. Abah, E. Lutz, F. Schmidt-Kaler, and K. Singer. A single-atom heat engine. *Science*, 352(6283):325, 2016.

[57] K. E. Dorfman, D. V. Voronine, S. Mukamel, and M. O. Scully. Photosynthetic reaction center as a quantum heat engine. *Proceedings of the National Academy of Sciences*, 110(8):2746, 2013.

[58] C. Creatore, M. A. Parker, S. Emmott, and A. W. Chin. Efficient biologically inspired photocell enhanced by delocalized quantum states. *Phys. Rev. Lett.*, 111:253601, 2013.

[59] N. Killoran, S. F. Huelga, and M. B. Plenio. Enhancing light-harvesting power with coherent vibrational interactions: A quantum heat engine picture. *J. Chem. Phys.*, 143(15):155102, 2015.

[60] J. Ye, D. W. Vernooy, and H. J. Kimble. Trapping of single atoms in cavity QED. *Phys. Rev. Lett.*, 83:4987, 1999.

[61] J. McKeever, J. R. Buck, A. D. Boozer, A. Kuzmich, H.-C. Nägerl, D. M. Stamper-Kurn, and H. J. Kimble. State-insensitive cooling and trapping of single atoms in an optical cavity. *Phys. Rev. Lett.*, 90:133602, 2003.

[62] K. M. Birnbaum, A. Boca, R. Miller, A. D. Boozer, T. E. Northup, and H. J. Kimble. Photon blockade in an optical cavity with one trapped atom. *Nature*, 436(7047):87–90.

[63] K. M. Fortier, S. Y. Kim, M. J. Gibbons, P. Ahmadi, and M. S. Chapman. Deterministic loading of individual atoms to a high-finesse optical cavity. *Phys. Rev. Lett.*, 98:233601, 2007.

[64] C. Russo, H. G. Barros, A. Stute, F. Dubin, E. S. Phillips, T. Monz, T. E. Northup, C. Becher, T. Salzburger, H. Ritsch, P. O. Schmidt, and R. Blatt. Raman spectroscopy of a single ion coupled to a high-finesse cavity. *App. Phys. B*, 95(2):205, 2009.

[65] J. D. Sterk, L. Luo, T. A. Manning, P. Maunz, and C. Monroe. Photon collection from a trapped ion-cavity system. *Phys. Rev. A*, 85:062308, 2012.

[66] A. Stute, B. Casabone, B. Brandstätter, D. Habicher, H. G. Barros, P. O. Schmidt, T. E. Northup, and R. Blatt. Toward an ion-photon quantum interface in an optical cavity. *App. Phys. B*, 107(4):1145, 2012.

[67] K. Zhang, F. Bariani, and P. Meystre. Quantum optomechanical heat engine. *Phys. Rev. Lett.*, 112:150602, 2014.

[68] K. Zhang, F. Bariani, and P. Meystre. Theory of an optomechanical quantum heat engine. *Phys. Rev. A*, 90:023819, 2014.

[69] R. Uzdin, A. Levy, and R. Kosloff. Equivalence of quantum heat machines, and quantum-thermodynamic signatures. *Phys. Rev. X*, 5:031044, 2015.

[70] M. O. Scully, M. S. Zubairy, G. S. Agarwal, and H. Walther. Extracting work from a single heat bath via vanishing quantum coherence. *Science*, 299(5608):862, 2003.

[71] M. Bruderer and D. Jaksch. Probing BEC phase fluctuations with atomic quantum dots. *New J. Phys.*, 8(6):87, 2006.

[72] C. Sabín, A. White, L. Hackermuller, and I. Fuentes. Impurities as a quantum thermometer for a Bose-Einstein condensate. *Sci. Rep.*, 4:6436, 2014.

[73] A. Recati, P. O. Fedichev, W. Zwerger, J. von Delft, and P. Zoller. Atomic quantum dots coupled to a reservoir of a superfluid Bose-Einstein condensate. *Phys. Rev. Lett.*, 94(4):040404, 2005.

[74] T. H. Johnson, S. R. Clark, M. Bruderer, and D. Jaksch. Impurity transport through a strongly interacting bosonic quantum gas. *Phys. Rev. A*, 84:023617, 2011.

[75] F. Grusdt, N. Y Yao, D. A. Abanin, M. Fleischhauer, and E. A. Demler. Interferometric measurements of many-body topological invariants using mobile impurities. *Nat. Comm.*, 7:11994, 2016.

[76] M. Bruderer, A. Klein, S. R. Clark, and D. Jaksch. Polaron physics in optical lattices. *Phys. Rev. A*, 76:011605, 2007.

[77] J. Wang, M. Gacesa, and R. Côté. Rydberg electrons in a Bose-Einstein condensate. *Phys. Rev. Lett.*, 114:243003, 2015.

[78] R. Dorner, J. Goold, and V. Vedral. Towards quantum simulations of biological information flow. *Interface Focus*, 2(4):522, 2012.

[79] G. E. Astrakharchik and L. P. Pitaevskii. Motion of a heavy impurity through a Bose-Einstein condensate. *Phys. Rev. A*, 70:013608, 2004.

[80] J. Goold, T. Fogarty, N. Lo Gullo, M. Paternostro, and Th. Busch. Orthogonality catastrophe as a consequence of qubit embedding in an ultracold Fermi gas. *Phys. Rev. A*, 84:063632, 2011.

[81] A. Sindona, J. Goold, N. Lo Gullo, S. Lorenzo, and F. Plastina. Orthogonality catastrophe and decoherence in a trapped-fermion environment. *Phys. Rev. Lett.*, 111:165303, 2013.

[82] M. A. Cirone, G. De Chiara, G. M. Palma, and A. Recati. Collective decoherence of cold atoms coupled to a Bose-Einstein condensate. *New J. Phys.*, 11(10):103055, 2009.

[83] P. Haikka, S. McEndoo, G. De Chiara, G. M. Palma, and S. Maniscalco. Quantifying, characterizing, and controlling information flow in ultracold atomic gases. *Phys. Rev. A*, 84:031602, 2011.

[84] P. Haikka, S. McEndoo, and S. Maniscalco. Non-Markovian probes in ultracold gases. *Phys. Rev. A*, 87(1):12127, 2013.

[85] A. Retzker, J. I. Cirac, M. B. Plenio, and B. Reznik. Methods for detecting acceleration radiation in a Bose-Einstein condensate. *Phys. Rev. Lett.*, 101:110402, 2008.

[86] P. O. Fedichev and U. R. Fischer. Gibbons-Hawking effect in the sonic de Sitter spacetime of an expanding Bose-Einstein-condensed gas. *Phys. Rev. Lett.*, 91:240407, 2003.

[87] A. Griessner, A. J. Daley, S. R. Clark, D. Jaksch, and P. Zoller. Dark-state cooling of atoms by superfluid immersion. *Phys. Rev. Lett.*, 97:220403, 2006.

[88] A. Griessner, A. J. Daley, S. R. Clark, D. Jaksch, and P. Zoller. Dissipative dynamics of atomic Hubbard models coupled to a phonon bath: dark state cooling of atoms within a Bloch band of an optical lattice. *New J. Phys.*, 9(2):44, 2007.

[89] A. J. Daley, P. O. Fedichev, and P. Zoller. Single-atom cooling by superfluid immersion: A nondestructive method for qubits. *Phys. Rev. A*, 69:022306, 2004.

[90] A. Klein and M. Fleischhauer. Interaction of impurity atoms in Bose-Einstein condensates. *Phys. Rev. A*, 71:033605, 2005.

[91] D. M. Gangardt and A. Kamenev. Bloch oscillations in a one-dimensional spinor gas. *Phys. Rev. Lett.*, 102:070402, 2009.

[92] A. Lamacraft. Dispersion relation and spectral function of an impurity in a one-dimensional quantum liquid. *Phys. Rev. B*, 79:241105, 2009.

[93] M. D. Girardeau and A. Minguzzi. Motion of an impurity particle in an ultracold quasi-one-dimensional gas of hard-core bosons. *Phys. Rev. A*, 79:033610, 2009.

[94] B. Olmos, W. Li, S. Hofferberth, and I. Lesanovsky. Amplifying single impurities immersed in a gas of ultracold atoms. *Phys. Rev. A*, 84:041607, 2011.

[95] K. Günter, T. Stöferle, H. Moritz, M. Köhl, and T. Esslinger. Bose-Fermi mixtures in a three-dimensional optical lattice. *Phys. Rev. Lett.*, 96:180402, 2006.

[96] S. Will, T. Best, S. Braun, U. Schneider, and I. Bloch. Coherent interaction of a single fermion with a small bosonic field. *Phys. Rev. Lett.*, 106:115305, 2011.

[97] J. Catani, G. Lamporesi, D. Naik, M. Gring, M. Inguscio, F. Minardi, A. Kantian, and T. Giamarchi. Quantum dynamics of impurities in a one-dimensional Bose gas. *Phys. Rev. A*, 85:023623, 2012.

[98] N. Spethmann, F. Kindermann, S. John, C. Weber, D. Meschede, and A. Widera. Dynamics of single neutral impurity atoms immersed in an ultracold gas. *Phys. Rev. Lett.*, 109:235301, 2012.

[99] R. Scelle, T. Rentrop, A. Trautmann, T. Schuster, and M. K. Oberthaler. Motional coherence of fermions immersed in a Bose gas. *Phys. Rev. Lett.*, 111:070401, 2013.

[100] M. Hohmann, F. Kindermann, B. Gänger, T. Lausch, D. Mayer, F. Schmidt, and A. Widera. Neutral impurities in a Bose-Einstein condensate for simulation of the Fröhlich-polaron. *Euro. Phys. J. Quant. Tech.*, 2(1):1, 2015.

[101] M. Cetina, M. Jag, R. S. Lous, J. T. M. Walraven, R. Grimm, R. S. Christensen, and G. M. Bruun. Decoherence of impurities in a Fermi sea of ultracold atoms. *Phys. Rev. Lett.*, 115:135302, 2015.

[102] M. Hohmann, F. Kindermann, T. Lausch, D. Mayer, F. Schmidt, and A. Widera. Single-atom thermometer for ultracold gases. *Phys. Rev. A*, 93:043607, 2016.

[103] F. M. Spiegelhalder, A. Trenkwalder, D. Naik, G. Hendl, F. Schreck, and R. Grimm. Collisional stability of ^{40}K immersed in a strongly interacting Fermi gas of ^{6}Li. *Phys. Rev. Lett.*, 103:223203, 2009.

[104] V. V. Ivanov, A. Khramov, A. H. Hansen, W. H. Dowd, F. Münchow, A. O. Jamison, and S. Gupta. Sympathetic cooling in an optically trapped mixture of alkali and spin-singlet atoms. *Phys. Rev. Lett.*, 106:153201, 2011.

[105] H. Hara, Y. Takasu, Y. Yamaoka, J. M. Doyle, and Y. Takahashi. Quantum degenerate mixtures of alkali and alkaline-earth-like atoms. *Phys. Rev. Lett.*, 106:205304, 2011.

[106] H. Hara, H. Konishi, S. Nakajima, Y. Takasu, and Y. Takahashi. A three-dimensional optical lattice of ytterbium and lithium atomic gas mixture. *J. Phys. Soc. Jap.*, 83(1):014003, 2014.

[107] C. Zipkes, S. Palzer, C. Sias, and M. Köhl. A trapped single ion inside a Bose-Einstein condensate. *Nature*, 464(7287):388, 2010.

[108] S. Schmid, A. Härter, and J. H. Denschlag. Dynamics of a cold trapped ion in a Bose-Einstein condensate. *Phys. Rev. Lett.*, 105:133202, 2010.

[109] J. B. Balewski, A. T. Krupp, A. Gaj, D. Peter, H. P. Büchler, R. Löw, S. Hofferberth, and T. Pfau. Coupling a single electron to a Bose-Einstein condensate. *Nature*, 502(7473):664, 2013.

[110] T. Karpiuk, M. Brewczyk, K. Rzążewski, A. Gaj, J. B. Balewski, A. T. Krupp, M. Schlagmüller, R. Löw, S. Hofferberth, and T. Pfau. Imaging single Rydberg electrons in a Bose-Einstein condensate. *New J. Phys.*, 17(5):053046, 2015.

[111] T. C. Liebisch, M. Schlagmüller, F. Engel, H. Nguyen, J. Balewski, G. Lochead, F. Böttcher, K. M. Westphal, K. S. Kleinbach, T. Schmid, A. Gaj, R. Löw, S. Hofferberth, T. Pfau, J. Pérez-Ríos, and C. H. Greene. Controlling Rydberg atom excitations in dense background gases. *J. Phys. B*, 49(18):182001, 2016.

[112] L. Mazzola, G. De Chiara, and M. Paternostro. Measuring the characteristic function of the work distribution. *Phys. Rev. Lett.*, 110:230602, 2013.

[113] R. Dorner, S. R. Clark, L. Heaney, R. Fazio, J. Goold, and V. Vedral. Extracting quantum work statistics and fluctuation theorems by single-qubit interferometry. *Phys. Rev. Lett.*, 110(23):230601, 2013.

[114] T. B. Batalhão, A. M. Souza, L. Mazzola, R. Auccaise, R. S. Sarthour, I. S. Oliveira, J. Goold, G. De Chiara, M. Paternostro, and R. M. Serra. Experimental recon-

struction of work distribution and study of fluctuation relations in a closed quantum system. *Phys. Rev. Lett.*, 113:140601, 2014.

[115] M. Campisi, P. Hänggi, and P. Talkner. *Colloquium* : Quantum fluctuation relations: Foundations and applications. *Rev. Mod. Phys.*, 83:771, 2011.

[116] J. Goold, M. Huber, A. Riera, L. del Rio, and P. Skrzypczyk. The role of quantum information in thermodynamics — a topical review. *J. Phys. A*, 49(14):143001, 2016.

[117] S. Jevtic, D. Newman, T. Rudolph, and T. M. Stace. Single-qubit thermometry. *Phys. Rev. A*, 91:012331, 2015.

[118] L. A. Correa, M. Mehboudi, G. Adesso, and A. Sanpera. Individual quantum probes for optimal thermometry. *Phys. Rev. Lett.*, 114:220405, 2015.

[119] M. Jarzyna and M. Zwierz. Quantum interferometric measurements of temperature. *Phys. Rev. A*, 92:032112, 2015.

[120] L.-S. Guo, B.-M. Xu, J. Zou, and B. Shao. Improved thermometry of low-temperature quantum systems by a ring-structure probe. *Phys. Rev. A*, 92:052112, 2015.

[121] A. Minguzzi, G. Ferrari, and Y. Castin. Dynamic structure factor of a superfluid Fermi gas. *Euro. Phys. J. D*, 17(1):49, 2001.

[122] H. P. Büchler, P. Zoller, and W. Zwerger. Spectroscopy of superfluid pairing in atomic Fermi gases. *Phys. Rev. Lett.*, 93:080401, 2004.

[123] R. Combescot, M. Yu. Kagan, and S. Stringari. Collective mode of homogeneous superfluid Fermi gases in the BEC-BCS crossover. *Phys. Rev. A*, 74:042717, 2006.

[124] H. Hu. Many-body theories of density response for a strongly correlated Fermi gas. *Fron. Phys.*, 7(1):98, 2012.

[125] H Guo, C.-C. Chien, and Y. He. Theories of linear response in BCS superfluids and how they meet fundamental constraints. *J. Low Temp. Phys.*, 172(1):5, 2013.

[126] L. He. Dynamic density and spin responses of a superfluid Fermi gas in the BCS-BEC crossover: Path integral formulation and pair fluctuation theory. *Ann. Phys.*, 373:470, 2016.

[127] M. Greiner, C. A. Regal, and D. S. Jin. Emergence of a molecular Bose-Einstein condensate from a Fermi gas. *Nature*, 426(6966):537, 2003.

[128] W. Zwerger (Ed.). *The BCS-BEC Crossover and the Unitary Fermi Gas.* Springer, Berlin Heidelberg, 2012.

[129] Mohit Randeria and Edward Taylor. Crossover from Bardeen-Cooper-Schrieffer to Bose-Einstein condensation and the unitary Fermi gas. *Ann. Rev. Cond. Matt. Phys.*, 5(1):209, 2014.

[130] Q. Chen, J. Stajic, S. Tan, and K. Levin. BCS-BEC crossover: From high temperature superconductors to ultracold superfluids. *Phys. Rep.*, 412(1):1, 2005.

[131] T. Schäfer and D. Teaney. Nearly perfect fluidity: from cold atomic gases to hot quark gluon plasmas. *Rep. Prog. Phys.*, 72(12):126001, 2009.

[132] G. Veeravalli, E. Kuhnle, P. Dyke, and C. J. Vale. Bragg spectroscopy of a strongly interacting Fermi gas. *Phys. Rev. Lett.*, 101:250403, 2008.

[133] E. D. Kuhnle, H. Hu, X.-J. Liu, P. Dyke, M. Mark, P. D. Drummond, P. Hannaford, and C. J. Vale. Universal behavior of pair correlations in a strongly interacting Fermi gas. *Phys. Rev. Lett.*, 105:070402, 2010.

[134] S. Hoinka, M. Lingham, K. Fenech, H. Hu, C. J. Vale, J. E. Drut, and S. Gandolfi. Precise determination of the structure factor and contact in a unitary Fermi gas. *Phys. Rev. Lett.*, 110:055305, 2013.

[135] S. Hoinka. *Precision Bragg spectroscopy of the density and spin response of a strongly interacting Fermi gas.* PhD thesis, Swinburne University of Technology, Melbourne, Australia, 2014.

[136] M. G. Lingham, K. Fenech, S. Hoinka, and C. J. Vale. Local observation of pair condensation in a Fermi gas at unitarity. *Phys. Rev. Lett.*, 112:100404, 2014.

[137] M. G. Lingham, K. Fenech, T. Peppler, S. Hoinka, P. Dyke, P. Hannaford, and C. J. Vale. Bragg spectroscopy of strongly interacting Fermi gases. *J. Mod. Opt.*, 63(18):1783, 2016.

[138] G. Lindblad. On the generator of quantum dynamical semigroups. *Math. Phys.*, 48:119–130, 1976.

[139] V. Gorini, A. Kossakowski, and E. C. G. Sudarshan. Completely positive dynamical semigroups of N-level systems. *J. Math. Phys.*, 17:821, 1976.

[140] S. M. Barnett and P. L. Knight. Dissipation in a fundamental model of quantum optical resonance. *Phys. Rev. A*, 33(4):2444, 1986.

[141] F. Verstraete, J. J. Garcia-Ripoll, and J. I. Cirac. Matrix product density operators: simulation of finite-temperature and dissipative systems. *Phys. Rev. Lett.*, 93:207204, 2004.

[142] M. Zwolak and G. Vidal. Mixed-state dynamics in one-dimensional quantum lattice systems: A time-dependent superoperator renormalization algorithm. *Phys. Rev. Lett.*, 93:207205, 2004.

[143] T. Prosen and M. Žnidarič. Matrix product simulations of non-equilibrium steady states of quantum spin chains. *J. Stat. Mech.*, 2009:P02035, 2009.

[144] G. S. Engel, T. R. Calhoun, E. L. Read, T. K. Ahn, T. Mancal, Y. C. Cheng, R. E. Blankenship, and G. R. Fleming. Evidence for wavelike energy transfer through quantum coherence in photosynthetic systems. *Nature*, 446:782, 2007.

[145] M. Mohseni, P. Rebentrost, S. Lloyd, and A. Aspuru-Guzik. Environment-assisted quantum walks in photosynthetic energy transfer. *J. Chem. Phys.*, 129(17):174106, 2008.

[146] M. B. Plenio and S. F. Huelga. Dephasing-assisted transport: quantum networks and biomolecules. *New J. Phys.*, 10:113019, 2008.

[147] E. Collini and G. D. Scholes. Coherent intrachain energy migration in a conjugated polymer at room temperature. *Science*, 323:369, 2009.

[148] A. Nazir. Correlation-dependent coherent to incoherent transitions in resonant energy transfer dynamics. *Phys. Rev. Lett.*, 103:146404, 2009.

[149] G. Benenti, G. Casati, T. Prosen, D. Rossini, and M. Žnidarič. Charge and spin transport in strongly correlated one-dimensional quantum systems driven far from equilibrium. *Phys. Rev. B*, 80:35110, 2009.

[150] J. J. Mendoza-Arenas, T. Grujic, D. Jaksch, and S. R. Clark. Dephasing enhanced transport in nonequilibrium strongly correlated quantum systems. *Phys. Rev. B*, 87:235130, 2013.

[151] A. Bermudez, M. Bruderer, and M. B. Plenio. Controlling and measuring quantum transport of heat in trapped-ion crystals. *Phys. Rev. Lett.*, 111:040601, 2013.

[152] J.-P. Brantut, J. Meineke, D. Stadler, S. Krinner, and T. Esslinger. Conduction of ultracold fermions through a mesoscopic channel. *Science*, 337:1069, 2012.

[153] C D'Errico, M Moratti, E Lucioni, L Tanzi, B Deissler, M Inguscio, G Modugno, M B Plenio, and F Caruso. Quantum diffusion with disorder, noise and interaction. *New J. Phys.*, 15(4):045007, 2013.

[154] M. Michel, M. Hartmann, J. Gemmer, and G. Mahler. Fourier's Law confirmed for a class of small quantum systems. *Euro. Phys. J. B*, 34(3):325, 2003.

[155] D. Manzano, M. Tiersch, A. Asadian, and H. J. Briegel. Quantum transport efficiency and Fourier's law. *Phys. Rev. E*, 86:061118, 2012.

[156] T. Prosen. Third quantization: a general method to solve master equations for quadratic open Fermi systems. *New J. Phys.*, 10(4):043026, 2008.

[157] T. Prosen and I. Pižorn. Quantum phase transition in a far-from-equilibrium steady state of an XY spin chain. *Phys. Rev. Lett.*, 101:105701, 2008.

[158] M. Žnidarič. Exact solution for a diffusive nonequilibrium steady state of an open quantum chain. *J. Stat. Mech.*, 2010:L05002, 2010.

[159] S. R. Clark, J. Prior, M. J. Hartmann, D. Jaksch, and M. B. Plenio. Exact matrix product solutions in the Heisenberg picture of an open quantum spin chain. *New J. Phys.*, 12(2):025005, 2010.

[160] M. Žnidarič. Solvable quantum nonequilibrium model exhibiting a phase transition and a matrix product representation. *Phys. Rev. E*, 83(1):011108, 2011.

[161] Tomaž Prosen. Exact nonequilibrium steady state of a strongly driven open XXZ chain. *Phys. Rev. Lett.*, 107:137201, 2011.

[162] D. Karevski, V. Popkov, and G. M. Schütz. Exact matrix product solution for the boundary-driven Lindblad XXZ chain. *Phys. Rev. Lett.*, 110:047201, 2013.

[163] H. Wichterich, M. J. Henrich, H. Breuer, J. Gemmer, and M. Michel. Modeling heat transport through completely positive maps. *Phys. Rev. E*, 76:031115, 2007.

[164] Á. Rivas, A. D. K. Plato, S. F. Huelga, and M. B. Plenio. Markovian master equations: a critical study. *New J. Phys.*, 12(11):113032, 2010.

[165] A. Levy and R. Kosloff. The local approach to quantum transport may violate the second law of thermodynamics. *Europhys. Lett.*, 107(2):20004, 2014.

[166] N. Kamiya. Quantum-to-classical reduction of quantum master equations. *Prog. Theor. Exp. Phys.*, 2015(4):043A02, 2015.

[167] A. S. Trushechkin and I. V. Volovich. Perturbative treatment of inter-site couplings in the local description of open quantum networks. *Europhys. Lett.*, 113(3):30005, 2016.

[168] H. J. Carmichael and D. F. Walls. Master equation for strongly interacting systems. *J. Phys. A*, 6(10):1552, 1973.

[169] J. J. Mendoza-Arenas, S. Al-Assam, S. R. Clark, and D. Jaksch. Heat transport in an XXZ spin chain: from ballistic to diffusive regimes and dephasing enhancement. *J. Stat. Mech.*, 2013:P07007, 2013.

[170] E. Collini and G. D. Scholes. Electronic and Vibrational Coherences in Resonance Energy Transfer along MEH-PPV Chains at Room Temperature. *J. Phys. Chem. A*, 113:4223, 2009.

[171] D. Jérome and H.J. Schulz. Organic conductors and superconductors. *Adv. Phys.*, 31(4):299–490, 1982.

[172] M. Dressel, K. Petukhov, B. Salameh, P. Zornoza, and T. Giamarchi. Scaling behavior of the longitudinal and transverse transport in quasi-one-dimensional organic conductors. *Phys. Rev. B*, 71:075104, 2005.

[173] B. Köhler, E. Rose, M. Dumm, G. Untereiner, and M. Dressel. Comprehensive transport study of anisotropy and ordering phenomena in quasi-one-dimensional

$(\mathbf{TMTTF})_2X$ salts $(X = \mathbf{PF}_6, \mathbf{AsF}_6, \mathbf{SbF}_6, \mathbf{BF}_4, \mathbf{ClO}_4, \mathbf{ReO}_4)$. *Phys. Rev. B*, 84:035124, 2011.

[174] N. Motoyama, H. Eisaki, and S. Uchida. Magnetic susceptibility of ideal spin 1/2 Heisenberg antiferromagnetic chain systems, Sr_2CuO_3 and $SrCuO_2$. *Phys. Rev. Lett.*, 76:3212, 1996.

[175] I. Tsukada, Y. Sasago, K. Uchinokura, A. Zheludev, S. Maslov, G. Shirane, K. Kakurai, and E. Ressouche. $BaCu_2Si_2O_7$: A quasi-one-dimensional $S = 1/2$ antiferromagnetic chain system. *Phys. Rev. B*, 60:6601, 1999.

[176] M. Baenitz, C. Geibel, M. Dischner, G. Sparn, F. Steglich, H. H. Otto, M. Meibohm, and A. A. Gippius. $CuSiO_3$: A quasi-one-dimensional $S = \frac{1}{2}$ antiferromagnetic chain system. *Phys. Rev. B*, 62:12201, 2000.

[177] U. Busch and K. A. Penson. Tight-binding electrons on open chains: Density distribution and correlations. *Phys. Rev. B*, 36:9271, 1987.

[178] D. M. Newns. Self-consistent model of hydrogen chemisorption. *Phys. Rev.*, 178(3):1123, 1969.

[179] M. Michel, O. Hess, H. Wichterich, and J. Gemmer. Transport in open spin chains: A Monte Carlo wave-function approach. *Phys. Rev. B*, 77:104303, 2008.

[180] J. Sirker, R. G. Pereira, and I. Affleck. Diffusion and ballistic transport in one-dimensional quantum systems. *Phys. Rev. Lett.*, 103:216602, 2009.

[181] Marko Žnidarič, Tomaž Prosen, and Peter Prelovšek. Many-body localization in the Heisenberg XXZ magnet in a random field. *Phys. Rev. B*, 77(6):064426, 2008.

[182] M. Žnidarič. Dephasing-induced diffusive transport in the anisotropic Heisenberg model. *New J. Phys.*, 12:043001, 2010.

[183] Marko Žnidarič. Magnetization transport in spin ladders and next-nearest-neighbor chains. *Phys. Rev. B*, 88:205135, 2013.

[184] M. Scala, B. Militello, A. Messina, S. Maniscalco, J. Piilo, and K.-A. Suominen. Cavity losses for the dissipative Jaynes-Cummings Hamiltonian beyond rotating wave approximation. *J. Phys. A*, 40(48):14527, 2007.

[185] Yu Zhang, Shuguang Chen, and GuanHua Chen. First-principles time-dependent quantum transport theory. *Phys. Rev. B*, 87:085110, 2013.

[186] S. Carnot. *Réflexions sur la puissance motrice du feu.* Vrin, Paris, 1978.

[187] V. Vedral, M. B. Plenio, M. A. Rippin, and P. L. Knight. Quantifying entanglement. *Phys. Rev. Lett.*, 78:2275, 1997.

[188] F. G. S. L. Brandão, M. Horodecki, J. Oppenheim, J. M. Renes, and R. W. Spekkens. Resource theory of quantum states out of thermal equilibrium. *Phys. Rev. Lett.*, 111:250404, 2013.

[189] F. G. S. L. Brandão, M. Horodecki, N. H. Y. Ng, J. Oppenheim, and S. Wehner. The second laws of quantum thermodynamics. *Proc. Nat. Ac. Sci.*, 112(11):201411728, 2015.

[190] O. C. O. Dahlsten, R. Renner, E. Rieper, and V. Vedral. Inadequacy of von Neumann entropy for characterizing extractable work. *New J. Phys.*, 13(5):053015, 2011.

[191] M. Huber, M. Perarnau-Llobet, K. V. Hovhannisyan, P. Skrzypczyk, C. Klöckl, N. Brunner, and A. Acín. Thermodynamic cost of creating correlations. *New J. Phys.*, 17(6):065008, 2015.

[192] M. Perarnau-Llobet, K. V. Hovhannisyan, M. Huber, P. Skrzypczyk, N. Brunner, and A. Acín. Extractable work from correlations. *Phys. Rev. X*, 5:041011, 2015.

[193] P. Ćwikliński, M. Studziński, M. Horodecki, and J. Oppenheim. Limitations on the evolution of quantum coherences: Towards fully quantum second laws of thermodynamics. *Phys. Rev. Lett.*, 115(21):210403, 2015.

[194] M. Lostaglio, D. Jennings, and T. Rudolph. Description of quantum coherence in thermodynamic processes requires constraints beyond free energy. *Nat. Comm.*, 6:6383, 2015.

[195] K. Korzekwa, M. Lostaglio, J. Oppenheim, and D. Jennings. The extraction of work from quantum coherence. *New J. Phys.*, 18(2):023045, 2016.

[196] A. Misra, U. Singh, S. Bhattacharya, and A. K. Pati. Energy cost of creating quantum coherence. *Phys. Rev. A*, 93:052335, 2016.

[197] R. Alicki. The quantum open system as a model of the heat engine. *J. Phys. A*, 12(5):L103, 1979.

[198] R. Kosloff. A quantum mechanical open system as a model of a heat engine. *J. Chem. Phys.*, 80(4):1625, 1984.

[199] J.-P. Brantut, C. Grenier, J. Meineke, D. Stadler, S. Krinner, C. Kollath, T. Esslinger, and A. Georges. A thermoelectric heat engine with ultracold atoms. *Science*, 342(6159):713, 2013.

[200] C. Bergenfeldt, P. Samuelsson, B. Sothmann, C. Flindt, and M. Büttiker. Hybrid microwave-cavity heat engine. *Phys. Rev. Lett.*, 112:076803, 2014.

[201] P. P. Hofer and B. Sothmann. Quantum heat engines based on electronic Mach-Zehnder interferometers. *Phys. Rev. B*, 91:195406, 2015.

[202] P. P. Hofer, J.-R. Souquet, and A. A. Clerk. Quantum heat engine based on photon-assisted Cooper pair tunneling. *Phys. Rev. B*, 93:041418, 2016.

[203] N. Brunner, N. Linden, S. Popescu, and P. Skrzypczyk. Virtual qubits, virtual temperatures, and the foundations of thermodynamics. *Phys. Rev. E*, 85:051117, 2012.

[204] J. B. Brask, G. Haack, N. Brunner, and M. Huber. Autonomous quantum thermal machine for generating steady-state entanglement. *New J. Phys.*, 17(11):113029, 2015.

[205] J. P. Palao, R. Kosloff, and J. M. Gordon. Quantum thermodynamic cooling cycle. *Phys. Rev. E*, 64:056130, 2001.

[206] R. Kosloff and A. Levy. Quantum heat engines and refrigerators: Continuous devices. *Ann. Rev. Phys. Chem.*, 65(1):365, 2014.

[207] N. Brunner, M. Huber, N. Linden, S. Popescu, R. Silva, and P. Skrzypczyk. Entanglement enhances cooling in microscopic quantum refrigerators. *Phys. Rev. E*, 89(3):32115, 2014.

[208] L. A. Correa, J. P. Palao, G. Adesso, and D. Alonso. Performance bound for quantum absorption refrigerators. *Phys. Rev. E*, 87:042131, 2013.

[209] P. Horak, G. Hechenblaikner, K. M. Gheri, H. Stecher, and H. Ritsch. Cavity-induced atom cooling in the strong coupling regime. *Phys. Rev. Lett.*, 79:4974, 1997.

[210] P. Maunz, T. Puppe, I. Schuster, N. Syassen, P. W. H. Pinkse, and G. Rempe. Cavity cooling of a single atom. *Nature*, 428(6978):50.

[211] S. Nuszmann, K. Murr, M. Hijlkema, B. Weber, A. Kuhn, and G. Rempe. Vacuum-stimulated cooling of single atoms in three dimensions. *Nat. Phys.*, 1(2):122.

[212] D. R. Leibrandt, J. Labaziewicz, V. Vuletić, and I. L. Chuang. Cavity sideband cooling of a single trapped ion. *Phys. Rev. Lett.*, 103:103001, 2009.

[213] C. A. Blockley, D. F. Walls, and H. Risken. Quantum collapses and revivals in a quantized trap. *Europhys. Lett.*, 17:509, 1992.

[214] V. Bužek, G. Drobný, M. S. Kim, G. Adam, and P. L. Knight. Cavity QED with cold trapped ions. *Phys. Rev. A*, 56:2352, 1997.

[215] E. D. Black. An introduction to Pound-Drever-Hall laser frequency stabilization. *Am. J. Phys.*, 69(1):79, 2001.

[216] M. B. Plenio and S. F. Huelga. Entangled light from white noise. *Phys. Rev. Lett.*, 88:197901, 2002.

[217] M. Brownnutt, M. Kumph, P. Rabl, and R. Blatt. Ion-trap measurements of electric-field noise near surfaces. *Rev. Mod. Phys.*, 87:1419, 2015.

[218] P. F. Herskind, A. Dantan, J. P. Marler, M. Albert, and M. Drewsen. Realization of collective strong coupling with ion Coulomb crystals in an optical cavity. *Nat. Phys.*, 5(7):494.

[219] M. Albert, J. P. Marler, P. F. Herskind, A. Dantan, and M. Drewsen. Collective strong coupling between ion Coulomb crystals and an optical cavity field: Theory and experiment. *Phys. Rev. A*, 85:023818, 2012.

[220] S. Begley, M. Vogt, G. K. Gulati, H. Takahashi, and M. Keller. Optimized multi-ion cavity coupling. *Phys. Rev. Lett.*, 116:223001, 2016.

[221] K. Brandner, M. Bauer, M. T. Schmid, and U. Seifert. Coherence-enhanced efficiency of feedback-driven quantum engines. *New J. Phys.*, 17(6):065006, 2015.

[222] M. D. Vidrighin, O. Dahlsten, M. Barbieri, M. S. Kim, V. Vedral, and I. A. Walmsley. Photonic Maxwell's demon. *Phys. Rev. Lett.*, 116:050401, 2016.

[223] K. W. Murch, U. Vool, D. Zhou, S. J. Weber, S. M. Girvin, and I. Siddiqi. Cavity-assisted quantum bath engineering. *Phys. Rev. Lett.*, 109:183602, 2012.

[224] C. J. Myatt, B. E. King, Q. A. Turchette, C. A. Sackett, D. Kielpinski, W. M. Itano, C. Monroe, and D. J. Wineland. Decoherence of quantum superpositions through coupling to engineered reservoirs. *Nature*, 403(6767):269, 2000.

[225] K. Micadei, R. M. Serra, and L. C. Céleri. Thermodynamic cost of acquiring information. *Phys. Rev. E*, 88:062123, 2013.

[226] F. Tonner and G. Mahler. Autonomous quantum thermodynamic machines. *Phys. Rev. E*, 72:066118, 2005.

[227] A. S. L. Malabarba, A. J. Short, and P. Kammerlander. Clock-driven quantum thermal engines. *New J. Phys.*, 17(4):045027, 2015.

[228] M. P. Woods, R. Silva, and J. Oppenheim. Autonomous quantum machines and finite sized clocks. *arXiv:1607.04591 [quant-ph]*, 2016.

[229] S. Oviedo-Casado, J. Prior, A. W. Chin, R. Rosenbach, S. F. Huelga, and M. B. Plenio. Phase-dependent exciton transport and energy harvesting from thermal environments. *Phys. Rev. A*, 93:020102, 2016.

[230] T. Baumgratz, M. Cramer, and M. B. Plenio. Quantifying coherence. *Phys. Rev. Lett.*, 113:140401, 2014.

[231] A. Winter and D. Yang. Operational resource theory of coherence. *Phys. Rev. Lett.*, 116:120404, 2016.

[232] E. Chitambar and G. Gour. Critical examination of incoherent operations and a physically consistent resource theory of quantum coherence. *Phys. Rev. Lett.*, 117:030401, 2016.

[233] P. Kammerlander and J. Anders. Coherence and measurement in quantum thermodynamics. *Sci. Rep.*, 6:22174, 2016.

[234] J. Åberg. Catalytic coherence. *Phys. Rev. Lett.*, 113(15):150402, 2014.

[235] P. P. Hofer, M. Perarnau-Llobet, J. B. Brask, R. Silva, M. Huber, and N. Brunner. Autonomous quantum refrigerator in a circuit-QED architecture based on a Josephson junction. *arXiv:1607.05218 [quant-ph]*, 2016.

[236] J. B. Brask and N. Brunner. Small quantum absorption refrigerator in the transient regime: Time scales, enhanced cooling, and entanglement. *Phys. Rev. E*, 92:062101, 2015.

[237] S. Das, A. Misra, A. K. Pal, A. S. De, and U. Sen. Necessarily transient quantum refrigerator. *arXiv:1606.06985 [quant-ph]*, 2016.

[238] J. Prior, A. W. Chin, S. F. Huelga, and M. B. Plenio. Efficient simulation of strong system-environment interactions. *Phys. Rev. Lett.*, 105:050404, 2010.

[239] A. W. Chin, Á. Rivas, S. F. Huelga, and M. B. Plenio. Exact mapping between system-reservoir quantum models and semi-infinite discrete chains using orthogonal polynomials. *J. Math. Phys.*, 51(9), 2010.

[240] N. Poli, F.-Y. Wang, M. G. Tarallo, A. Alberti, M. Prevedelli, and G. M. Tino. Precision measurement of gravity with cold atoms in an optical lattice and comparison with a classical gravimeter. *Phys. Rev. Lett.*, 106:038501, 2011.

[241] A. D. Cronin, J. Schmiedmayer, and D. E. Pritchard. Optics and interferometry with atoms and molecules. *Rev. Mod. Phys.*, 81:1051, 2009.

[242] C. Sabín, D. E. Bruschi, M. Ahmadi, and I. Fuentes. Phonon creation by gravitational waves. *New J. Phys.*, 16(8):085003, 2014.

[243] S. Hofferberth, I. Lesanovsky, T. Schumm, A. Imambekov, V. Gritsev, E. Demler, and J. Schmiedmayer. Probing quantum and thermal noise in an interacting many-body system. *Nat. Phys.*, 4(6):489, 2008.

[244] J. Armijo. Direct observation of quantum phonon fluctuations in a one-dimensional Bose gas. *Phys. Rev. Lett.*, 108:225306, 2012.

[245] S. Hofferberth, I. Lesanovsky, B. Fischer, T. Schumm, and J. Schmiedmayer. Non-equilibrium coherence dynamics in one-dimensional Bose gases. *Nature*, 449(7160):324, 2007.

[246] M. Gring, M. Kuhnert, T. Langen, T. Kitagawa, B. Rauer, M. Schreitl, I. Mazets, D. Adu Smith, E. Demler, and J. Schmiedmayer. Relaxation and prethermalization in an isolated quantum system. *Science*, 337(6100):1318, 2012.

[247] J. Eisert, M. Friesdorf, and C. Gogolin. Quantum many-body systems out of equilibrium. *Nat. Phys.*, 11(2):124, 2015.

[248] J. Choi, S. Hild, J. Zeiher, P. Schauß, A. Rubio-Abadal, T. Yefsah, V. Khemani, D. A. Huse, I. Bloch, and C. Gross. Exploring the many-body localization transition in two dimensions. *Science*, 352(6293):1547, 2016.

[249] R. Gati, J. Esteve, B. Hemmerling, T. B. Ottenstein, J. Appmeier, A. Weller, and M. K. Oberthaler. A primary noise thermometer for ultracold Bose gases. *New J. Phys.*, 8(9):189, 2006.

[250] A. E. Leanhardt, T. A. Pasquini, M. Saba, A. Schirotzek, Y. Shin, D. Kielpinski, D. E. Pritchard, and W. Ketterle. Cooling Bose-Einstein condensates below 500 picokelvin. *Science*, 301(5639):1513, 2003.

[251] J. F. Sherson, C. Weitenberg, M. Endres, M. Cheneau, I. Bloch, and S. Kuhr. Single-atom-resolved fluorescence imaging of an atomic Mott insulator. *Nature*, 467(7311):68, 2010.

[252] R. Olf, F. Fang, G. E. Marti, A. MacRae, and D. M. Stamper-Kurn. Thermometry and cooling of a Bose gas to 0.02 times the condensation temperature. *Nat. Phys.*, 11(9):720, 2015.

[253] J. Sebby-Strabley, M. Anderlini, P. S. Jessen, and J. V. Porto. Lattice of double wells for manipulating pairs of cold atoms. *Phys. Rev. A*, 73:033605, 2006.

[254] J. Sebby-Strabley, B. L. Brown, M. Anderlini, P. J. Lee, W. D. Phillips, J. V. Porto, and P. R. Johnson. Preparing and probing atomic number states with an atom interferometer. *Phys. Rev. Lett.*, 98:200405, 2007.

[255] S. Fölling, S. Trotzky, P. Cheinet, M. Feld, R. Saers, A. Widera, T. Müller, and I. Bloch. Direct observation of second-order atom tunnelling. *Nature*, 448:1029, 2007.

[256] C. J. Pethick and H. Smith. *Bose-Einstein Condensation in Dilute Gases*. Cambridge University Press, Cambridge, 2nd edition, 2008.

[257] A. J. Leggett. Bose-Einstein condensation in the alkali gases: Some fundamental concepts. *Rev. Mod. Phys.*, 73:307, 2001.

[258] L. D. Landau and E. M. Lifschitz. *Quantum Mechanics (Non-Relativistic Theory)*. Butterworth-Heinemann, Oxford, 3rd edition, 2003.

[259] C. Chin, R. Grimm, P. Julienne, and E. Tiesinga. Feshbach resonances in ultracold gases. *Rev. Mod. Phys.*, 82:1225, 2010.

[260] D. A. Russell, J. P. Titlow, and Y.-J. Bemmen. Acoustic monopoles, dipoles, and quadrupoles: An experiment revisited. *Am. J. Phys.*, 67(8):660, 1999.

[261] G. Huber, F. Schmidt-Kaler, S. Deffner, and E. Lutz. Employing trapped cold ions to verify the quantum Jarzynski equality. *Phys. Rev. Lett.*, 101:070403, 2008.

[262] S. An, J.-N. Zhang, M. Um, D. Lv, Y. Lu, J. Zhang, Z.-Q. Yin, H. T. Quan, and K. Kim. Experimental test of the quantum Jarzynski equality with a trapped-ion system. *Nat. Phys.*, 11(2):193, 2015.

[263] D. Jaksch, C. Bruder, J. Cirac, C. Gardiner, and P. Zoller. Cold bosonic atoms in optical lattices. *Phys. Rev. Lett.*, 81(15):3108, 1998.

[264] M. Greiner, O. Mandel, T. Esslinger, T. W. Hänsch, and I. Bloch. Quantum phase transition from a superfluid to a Mott insulator in a gas of ultracold atoms. *Nature*, 415(6867):39, 2002.

[265] D Jaksch, H.-J. Briegel, J I Cirac, C W Gardiner, and P Zoller. Entanglement of atoms via cold controlled collisions. *Phys. Rev. Lett.*, 82(9):1975, 1999.

[266] G. Vidal. Efficient simulation of one-dimensional quantum many-body systems. *Phys. Rev. Lett.*, 93:40502, 2004.

[267] Steven R. White and Adrian E. Feiguin. Real-time evolution using the density matrix renormalization group. *Phys. Rev. Lett.*, 93:076401, 2004.

[268] U. Schöllwock. The density-matrix renormalization group in the age of matrix product states. *Ann. Phys.*, 326(1):96, 2011.

[269] T. H. Johnson, S. R. Clark, and D. Jaksch. Dynamical simulations of classical stochastic systems using matrix product states. *Phys. Rev. E*, 82:036702, 2010.

[270] G. Astrakharchik, R. Combescot, and L. Pitaevskii. Fluctuations of the number of particles within a given volume in cold quantum gases. *Phys. Rev. A*, 76(6):063616, 2007.

[271] S. Tan. Large momentum part of a strongly correlated Fermi gas. *Ann. Phys.*, 323(12):2971, 2008.

[272] S. Tan. Generalized virial theorem and pressure relation for a strongly correlated Fermi gas. *Ann. Phys.*, 323(12):2987, 2008.

[273] S. Tan. Energetics of a strongly correlated Fermi gas. *Ann. Phys.*, 323(12):2952, 2008.

[274] P. Hauke, M. Heyl, L. Tagliacozzo, and P. Zoller. Measuring multipartite entanglement through dynamic susceptibilities. *Nat. Phys.*, 12:778, 2016.

[275] J. Kinast, S. L. Hemmer, M. E. Gehm, A. Turlapov, and J. E. Thomas. Evidence for superfluidity in a resonantly interacting Fermi gas. *Phys. Rev. Lett.*, 92:150402, 2004.

[276] A. Altmeyer, S. Riedl, C. Kohstall, M. J. Wright, R. Geursen, M. Bartenstein, C. Chin, J. Hecker Denschlag, and R. Grimm. Precision measurements of collective oscillations in the BEC-BCS crossover. *Phys. Rev. Lett.*, 98:040401, 2007.

[277] S. Riedl, E. R. Sánchez Guajardo, C. Kohstall, A. Altmeyer, M. J. Wright, J. Hecker Denschlag, R. Grimm, G. M. Bruun, and H. Smith. Collective oscillations of a Fermi gas in the unitarity limit: Temperature effects and the role of pair correlations. *Phys. Rev. A*, 78:053609, 2008.

[278] R. Combescot, S. Giorgini, and S. Stringari. Molecular signatures in the structure factor of an interacting Fermi gas. *Europhys. Lett.*, 75(5):695, 2006.

[279] D. Pines and P. Nozières. *The Theory of Quantum Liquids*. Addison-Wesley, New York, 1989.

[280] J. Stenger, S. Inouye, A. P. Chikkatur, D. M. Stamper-Kurn, D. E. Pritchard, and W. Ketterle. Bragg spectroscopy of a Bose-Einstein condensate. *Phys. Rev. Lett.*, 82:4569, 1999.

[281] D. M. Stamper-Kurn, A. P. Chikkatur, A. Görlitz, S. Inouye, S. Gupta, D. E. Pritchard, and W. Ketterle. Excitation of phonons in a Bose-Einstein condensate by light scattering. *Phys. Rev. Lett.*, 83:2876, 1999.

[282] J. Steinhauer, R. Ozeri, N. Katz, and N. Davidson. Excitation spectrum of a Bose-Einstein condensate. *Phys. Rev. Lett.*, 88:120407, 2002.

[283] L. Han and C. A. R. Sá de Melo. Evolution from Bardeen-Cooper-Schrieffer to Bose-Einstein condensate superfluidity in the presence of disorder. *New J. Phys.*, 13(5):055012, 2011.

[284] Y. Nishida. Polaronic atom-trimer continuity in three-component Fermi gases. *Phys. Rev. Lett.*, 114:115302, 2015.

[285] W. Yi and X. Cui. Polarons in ultracold Fermi superfluids. *Phys. Rev. A*, 92:013620, 2015.

[286] G. Lombardi and J. Tempere. Polaronic effects of an impurity in a Fermi superfluid away from the BEC limit. *arXiv:1604.00776 [quant-ph]*, 2016.

[287] A. J. Leggett. Cooper pairing in spin-polarized Fermi systems. *J. Phys. Coll.*, 41(C7):C7–19, 1980.

[288] P. Nozieres and S. Schmitt-Rink. Bose condensation in an attractive fermion gas: From weak to strong coupling superconductivity. *J. Low Temp. Phys.*, 59:195, 1985.

[289] C. A. R. Sá de Melo, M. Randeria, and J. R. Engelbrecht. Crossover from BCS to Bose superconductivity: Transition temperature and time-dependent Ginzburg-Landau theory. *Phys. Rev. Lett.*, 71:3202, 1993.

[290] J. R. Engelbrecht, M. Randeria, and C. A. R. Sá de Melo. BCS to Bose crossover: Broken-symmetry state. *Phys. Rev. B*, 55:15153, 1997.

[291] S. Giorgini, L. P. Pitaevskii, and S. Stringari. Theory of ultracold atomic Fermi gases. *Rev. Mod. Phys.*, 80:1215, 2008.

[292] H. Bruus and K. Flensberg. *Many-body quantum theory in condensed matter physics*. Oxford University Press, Oxford, 2004.

[293] P. W. Anderson. Random-phase approximation in the theory of superconductivity. *Phys. Rev.*, 112:1900, 1958.

[294] L. D. Landau and E. M. Lifshitz. *Statistical Physics, Part 1*. Butterworth-Heinemann, Oxford, 3rd edition, 2010.

[295] P. W. Anderson. Coherent excited states in the theory of superconductivity: Gauge invariance and the Meissner effect. *Phys. Rev.*, 110:827, 1958.

[296] H. B. Callen and T. A. Welton. Irreversibility and generalized noise. *Phys. Rev.*, 83:34, 1951.

[297] H. Guo, C-C. Chien, Y. He, and K. L. Fundamental constraints on linear response theories of Fermi superfluids above and below T_c. *Int. J. Mod. Phys. B*, 27(16):1330010, 2013.

[298] R. Côté and A. Griffin. Cooper-pair-condensate fluctuations and plasmons in layered superconductors. *Phys. Rev. B*, 48:10404, 1993.

[299] P. Zou, E. D. Kuhnle, C. J. Vale, and H. Hu. Quantitative comparison between theoretical predictions and experimental results for Bragg spectroscopy of a strongly interacting Fermi superfluid. *Phys. Rev. A*, 82:061605, 2010.

[300] A. W. Chin, J. Prior, R. Rosenbach, F. Caycedo-Soler, S. F. Huelga, and M. B. Plenio. The role of non-equilibrium vibrational structures in electronic coherence and recoherence in pigment-protein complexes. *Nat. Phys.*, 9(2):113, 2013.

[301] S. F. Huelga and M. B. Plenio. Vibrations, quanta and biology. *Cont. Phys.*, 54(4):181, 2013.

[302] J. Iles-Smith, N. Lambert, and A. Nazir. Environmental dynamics, correlations, and the emergence of noncanonical equilibrium states in open quantum systems. *Phys. Rev. A*, 90:032114, 2014.

[303] T. D. Lee, Kerson Huang, and C. N. Yang. Eigenvalues and eigenfunctions of a Bose system of hard spheres and its low-temperature properties. *Phys. Rev.*, 106:1135, 1957.

[304] T. J. Elliott and T. H. Johnson. Nondestructive probing of means, variances, and correlations of ultracold-atomic-system densities via qubit impurities. *Phys. Rev. A*, 93:043612, 2016.

[305] S. Fölling, F. Gerbier, A. Widera, O. Mandel, T. Gericke, and I. Bloch. Spatial quantum noise interferometry in expanding ultracold atom clouds. *Nature*, 434(7032):481, 2005.

[306] M. J. Stephen. Transport equations for superconductors. *Phys. Rev.*, 139:A197, 1965.

[307] O. Betbeder-Matibet and P. Nozieres. Transport equations in clean superconductors. *Ann. Phys.*, 51(3):392, 1969.

[308] R. Combescot. Spin waves in superfluid ^{3}He: Collisionless regime. *Phys. Rev. A*, 10:1700, 1974.

[309] L. Jacak. Collective excitations of ^{3}He-B: the method of the kinetic equation. *J. Phys. C*, 10(23):4701, 1977.

[310] R. Combescot. Dispersion relations of the high-frequency modes in ^{3}He-B. *J. Low Temp. Phys.*, 49(3):295, 1982.

[311] P. Wölfle. Attenuation of zero sound in liquid ^{3}He: A probe of superfluid pairing. *Phys. Rev. Lett.*, 30:1169, 1973.

[312] M. Randeria, J.-M. Duan, and L.-Y. Shieh. Superconductivity in a two-dimensional Fermi gas: Evolution from Cooper pairing to Bose condensation. *Phys. Rev. B*, 41:327, 1990.

Appendix A

Phase sensitivity analysis for quantum single-shot cooling

In this appendix, we provide details of the phase sensitivity analysis used in Chapter 3. Specifically, we consider the effect on quantum single-shot cooling of coherence added to the initial quantum state with a small amount of phase noise. In order to gain some analytical insight, we suppose that the dynamics can be treated as approximately unitary over the time scales of interest. This is a decent approximation in the strong-coupling limit, where g is much larger than the relaxation rate.

We define the populations $a(t) = \langle 001| \rho_A(t) |001\rangle$ and $b(t) = \langle 110| \rho_A(t) |110\rangle$, and the coherence $\mathcal{C}(t) = \langle 110| \rho_A(t) |001\rangle$, where $\rho_A(t)$ denotes the reduced quantum state of the refrigerator qubits. We also introduce the convenient parametrisations $S = [a(0) + b(0)]/2$, $D = [b(0) - a(0)]/2$ and $\mathcal{C}(0) = \mathrm{i}r\mathrm{e}^{\mathrm{i}\phi}$, where $r > 0$ is the magnitude and ϕ is the phase. The refrigeration condition $T_v < T_1$, where T_v is the virtual temperature (3.23) and T_1 is the initial temperature of the target qubit, implies that $D > 0$.

At short times, the effect of dissipation can be approximately neglected, and the evolution of the populations $a(t)$ and $b(t)$ is analogous to that of a resonantly driven two-level system. In this approximation, the populations at time t are given by

$$a(t) = S - D\cos(2gt) + r\cos(\phi)\sin(2gt), \tag{A.1}$$

and $b(t) = 2S - a(t)$. The population difference of the target qubit is given by

$$\langle \sigma_1^z(t) \rangle = \langle \sigma_1^z(0) \rangle + 2\left[a(0) - a(t)\right], \tag{A.2}$$

which is related to the effective temperature by Eq. (3.23). From this we find that the first temperature minimum occurs at time

$$t_{\min}(\phi) = \frac{1}{2g}\left(\pi - \tan^{-1}\left[\frac{r\cos(\phi)}{D}\right]\right), \tag{A.3}$$

with the populations at that time given by

$$a(t_{\min}) = S + \sqrt{D^2 + r^2\cos^2(\phi)}. \tag{A.4}$$

The amplitude of the population oscillations is therefore maximised by choosing $\phi = 0$, i.e. a purely imaginary initial coherence, as expected from Eq. (3.24). With the choice of $\phi = 0$, the optimal time to extract the target qubit is given by $t_{\rm opt} = t_{\rm min}(0)$.

We now suppose that each qubit entering the refrigerator is prepared with a random phase ϕ of the coherence in the transport subspace, due to experimental noise, for example. These phase shifts are described by some probability distribution function $p(\phi)$. In order to find the dynamics of the resulting ensemble of target qubits, we average Eq. (A.1) over the distribution $p(\phi)$. This procedure leads to the replacement of $\cos(\phi)$ in all expressions by

$$\overline{\cos(\phi)} = \int_{-\pi}^{\pi} \mathrm{d}\phi \, p(\phi) \cos(\phi). \tag{A.5}$$

As a simple but broadly relevant example, we assume that phase shift has zero mean $\overline{\phi} = 0$, and that its variance $\overline{\phi^2}$ is smaller than unity. We also suppose that its cumulants are rapidly decreasing, so that $p(\phi)$ may be approximated by a Gaussian distribution. Under these assumptions, we obtain

$$\overline{\cos(\phi)} = \mathrm{e}^{-\overline{\phi^2}/2}. \tag{A.6}$$

We find from Eq. (A.3) that the minimum temperature of the ensemble occurs at time

$$t'_{\rm opt} = \frac{1}{2g}\left(\pi - \tan^{-1}\left[\frac{r\mathrm{e}^{-\overline{\phi^2}/2}}{D}\right]\right), \tag{A.7}$$

so that $t'_{\rm opt} > t_{\rm opt}$ in this approximation. In the following, primed variables indicate quantities in the presence of noise, while the unprimed variables denote the corresponding quantities in the absence of noise.

In order to find the shift in the ensemble temperature due to the phase noise, we consider two distinct scenarios. In the first scenario, we assume that some information about the phase distribution is known, so that it is possible to predict in advance the optimal time $t'_{\rm opt}$ to extract the qubit. This information could be obtained by expending some qubits in order to characterise the noisy preparation by quantum state tomography. In this case, the phase noise leads to a change in the population difference of the target qubit given by

$$\begin{aligned}
\Delta\langle\sigma_1^z\rangle &= \langle\sigma_1^z(t'_{\rm opt})\rangle' - \langle\sigma_1^z(t_{\rm opt})\rangle \\
&= 2\sqrt{D^2 + r^2} - 2\sqrt{D^2 + r^2\mathrm{e}^{-\overline{\phi^2}}} \\
&\approx \frac{r^2}{\sqrt{D^2 + r^2}}\left(1 - \mathrm{e}^{-\overline{\phi^2}}\right).
\end{aligned} \tag{A.8}$$

In the second scenario, we assume that no information about the phase noise distri-

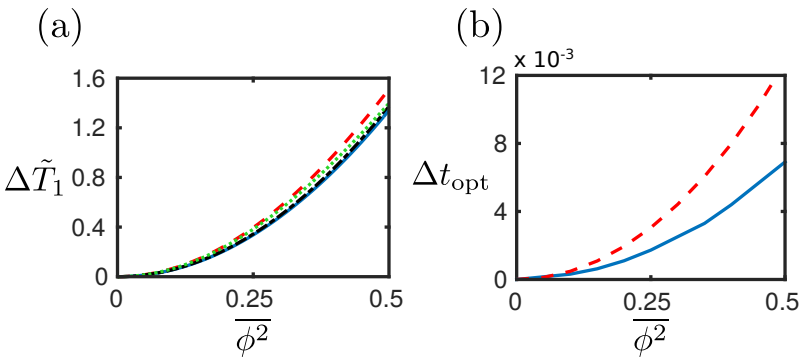


Figure A.1. Comparison of exact numerical and approximate analytical results for the effect of Gaussian zero-mean phase noise characterised by its variance $\overline{\phi^2}$. The same parameters are used as in Figure 3.2(a), with 5% of the maximum initial coherence. (a) Shift in the target qubit temperature when extracted: numerical (blue solid line) and analytical (red dashed line) results when the phase noise distribution is not known, numerical (black dot-dashed) and analytical (green dotted line) results when the phase noise distribution is known. (b) Shift in the time of the temperature minimum $\Delta t_{\rm opt} = t'_{\rm opt} - t_{\rm opt}$: numerical (blue solid line) and analytical (red dashed line) results.

bution is known, so that the experimenter extracts the target qubit at the incorrect time $t_{\rm opt}$. For example, this scenario applies if only a single qubit is available for cooling, so that the noisy preparation cannot be characterised in advance. In this case, phase noise changes the population difference by the amount

$$\begin{aligned}\Delta\langle\sigma_1^z\rangle &= \langle\sigma_1^z(t_{\rm opt})\rangle' - \langle\sigma_1^z(t_{\rm opt})\rangle \\ &= \frac{2r^2}{\sqrt{D^2+r^2}}\left(1-\mathrm{e}^{-\overline{\phi^2}/2}\right). \end{aligned} \tag{A.9}$$

Note that it is also possible to consider the case where only partial information about the noise distribution is known, in which case we expect $\Delta\langle\sigma_1^z\rangle$ to lie somewhere between Eqs. (A.8) and (A.9).

In any case, assuming that the effect of phase noise is small, we find that the expected shift in the ensemble temperature to lowest order in $\Delta\langle\sigma_1^z\rangle$ is

$$\Delta\tilde{T}_1 = \frac{2\tilde{T}_1^2}{E_1}\cosh^2\left(\frac{E_1}{2\tilde{T}_1}\right)\Delta\langle\sigma_1^z\rangle, \tag{A.10}$$

where $\tilde{T}_1$ denotes the optimal temperature in the absence of phase noise. This equation indicates that the effect of phase fluctuations is minimised when $\tilde{T}_1 \sim E_1$, while the most drastic effects occur for very large or very small target temperatures. In particular, the right-hand side of Eq. (A.10) diverges as $\tilde{T}_1 \to 0$, which indicates that even vanishingly small fluctuations in the initial coherence phase may prevent one from using this coherence to cool the target qubit to its ground state.

In Figure A.1(a) we numerically calculate and plot an example of the change in the final temperature of the target qubit when it is disconnected from the machine, either with or without sufficient knowledge of the phase noise distribution to predict the optimal extraction time. We see that in fact it makes little difference to the temperature whether or not the optimal extraction time is known precisely, since the shift in this time due to phase noise is rather small (Figure A.1(b)). Our approximate analytical results are also shown in Figure A.1 for comparison.

Appendix B

Stochastic absorption refrigerator model

In this appendix, we derive an effective stochastic model of the quantum absorption refrigerator in the deep weak-coupling limit. Our analysis follows Ref. [166], and rests on the assumption that the characteristic dephasing rate Γ due to the action of the thermal baths is much larger than the coherent coupling g between the qubits.

Working in the weak-coupling limit, we begin with the master equation (3.15) written as

$$\frac{\mathrm{d}\rho_A}{\mathrm{d}t} = \mathcal{L}\rho_A, \tag{B.1}$$

and decompose the Liouvillian as $\mathcal{L} = \mathcal{L}_0 + \mathcal{V}$, where $\mathcal{V}\rho = \mathrm{i}[\rho, V]$. The quantum state can be expanded in the eigenbasis of $\mathcal{L}$ as

$$\rho_A(t) = \sum_\lambda \mathrm{e}^{\lambda t}\rho_A^{(\lambda)}, \tag{B.2}$$

where $\rho_A^{(\lambda)}$ is a right eigenvector of $\mathcal{L}$ with complex eigenvalue λ. Since $\mathrm{Re}(\lambda) \leq 0$, we see that only the eigenvalues with the largest real part are relevant as $t \to \infty$. In this basis the master equation reduces to the eigenvalue equation

$$(\mathcal{L}_0 + \mathcal{V})\,\rho_A^{(\lambda)} = \lambda\rho_A^{(\lambda)}. \tag{B.3}$$

The eigenvalues of $\mathcal{L}_0$ are of order Γ, while the eigenvalues of $\mathcal{V}$ are of order g. In the limit $g \ll \Gamma$, the effect of $\mathcal{V}$ may be incorporated using second-order perturbation theory.

To that end, we introduce a projector $\mathcal{P}$ onto the space of populations (diagonal matrix elements), defined by

$$\mathcal{P}\rho = \sum_{n=0}^{7} \langle n|\,\rho\,|n\rangle\,|n\rangle\langle n|\,, \tag{B.4}$$

where $|n\rangle$ denotes a computational basis state in binary representation, e.g. $|2\rangle = |010\rangle$. We also define the orthogonal projector $\mathcal{Q} = 1 - \mathcal{P}$, which projects onto the space of coherences (off-diagonal matrix elements). We refer to the spaces of populations and coherences as the $\mathcal{P}$-space and the $\mathcal{Q}$-space, respectively. It is readily verified that the following properties

hold:

$$\mathcal{P}\mathcal{V}\mathcal{P} = 0, \tag{B.5}$$

$$[\mathcal{P}, \mathcal{L}_0] = [\mathcal{Q}, \mathcal{L}_0] = 0. \tag{B.6}$$

Eq. (B.5) states that the interaction $\mathcal{V}$ only couples populations to coherences, while Eq. (B.6) reflects the fact that the local Liouvillian $\mathcal{L}_0$ does not couple populations and coherences, i.e. it is block-diagonal.

By introducing the identity $1 = \mathcal{Q} + \mathcal{P}$ into both sides of the eigenvalue equation (B.3), we obtain

$$\lambda\mathcal{P}\rho_A^{(\lambda)} = \mathcal{L}_0\mathcal{P}\rho_A^{(\lambda)} + \mathcal{P}\mathcal{V}\mathcal{Q}\rho_A^{(\lambda)}, \tag{B.7}$$

$$\lambda\mathcal{Q}\rho_A^{(\lambda)} = \mathcal{L}_0\mathcal{Q}\rho_A^{(\lambda)} + \mathcal{Q}\mathcal{V}\mathcal{Q}\rho_A^{(\lambda)} + \mathcal{V}\mathcal{P}\rho_A^{(\lambda)}, \tag{B.8}$$

where Eqs. (B.5) and (B.6) have been used. We now solve Eq. (B.8) for $\mathcal{Q}\rho_A^{(\lambda)}$ and substitute the result back into Eq. (B.7), finding

$$\lambda\mathcal{P}\rho_A^{(\lambda)} = \mathcal{L}_0\mathcal{P}\rho_A^{(\lambda)} + \mathcal{P}\mathcal{V}\left(\lambda - \mathcal{Q}\mathcal{V} - \mathcal{L}_0\right)^{-1}\mathcal{V}\mathcal{P}\rho_A^{(\lambda)}. \tag{B.9}$$

Since we are looking for eigenvalues λ which are small in magnitude, we may neglect the term $\lambda - \mathcal{Q}\mathcal{V}$, which is of order g, in comparison to $\mathcal{L}_0$, which is of order Γ. Hence we obtain the approximate eigenvalue equation

$$\lambda\mathcal{P}\rho_A^{(\lambda)} = \mathcal{L}_{\text{eff}}\mathcal{P}\rho_A^{(\lambda)}, \tag{B.10}$$

where

$$\mathcal{L}_{\text{eff}} = \mathcal{L}_0 - \mathcal{P}\mathcal{V}\mathcal{L}_0^{-1}\mathcal{V}\mathcal{P}. \tag{B.11}$$

As $t \to \infty$, the master equation (B.1) can therefore be approximated in the $\mathcal{P}$-space by

$$\frac{\mathrm{d}\rho_A}{\mathrm{d}t} = \mathcal{L}_{\text{eff}}\rho_A. \tag{B.12}$$

Note that $\mathcal{L}_{\text{eff}}$ is well defined by Eq. (B.11) despite the fact that the unperturbed Liouvillian possesses a zero eigenvector: the steady-state solution ρ_∞ satisfying $\mathcal{L}_0\rho_\infty = 0$. This is because the unique steady-state solution lies in the $\mathcal{P}$-space, i.e. $\rho_\infty = \mathcal{P}\rho_\infty$. Furthermore, one can write $\mathcal{V}\mathcal{P} = \mathcal{Q}\mathcal{V}\mathcal{P}$ by virtue of Eq. (B.5). Therefore, the operator $\mathcal{L}_0^{-1}$ acts only in the $\mathcal{Q}$-space, where all eigenvalues of $\mathcal{L}_0$ are nonzero.

In order to calculate $\mathcal{L}_{\text{eff}}$ explicitly, we note that $\mathcal{V}$ annihilates all populations apart from $|001\rangle\langle 001|$ and $|110\rangle\langle 110|$. The action of $\mathcal{L}_{\text{eff}}$ can therefore be found from its action

on these two populations. We also make use of the fact that

$$\begin{aligned}\mathcal{L}_0 \left|001\right\rangle\!\left\langle 110\right| &= -\Gamma \left|001\right\rangle\!\left\langle 110\right|, \\ \mathcal{L}_0 \left|110\right\rangle\!\left\langle 001\right| &= -\Gamma \left|110\right\rangle\!\left\langle 001\right|,\end{aligned} \tag{B.13}$$

with

$$\Gamma = \frac{1}{2}\sum_{i=1}^{3}\left[\gamma_i(E_i) + \gamma_i(-E_i)\right], \tag{B.14}$$

where $\gamma_i(\nu)$ is defined above Eq. (3.14). Using these properties, a straightforward calculation yields the result

$$\mathcal{L}_{\text{eff}} = \mathcal{L}_0 + \frac{2g^2}{\Gamma}\mathcal{D}[B] + \frac{2g^2}{\Gamma}\mathcal{D}[B^\dagger], \tag{B.15}$$

where $B = \left|001\right\rangle\!\left\langle 110\right|$. This effective Liouvillian describes transport as a stochastic process, which transfers population symmetrically between the states $|001\rangle$ and $|110\rangle$ spanning the transport subspace at a rate $2g^2/\Gamma$.

Appendix C

Dynamic structure factor in BCS theory

In this appendix, we derive the dynamic structure factor (DSF) for Chapter 5 using a collisionless kinetic equation. This method has been previously used by a number of authors in the context of Bardeen-Cooper-Schrieffer (BCS) theory, for example to study quasiparticle transport [306,307], and the dispersion relations [308–310] and damping rates [311] of collective modes. We follow in particular the presentation of Refs. [123,310].

C.1 Static BCS framework

We first briefly review the static BCS framework. Starting with the bare Hamiltonian (5.1), the standard BCS Hamiltonian is obtained by neglecting fluctuations of the pair field $\Psi_\downarrow(\mathbf{r})\Psi_\uparrow(\mathbf{r})$ around its mean value $\Delta(\mathbf{r})/g$ given by Eq. (5.2). Taking into account the spatial constancy of $\Delta(\mathbf{r})$ at equilibrium, we find that

$$H_{\rm BCS} = \sum_{\mathbf{k}} \sum_{\lambda,\mu=1,2} c^\dagger_{\mathbf{k}\lambda} [h_{\mathbf{k}}]_{\lambda\mu} c_{\mathbf{k}\mu}, \tag{C.1}$$

where the fermion operators in the Nambu representation are $c_{\mathbf{k}1} = c_{\mathbf{k}\uparrow}$ and $c_{\mathbf{k}2} = c^\dagger_{-\mathbf{k}\downarrow}$, while $[h_{\mathbf{k}}]_{\lambda\mu}$ are the elements of the matrix

$$h_{\mathbf{k}} = \begin{pmatrix} \xi_{\mathbf{k}} & \Delta \\ \Delta & -\xi_{\mathbf{k}} \end{pmatrix}, \tag{C.2}$$

and we have neglected an overall energy shift.

The BCS Hamiltonian is diagonalised by the well-known Bogoliubov-Valatin transformation

$$U_{\mathbf{k}} = \begin{pmatrix} u_{\mathbf{k}} & v_{\mathbf{k}} \\ -v_{\mathbf{k}} & u_{\mathbf{k}} \end{pmatrix}, \tag{C.3}$$

where $u^2_{\mathbf{k}} = 1 - v^2_{\mathbf{k}} = 1/2 + \xi_{\mathbf{k}}/2E_{\mathbf{k}}$. After diagonalisation, the BCS Hamiltonian describes free fermionic modes with dispersion relation $E_{\mathbf{k}} = \sqrt{\Delta^2 + \xi^2_{\mathbf{k}}}$. At finite temperature $T = 1/\beta$, these quasiparticle modes are occupied according to the Fermi-Dirac distribution $f_{\mathbf{k}} = (\mathrm{e}^{\beta E_{\mathbf{k}}} + 1)^{-1}$. Self-consistency of the order parameter definition (5.2) leads to the

bare gap equation

$$-1 = \frac{g}{V}\sum_{\mathbf{k}} \frac{\tanh(\beta E_{\mathbf{k}}/2)}{2E_{\mathbf{k}}}. \tag{C.4}$$

The UV divergence in the gap equation is remedied by expressing the bare coupling constant g in terms of the physical scattering length using the relation [289, 312]

$$\frac{m}{4\pi a_s} = -g^{-1} + \frac{1}{V}\sum_{\mathbf{k}} \frac{1}{2\varepsilon_{\mathbf{k}}}, \tag{C.5}$$

resulting in the renormalised gap equation

$$\frac{m}{4\pi a_s} = \frac{1}{2}\sum_{\mathbf{k}} \left(\frac{1}{\varepsilon_{\mathbf{k}}} - \frac{\tanh(\beta E_{\mathbf{k}}/2)}{E_{\mathbf{k}}} \right). \tag{C.6}$$

The constraint of fixed density leads to the condition

$$\varrho_0 = \frac{1}{V}\sum_{\mathbf{k}} \left(1 - \tanh(\beta E_{\mathbf{k}}/2)\frac{\xi_{\mathbf{k}}}{E_{\mathbf{k}}} \right). \tag{C.7}$$

Eqs. (C.6) and (C.7) reduce to Eqs. (5.5) and (5.6) in the limit $T \ll \Theta_0$, so that $\tanh(\beta E_{\mathbf{k}}/2) \approx 1$.

C.2 Derivation of the susceptibility

In order to account properly for the collective mode, we derive the response of the gas to a perturbing classical field $\delta U(\mathbf{r}, t)$, which couples to the density via the Hamiltonian

$$\delta H_{\mathrm{BCS}}(t) = \int \mathrm{d}^3\mathbf{r} \, \left[\delta U(\mathbf{r}, t)\varrho(\mathbf{r}) + \delta\Delta(\mathbf{r}, t)\Psi^\dagger_\uparrow(\mathbf{r})\Psi^\dagger_\downarrow(\mathbf{r}) + \delta\Delta^*(\mathbf{r}, t)\Psi_\downarrow(\mathbf{r})\Psi_\uparrow(\mathbf{r}) \right]. \tag{C.8}$$

Self-consistency requires that we include a contribution $\delta\Delta(\mathbf{r}, t)$ coupled to the pair field $\Psi^\dagger_\uparrow(\mathbf{r})\Psi^\dagger_\downarrow(\mathbf{r})$ in the same way as $\Delta(\mathbf{r})$. This accounts for perturbations of the order parameter due to changes in the local density induced by the external field. We now introduce the Fourier transforms

$$\begin{aligned} \delta U(\mathbf{q}, \nu) &= \int \mathrm{d}^3\mathbf{r} \int \mathrm{d}t \, \mathrm{e}^{\mathrm{i}(\nu t - \mathbf{q}\cdot\mathbf{r})}\delta U(\mathbf{r}, t), \\ \delta\Delta(\mathbf{q}, \nu) &= \int \mathrm{d}^3\mathbf{r} \int \mathrm{d}t \, \mathrm{e}^{\mathrm{i}(\nu t - \mathbf{q}\cdot\mathbf{r})}\delta\Delta(\mathbf{r}, t). \end{aligned} \tag{C.9}$$

Each Fourier component of Eq. (C.8) contributes a term of the form

$$\sum_{\mathbf{k}\lambda\mu} c^\dagger_{\mathbf{k}+\mathbf{q}/2\lambda}[\delta h]_{\lambda\mu} c_{\mathbf{k}-\mathbf{q}/2\mu}, \tag{C.10}$$

with

$$\delta h = \begin{pmatrix} \delta U & \delta\Delta \\ \delta\Delta^* & -\delta U \end{pmatrix}, \tag{C.11}$$

where the functional frequency-momentum dependence of $\delta U(\mathbf{q},\nu)$ and $\delta\Delta(\mathbf{q},\nu)$ has been suppressed for simplicity.

The induced change in the density due to the perturbation (C.8) is given in the linear-response approximation by

$$\langle \varrho_{\mathbf{q}}(t)\rangle = \frac{1}{2\pi}\int_{-\infty}^{\infty} \mathrm{d}\nu\ \mathrm{e}^{-\mathrm{i}\nu t}\chi(\mathbf{q},\nu)\delta U(\mathbf{q},\nu), \tag{C.12}$$

which defines the linear dynamical susceptibility or response function $\chi(\mathbf{q},\nu)$. The causal response of the system is determined by $\chi(\mathbf{q},\nu+\mathrm{i}\epsilon)$, where ϵ is a positive infinitesimal, corresponding to the perturbation (C.8) being adiabatically switched on in the distant past [279]. The dynamic structure factor is then found from the imaginary part of $\chi(\mathbf{q},\nu+\mathrm{i}\epsilon)$ using Eq. (5.21).

In order to compute $\chi(\mathbf{q},\nu)$ we use a kinetic equation for the single-particle reduced density matrix (RDM) $R_{\mathbf{k}\mathbf{k}'}$, with elements

$$[R_{\mathbf{k}\mathbf{k}'}]_{\lambda\mu} = \langle c^\dagger_{\mathbf{k}\lambda} c_{\mathbf{k}'\mu}\rangle. \tag{C.13}$$

The equation of motion for $R_{\mathbf{k}\mathbf{k}'}$ is found using the Heisenberg equation generated by $H_{\mathrm{BCS}}+\delta H_{\mathrm{BCS}}$ and the anticommutation relations $\{c_{\mathbf{k}\lambda}, c^\dagger_{\mathbf{k}'\mu}\} = \delta_{\mathbf{k}\mathbf{k}'}\delta_{\lambda\mu}$. We may write $R_{\mathbf{k}\mathbf{k}'} = R^0_{\mathbf{k}}\delta_{\mathbf{k}\mathbf{k}'} + \delta R_{\mathbf{k}\mathbf{k}'}$, where $\delta R_{\mathbf{k}\mathbf{k}'}$ is a small deviation from the equilibrium RDM given by

$$R^0_{\mathbf{k}} = \frac{1}{2}\left(\mathbb{1} - \frac{\tanh(\beta E_{\mathbf{k}}/2)}{E_{\mathbf{k}}} h_{\mathbf{k}}\right). \tag{C.14}$$

After linearising the equation of motion and neglecting the transient solutions, we find that each Fourier component of the perturbation leads to a fluctuating part of the RDM with the same frequency and wave vector, i.e. $\delta R_{\mathbf{k}\mathbf{k}'} \propto \delta_{\mathbf{k}+\mathbf{q},\mathbf{k}'}\mathrm{e}^{-\mathrm{i}\nu t}$. Each Fourier component may therefore be treated separately. Using the parametrisation $R_{\mathbf{k}-\mathbf{q}/2,\mathbf{k}+\mathbf{q}/2}(t) = \delta R_{\mathbf{k}}\mathrm{e}^{-\mathrm{i}\nu t}$, we obtain the linearised kinetic equation

$$\nu\delta R_{\mathbf{k}} = \delta R_{\mathbf{k}} h^T_{\mathbf{k}+\mathbf{q}/2} - h^T_{\mathbf{k}-\mathbf{q}/2}\delta R_{\mathbf{k}} + R^0_{\mathbf{k}-\mathbf{q}/2}\delta h^T - \delta h^T R^0_{\mathbf{k}+\mathbf{q}/2}, \tag{C.15}$$

where the superscript T denotes the matrix transpose in the Nambu spinor space.

It is convenient to first multiply Eq. (C.15) on the left and right by $U_{\mathbf{k}-\mathbf{q}/2}$ and $U^\dagger_{\mathbf{k}+\mathbf{q}/2}$ respectively, which diagonalises $h_{\mathbf{k}}$ and $R^0_{\mathbf{k}}$. The kinetic equation is then straightforward to solve for $\delta R_{\mathbf{k}}$ in terms of δh. After some tedious algebra, we obtain (c.f. Eqs. (15) and

(16) of Ref. [310])

$$\begin{aligned}[\delta R_{\mathbf{k}}(\mathbf{q},\nu)]_{11} = \frac{1-f'-f}{(E'+E)^2-\nu^2}\Big\{&-\delta U\left[(E'+E)(u'v+uv')^2+\nu(u'^2v^2-u^2v'^2)\right]\\ &+\delta\Delta\left[(E'+E)uv(u'^2-v'^2)+\nu uv\right]+\delta\Delta^*\left[(E'+E)u'v'(u^2-v^2)-\nu u'v'\right]\Big\}\\ &+\frac{f'-f}{(E'-E)^2-\nu^2}\Big\{\delta U\left[(E'-E)(u'u-v'v)^2+\nu(u'^2u^2-v'^2v^2)\right]\\ &+\delta\Delta\left[(E'-E)uv(u'^2-v'^2)+\nu uv\right]+\delta\Delta^*\left[(E'-E)u'v'(u^2-v^2)+\nu u'v'\right]\Big\},\end{aligned} \tag{C.16}$$

$$\begin{aligned}[\delta R_{\mathbf{k}}(\mathbf{q},\nu)]_{12} = \frac{1-f'-f}{(E'+E)^2-\nu^2}\Big\{&\delta U(u'v+uv')\left[(E'+E)(u'u-v'v)-\nu(u'u+v'v)\right]\\ &+2\delta\Delta u'v'uv(E'+E)-\delta\Delta^*\left[(E'+E)(u'^2u^2+v'^2v^2)-\nu(u'^2u^2-v'^2v^2)\right]\Big\}\\ &+\frac{f'-f}{(E'-E)^2-\nu^2}\Big\{\delta U(u'u-v'v)\left[(E'-E)(u'v+uv')-\nu(u'v-uv')\right]\\ &+2\delta\Delta u'v'uv(E'-E)+\delta\Delta^*\left[(E'-E)(u'^2v^2+u^2v'^2)-\nu(u'^2v^2-u^2v'^2)\right]\Big\},\end{aligned} \tag{C.17}$$

while $[\delta R_{\mathbf{k}}(\mathbf{q},\nu)]_{22} = -[\delta R_{\mathbf{k}}(\mathbf{q},-\nu)]^*_{11}$ and $[\delta R_{\mathbf{k}}(\mathbf{q},\nu)]_{21} = [\delta R_{\mathbf{k}}(\mathbf{q},-\nu)]^*_{12}$.

The order parameter is related via Eq. (5.2) to the RDM, which implies the self-consistency condition

$$\delta\Delta = \frac{g}{V}\sum_{\mathbf{k}}\langle c_{-\mathbf{k}+\mathbf{q}/2\downarrow}c_{\mathbf{k}+\mathbf{q}/2\uparrow}\rangle. \tag{C.18}$$

The interaction strength g can be eliminated using the bare gap equation (C.4) to yield

$$\sum_{\mathbf{k}}\left([\delta R_{\mathbf{k}}]_{21}+\frac{\tanh(\beta E_{\mathbf{k}}/2)}{2E_{\mathbf{k}}}\delta\Delta\right)=\sum_{\mathbf{k}}\left([\delta R_{\mathbf{k}}]_{12}+\frac{\tanh(\beta E_{\mathbf{k}}/2)}{2E_{\mathbf{k}}}\delta\Delta^*\right)=0. \tag{C.19}$$

These relations close the set of equations, which can then be solved for the susceptibility using Eq. (C.12), which corresponds to

$$\frac{1}{V}\sum_{\mathbf{k}}2[\delta R_{\mathbf{k}}(\mathbf{q},\nu)]_{11} = \chi(\mathbf{q},\nu)\delta U(\mathbf{q},\nu). \tag{C.20}$$

In order to present the result compactly, we use a shorthand notation where unprimed variables carry the subscript $\mathbf{k}-\mathbf{q}/2$, while primed variables carry the subscript $\mathbf{k}+\mathbf{q}/2$, e.g. $E = E_{\mathbf{k}-\mathbf{q}/2}$ and $E' = E_{\mathbf{k}+\mathbf{q}/2}$. The response function then takes the form $\chi(\mathbf{q},\nu) =$

$\chi_{\text{pair}}(\mathbf{q},\nu)+\chi_{\text{coll}}(\mathbf{q},\nu)$, where the pair contribution reads as

$$\chi_{\text{pair}}(\mathbf{q},\nu)=-\frac{1}{V}\sum_{\mathbf{k}}\left\{\frac{(1-f-f')(E+E')}{(E+E')^2-\nu^2}\frac{EE'-\xi\xi'+\Delta^2}{EE'}\right.$$
$$\left.-\frac{(f-f')(E-E')}{(E-E')^2-\nu^2}\frac{EE'+\xi\xi'-\Delta^2}{EE'}\right\}. \tag{C.21}$$

The collective mode contribution is given by

$$\chi_{\text{coll}}(\mathbf{q},\nu)=\Delta^2\frac{A_1^2I_{11}+\nu^2A_2^2I_{22}-2\nu^2A_1A_2I_{12}}{I_{11}I_{22}-\nu^2I_{12}^2}, \tag{C.22}$$

where we defined

$$A_1(\mathbf{q},\nu)=\frac{1}{V}\sum_{\mathbf{k}}\left\{\frac{(1-f-f')(E+E')}{(E+E')^2-\nu^2}\frac{\xi+\xi'}{EE'}+\frac{(f-f')(E-E')}{(E-E')^2-\nu^2}\frac{\xi+\xi'}{EE'}\right\}, \tag{C.23}$$

$$A_2(\mathbf{q},\nu)=\frac{1}{V}\sum_{\mathbf{k}}\left\{\frac{(1-f-f')(E+E')}{(E+E')^2-\nu^2}\frac{1}{EE'}+\frac{(f-f')(E-E')}{(E-E')^2-\nu^2}\frac{1}{EE'}\right\}, \tag{C.24}$$

$$I_{11}(\mathbf{q},\nu)=\frac{1}{V}\sum_{\mathbf{k}}\left\{\frac{(1-f-f')(E+E')}{(E+E')^2-\nu^2}\frac{EE'+\xi\xi'+\Delta^2}{EE'}\right.$$
$$\left.-\frac{(f-f')(E-E')}{(E-E')^2-\nu^2}\frac{EE'-\xi\xi'-\Delta^2}{EE'}-\frac{1-2f_{\mathbf{k}}}{E_{\mathbf{k}}}\right\}, \tag{C.25}$$

$$I_{22}(\mathbf{q},\nu)=\frac{1}{V}\sum_{\mathbf{k}}\left\{\frac{(1-f-f')(E+E')}{(E+E')^2-\nu^2}\frac{EE'+\xi\xi'-\Delta^2}{EE'}\right.$$
$$\left.-\frac{(f-f')(E-E')}{(E-E')^2-\nu^2}\frac{EE'-\xi\xi'+\Delta^2}{EE'}-\frac{1-2f_{\mathbf{k}}}{E_{\mathbf{k}}}\right\}, \tag{C.26}$$

$$I_{12}(\mathbf{q},\nu)=\frac{1}{V}\sum_{\mathbf{k}}\left\{\frac{1-f-f'}{(E+E')^2-\nu^2}\frac{E\xi'+E'\xi}{EE'}+\frac{f-f'}{(E-E')^2-\nu^2}\frac{E\xi'-E'\xi}{EE'}\right\}. \tag{C.27}$$

C.3 Dynamic structure factor

In Eqs. (C.21)–(C.27) we see two kinds of terms: the Beliaev contributions having poles at frequencies $\nu=\pm(E_{\mathbf{k}+\mathbf{q}/2}+E_{\mathbf{k}-\mathbf{q}/2})$ and the Landau contributions with poles at $\nu=\pm(E_{\mathbf{k}+\mathbf{q}/2}-E_{\mathbf{k}-\mathbf{q}/2})$. These describe processes of the type depicted in Figs. 5.3(a) and (b), respectively. From here on, we specialise to temperatures $T\ll\Theta_0$, so that the Fermi factors in Eqs. (C.21)–(C.27) can be set to zero. In particular, this means that all Landau contributions vanish.

For frequencies $\nu<\Theta_0$, the imaginary parts of the Beliaev terms appearing in the integrals (C.21) and (C.23)–(C.26) are zero. Therefore, the only contribution to the DSF comes from the pole of Eq. (C.22) corresponding to the collective mode resonance. To see

this, we write

$$\chi_{\text{coll}}(\mathbf{q},\nu) = \frac{B(\mathbf{q},\nu)}{\nu^2 - \Omega^2(\mathbf{q},\nu)}, \tag{C.28}$$

where

$$B(\mathbf{q},\nu) = -\Delta^2 \frac{A_1^2 I_{11} + \nu^2 A_2^2 I_{22} - 2\nu^2 A_1 A_2 I_{12}}{I_{12}^2}, \tag{C.29}$$

$$\Omega(\mathbf{q},\nu) = \frac{\sqrt{I_{11} I_{22}}}{I_{12}}. \tag{C.30}$$

The dispersion relation of the collective mode is given by the solution of the nonlinear equation $\omega_{\mathbf{q}} = \Omega(\mathbf{q},\omega_{\mathbf{q}})$. The imaginary part of the susceptibility is found to be

$$\text{Im}\left[\chi_{\text{coll}}(\mathbf{q},\nu+\text{i}\epsilon)\right] = \pi M_{\mathbf{q}} \left[\delta(\nu+\omega_{\mathbf{q}}) - \delta(\nu-\omega_{\mathbf{q}})\right], \tag{C.31}$$

where the spectral weight is defined as

$$M_{\mathbf{q}} = \frac{B(\mathbf{q},\omega_{\mathbf{q}})}{2\omega_{\mathbf{q}}} \left| 1 - \frac{\text{d}\Omega(\mathbf{q},\nu)}{\text{d}\nu} \right|^{-1}_{\nu=\omega_{\mathbf{q}}}. \tag{C.32}$$

Using Eq. (5.21), we finally obtain the DSF

$$S(\mathbf{q},\nu) = M_{\mathbf{q}} \left[(1+n_{\mathbf{q}})\delta(\nu-\omega_{\mathbf{q}}) + n_{\mathbf{q}}\delta(\nu+\omega_{\mathbf{q}})\right], \tag{C.33}$$

valid for $\nu < \Theta_0$, where $n_{\mathbf{q}} = (\text{e}^{\beta\omega_{\mathbf{q}}} - 1)^{-1}$ is the Bose-Einstein distribution. Eq. (C.33) reduces to Eq. (5.28) in the limit $T \ll \nu$.

Note that the DSF at $T = 0$ can be derived from Eq. (C.28) in the alternative form

$$S(\mathbf{q},\nu) = C_\nu \delta(q - q_\nu), \tag{C.34}$$

where q_ν is the magnitude of a wave vector $\mathbf{q}_\nu$ such that $\omega_{\mathbf{q}_\nu} = \nu$, while we defined

$$C_\nu = \frac{B(\mathbf{q}_\nu,\nu)}{2\nu} \left| \frac{\text{d}\Omega(\mathbf{q},\nu)}{\text{d}\nu} \right|^{-1}_{q=q_\nu}. \tag{C.35}$$

However, Eq. (C.34) can also be obtained directly from Eq. (C.33) by a simple change of variables in the delta function, from which it follows that

$$M_{\mathbf{q}_\nu} D_{\text{ph}}(\nu) = \frac{q_\nu^2}{2\pi^2} C_\nu, \tag{C.36}$$

where $D_{\text{ph}}(\nu)$ is the phonon density of states defined in Eq. (5.30). Eqs. (C.35) and (C.36) provide an efficient way to compute the spectral function (5.29) for $\nu < \Theta_0$. This method is used in particular to generate the pink dotted line in Fig. 5.4(g).

In the limit $\mathbf{q} \to 0$ and $\nu \to 0$, we can find explicit analytical expressions for $\omega_{\mathbf{q}}$ and $M_{\mathbf{q}}$. To do so, we need the identity [123]

$$\sum_{\mathbf{k}} \left\{ \frac{E+E'}{EE'} \frac{EE'+\xi\xi'+\Delta^2}{(E+E')^2-\nu^2} - \frac{1}{E_{\mathbf{k}}} \right\} = \sum_{\mathbf{k}} \frac{E+E'}{2EE'} \frac{\nu^2-(\mathbf{k}\cdot\mathbf{q}/m)^2}{(E+E')^2-\nu^2}. \tag{C.37}$$

This makes it straightforward to check, in the low-frequency and long-wavelength limit, that $I_{11}(\mathbf{q},\nu) \approx \nu^2 J_2/4 - q^2 J_4/12m^2$, as well as $A_1(0,0) = J_\xi$, $A_2(0,0) = J_2/2$, $I_{12}(0,0) = J_\xi/2$, and $I_{22}(0,0) = -\Delta^2 J_2$, where J_2, J_4 and J_ξ are given in Eq. (5.8). In this approximation, the solution of $\omega_{\mathbf{q}} = \Omega(\mathbf{q},\omega_{\mathbf{q}})$ is found to be simply $\omega_{\mathbf{q}} = cq$, with c the sound speed given by Eq. (5.7). The collective mode response function is approximately

$$\chi_{\text{coll}}(\mathbf{q},\nu) \approx \frac{\Delta^2 J_2^2 \nu^2 + J_\xi^2 \omega_{\mathbf{q}}^2}{J_2(\nu^2-\omega_{\mathbf{q}}^2)}. \tag{C.38}$$

Upon using the relation $\Delta^2 J_4 = 3m\rho_0$, valid for $T \ll \Theta_0$ [123], we find a DSF of the form Eq. (C.33) with $M_{\mathbf{q}} = \varrho_0 \varepsilon_{\mathbf{q}}/\omega_{\mathbf{q}}$.

At frequencies $\nu > \Theta_0$, the imaginary parts of $\chi_{\text{pair}}(\mathbf{q},\nu+\mathrm{i}\epsilon)$, $\Omega(\mathbf{q},\nu+\mathrm{i}\epsilon)$ and $B(\mathbf{q},\nu+\mathrm{i}\epsilon)$ are all nonzero. These contributions are due to the Beliaev terms in the Eqs. (C.21) and (C.23)–(C.27), reflecting the contribution of fermionic pair excitations at frequencies above the gap. For example, direct pair production from the static condensate is described by the term

$$\begin{aligned} S_{\text{pair}}(\mathbf{q},\nu) &= -\frac{1}{\pi}\text{Im}\left[\chi_{\text{pair}}(\mathbf{q},\nu+\mathrm{i}\epsilon)\right] \\ &= \frac{1}{V}\sum_{\mathbf{k}} \frac{EE'-\xi\xi'+\Delta^2}{2EE'} \delta(\nu-E-E'), \end{aligned} \tag{C.39}$$

assuming as usual that $T \ll \Theta_0$. The imaginary part of $\Omega(\mathbf{q},\nu+\mathrm{i}\epsilon)$ can be interpreted as the damping rate of collective mode excitations due to Beliaev decay. This broadens the pole of Eq. (C.22), ultimately leading to contributions to the DSF of Lorentzian-like form. However, the explicit expression is cumbersome and yields little insight, therefore we do not quote it here.

Finally, we comment that at higher temperatures $T \gtrsim \Theta_0$, the Landau terms in Eqs. (C.21) and (C.23)–(C.27) become significant, leading to further contributions to the imaginary parts of $\chi_{\text{pair}}(\mathbf{q},\nu+\mathrm{i}\epsilon)$, $\Omega(\mathbf{q},\nu+\mathrm{i}\epsilon)$ and $B(\mathbf{q},\nu+\mathrm{i}\epsilon)$. These play a similar role to the Beliaev contributions discussed above, except that they may be appreciable even at frequencies $\nu \ll \Theta_0$.

Appendix D

Impurities in a neutral Fermi superfluid

D.1 Single impurity

In this appendix, we provide technical details of the master equation (and its derivation) used in Chapter 5. We first consider the problem of a single impurity immersed in a neutral Fermi superfluid. In particular, we prove the assertion made in the main text that bath-induced dephasing and transitions between degenerate sublevels can be neglected. We consider an isotropic potential confining the impurity, therefore each energy level above the ground state is triply degenerate. Including only the lowest two energy levels, the autonomous Hamiltonian of the impurity is

$$H_A = \sum_{a=1,2,3} \omega_0 \, |a\rangle\langle a| \,, \tag{D.1}$$

where $|a\rangle$ describes a motional excitation in the x_a direction, with $\{x_1, x_2, x_3\} = \{x, y, z\}$, while the ground state is denoted $|0\rangle$. All higher motional states are assumed to be off-resonant. In the following, Latin indices such as $a = 1, 2, 3$ enumerate only states in the excited manifold, while Greek indices such as $\alpha = 0, 1, 2, 3$ refer to all states.

The impurity-gas interaction is given by

$$H_{AB} = \sum_{\alpha,\beta=0}^{3} A_{\alpha\beta} \otimes B_{\alpha\beta}, \tag{D.2}$$

where $A_{\alpha\beta} = |\alpha\rangle\langle\beta|$ and

$$B_{\alpha\beta} = \frac{1}{V} \sum_{\mathbf{q}\neq 0} \lambda_{\mathbf{q}}^{(\alpha\beta)} \rho_{\mathbf{q}}, \tag{D.3}$$

with

$$\lambda_{\mathbf{q}}^{(\alpha\beta)} = \kappa \int \mathrm{d}^3\mathbf{r} \, \mathrm{e}^{\mathrm{i}\mathbf{q}\cdot\mathbf{r}} \phi_\alpha(\mathbf{r}) \phi_\beta(\mathbf{r}). \tag{D.4}$$

The wave functions in the harmonic approximation are given by $\phi_0(\mathbf{r}) \propto \mathrm{e}^{-r^2/2\ell^2}$ and $\phi_a(\mathbf{r}) \propto x_a \mathrm{e}^{-r^2/2\ell^2}$, where the normalisation factors have been neglected. The coupling

constants are found to be, for $a \neq b$,

$$\begin{aligned}
\lambda_{\mathbf{q}}^{(00)} &= \kappa \mathrm{e}^{-\ell^2 q^2/4}, \\
\lambda_{\mathbf{q}}^{(a0)} &= \frac{\mathrm{i}\kappa}{\sqrt{2}} \ell q_j \mathrm{e}^{-\ell^2 q^2/4}, \\
\lambda_{\mathbf{q}}^{(ab)} &= -\frac{\kappa}{2} \ell^2 q_j q_k \mathrm{e}^{-\ell^2 q^2/4}, \\
\lambda_{\mathbf{q}}^{(aa)} &= \kappa \left(1 - \frac{\ell^2 q^2}{2}\right) \mathrm{e}^{-\ell^2 q^2/4},
\end{aligned} \tag{D.5}$$

where $\{q_1, q_2, q_3\} = \{q_x, q_y, q_z\}$ denote the Cartesian components of $\mathbf{q}$. Our choice of real-valued wave functions means that $\lambda_{\mathbf{q}}^{(\beta\alpha)} = \lambda_{\mathbf{q}}^{(\alpha\beta)}$.

We now derive a master equation for the impurity density operator under the same approximations as in Chapter 5. The result takes the form

$$\frac{\mathrm{d}\rho_A}{\mathrm{d}t} = \mathrm{i}[\rho_A, H_A + H_{LS}] + \sum_{\alpha,\beta,\alpha',\beta'} \Gamma_{\alpha\beta\alpha'\beta'} \left(A_{\alpha\beta} \rho_A A_{\alpha'\beta'}^\dagger - \frac{1}{2} \{ A_{\alpha'\beta'}^\dagger A_{\alpha\beta}, \rho_A \} \right), \tag{D.6}$$

where the Lamb-shift Hamiltonian is

$$H_{LS} = \sum_{\alpha,\beta} \Xi_{\alpha\beta} A_{\alpha\beta}, \tag{D.7}$$

and we have defined the incoherent rates

$$\Gamma_{\alpha\beta\alpha'\beta'} = 2\pi \mathcal{I}_{\alpha\beta\alpha'\beta'}(\omega_{\beta\alpha}), \tag{D.8}$$

and energies

$$\Xi_{\alpha\beta} = \sum_{\beta'} \mathsf{P} \int_0^\infty \mathrm{d}\nu \, \frac{\mathcal{I}_{\beta'\beta\beta'\alpha}(\nu)}{\omega_{\beta\beta'} - \nu}, \tag{D.9}$$

with $\omega_{\beta\alpha} = \omega_\beta - \omega_\alpha$ the difference in energy between states $|\alpha\rangle$ and $|\beta\rangle$, i.e.

$$\omega_{\beta\alpha} = \begin{cases} \omega_0 & (\alpha = 0, \beta \neq 0) \\ -\omega_0 & (\beta = 0, \alpha \neq 0) \\ 0 & (\text{otherwise}), \end{cases} \tag{D.10}$$

while the spectral functions are

$$I_{\alpha\beta\alpha'\beta'}(\nu) = \begin{cases} \dfrac{1}{V} \displaystyle\sum_{\mathbf{q}\neq 0} \left(\lambda_{\mathbf{q}}^{(\alpha\beta)}\right)^* \lambda_{\mathbf{q}}^{(\alpha'\beta')} S(\mathbf{q}, \nu) & (\omega_{\beta\alpha} = \omega_{\beta'\alpha'}) \\ 0 & (\text{otherwise}). \end{cases} \tag{D.11}$$

The inversion symmetry of the Fermi superfluid implies that $S(\mathbf{q}, \nu) = S(-\mathbf{q}, \nu)$. This leads to an enormous simplification, since most of the 256 functions $I_{\alpha\beta\alpha'\beta'}(\nu)$ can be

shown to vanish identically. In particular, $\mathcal{I}_{\alpha\beta\alpha'\beta'}(\nu) = 0$ if any pair of indices are equal to each other, while the other pair of indices are not equal to each other. Furthermore, $\mathcal{I}_{\alpha\beta\alpha'\beta'}(\nu) = 0$ if all four indices are different. This leaves in total 40 nonzero functions of the form $\mathcal{I}_{\alpha\beta\alpha\beta}(\nu) = \mathcal{I}_{\beta\alpha\alpha\beta}(\nu)$ or $\mathcal{I}_{\alpha\alpha\beta\beta}(\nu)$. However, due to isotropy and the index permutation symmetry we are actually left with only 5 independent functions: $\mathcal{I}_{0000}(\nu)$, $\mathcal{I}_{00aa}(\nu)$, $\mathcal{I}_{aabb}(\nu)$, $\mathcal{I}_{0a0a}(\nu)$, and $\mathcal{I}_{abab}(\nu)$, for $a \neq b$.

Referring to Eq. (D.9), the aforementioned conditions imply that $\Xi_{\alpha\beta}$ vanishes unless $\alpha = \beta$. Therefore, the Lamb-shift Hamiltonian (D.7) describes a simple energy shift for each state. Furthermore, each sublevel of the excited state receives an identical shift relative to the ground state due to rotation symmetry. These energy shifts can be absorbed into the definition of the trapping frequency ω_0 and shall be ignored from here on.

Regarding the incoherent part of the master equation (D.6), three types of terms can be distinguished. First we consider dephasing processes, which are governed by terms in Eq. (D.6) with $\alpha = \beta$ and $\alpha' = \beta'$. The corresponding rates of the form $\Gamma_{\alpha\alpha\alpha'\alpha'}$ can be shown to vanish even at finite temperature, assuming that $T \ll \Theta_0$. To demonstrate this, we use the fact that, as shown in Appendix C, the dynamic structure structure factor in the limit $\nu \to 0$ is given by

$$S(\mathbf{q}, \nu) = \frac{\varrho_0 \varepsilon_{\mathbf{q}}}{\omega_{\mathbf{q}}} \left[(1 + n_{\mathbf{q}})\delta(\nu - \omega_{\mathbf{q}}) + n_{\mathbf{q}}\delta(\nu + \omega_{\mathbf{q}})\right], \tag{D.12}$$

valid for $T \ll \Theta_0$, where $n_{\mathbf{q}} = (\mathrm{e}^{\beta\omega_{\mathbf{q}}} - 1)^{-1}$ is the Bose-Einstein distribution and $\omega_{\mathbf{q}} = cq$ is the sound-like dispersion relation of long-wavelength phonons. Plugging this into the definitions (D.8) and (D.11), we obtain, for example,

$$\begin{aligned}
\Gamma_{0000} &= \lim_{\nu\to 0} \frac{2\pi}{V} \sum_{\mathbf{q}} |\lambda_{\mathbf{q}}^{(00)}|^2 S(\mathbf{q}, \nu) \\
&= \frac{\kappa^2 \rho_0}{2\pi m c^5} \lim_{\nu\to 0} \left[\nu^3 \coth\left(\frac{\beta\nu}{2}\right)\right] \\
&= 0.
\end{aligned} \tag{D.13}$$

A similar argument demonstrates that $\Gamma_{00aa} = \Gamma_{aa00} = \Gamma_{aabb} = 0$, therefore dephasing processes do not contribute to the master equation.

The second kind of incoherent process we consider are transitions between the three states comprising the upper energy level, occurring at a rate Γ_{abab}. It is straightforward to show that this rate also vanishes, following an analogous argument to the one presented in Eq. (D.13). In particular, we have that $\mathcal{I}_{abab}(\nu) \sim \nu^6$ as $\nu \to 0$. This shows that the rate of incoherent transitions between these sublevels is negligible, even if an anisotropic perturbation breaks the degeneracy and a small energy difference ν exists between these states.

The third kind of dissipative process corresponds to incoherent transitions between the ground and excited states, occurring at the rates Γ_{0a0a} and Γ_{a0a0}. If we assume that $\omega_0 \gg T$, as in Chapter 5, the rates Γ_{a0a0} are vanishingly small, and thus the probability of a transition from the ground state to one of the excited states is negligible. The state of the system thus remains within the subspace comprising the ground state and whichever excited motional state is addressed in the experiment. We conclude that the two-level approximation is valid, so long as $T \ll \omega_0, \Theta_0$. Within the qubit subspace, the master equation (D.6) is thus equivalent to the equation (5.14) in the main text, with $\gamma^- = \Gamma_{0a0a}$ and $\gamma^+ \approx 0$.

D.2 Multiple impurities

Now we consider the case where N impurities are immersed in the superfluid. In this section, we consider only two states for each impurity, which will be shown to be a self-consistent approximation. We assume that the energy splitting of each impurity qubit is identical, leading to the autonomous Hamiltonian

$$H_A = \sum_{j=1}^{N} \omega_0 \sigma_j^+ \sigma_j^-, \tag{D.14}$$

where $\sigma_j^+ = (\sigma_j^-)^\dagger = |1_j\rangle\langle 0_j|$ is the usual raising operator pertaining to impurity j.

We assume that the minimum of the potential confining impurity j is at position $\mathbf{x}_j$. The excited state of qubit j corresponds to motion in the direction parallel to the unit vector $\hat{\mathbf{d}}_j$, which may be different for each impurity. The vector $\hat{\mathbf{d}}_j$ can be understood as a kind of dimensionless acoustic dipole moment associated with each impurity. The interaction between the impurities will be seen to depend on the relative orientation of these dipole moments and their mutual separation vector.

We write the interaction between the impurities and the Fermi gas as

$$\begin{aligned} H_{AB} &= \kappa \sum_{j=1}^{N} \sum_{m,n=0}^{1} |m_j\rangle\langle n_j| \otimes \int \mathrm{d}^3\mathbf{r}\; \phi_m^{(j)}(\mathbf{r}-\mathbf{x}_j)\phi_n^{(j)}(\mathbf{r}-\mathbf{x}_j)\varrho(\mathbf{r}) \\ &= \frac{1}{V} \sum_{j=1}^{N} \sum_{m,n=0}^{1} |m_j\rangle\langle n_j| \otimes \sum_{\mathbf{q}\neq 0} \lambda_{\mathbf{q},j}^{(mn)} \mathrm{e}^{\mathrm{i}\mathbf{q}\cdot\mathbf{x}_j} \varrho_{\mathbf{q}}, \end{aligned} \tag{D.15}$$

where $\phi_m^{(j)}(\mathbf{r}-\mathbf{x}_j)$ denotes the wave function of impurity j in state $|m\rangle$, and the coupling constants are

$$\lambda_{\mathbf{q},j}^{(mn)} = \kappa \int \mathrm{d}^3\mathbf{r}\; \mathrm{e}^{\mathrm{i}\mathbf{q}\cdot\mathbf{r}} \phi_m^{(j)}(\mathbf{r})\phi_n^{(j)}(\mathbf{r}). \tag{D.16}$$

Upon deriving the master equation, the terms in Eq. (D.15) with $m = n$ give rise to three

contributions: dephasing, yet the rate for this vanishes according to the arguments in Section D.1; local energy shifts, which can be absorbed into the definition of the impurity trap frequencies; and a bath-mediated interaction between the qubits of the form $\sigma_j^z\sigma_k^z$, which does not affect the dynamics of populations in the energy eigenbasis. Since we are interested in the evolution of states that are diagonal in energy, we ignore these terms and obtain the simplified interaction Hamiltonian

$$H_{AB} = \frac{1}{V}\sum_j\sum_{\mathbf{q}\neq 0}\left(\lambda_{\mathbf{q},j}\mathrm{e}^{\mathrm{i}\mathbf{q}\cdot\mathbf{x}_j}\sigma_j^+\otimes\varrho_{\mathbf{q}} + \lambda_{\mathbf{q},j}^*\mathrm{e}^{-\mathrm{i}\mathbf{q}\cdot\mathbf{x}_j}\sigma_j^-\otimes\varrho_{\mathbf{q}}^\dagger\right), \tag{D.17}$$

where $\lambda_{\mathbf{q},j} = \lambda_{\mathbf{q},j}^{(10)}$.

We now derive a master equation describing the impurity density operator ρ_A under the same approximations as in Chapter 5. Neglecting the bath-induced renormalisation of the local qubit energies, and working at temperatures $T \ll \omega_0$, the master equation reads as

$$\frac{\mathrm{d}\rho_A}{\mathrm{d}t} = \mathrm{i}[\rho_A, H_A] + \mathrm{i}\sum_{j\neq k}\eta_{jk}[\rho_A, \sigma_j^+\sigma_k^-] + \sum_{j,k}\Gamma_{jk}\left(\sigma_j^-\rho_A\sigma_k^+ - \frac{1}{2}\{\sigma_k^+\sigma_j^-, \rho_A\}\right). \tag{D.18}$$

The couplings appearing above are given in terms of the spectral functions

$$\mathcal{I}_{jk}(\nu) = \frac{1}{V}\sum_{\mathbf{q}\neq 0}\lambda_{\mathbf{q},j}^*\lambda_{\mathbf{q},k}\cos\left(\mathbf{q}\cdot\mathbf{r}_{jk}\right)S(\mathbf{q},\nu), \tag{D.19}$$

where $\mathbf{r}_{jk} = \mathbf{x}_j - \mathbf{x}_k$ denotes the separation between impurities j and k. Note that $\mathcal{I}_{jk}(\nu)$ reduces to our standard definition (5.15) for $j = k$. The parameters entering the master equation above are given explicitly by

$$\Gamma_{jk} = 2\pi\mathcal{I}_{jk}(\omega_0), \tag{D.20}$$

$$\eta_{jk} = \mathsf{P}\int_0^\infty \mathrm{d}\nu\ \frac{\mathcal{I}_{jk}(\nu)}{\omega_0 - \nu}. \tag{D.21}$$

Our goal now is to find a spatial configuration such that $\mathcal{I}_{jk}(\nu) = 0$ for $j \neq k$, so that the impurities effectively decouple from one another. Evaluating the spectral functions in the thermodynamic limit, we use rotation invariance to obtain

$$\mathcal{I}_{jk}(\nu) = \kappa^2\int\frac{\mathrm{d}^3\mathbf{q}}{(2\pi)^3}\ \Phi_{jk}(q)S(\mathbf{q},\nu), \tag{D.22}$$

where we defined the dimensionless form factors

$$\Phi_{jk}(q) = \frac{1}{4\pi\kappa^2}\int_{S^2}\mathrm{d}\Sigma_{\mathbf{q}}\ \lambda_{\mathbf{q},j}^*\lambda_{\mathbf{q},k}\cos(\mathbf{q}\cdot\mathbf{r}), \tag{D.23}$$

while $\mathrm{d}\Sigma_{\mathbf{q}}$ denotes the surface element on the unit sphere in momentum space. Within the isotropic, harmonic approximation for the impurity wave functions, we have that $\phi_m^{(j)}(\mathbf{r}) \propto H_m(\hat{\mathbf{d}}_j \cdot \mathbf{r}/\ell)\mathrm{e}^{-r^2/2\ell^2}$, where $H_m(z)$ denotes the m^{th} Hermite polynomial. Hence, the leading-order contribution to Eq. (D.23) as $r_{jk} \to \infty$ is

$$\Phi_{jk}(q) \approx \frac{1}{2}\ell^2 q^2 \mathrm{e}^{-\ell^2 q^2/2}\mathrm{sinc}(qr_{jk}) \left(\hat{\mathbf{d}}_j \cdot \hat{\mathbf{r}}_{jk}\right)\left(\hat{\mathbf{d}}_k \cdot \hat{\mathbf{r}}_{jk}\right), \tag{D.24}$$

where $\hat{\mathbf{r}}_{jk}$ is a unit vector parallel to $\mathbf{r}_{jk}$. This approximation is valid in the limit $qr_{jk} \gg 1$, and since only values $q \sim \ell^{-1}$ contribute to Eq. (D.24) significantly, this corresponds to the far-field condition $r_{jk} \gg \ell$.

Now consider the case where the motion of each impurity is excited in the same direction $\hat{\mathbf{d}}_j = \hat{\mathbf{d}}$. By arranging the impurities in a regular array with lattice vector $\mathbf{b}$, such that $\mathbf{b} \cdot \hat{\mathbf{d}} = 0$ and $b \gg \ell$, it follows from Eq. (D.24) that $\Phi_{jk}(q) = 0$ for $j \neq k$. In such a configuration, the impurities evolve independently according to the master equation (5.14) in the main text. Note also that Eq. (D.24) implies that the population of each impurity's motional states in directions orthogonal to $\hat{\mathbf{d}}$ are not influenced by the other impurities in the lattice. Therefore, the two-level approximation is self-consistent.